FACULTY OF ENGINEERING
AND ARCHITECTURE

Impact of Ageing on Arterial Physiology and Hemodynamics: Insights from 1D Modelling and In Vivo Data

Daimé Campos Arias

Doctoral dissertation submitted to obtain the academic degree of
Doctor of Biomedical Engineering

Supervisors
Prof. Patrick Segers, PhD* - Prof. Tania Rodriguez Moliner, PhD**

* Department of Electronics and Information Systems
Faculty of Engineering and Architecture, Ghent University

** Department of Machinery Construction Technology
Faculty of Mechanical Engineering, Universidad Tecnológica de La Habana José Antonio Echeverría, Cuba

July 2021

GHENT
UNIVERSITY

ISBN 978-94-6355-507-4
NUR 954
Wettelijk depot: D/2021/10.500/55

Members of the Examination Board

Chair

Honorary Prof. Ronny Verhoeven, PhD, Ghent University

Other members entitled to vote

Jordi Alastruey, PhD, King's College London, United Kingdom
Prof. Charlotte Debbaut, PhD, Ghent University
Koen D. Reesink, PhD, Universiteit Maastricht, the Netherlands
Prof. Ernst Rietzschel, PhD, Ghent University
Prof. Barbara Vanderstraeten, PhD, Ghent University

Supervisors

Prof. Patrick Segers, PhD, Ghent University
Prof. Tania Rodriguez Moliner, PhD, Universidad Tecnológica de La Habana José Antonio Echeverría, Cuba

To Dylan, my little wonder

PREFACE

Some years ago I was starting a master in mathematical modelling at Cujae and in need of a research topic, when I was introduced to professor Melchor who suggested to study about arterial wall properties. The topic was completely new to me as I just had obtained my degree on nuclear engineering with a thesis on carbon nanotubes, but I found it very interesting and decided to join the Biomechanics research group at Cujae. Not long after that I found myself giving a presentation to the professors of Ghent University that were part of a project between both universities. Back then my English was very poor and my presentation was a very basic research on the state-of-the-art. Professor Patrick Segers, who was the leader of the project for the Belgian side (prof. Tania was it for the Cuban one), took an interest and offered me a more concrete research purpose. It was then when this journey towards a PhD started, although it did not materialize until much later, when I had my first internship in Ghent, and more formally when I got a scholarship from UGent four years ago. Doing a PhD has been very challenging. I had to overcome many stressful periods and a couple of existential crises, but it has also involved many rewarding moments and a lot of personal growing. It has given me a more scientific perspective, and hopefully my research will show to be a valuable contribution to the scientific community. The following words are for all the people that were there for me, helping me all the way.

My first thank you goes to my supervisor Patrick. Thank you for all your patience (I know you have needed a lot of it with me), for your support in the difficult times, for your incredible efficiency providing feedback to my written works, for challenging my reasoning with your comments and your constructive critics, and for having more confidence in me than myself. I will always be grateful that you gave me such a fantastic opportunity (even when I barely could speak English to you in our first meeting). I am also very grateful to Tania for all the support and encouragement, for giving me the opportunity to be part of the project although I was one of the last to join the lab, for helping me with the bureaucracy in Cujae, and for not doubting in taking over the supervisor role when we lost professor Melchor.

I wish to thank all the colleagues and professors that collaborated with me for the different papers. To professors Ernst Rietzschel and Julio Chirinos for your invaluable insights in our recent work with the Asklepios study. To Marc De Buyzere for all the insights in statistics. To professor Nikos Stergiopulos for allowing me to make use of the 1D model. To Lisse Vera for our work with the horse model. To Jim Georgakopoulos for answering all my questions on the C-Pulse device.

I would also like to thank all the members of the exam committee for accepting to be part of it with such short notice, and for all your suggestions to improve this thesis.

My PhD was of the sandwich-type, allowing me to go forth and back between my home university (Cujae) and UGent, and giving me the opportunity to work with many people from both universities. Thank you to all past and present colleagues at bioMMeda, it has been great to be surrounded with people from so many nationalities (Italy, Belgium, Iran, China, Brazil, India). Thanks to Daniela and Ghazal for our trip together. To Viviana and Federico for the great dinners. To Guille, Danilo, Shengda, and Amith for the fun moments. As a Cuban that never travelled abroad before, it was a dream come true to come to Europe the first time, but also very shocking; I am sincerely grateful to Saskia for all the administrative arrangements, making the whole experience much easier. Thanks also to Jurgen for all the technical assistance. I also want to thank all the former colleagues at Cujae (Marón, Tere, China, Yolanda, Orestes, Annamaris, Sandra, Guivey, Alejandro, Ernestico, Osmel, Dariel, and many others) for all the good memories.

My special thank you is for Nic, for being the most wonderful partner one could wish for. Thank you for your patience in handling my stress, for answering my many questions, for proofreading this thesis, and for not letting me starve during the deadline periods. This PhD would not have been possible without your unconditional support and motivation. Especially, thank you for taking such good care of our little one in these last weeks, allowing me to focus during this final stage of my PhD. I would also want to thank my family in law for all their encouragement and for making the physical distance from my family more bearable.

Por último, quiero agradecer a todas mis amistades y familiares, que aún desde lejos han estado al tanto de mis proyectos. A Annamaris por ser la mejor amiga, por siempre preocuparte por mí, y porque también eres responsable de que yo haya decidido empezar esta experiencia única que ha sido el doctorado. En especial gracias a mi familia por siempre creer en mí y apoyarme en todas mis decisiones. A mi mamá, gracias por siempre estar ahí para mí – yo sé que estás más orgullosa de que yo haya terminado el doctorado que yo misma. A mi papá, gracias por tu apoyo incondicional, por haberme motivado a continuar hasta el final, y por siempre estar dispuesto a escuchar sobre mi investigación. A mis hermanas, mi hermano, y Ligxa, por haber escuchado pacientemente mis quejas durante estos años. Gracias a mi abuelo Edecio que me animó tanto a aprender inglés para poder estudiar en una universidad extranjera, y a mi abuela Iris por darme tanto cariño. Finalmente, gracias a la personita que me ha acompañado en la última parte de este viaje, por darme el coraje necesario para terminar y un nuevo propósito de vida. Lo siento por hacerte pasar por todo este estrés. ¡Llegaste último, pero eres quien más importa!

Daimé Campos Arias
Ghent, July 2021

SUMMARY

INTRODUCTION

Cardiovascular diseases (CVDs) remain one of the main causes of mortality and morbidity worldwide, with major incidence in the ageing and elderly population. Global demographic trends continue to project an increase in this population in the next decades, wherewith older adults are expected to present a major burden for the healthcare system in the future. Detrimental hemodynamic changes associated with ageing have been found to influence the development and progression of various CVDs. Moreover, the increasing study of pulse wave propagation in the arterial system has allowed researchers to explain specific age-related changes in hemodynamics and their association with the risk of CVD. Therefore, it is of primary importance to study the effects of ageing on the hemodynamics and arterial function, in order to determine the mechanisms by which they relate to the risk of CVD; and to deepen the understanding of pressure and flow wave propagation phenomena in the arterial tree, which is also of interest for the development of new therapies and diagnosis of CVD.

This thesis was developed within this context and it was structured in three main parts. Part I comprises a description of fundamental hemodynamics and cardiovascular concepts and state of knowledge, which are important to understand the series of studies that conform this PhD project. The first aim of this dissertation is to gain a deeper understanding of arterial hemodynamics and wave travel and reflection, from the use of an *in silico* one-dimensional (1D) model of the systemic circulation in different applications. These studies are clustered in Part II. A second major aim is to investigate and assess the effective impact of ageing on arterial system properties and wave travel. For this purpose in Part III, we explore the longitudinal *in vivo* data of the Asklepios large population of middle-aged subjects.

HEMODYNAMICS AND WAVE PROPAGATION IN THE ARTERIAL TREE

Anatomy, physiology and basic hemodynamic principles

Chapter 1 gives a brief description of the anatomy and physiology of the human cardiovascular system, focusing on the heart and the arterial system. A second section provides an overview of the cardiovascular pathologies of interest in the current dissertation, namely heart failure and arterial stiffening with ageing. Pulse wave velocity (PWV) is then introduced as an easier and valid way of quantifying large artery stiffness, with a prognostic value for CVDs. The relevant methods for its estimation are explained, with a major focus on transit time methods and loop-based methods to estimate PWV at a single location. Pressure and flow wave propagation in the cardiovascular system is described, as it is a primary object of study of this dissertation, with particular emphasis on wave reflections and wave separation analysis. Finally, in the last part of this section, wave intensity and wave power analysis are explained, which will be used in subsequent chapters to provide insight on wave dynamics in the cardiovascular system.

Modelling the cardiovascular system

One-dimensional models of the cardiovascular system are a powerful tool to understand pulse wave propagation along the systemic arterial system in normal conditions, or how the propagation patterns are affected by changes in the geometry and functional properties of the arterial system, due to pathologies, anatomical variations, or clinical interventions. Because modelling allows for the flexibility of investigating these different scenarios in well controlled simulations, it can contribute valuably to answering physiological and pathophysiological questions arising in cardiovascular research. In this thesis we make use of a 1D model of the systemic arterial tree, which has been previously developed and validated with *in vivo* data in humans, to study pulse wave propagation and arterial hemodynamics in several applications. The mathematical formulation and description of the 1D model of the systemic circulation is provided in Chapter 2. Here we focus on describing the general features of the model relevant for the studies grouped in Part II of the thesis. In each of these studies, subsequent adaptations to the model were made in order to meet their respective objectives.

APPLICATIONS OF THE 1D MODEL OF THE SYSTEMIC ARTERIAL TREE

Hemodynamic impact of the C-Pulse cardiac support device

In Chapter 3, the 1D model is applied to study the impact of a heart assist device on arterial hemodynamics. The C-Pulse heart assist system is an extra-aortic counterpulsation device intended to unload the heart in patients with heart failure while increasing coronary perfusion. We implement the function of the device in the model and simulate central and peripheral pressure and flow waveforms in assisted and unassisted cardiac cycles for three scenarios: control case representing a young and healthy subject, and two other cases representing a young and older subject with heart failure with reduced ejection fraction. The simulation outcomes are qualitatively compared with *in vivo* data measured noninvasively in three patients with heart failure and with invasive data measured in a pig. Wave intensity analysis is used to provide more insight into the effects of the device on pulse wave propagation. We showed that activation of the C-Pulse causes a diastolic augmentation in the pressure and flow waveforms, which is associated with a forward travelling compression wave; whereas a forward travelling expansion wave is associated with the device relaxation, with waves exerting an action in the vascular beds including coronary arteries. The stiffness of the arterial tree was found to be an important determinant of the hemodynamic benefits of the device, with stiffer aortas requiring higher values of the cuff inflation pressure for the same level of compression, leading in turn to stronger mechanical effects and enhanced perfusion.

Numerical assessment and comparison of loop-based local PWV methods

Several so-called loop-based methods have been proposed to estimate local PWV. However, previous studies have demonstrated inaccuracies in local PWV-estimates due to presence of wave reflections. In Chapter 4, we assess the accuracy of PWV-estimates from different loop methods throughout the human arterial tree, and quantify the impact of possible over- or underestimation of PWV on subsequent wave separation analysis, based on data from the 1D model. We simulate the physiological signals (i.e. pressure (P), flow (Q), flow velocity (U), area (A) and diameter (D) waveforms) needed for the estimations of local PWV methods in a reference case, and in a case with lower distensibility representing ageing. Local PWV by the PU-loop, ln(D)U-loop, ln(D)P-loop, and QA-loop methods, as well as a previously proposed reflection-correction method (PWV_{1-5}), are compared against the reference value obtained from the Bramwell-Hill equation. We showed that the PU-loop overestimates PWV by more than 20% for most arterial sites, while the ln(D)U- and QA-loop underestimate to the same extent at these same locations. The reflection-insensitive ln(D)P-loop and the frequency-domain method PWV_{1-5}, performed well for most vascular sites. Additionally, large errors in PWV estimates were attenuated in subsequent wave separation analysis, but the errors were site-dependent. We found the accuracy of loop-based methods to be highly dependent on the location where they are applied, thus we recommend great caution when interpreting results.

A 1D model of the arterial circulation in horses

Assessment, diagnosis and treatment of the cardiovascular system of the horse is an important field of study in veterinary science due to the socio-economic value of equestrian sports and horse breeding. Nonetheless, relatively little is known about equine arterial hemodynamics because it is technically and ethically challenging to investigate a large number of arteries. In Chapter 5, a 1D model of the equine arterial circulation is developed based on the human 1D model of the systemic arterial system, in order to further gain insight into equine arterial hemodynamics and physiology. Anatomical data of lengths, diameters and branching angles, collected *post-mortem* from five horses for the aorta and its most significant branches toward the head, abdominal organs and four limbs, are used as the input data for the model. Cardiac and arterial parameters of the model are tuned to equine physiology based on *in vivo* flow (ultrasound) and pressure (invasive) data measured at few arterial locations, as well as data from the literature. Given the large arterial diameters, Womersley correction is used upon computation of friction coefficients. Overall, model predictions were in line with measured pressure and flow waveforms. Inclusion of gravity in the model improved predicted waveforms. The resulting horse model can be used in the future to study various types of pathologies or physiological changes in local pressure and flow profiles, as a result of strenuous exercise or changes due to ageing, breed or gender.

ARTERIAL AGEING, HEMODYNAMICS AND STIFFNESS IN MIDDLE-AGED INDIVIDUALS: INSIGHTS FROM THE ASKLEPIOS STUDY

Longitudinal changes of PWV, input impedance, and wave reflection parameters

Virtually all knowledge we have on the impact of age on arterial hemodynamics and arterial system properties results from cross-sectional studies, where a representative sample of the population is screened at a given moment in time. The evolution of arterial system properties with age within the same individuals requires better understanding, which can only be determined from longitudinal studies. In Chapter 6 we use noninvasive ultrasound and applanation tonometry measurements in central arteries, in combination with computational derivation of parameters and statistical methods, to assess the 10-years longitudinal evolution of central input impedance parameters, wave reflection indices, and pulse wave velocity in the Asklepios population, a seemingly healthy middle-aged cohort at study initiation. Extra analyses also accounted for the influence of cardiovascular risk factors on the age-related changes in the arterial properties, as well as the longitudinal interplay of blood pressure and arterial stiffness. We found that PWV increases with ageing but less than expected from the cross-sectional data, and this increase was higher in older women compared to men. An increase in PWV was not paralleled by a decrease in arterial compliance, mainly in younger males. Moreover, aortic characteristic impedance decreased in the younger while increased for the older subjects. On the other hand, wave reflection decreased in the 10-years period, and systemic vascular resistance showed an increase in women and a decrease in men. Overall, the observed discrepancies between longitudinal and cross-sectional data remained after exclusion of hypertensive subjects, or when accounting for several cardiovascular risk factors. Our results might be an effect of aortic remodelling with ageing, or the influence of socio-economic or lifestyle factors, which cannot be determined without further studies. This work evidences that cross-sectional studies fall short in reflecting the effective impact of ageing on arterial system properties.

Conclusions

The major findings of the thesis are summarized in a concluding chapter. We also discussed general limitations of the studies and look into the future perspectives, suggesting directions for future work.

SAMENVATTING

INLEIDING

Hart- en vaatziekten (HVZ) zijn nog steeds de wereldwijde hoofdoorzaak van mortaliteit en morbiditeit, en dit vooral bij het oudere en vergrijzende deel van de bevolking. Globale demografische trends wijzen op een toename van de vergrijzing de komende decades, met de daarbij horende stijgende druk op de toekomstige gezondheidszorg. Men heeft aangetoond dat veranderingen in de hemodynamica als gevolg van veroudering de ontwikkeling en het verloop van diverse HVZ nadelig beïnvloeden. Bovendien laat toegenomen kennis over het fenomeen polsgolfpropagatie (Engels: pulse wave propagation) in het arteriële systeem onderzoekers toe om bepaalde leeftijdsgerelateerde veranderingen in de hemodynamica te verklaren en deze te koppelen aan het risico op HVZ. Om de mechanismen die verantwoordelijk zijn voor een verhoogd risico op HVZ bloot te leggen is het dus van essentieel belang de invloed van veroudering op de hemodynamica en arteriële werking te onderzoeken. De vooruitgang van ons begrip van druk- en stroomgolfpropagatiefenomenen binnen het bloedvatenstelsel is daarnaast belangrijk voor de ontwikkeling van nieuwe behandelingswijzen en de diagnose van HVZ.

Deze thesis is tot stand gekomen binnen bovengenoemde context en is opgedeeld in drie hoofddelen. Deel I omvat een beschrijving van fundamentele hemodynamische en cardiovasculaire concepten en de huidige stand van kennis, wat nodig is voor een goed begrip van de reeks papers die is opgenomen in dit doctoraatsonderzoek. Het eerste doel van dit proefschrift is het verkrijgen van een dieper inzicht in arteriële hemodynamica en golfpropagatie en -reflectie, door het gebruik van een *in silico* eendimensionaal (1D) model van de bloedsomloop binnen verschillende toepassingen. De papers voortkomend uit dit onderzoek zijn als afzonderlijke hoofdstukken in Deel II van deze thesis opgenomen. Een tweede belangrijk doel van deze studie is te onderzoeken en te bepalen wat de impact is van veroudering op de eigenschappen van het arteriële systeem en golfpropagatie. Daarom belicht Deel III de *in vivo* longitudinale gegevens uit de Asklepios studie, die een grote populatie van individuen van middelbare leeftijd omvat.

HEMODYNAMICA EN GOLFPROPAGATIE IN HET SLAGADERSTELSEL

Anatomie, fysiologie en fundamentele hemodynamische begrippen

Hoofdstuk 1 geeft eerst een beknopte beschrijving van de anatomie en de fysiologie van het menselijke hart-en bloedvatenstelsel, met een focus op het hart en het arteriële systeem. Een tweede sectie bevat een overzicht van de voor dit onderzoek belangrijke pathologieën, namelijk hartfalen en vaatwandverstijving door veroudering. Vervolgens wordt het begrip polsgolfsnelheid (Engels: pulse wave velocity, PWV) geïntroduceerd als een eenvoudigere doch valide manier om arteriële stijfheid te kwantificeren, met bovendien prognostische waarde voor HVZ. De relevante methoden voor de schatting van PWV worden uitgelegd, met nadruk op transittijdmethoden en lus-gebaseerde methoden om PWV te bepalen op een enkele locatie. Druk- en stroompolspropagatie in het cardiovasculair stelsel worden beschreven, met een focus op golfreflecties en golfseparatie-analyse. In het laatste deel van dit hoofdstuk worden golfintensiteit- en golfvermogenanalyse uitgelegd, vermits deze in de volgende hoofdstukken zullen gebruikt worden om inzicht te verkrijgen in de golfdynamica in het hart- en bloedvatenstelsel.

Modellering van het cardiovasculair stelsel

Eendimensionale modellen van het cardiovasculair stelsel zijn een krachtige tool bij de beschrijving van polsgolfpropagatie doorheen het arteriële systeem in normale omstandigheden, of bij de studie naar het effect van wijzigingen in de geometrische en functionele eigenschappen van het arteriële systeem op golfpropagatiepatronen als gevolg van pathologieën, anatomische variaties of klinische interventies. Modellering laat toe om heel flexibel verschillende scenario's in goed gecontroleerde omstandigheden te simuleren en draagt aldus bij tot het beantwoorden van bepaalde fysiologische en pathofysiologische vraagstukken binnen het cardiovasculaire onderzoeksdomein. In deze thesis maken we gebruik van een eerder ontwikkeld en met behulp van *in vivo* data gevalideerd 1D-model van de systemische arteriële circulatie bij mensen, om polsgolfpropagatie en arteriële hemodynamica te bestuderen binnen verschillende toepassingen. Een wiskundige beschrijving van het 1D-model van de systemische circulatie wordt gegeven in Hoofdstuk 2. Hierbij focussen we op de algemene eigenschappen van het model die relevant zijn voor de publicaties opgenomen in Deel II van deze thesis. Het 1D-model werd voor elk van deze publicaties aangepast om te voldoen aan hun respectieve objectieven.

TOEPASSINGEN VAN HET 1D-MODEL VAN DE SYSTEMISCHE ARTERIËLE CIRCULATIE

Hemodynamische impact van het C-Pulse cardiac support device

In Hoofdstuk 3 wordt het 1D-model toegepast om de invloed van een hartondersteunend apparaat op de arteriële hemodynamica te bestuderen. Het C-Pulse cardiac support device is een extra-aortische tegenpulsatiepomp bedoeld om de hartspier van patiënten met hartfalen te ontlasten en de coronaire perfusie te bevorderen. We implementeren de werking van het device in het model en simuleren de centrale en perifere druk- en stroomgolfvormen in hartcycli met en zonder ondersteuning voor de volgende drie scenario's: als controle-case een jonge en gezonde persoon, en vervolgens een jonge en een oude persoon met hartfalen en verminderde ejectiefractie. De uitkomsten van de simulaties worden kwalitatief vergeleken met *in vivo* data afkomstig uit non-invasieve metingen bij drie patiënten met hartfalen en een invasieve meting in een varkensmodel. Vervolgens verkrijgen we via golfintensiteitanalyse inzicht in de effecten van het device op polsgolfpropagatie. We tonen aan dat activatie van het C-Pulse apparaat een diastole verhoging in de druk- en stroomgolfvormen veroorzaakt, hetgeen geassocieerd wordt met een voorwaarts bewegende compressiegolf; terwijl een voorwaarts bewegende expansiegolf geassocieerd wordt met de relaxatiefase van het apparaat, waarbij deze golven zorgen voor extra perfusie van de bloedvaten met inbegrip van de kransslagaders. We toonden aan dat vasculaire stijfheid een belangrijke determinant is voor de goede hemodynamische werking van het C-Pulse apparaat, waarbij een stijvere aorta een hogere cuffinflatiedruk vereist voor eenzelfde mate van compressie, hetgeen leidt tot sterkere mechanische effecten en een verbeterde perfusie.

Numerieke beschrijving en vergelijking van lus-gebaseerde lokale PWV-methoden

Er bestaan verschillende zogenaamde lus-gebaseerde methoden om lokale PWV te benaderen. Voorgaande studies hebben echter aangetoond dat er onnauwkeurigheden optreden in lokale PWV-schattingen als gevolg van golfreflecties. In Hoofdstuk 4 bepalen we de accuraatheid van PWV-benaderingen uit verschillende lus-methoden doorheen het arteriële systeem van de mens, en kwantificeren we de impact van mogelijke over- of onderschattingen van PWV op golfseparatie-analyse, gebaseerd op data van het 1D-model. We simuleren de fysiologische signalen (golfvormen voor druk (P), debiet (Q), stroomsnelheid (U), doorsnede-oppervlakte (A) en diameter (D)) nodig voor de bepaling van lokale PWV via verschillende methoden bij een referentiecase en bij een case met lagere distensibiliteit ten gevolge van veroudering. Uitkomsten voor lokale PWV bij de PU-lus, ln(D)U-lus, ln(D)P-lus en QA-lus methode, alsook bij de eerder voorgestelde reflectie-correctie methode

(PWV_{1-5}), worden vergeleken ten opzichte van de referentiewaarde bekomen door de Bramwell-Hillvergelijking. We toonden aan de de PU-lus de PWV met meer dan 20% overschat voor de meeste arteriële sites, terwijl de ln(D)U- en QA-lus de PWV evenveel onderschatten op dezelfde locaties. De reflectie-ongevoelige ln(D)P-lus en de frequentiedomein-methode PWV_{1-5} presteerden goed op de meeste vasculaire sites. Verder konden we waarnemen dat grote afwijkingen in PWV-schattingen worden afgezwakt bij separatieanalyse, hoewel locatieafhankelijk. We besloten dat de nauwkeurigheid van lus-gebaseerde methoden sterk afhangt van de locatie waarop ze worden toegepast, en raadden dus grote voorzichtigheid aan bij de interpretatie van zulke uitkomsten.

Een 1D-model van de arteriële bloedsomloop bij paarden

De beschrijving, diagnose en behandeling van het hart-en vaatstelsel van paarden is een belangrijk onderzoeksgebied binnen de diergeneeskunde door de hoge socio-economische waarde van de paardensport en -fokkerij. Nochtans is er relatief weinig bekend omtrent de arteriële hemodynamica bij paarden omdat het technisch en ethisch uitdagend is om zo'n groot aantal bloedvaten te onderzoeken. In Hoofdstuk 5 ontwikkelen we een 1D-model van de arteriële circulatie bij paarden, gebaseerd op het eerder genoemde 1D-model voor mensen, met als doel verder inzicht te verkrijgen in de arteriële hemodynamica en fysiologie van het paard. Anatomische data zoals lengte, diameter en vertakkingshoek, opgemeten *post-mortem* bij vijf paarden voor de aorta en haar voornaamste vertakkingen richting de kop, de abdominale organen en de vier ledematen, worden gebruikt als input voor het model. De parameters voor het hart en de slagaders worden aangepast naar de fysiologie van het paard gebaseerd op *in vivo* metingen van bloedstroom (echografie) en bloeddruk (invasief) op verschillende arteriële sites, aangevuld met data uit de literatuur. Womersley-correctie, gebaseerd op de berekening van wrijvingscoëfficiënten, is nodig omwille van de grote diameters van de bloedvaten. Over het algemeen waren de uitkomsten van het model in lijn met de gemeten golfvormen voor druk en snelheid. Inclusie van zwaartekracht in het model verbeterde de voorspelde golfvormen. Het hier ontwikkelde model voor het paard kan in de toekomst gebruikt worden voor de studie van verschillende pathologische en fysiologische veranderingen in lokale druk- en stroomprofielen, bijvoorbeeld onder invloed van uitputtende inspanning, leeftijd, ras of geslacht.

ARTERIËLE VEROUDERING, HEMODYNAMICA EN STIJFHEID BIJ INDIVIDUEN VAN MIDDELBARE LEEFTIJD: INZICHTEN UIT DE ASKLEPIOS STUDIE

Longitudinale veranderingen van PWV, input-impedantie en golfreflectieparameters

Nagenoeg al onze kennis omtrent de impact van leeftijd op arteriële hemodynamica en de eigenschappen van de bloedcirculatie is afkomstig uit cross-sectioneel onderzoek, waarbij een representatief deel van de bevolking gescreend wordt op een gegeven ogenblik in de tijd. De verandering van de bloedcirculatie als gevolg van veroudering binnen eenzelfde individu vereist echter inzichten die enkel kunnen bekomen worden uit longitudinale studies. In Hoofdstuk 6 combineren we non-invasieve echografische en applanatietonometrie metingen in de centrale slagaders met computationeel afgeleide parameters en statistiek om de longitudinale evolutie van centrale input-impedantie, golfreflecties, en PWV te beschrijven voor de Asklepios studie, een cohorte van individuen van middelbare leeftijd in schijnbaar goede gezondheid bij aanvang van de studie. Bijkomende analyses hielden ook rekening met de invloed van cardiovasculaire risicofactoren op leeftijdsgerelateerde veranderingen in de arteriële eigenschappen en het longitudinale samenspel van bloeddruk en arteriële stijfheid. We observeerden dat PWV toeneemt met de leeftijd, doch in mindere mate dan zou afgeleid worden uit cross-sectionele data. Deze toename was bovendien groter bij vrouwen dan bij mannen. Een toename van de PWV ging niet hand in hand met een afname van de arteriële compliantie, en dit vooral bij jongere mannen. Bovendien nam de karakteristieke impedantie van de aorta af bij jongere proefpersonen terwijl deze toenam voor oudere. Anderzijds was er een afname van de golfreflecties over de tienjarige looptijd van het onderzoek, terwijl de systemische vasculaire weerstand een toename vertoonde bij vrouwen en een afname bij mannen. Over het algemeen bleven de verschillen tussen observaties uit longitudinaal en cross-sectioneel onderzoek overeind, ook na exclusie van personen met hypertensie en rekening houdend met verschillende cardiovasculaire risicofactoren. We veronderstellen dat hermodellering van de aorta bij veroudering, de invloed van socio-economische factoren of veranderingen in levensstijl mogelijke verklaringen vormen voor onze bevindingen, maar verder onderzoek is noodzakelijk om deze te bevestigen. Deze paper toont aan dat cross-sectionele studies tekortschieten bij het observeren van de effectieve impact van veroudering op de eigenschappen van het bloedvatenstelsel.

CONCLUSIE

De belangrijkste bevindingen van deze thesis worden samengevat in een besluitend hoofdstuk. We lijsten ook de voornaamste beperkingen van de verschillende studies op en werpen een blik op de toekomst met aanbevelingen voor verder bijkomend onderzoek.

CONTENTS

List of Figures

LIST OF TABLES

ABBREVIATIONS AND SYMBOLS

Abbreviations

0D	Zero-dimensional
1D	One-dimensional
3D	Three-dimensional
AIx	Augmentation index
ANCOVA	Analysis of covariance
ANOVA	Analysis of variance
AP	Augmented pressure
BCW	Backward compression wave
BEW	Backward expansion wave
BLSA	Baltimore longitudinal study of ageing
BMI	Body mass index
BP	Blood pressure
BSA	Body surface area
CCA	Common carotid artery
cfPWV	Carotid-femoral pulse wave velocity
CIs	Confidence intervals
CO	Cardiac output
CV	Cardiovascular
CVD	Cardiovascular disease
DBP	Diastolic blood pressure
ECG	Electrocardiogram
EDV	End-diastolic volume
EF	Ejection fraction
ES	End-systole
ESP	End-systolic pressure
ESV	End-systolic volume
EVA	Early vascular ageing
FCW	Forward compression wave
FEW	Forward expansion wave
FHS	Framingham heart study

HF	Heart failure
HFpEF	Heart failure with preserved ejection fraction
HFrEF	Heart failure with reduced ejection fraction
HR	Heart rate
IABP	Intraaortic balloon pump
LME	Linear mixed-effect
LV	Left ventricle
LVAD	Left ventricular assist device
LVOT	Left ventricular outflow tract
MAP	Mean arterial pressure
MRI	Magnetic resonance imaging
MSE	Mean squared error
PP	Pulse pressure
PPM	Pulse pressure method
PWV	Pulse wave velocity
RV	Right ventricle
RWTT	Reflected wave transit time
SBP	Systolic blood pressure
SD	Standard deviation
SEM	Standard error of the mean
SUPERNOVA	Supernormal vascular ageing
SV	Stroke volume
SVR	Systemic vascular resistance
TT	Transit time
WIA	Wave intensity analysis
WK	Windkessel
WPA	Wave power analysis
WSA	Wave separation analysis

Symbols

α	Womersley number	[-]
Γ	Reflection coefficient	[-]
κ	Constant of proportionality	[s/mL]
μ	Dynamic viscosity	[Pa·s]
ω	Angular frequency	[rad/s]
$\overline{d}$	Mean arterial lumen diameter	[m]
π	Pi number	[3.1416]
ψ	Arterial wall seepage	[m^2/s]
ρ	Density	[kg/m^3]
τ	Wall shear stress	[Pa]

b	Body force	[N/m^3]
$\mathrm{d}\pi$	Wave power	[W]
$\mathrm{d}I$	Wave intensity	[W/m^2]
u	Vector of fluid velocity	[m/s]
A	Cross-sectional area	[m^2]
c	Wave speed	[m/s]
C_A	Area compliance	[m^2/mmHg]
C_V	Volume compliance	[m^3/mmHg]
C_T	Terminal compliance	[m^3/Pa]
D	Diameter	[m]
D_w	Distensibility	[mmHg^{-1}]
E_max	Maximal elastance	[Pa/m^3]
E_min	Minimal elastance	[Pa/m^3]
f	Frequency	[s^{-1}]
g	Gravitational acceleration constant	[9.81 m/s^2]
J_0, J_1	Bessel functions of first kind of order 0 and 1	[-]
L	Distance	[m]
m	Mass	[kg]
P	Blood pressure	[mmHg]
$P_\mathrm{end\text{-}dias}$	End-diastolic pressure	[mmHg]
P_maxC, P_width	Langewouters model coefficients	[mmHg]
P_b	Backward pressure waveform	[mmHg]
P_f	Forward pressure waveform	[mmHg]
Q	Blood flow	[mL/s]
R	Lumen radius	[m]
r	Radial coordinate	[m]
R_1	Proximal resistance	[mmHg·s/mL]
R_2	Distal resistance	[mmHg·s/mL]
R_T	Total peripheral resistance	[mmHg·s/mL]
T	Period	[s]
t	Time	[s]
t_max	Time to maximum elastance	[s]
U	Flow velocity	[m/s]
u	Longitudinal velocity	[m/s]
V_0	Dead volume	[mL]
x	Spatial location	[m]
Z	Impedance	[mmHg·s/mL]
Z_c	Characteristic impedance	[mmHg·s/mL]
Z_in	Input impedance	[mmHg·s/mL]
T_inf	Inflection point	[s]
T_sho	Shoulder point	[s]
V	Volume	[m^3]

INTRODUCTION

MOTIVATION

Cardiovascular diseases (CVDs) such as coronary heart disease, stroke (cerebrovascular disease), hypertension (increased blood pressure), peripheral artery disease, and heart failure, are the primary cause of morbidity and mortality worldwide, representing 31% of all yearly deaths worldwide according to data from the World Health Organization published in 2016 [1]. With age being a key factor in the incidence of cardiovascular disease (see Figure i) and considering that the world's population is growing older (the proportion of the world's population over 60 years will nearly double by 2050 [1]), major health and economic burdens are to be expected in the future for the elderly. Age-related degenerative hemodynamic changes and various disease states play a central role in the pathogenesis of CVDs [2–4]. Therefore, it is of primary importance to gain a deeper understanding of the effects of ageing on the hemodynamics and arterial function, and the mechanism underlying the interplay of ageing with CVD events, in order to improve diagnosis and treatment therapies.

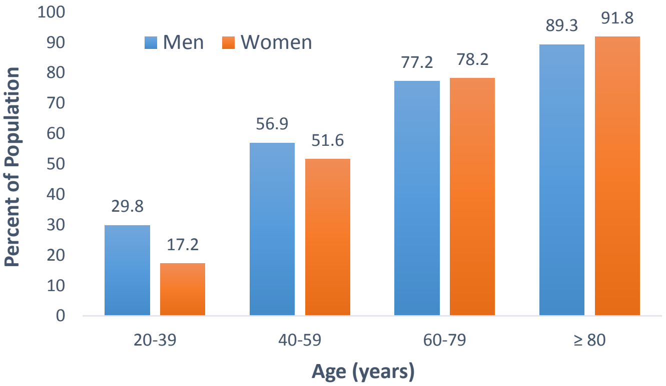

Figure i: Prevalence of cardiovascular disease by age and sex. Cardiovascular disease includes coronary heart disease, heart failure, stroke and hypertension. Data from the National Health and Nutrition Examination Survey 2013-2016 (USA) [5].

Many of the observed changes in hemodynamics occurring with ageing and that are associated with CVDs are explained by pressure (and flow) wave propagation and reflection. Pulse wave propagation in the arterial system is the result of the contracting action of the heart and the elastic properties of the large arteries, which dilate in systole to accommodate a part of the ejected blood volume in each cardiac cycle and store elastic energy which is then used in diastole to drive the blood towards the peripheral circulation. This arterial pulse propagates in the form of pressure, flow (velocity) or diameter waveforms at a certain speed known as the pulse wave velocity (PWV). Pulse waveforms propagate from the heart to the periphery (forward direction), but they also get reflected (backward direction) at sites of impedance mismatch or any other variation in the mechanical properties or arterial geometry [6], producing continuous changes in the measured blood pressure and flow (velocity) waveforms. Therefore, pressure and flow pulse waveforms contain information on the functionality and morphology of the cardiovascular system, which is important for diagnostic and treatment planning. For instance, although the increase in aortic systolic and pulse pressure with ageing is widely recognized [7, 8], the underlying mechanism is still being investigated and subject to some controversy. The conventional and most popular approach attributes this increase in blood pressure to wave reflections arriving earlier during systole, resulting from increased arterial stiffness and the corresponding increase in PWV [9]. An alternative perspective on the contrary, ascribes this to augmentation in the forward pressure wave due to increased characteristic impedance of the proximal aorta [10, 11]. Overall, studies to understand these phenomena are based on *in vivo* data in humans or animals, as well as *in vitro* experiments and computational models.

Computational models of the cardiovascular system are regarded as a valuable tool for the study of wave propagation effects on the arterial network. Modelling allows to study these hemodynamics phenomena while offering several advantages over *in vivo* studies. For instance, by changing the model parameters, a wide range of physiological or pathological conditions may be studied, contributing to further knowledge in the diagnostics and treatment of cardiovascular diseases; also we can estimate data at specific locations that are otherwise not available with noninvasive measurements. Nevertheless, modelling of the cardiovascular system is not an easy task since the complex mechanical properties of arteries have to be accounted for, as well as the complexity of the arterial tree geometry and the rheological properties of the blood. Validation of the models require data obtained *in vivo* or *in vitro*, which add a degree of difficulty to the modelling task. In this dissertation we exploit the potentialities of a previously validated 1D model of the systemic arterial tree, coupled to a lumped parameter model of the heart [12].

The availability of noninvasive techniques, to image anatomical structures and measure pressure and flow (velocity) waveforms has opened the door for large scale *in vivo* studies that include assessment of arterial hemodynamics. Traditional *cross-sectional* studies, where a large part of the population is screened at a moment in time, have allowed for a better understanding of cardiovascular diseases, and the definition of cardiovascular risk factors such as ageing, smoking, high blood pressure or obesity [13]. These studies have also been used to define normal and reference values for physiological parameters such as PWV [14]. To elucidate the interplay of ageing and cardiovascular hemodynamics, *longitudinal* population studies, where the same subjects are followed over time, become more relevant. The Asklepios Study is a longitudinal population study on healthy ageing, integrating noninvasive cardiac and arterial hemodynamic measurements and computational estimations, in a cohort of 2524 middle-aged subjects over a period of ten years [15]. In this dissertation we make use of the Asklepios database to obtain a better understanding of the longitudinal relationship of ageing with arterial hemodynamic parameters such as impedance, wave reflection, and PWV, in the middle-aged.

Research Objectives

The main goals of this thesis are to (i) make use of the 1D arterial network model to acquire a broader insight in arterial hemodynamics and wave travel and reflection in a number of selected applications; and (ii) make use of the longitudinal data of the Asklepios population database to assess the effective impact of ageing on arterial system properties and arterial wave reflections *in vivo*.

The 1D model of the systemic circulation [12] has been developed in the Laboratory of Hemodynamics and Cardiovascular Technology of the Ecole Polytechnique Fédérale de Lausanne (prof. Nikos Stergiopulos). This model has proven to be a useful tool to investigate age-related changes in hemodynamics and arterial function [16–22], allowing realistic simulations of hemodynamic measures under different conditions and at locations in the arterial tree that are otherwise difficult to access with noninvasive measurements. The Asklepios study [15] was initiated in 2002 by prof. Ernst Rietzschel in a close collaboration with the general practitioners of the twinned Belgian communities of Erpe-Mere and Nieuwerkerken. The study involves a cohort of 2524 middle-aged subjects, free from overt cardiovascular disease at study initiation, that underwent two rounds of measurements with a span of ten years. Measurements included questionnaires, conventional risk factors and a deep phenotyping of cardiovascular structure and function using ultrasound and applanation tonometry.

Structure

The thesis is divided in three parts: an introductory part summarizing important hemodynamic concepts, a middle part that includes several studies based on the 1D arterial model, and a final part including the analysis of longitudinal data from the Asklepios population.

Part I gives a brief overview of the anatomy of the cardiovascular system and relevant hemodynamics principles, as well as the description of the 1D model of the cardiovascular system. This sets the basis for a better understanding of the studies conducted during this PhD project. More specifically, Chapter 1 focuses on the description of the systemic arterial tree, the pressure and flow wave propagation phenomenon, and stiffening of arteries with ageing. In Chapter 2, the mathematical formulation and description of the 1D model of the systemic circulation, which is used as a tool for different studies throughout this dissertation, is provided.

Part II includes several *in silico* studies on arterial hemodynamics based on data obtained with the 1D cardiovascular model. First, the 1D model is applied to study the impact of a heart assist device on arterial hemodynamics (Chapter 3). Second, in Chapter 4 the model is used to provide numerical insight into the performance of loop-based local pulse wave velocity methods, throughout the systemic arterial tree. Lastly, given that the 1D model has proven to be a valuable tool for the study of several pathophysiological conditions in humans, in Chapter 5 we aimed to adapt the human model to the equine physiology, based on a limited number of *in vivo* and *in vitro* measurements and the subsequent derivation of the model parameters. The resulting computational equine model provides the veterinary community with a tool that can be used for further studies of pathologies such as aortic rupture, or physiological changes due to ageing or exercise.

Part III contains a single chapter (Chapter 6) discussing the impact of ten years of ageing on central hemodynamic parameters, from noninvasive data of the Asklepios large-scale population of middle-aged subjects. The study specifically focuses on the longitudinal changes of pulse wave velocity, input impedance, and wave reflection parameters, and how these effective changes compare to previous cross-sectional perspectives. The study also considered the influence of cardiovascular risk factors on the age-related changes in the arterial properties, as well as the longitudinal interplay of blood pressure and arterial stiffness.

Finally, a concluding chapter gives a summary of the major findings of the above described studies, and looks into the future perspectives.

LIST OF PUBLICATIONS

- **D. Campos Arias**, M.L. De Buyzere, J.A. Chirinos, E.R. Rietzschel and P. Segers, 'Longitudinal changes of input impedance, pulse wave velocity, and wave reflection in a middle-aged population: the Asklepios Study', *Hypertension*, vol. 77, no. 4, pp. 1154-1165, 2021.
- L. Vera*, **D. Campos Arias***, S. Muylle, N. Stergiopulos, P. Segers and G. van Loon, 'A 1D computer model of the arterial circulation in horses: An important resource for studying global interactions between heart and vessels under normal and pathological conditions', *PLoS One*, vol. 14, no. 8, pp. e0221425, 2019.

  * *L. Vera and D. Campos Arias contributed equally to this work.*
- **D. Campos Arias**, N. Stergiopulos, T. Rodríguez Moliner and P. Segers, 'Mapping the site-specific accuracy of loop-based local pulse wave velocity estimation and reflection magnitude: a 1D arterial network model analysis', *Physiological Measurement*, vol. 40, no. 7, pp. 1–14, 2019.
- **D. Campos Arias**, F. Londono, T. Rodríguez Moliner, D. Georgakopoulos, N. Stergiopulos and P. Segers, 'Hemodynamic impact of the C-Pulse cardiac support device: a 1-D arterial model study', *Artificial Organs*, vol. 41, no. 10, pp. E141–E154, 2017.

I

Hemodynamics and wave propagation in the arterial tree

Chapters

CHAPTER 1

ANATOMY, PHYSIOLOGY AND BASIC HEMODYNAMIC PRINCIPLES

This chapter first provides a general overview of the cardiovascular system, with a major focus on the physiology of the heart and the cardiac cycle on the one side, and the arterial system on the other side. A brief description of the here relevant cardiovascular pathologies is provided, with an emphasis on heart failure and the impact of ageing on the functionality of the arterial system, as well as its association to arterial stiffness. The third section provides a brief introduction to pulse wave velocity and its estimation methods used during this thesis. A concise description of the transit time methods, and the loop methods to estimate local pulse wave velocity, is given. This section is followed by an overview of impedance analysis, with a description of its core parameters: resistance, compliance and characteristic impedance. Lastly, attention is given to wave reflections and the methods to perform wave separation analysis; wave separation in the frequency and time domain. Wave separation in the time domain is derived from wave intensity analysis, which is explained in the last part of this section, along with a similar and more recent technique, called wave power analysis.

1.1 CARDIOVASCULAR PHYSIOLOGY

The cardiovascular system (Figure 1.1) transports blood in large organisms through a closed circuit, and with it vital substances like oxygen, nutrients and hormones. Another function of the cardiovascular (CV) system is to remove metabolic waste products such as carbon dioxide. The CV system encompasses the heart, the lungs and blood vessels, which in turn are classified in arteries, arterioles, veins, venules, and capillary vessels [23]. Another component of the cardiovascular system is the lymphatic system, consisting of lymphatic nodes and vessels which do not contain blood but lymph [23]. Although this system plays an important function in the CV circulation and is closely related to blood vessels, it is not relevant for this thesis and is therefore not going to be further discussed.

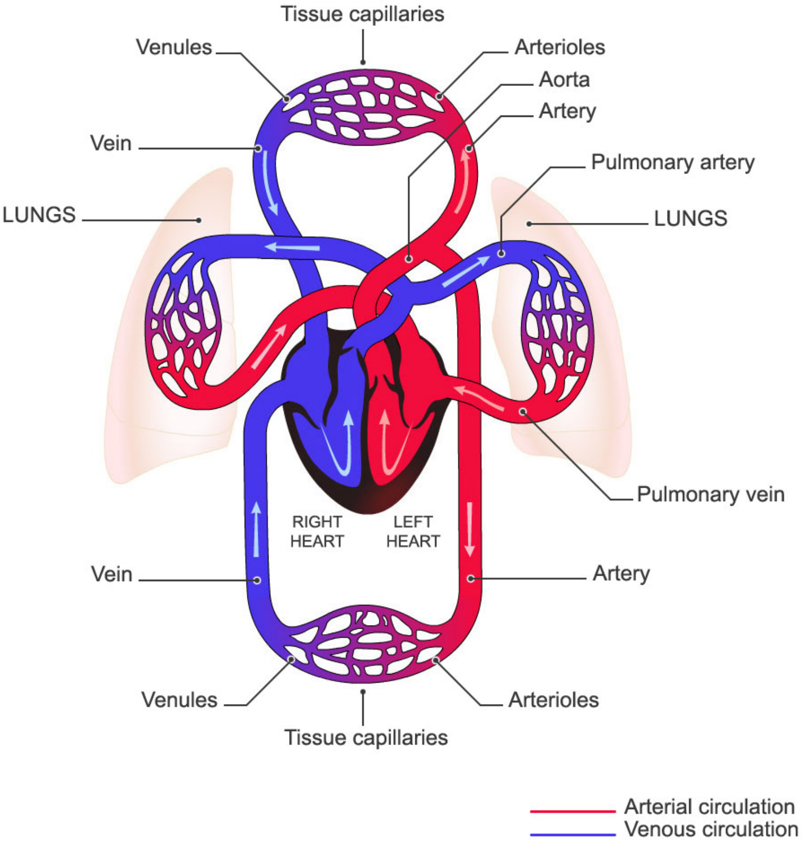

Figure 1.1: Scheme of the cardiovascular system. Image taken from: sphweb.bumc.bu.edu.

The circulatory cycle begins when blood rich in oxygen is pumped by the heart from the left ventricle into the aorta (largest artery). This blood drives throughout the entire systemic arterial tree with a relatively high perfusion pressure, oxygenating the different organs where the interchange between oxygen and carbon dioxide, as well as other substances, takes place. Blood rich in carbon dioxide is transported back through the venous system to the chambers in the right side of the heart, from where it is pumped to the lungs. In the lungs the blood is reoxygenated, and is then transported back to the left side of the heart where it is ejected to the aorta, starting a new cycle. Pulmonary circulation (heart-lungs-heart), systemic circulation (heart-blood vessels in the body-heart) and coronary circulation (amount of blood to the heart), form the cardiovascular circulation.

1.1.1 The heart

The heart is a hollow muscular organ that rhythmically contracts and pumps blood from the venous side (low pressure circulation) to the arterial side (high pressure circulation) [23]. It can be seen as two pumps in series between which the systemic and pulmonary circulation take place. The heart is formed by four chambers, an atrium and a ventricle on the right side, and an atrium and a ventricle on the left side. Blood arriving to the heart from the systemic or pulmonary circulation is received in the atria and distributed back to the arteries by the ventricles (Figure 1.2). The heart also includes four valves to ensure unidirectional blood flow through the chambers; the tricuspid valve between the right atrium and right ventricle, the pulmonary valve between the right ventricle and pulmonary artery, the mitral valve between the left atrium and the left ventricle and finally, the aortic valve between the left ventricle and the aorta.

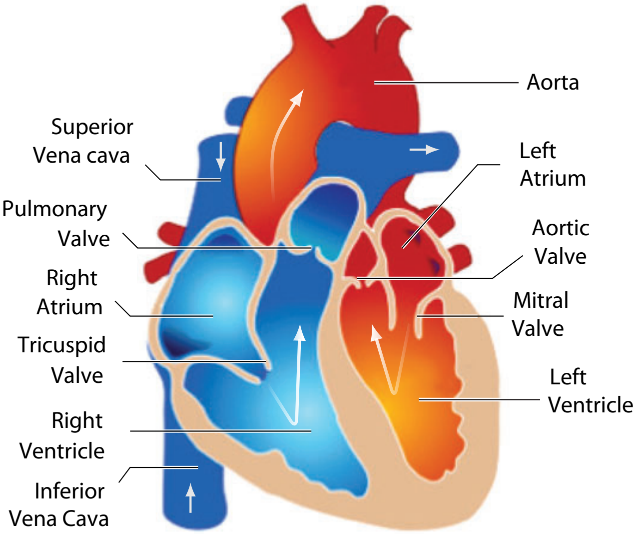

Figure 1.2: Scheme of the heart. Image adapted from [24].

1.1.1.1 *The cardiac cycle*

A complete cardiac cycle consists of a similar number of phases for the right and left side [24]. Figure 1.3 shows a representation of the pressure-volume loop in the left ventricle where the four main phases of the cardiac cycle have been indicated. The cardiac cycle is divided in systole and diastole. Systole refers to the contraction (phase I) and ventricular ejection events (phase II), and diastole refers to the relaxing (phase III) and ventricular filling (phase IV).

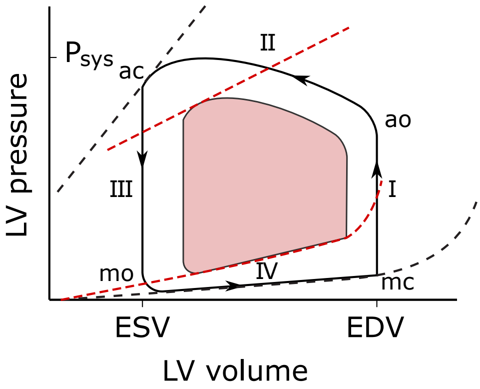

Figure 1.3: Representation of the pressure-volume loop of the left ventricle. The coloured loop represents the combination of systolic and diastolic failure that leads to reduced end-diastolic volume (EDV) and increased end-systolic volume (ESV). ao: opening of the aortic valve; ac: closure of the aortic valve; mo: opening of the mitral valve; mc: closure of the mitral valve.

Systole starts with the isovolumic contraction phase, when all the valves are closed and the ventricles are filled with blood. During this phase the ventricles experience a fast increase in pressure to relatively high levels but without altering the volume. When the pressure in the ventricle rises over the pressure in the aorta (pulmonary artery), the aortic (and pulmonary) valve opens giving rise to a fast ejection phase (see also Figure 1.4); while the valves in the atria stay closed. Pressures in the aorta and pulmonary artery then reach their maximum values. While the blood volume in the ventricles decreases due to the ejection, in the atria it increases by the blood filling phase. The right atrium receives venous blood from the systemic circulation at very low pressures via the superior and inferior vena cava, whereas the left atrium receives the blood coming from the lungs through the pulmonary veins. Then a reduction in the ejection takes place, where the pressure of the ventricles decreases below the aortic pressure, the pulmonary and aortic valves close, thereby ending systole and marking the start of diastole. As at this point all valves remain closed, the volume in the ventricles remains constant

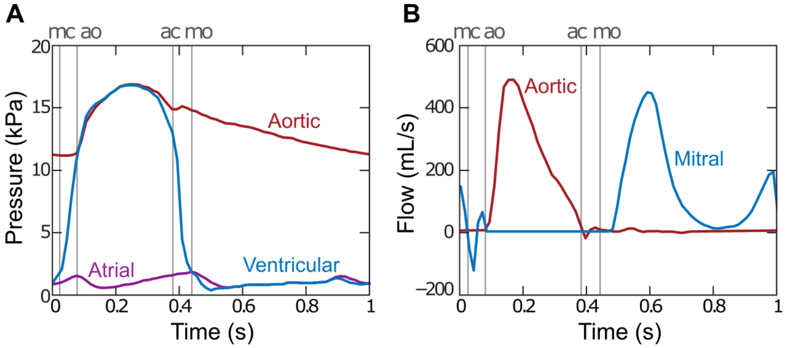

Figure 1.4: Pressure and flow in the left side of the heart during a cardiac cycle. (A) Aortic, ventricular and atrial pressure. (B) Aortic and mitral flow. The onset of the cardiac phases is indicated, with the closure of the mitral valve (mc), opening of the aortic valve (ao), closure of the aortic valve (ac), and opening of the mitral valve (mo). Adapted from [24].

(isovolumic relaxing phase); however the volume in the atria keeps increasing. The residual volume of blood that remains in the ventricles is called end-systolic volume (ESV). When the pressure in the ventricles falls below the atrial pressure, the valves between atria and ventricles (tricuspid and mitral) open and, with the help of the contraction of the atria, the ventricular filling starts. Once the atrial contraction ends, the atrial pressure starts falling until the closure of the valves occurs, which marks the end of diastole. At this point, the ventricles have reached their end-diastolic volume (EDV).

1.1.1.2 *The cardiac function*

The pump activity of the heart is usually expressed in terms of the cardiac output (CO), which is the amount of blood ejected in each contraction (stroke volume) multiplied by the heart rate or frequency (HR).

$$\mathrm{CO} = \mathrm{SV} \cdot \mathrm{HR} \tag{1.1}$$

In an average human adult the CO is about 5 L/min. The stroke volume (SV) is defined as the difference between EDV and ESV, and is influenced by two factors: the energy of contraction of the myocardium and the afterload. Cardiac muscle contraction may change in response to altered preload. If venous return to the heart is increased, ventricular preload increases, therefore there is an increase in ventricular EDV or pressure; this causes an increase in cardiac muscle contraction which leads to an increase in SV. This is known as the Frank-Starling mechanism [23]. The ventricular afterload is defined as the load that the ventricle must overcome to eject blood [23, 25]. The ejection fraction (EF) of the ventricle is defined as the ratio of the SV and the EDV, expressed as a percentage.

1.1.2 The systemic arterial system

The systemic arterial system carries the oxygenated blood from the heart to the tissues through the main artery, the aorta, that then successively branches in smaller arteries, arterioles and capillary vessels; these last ones allow for the direct interchange of blood with the tissues. Arteries are composed of three layers separated by elastic membranes [26], the intima, the media and the adventitia (Figure 1.5). The intima consists of a layer of endothelial cells in contact with the blood, and is subjected to shear stress of the blood flow. The media has the highest capacity of structural support, and is formed by smooth muscle cells, elastic fibers containing elastin, and collagen. This layer contributes the most to the mechanical properties of the artery. The adventitia consists mainly of collagen fibers (running in a predominantly longitudinal direction), with a small proportion of elastin. The elastin is responsible for the distensibility of the arteries, while collagen fibers prevent vascular rupture at high pressures.

The structure and organization of the arterial wall components vary from the aorta towards the periphery, mainly for the media layer [28]. In the large central arteries, elastic fibers are organized in concentric layers (lamellae) separated by thin layers of connective tissue, collagen fibres and sparse smooth muscle cells. This structure changes for smaller arteries, where the number of elastic lamellae decreases while there is an increase of spirally arranged smooth muscle cells, thus the central arteries are classified as elastic and the peripheral arteries as muscular [28–30]. The increased smooth

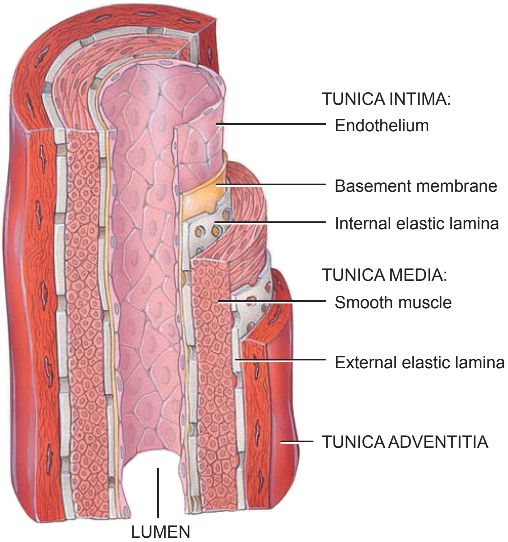

Figure 1.5: Layers of the arterial wall. Image adapted from [27].

muscle cells content and wall organization of smaller arteries and particularly arterioles in the periphery, enables them to alter their lumen, in order to regulate both vascular resistance and the continuous distribution of blood flow to the organs and tissues depending on their need [8, 28]. According to Poiseuille's law, resistance is inverse to the radius to the power four, therefore for the vessels in the periphery with a small radius, resistance is high. In contrast, the resistance of the large and mid-size arteries is low.

The elasticity of the arterial wall is associated with the content of elastin and collagen. Elastic fibers are highly extensible while collagen fibers are very stiff. In the unstretched artery, collagen fibres are wavy [31]. With increasing pressure, collagen waviness decreases leading to a stiffer arterial wall. This explains the nonlinear relation between distending pressure and arterial elastic properties (see Figure 1.6). From the nonlinear pressure-area relationship, area compliance can be estimated. Distensibility is obtained by normalizing compliance with respect to artery size. These measures are dependent on blood pressure (BP), decreasing with increasing pressure in the physiological range, and due to the nonlinear relation, compliance or distensibility are typically estimated at a working pressure. In clinical practice for example, area compliance (C_A) is often approximated from systolic-diastolic differences in cross-sectional area (ΔA) and pressure (PP, pulse pressure), $C_A = \Delta A/\text{PP}$, yielding a single value that can be interpreted as an average over the BP range. Thus, a decrease in arterial compliance leads to an increase in pulse pressure, as it can be seen with ageing. The same applies if information on diameter is known (e.g. diameter measured noninvasively with echo-tracking techniques).

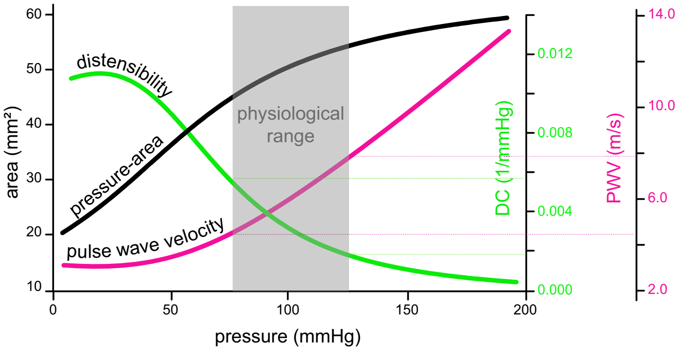

Figure 1.6: Typical nonlinear relation between the lumen cross-sectional area and blood pressure over a large pressure range (black curve). Decrease of the distensibility (DC) with pressure (green curve). Increase of the pulse wave velocity (PWV) with increasing blood pressure (magenta curve). Adapted from [29].

Elastic arteries, such as the aorta, passively dilate during systole, thereby acting as reservoirs for the ejected blood volume, and elastically recoil in diastole, releasing the stored blood volume to the organs. This elastic function of the arteries, known as the Windkessel effect, besides allowing for perfusion produces the wave propagation phenomenon [24] (see further section 1.5). The speed at which pulse waves propagate in the arterial system is called the pulse wave velocity (PWV), which can be inversely related to arterial compliance (or distensibility) through the Bramwell-Hill equation (see Figure 1.6 and section 1.3).

1.1.2.1 Arterial blood pressure

Arterial pressure ranges between a maximum value, the systolic blood pressure (SBP), and a minimum value, the diastolic blood pressure (DBP). The pulse pressure is defined as the difference between them (PP = SBP − DBP). Pressure, as well as flow waveforms, depend on both the performance of the heart and the characteristics of the arterial network. Pulse pressure increases as we move away from the heart (pressure amplification), whereas mean arterial pressure (MAP) gradually decreases. Normal arterial pressure is defined as a SBP = 90-120 mmHg and a DBP = 60-80 mmHg. The MAP is normally about 100 mmHg. Elevation in systolic or diastolic pressure above normal values, higher than 140 or 90 mmHg, respectively, defines the condition known as hypertension [23].

1.2 CARDIOVASCULAR PATHOLOGY

The cardiovascular system can be affected by several diseases, including hypertension, diseases intrinsic to the heart such as heart failure, and vascular disorders such as arterial stiffening, atherosclerosis (narrowing of the arterial wall due to formation of plaques), or aortic aneurysms, among others. These conditions may be also seen interrelated and associated with age-related changes. The two major pathologies that will be addressed in this work are heart failure and arterial stiffening, the latter affecting most humans as part of the ageing process.

1.2.1 Heart failure

Heart failure (HF) is a clinical syndrome caused by a structural and/or functional cardiac abnormality, resulting in a reduced cardiac output and/or elevated intracardiac pressures at rest or during stress [32]. Commonly, HF involves the left ventricle and may result from deficient contraction of the cardiac muscle (systolic dysfunction) or from deficient filling (diastolic dysfunction) [23]. Measurements of the left ventricle EF (defined previously in section 1.1.1.2) allow for a classification of heart failure. Normal values are ≥

50%. When EF < 40%, it is called HF with reduced EF (HFrEF); in the range 40–49%, HF with mid-range EF; and for HF patients with normal EF, HF with preserved EF (HFpEF) [32].

In systolic dysfunction, the contraction of the myocardium is impaired and as a result, the stroke volume decreases and there is a compensatory rise in preload [23]. As the heart loses its ability to eject blood, blood volume in the ventricle increases, which eventually leads to ventricular remodelling (dilation) in chronic failure. Because there is also a reduction in the EF (decrease in SV and increase in EDV due to increase in preload), systolic dysfunction is usually associated with HFrEF. One of the main causes of systolic dysfunction is coronary artery disease, which reduces the supply of oxygenated blood towards the heart [23]. A related common cause of HF is myocardial infarction, where the non-infarcted tissues have higher demand, which in time may cause functional changes leading to failure. Other causes of systolic dysfunction are heart valve diseases (stenosis and/or regurgitation). In the latter, the valve does not completely close allowing backflow, which affects the pressure-volume relationship during systole and diastole, leading to a reduced cardiac output and elevated venous pressure.

In diastolic dysfunction the ventricle becomes stiffer and/or does not relax normally after the contraction, which causes an impaired filling [23, 33]. Diastolic dysfunction may be a result of non-controlled chronic arterial hypertension, leading to ventricular hypertrophy (increased ventricular stiffening), or, in the elderly population, from age-related changes to cardiac structure leading to stiffer ventricle [23]. With diastolic dysfunction, end-diastolic pressure increases and ventricular filling decreases (decreased EDV), therefore SV is reduced and the EF may or may not change. Thus, diastolic dysfunction is typically associated with HFpEF.

It is usual in chronic heart failure to have a combination of both systolic and diastolic dysfunction [23, 33]. These failures combined reduce EDV and increase ESV (as seen from the pressure-volume loop Figure 1.3), thereby drastically reducing the SV. This combination of systolic and diastolic failure can lead to high end-diastolic pressure, which can cause pulmonary congestion and edema [23].

The treatment for HF depends on the severity of the disease. HF patients experience difficulties to breath, fatigue, and fluid retention either in the lungs or in the extremities. Furthermore, HF can severely limit the exercise capacity [32]. When the disease is diagnosed in early stages, it can be treated with drugs and medical interventions. Stronger treatments are required as the disease progresses, which might even lead to the implant of assist devices or heart transplants. Refer to Gafoor *et al.* [34] for a review of devices used in HF treatment.

1.2.2 Arterial ageing and stiffness

With ageing, the arterial wall experiences an elastin degradation and an increase in collagen fiber deposition, causing the arteries to become stiffer [8, 35, 36]. The aorta and major elastic arteries also experience morphological changes; they increase in diameter (dilation), and become more tortuous and elongated [9, 37–40]. The changes associated with ageing are less marked in the peripheral muscular arteries [10, 41, 42]. These age-related degenerative changes, particularly the increase in arterial stiffness, lead to an elevated BP which puts a higher mechanical stress on the vessels and organs, thereby influencing the incidence of stroke, renal and cardiac failure, and cardiovascular and all-cause mortality [2, 43–46].

Stiffening of the arteries leads to an increase in the speed at which waves travel in the arterial system [47, 48], thus PWV has emerged as a marker of arterial stiffness (see further section 1.3). Moreover, increased arterial stiffness in the aorta and central arteries such as the carotid, has been shown to be an independent predictor of cardiovascular morbidity and mortality, even in the presence of several CV risk factors including diabetes, hypertension, renal insufficiency or elderly population [2, 44, 45, 49–55]. Less associations have been found with peripheral arteries stiffness [42]. Therefore, the estimation of aortic stiffness, rather than peripheral stiffness, has become an increasing subject of research in the last decades, and measurements of arterial stiffness indices have been included in large-scale clinical trials [14, 54].

Several cross-sectional studies have demonstrated a significant association between age and aortic stiffness, showing that stiffness increases with ageing [10, 56–59]. To investigate the extent to which ageing influences the impact of CV risk factors on arterial hemodynamics, longitudinal large-scale population studies have been designed, such as the Framingham Heart Study (FHS) [54, 60], the Baltimore Longitudinal Study of Ageing (BLSA) [61, 62], the SardiNIA study [63, 64], or the Asklepios study [65], of which longitudinal data is further analysed in Chapter 6 of this thesis. Since the incidence and prevalence of hypertension increase with advancing age, with a rise in systolic blood pressure and pulse pressure, and hypertension is associated with increased morbidity and mortality [66], many studies have focused on determining the longitudinal relationship of BP and arterial stiffness [60, 61]. Arterial stiffness has been shown to have a complex relationship with BP. Increased BP has been associated with accelerated increase in PWV and *vice versa* [60, 62, 63]. Therefore, whether increased aortic stiffness is due to the higher operating pressure in hypertension, or whether stiffness precedes the development of hypertension, is a subject that requires further research.

Given that arterial stiffness is considered to quantify the cumulative impact of exposure of the CV system to risk factors, it has been introduced as a biomarker of the early vascular ageing (EVA) syndrome [67, 68], i.e. premature biological ageing of the arterial system (reflecting a decline in the subject's physiological and biochemical functionality that may result in early CVD) in comparison to their chronological ageing. An opposed and more recent concept is supernormal vascular ageing (SUPERNOVA) [69, 70], which refers to individuals with much healthier arteries (e.g. low arterial stiffness) than expected from their chronological age and sex (see Figure 1.7). This last concept indicates the importance of improving lifestyle factors, as a mechanism to influence the ageing process and achieve a better quality of life.

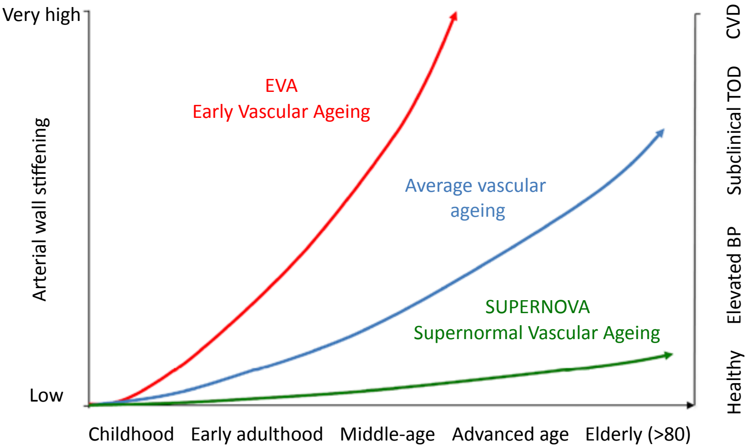

Figure 1.7: Illustration of the EVA and SUPERNOVA concepts in a life course. Progressive arterial wall stiffening with ageing is thought to parallel incident hypertension (elevated blood pressure (BP)), and then subclinical target organ damage (TOD), and then cardiovascular disease (CVD). EVA subjects reach each of these steps earlier than the average population, whereas SUPERNOVA subjects remain protected for a long period of time. Image taken from [69].

1.3 PULSE WAVE VELOCITY: A MARKER OF ARTERIAL STIFFNESS

Pulse wave velocity (PWV) or wave speed (c), is the speed at which the arterial pulse waves (pressure, flow or diameter) propagate along the arterial system, and depends on vessel dimensions and the elastic properties of the arterial wall (as seen previously from section 1.1.2). In a healthy young adult, reference values for the aorta range between 4.5 and 7.5 m/s [14]. Because PWV allows for an easier quantification of large arteries stiffness, it has been considered as a feasible diagnostic procedure in large clinical studies [3, 4], but it is not yet fully incorporated as a routine tool into clinical practice, which may be due to the variety of methods available to measure PWV. These measurement methods can be grouped mainly into two working principles; the so-called transit-time methods where PWV is measured over an arterial segment, providing an average value of its stiffness (Figure 1.8), and the methods that allow for an estimate of the value of PWV at a single location (Figure 1.9). An overview of the available methods and their pros and cons has been recently published by Segers *et al.* [71]. In what follows, the different approaches used during this thesis are briefly described.

1.3.1 Bramwell-Hill equation

The Bramwell-Hill equation [47] directly relates the local arterial wall compliance (C_A) and the wave speed:

$$c = \sqrt{\frac{A}{\rho}\frac{\mathrm{d}P}{\mathrm{d}A}} = \sqrt{\frac{A}{\rho C_A}} \tag{1.2}$$

with A the lumen cross-sectional area and ρ blood density. Distensibility (D_w) is the relative change in cross-sectional area (dA) in response to the change in pressure (dP),

$$D_w = \frac{1}{A}\frac{\mathrm{d}A}{\mathrm{d}P} = \frac{C_A}{A} \tag{1.3}$$

thus the Bramwell-Hill equation can be rewritten as:

$$c = \frac{1}{\sqrt{\rho D_w}} \tag{1.4}$$

From this equation it can be seen that a decrease in arterial distensibility, as occurs with increasing pressure, leads to an increase in PWV. This theoretical relation holds for a uniform elastic conduit in absence of wave reflections [31].

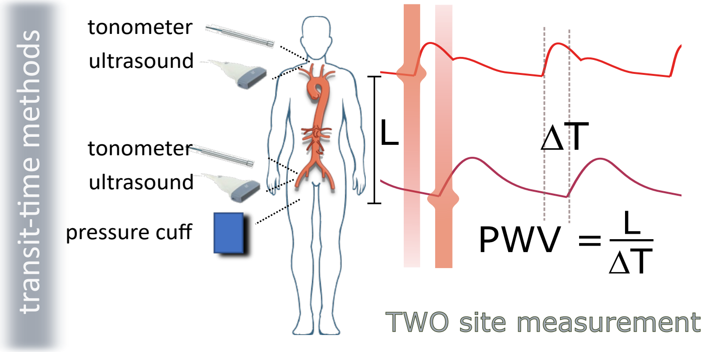

Figure 1.8: Overview of transit-time methods to measure PWV. Image courtesy of P. Segers.

1.3.2 Transit time methods to measure PWV

Transit time (TT) methods are based on the derivation of PWV as:

$$\mathrm{PWV} = \frac{L}{\Delta t} \tag{1.5}$$

where L is the distance between two measurement sites, and Δt, the travel time of the wave from one site to the other (see Figure 1.8). PWV estimated in this way has gained wide acceptance in the clinical community because of its simplicity.

The gold standard method for measuring PWV is based on catheterization, where accurate pressure signals can be recorded in the aorta [72, 73]; however, this is an invasive technique with clear limitations to be applicable as routine clinical practice. The various technologies used to noninvasively measure PWV include tonometry, ultrasound, oscillometry and magnetic resonance imaging (MRI) [71]. Typical combinations of the two measurement sites include carotid-femoral [45], brachial-ankle [74], cardio-ankle [75], or finger-toe [76]; the former being the recommendation of several guidance documents [45, 77, 78].

Despite the increasing use of these methods over the last decades [79], it remains difficult to accurately measure the real distance travelled by the waves between the two sites. For methods other than MRI and invasive catheterization, the path length is estimated from body surface measurements; small errors on these measurements have been shown to greatly influence the value of PWV [80, 81]. Another issue that requires caution when estimating PWV by TT methods, is the accurate identification of the foot of the waveform (typical fiducial point used for the time delay estimation) to obtain precise estimates of the transit time [82].

1.3.2.1 Carotid-femoral pulse wave velocity

Carotid-femoral pulse wave velocity (cfPWV) is to date the reference noninvasive technique to quantify central arterial stiffness [45, 77, 78]. Although it is only a surrogate for aortic stiffness, since it does not include the full aortic pathway, many studies have found it to be an independent predictor of incident CVD [2, 53, 83–85]. This method, implemented in several commercial devices [86], is the method used in the Asklepios population (see Chapter 6) to estimate PWV.

In the Asklepios study [15, 65], the pulse TT between the carotid and femoral arteries was estimated as ($\Delta T_{\text{Q-F}} - \Delta T_{\text{Q-C}}$), with $\Delta T_{\text{Q-F}}$ and $\Delta T_{\text{Q-C}}$ the time delay between the start of the QRS complex and the upstroke of flow measured with Doppler echography in the femoral and carotid artery, respectively. The subtracted method was used to estimate the distance as $(\Delta L_{\text{S-F}} - \Delta L_{\text{S-C}})$, with $\Delta L_{\text{S-F}}$ and $\Delta L_{\text{S-C}}$ the distance measured from sternum to femoral and carotid measuring sites, respectively. This way of estimating the distance attempts to correct for the portion where the wave travels simultaneously towards the carotid and femoral arteries. The subtracted distance is the recommended method in expert consensus documents [45, 72]; however, new recommendations consider the 80% of the direct measured body distance a better approximation [77]. Nevertheless, further studies have shown a good equivalence of aortic PWV measured invasively with cfPWV, using either the subtracted method or the 80% of the direct distance [73].

1.3.3 Local measurement of PWV

As can be seen from the Bramwell-Hill equation, PWV can be estimated by using measurements of pressure and area (or diameter). It is common practice to approximate this equation to obtain a single value of PWV,

$$\text{PWV} = \sqrt{\frac{A_{\text{dias}} \cdot \text{PP}}{\rho \Delta A}} \tag{1.6}$$

where PP is the pulse pressure, and $\Delta A = A_{\text{sys}} - A_{\text{dias}}$ is the difference between the area measured at systole and diastole. Local values of PWV can also

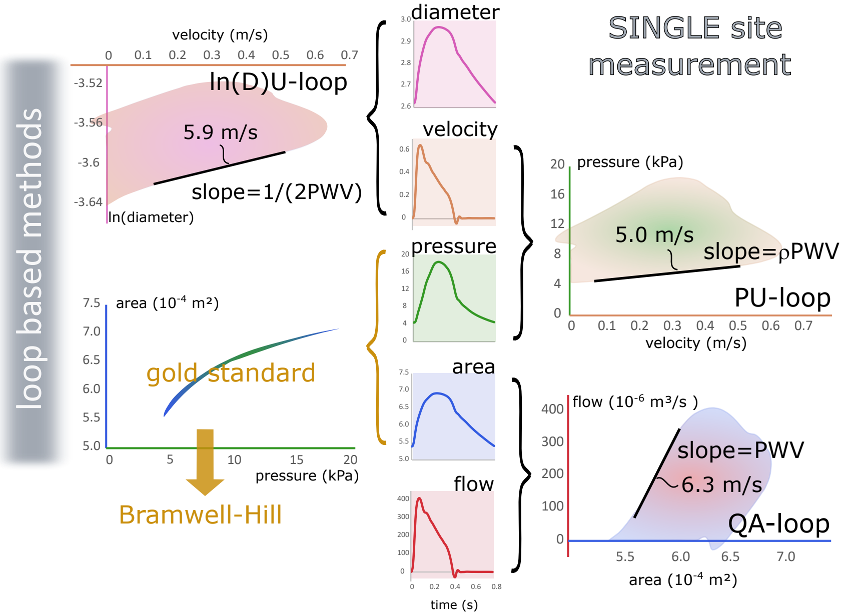

Figure 1.9: Overview of loop based methods to measure PWV. Image courtesy of P. Segers.

be derived from the loop that is formed by combining two simultaneous noninvasive measurements at a single location, given rise to the so-called loop methods (see Figure 1.9). These methods include signals of pressure, flow (velocity), area or diameter. In Chapter 4, a numerical comparison study of these methods is performed.

1.3.3.1 *Loop methods to assess local PWV*

The principle of the loop-based methods to derive PWV in a single location is based on the water hammer equation, which states that in absence of wave reflections, the change in pressure (dP) and flow velocity (dU) have a constant relationship.

$$\mathrm{d}P = c\rho \mathrm{d}U \tag{1.7}$$

It is usually assumed that the beginning of the cardiac cycle (early systole) is a reflection free period, under the assumption that the waves take some time to arrive from the reflection sites. Thus, during this period a linear relationship between the changes of pressure and flow velocity is anticipated.

PU-method

Based on the above, Khir *et al.* [87] showed that by forming a loop with the pressure and flow velocity signal (PU-loop), the slope of the linear segment in early systole equals ρc. Therefore, PWV_{PU} can be calculated directly from the slope of the linear segment in the loop over the density. To estimate the slope, a straight line can be fitted to the appropriate portion of the data, that can be chosen by visual inspection or other methods [88].

ln(D)U-method

Alternative approaches to the PU-loop method have been developed, based on the same principle but using variables other than pressure that are easier to obtain noninvasively. One of such methods is the ln(D)U-loop method [89], based on diameter (D) and flow velocity measurements. This method is derived by combining the Bramwell-Hill (1.4) and the water hammer (1.7) equations, and by expressing area as a function of diameter (assuming circular cross-section), which results in:

$$\mathrm{PWV}_{\ln(D)U} = \frac{1}{2}\frac{\mathrm{d}U}{\mathrm{d}\ln(D)} \tag{1.8}$$

As for the PU-loop, a linear portion can be expected in the ln(D)U-loop during early systole; the slope of the linear portion of the loop equals $1/(2\mathrm{PWV}_{\ln(D)U})$.

QA-method

The QA-loop method [90] is based on measurements of flow (Q) and cross-sectional area (A), two variables that can be obtained by ultrasound or MRI. This approach is derived from the combination of the Bramwell-Hill (1.4) and the water hammer (1.7) equations but with the resulting equation written as a function of flow,

$$\mathrm{PWV}_{QA} = \frac{\mathrm{d}Q}{\mathrm{d}A} \tag{1.9}$$

In this case, the slope of the QA-loop directly equals PWV_{QA}.

ln(D)P-method

Recently, another loop method was developed also based on pressure and diameter, the ln(D)P-loop method [91]. This method can be obtained by rewriting the Bramwell-Hill equation as a function of diameter in the form,

$$\mathrm{PWV}_{\ln(D)P} = \sqrt{\frac{1}{2\rho}\frac{\mathrm{d}P}{\mathrm{d}\ln(D)}} \tag{1.10}$$

Similarly to the previous methods, $\mathrm{PWV}_{\ln(D)P}$ can be derived from the slope of the linear segment of the loop constructed from plotting the natural logarithm of diameter as a function of pressure.

1.4 IMPEDANCE ANALYSIS

From the classic Fourier analysis, any pressure and flow waveform can be decomposed in a series of sinusoidal waves known as harmonics. Each of these harmonics has its own amplitude and phase angle, period, frequency and wavelength. The zeroth harmonic is a constant referring to the mean value with only the amplitude, e.g. mean arterial pressure for the pressure waveform (Figure 1.10). By summing up the harmonics (10-20 harmonics is sufficient), the measured signal can be reconstructed.

Input impedance (Z_{in}) is then defined as the ratio of harmonics of the measured pressure and flow waves [6]. Input impedance is a global measure that completely describes the arterial system, by accounting for the contributions of systemic vascular resistance (SVR, zero frequency), total arterial compliance (C, low frequencies), and characteristic impedance (Z_{c}, high frequencies). Since Z_{in} is a complex number obtained in the frequency domain, it is represented by the amplitude and phase angle for each specific frequency, with the frequencies being multiples of the heart frequency (see Figure 1.11). The impedance modulus is obtained from the ratio of the amplitudes of

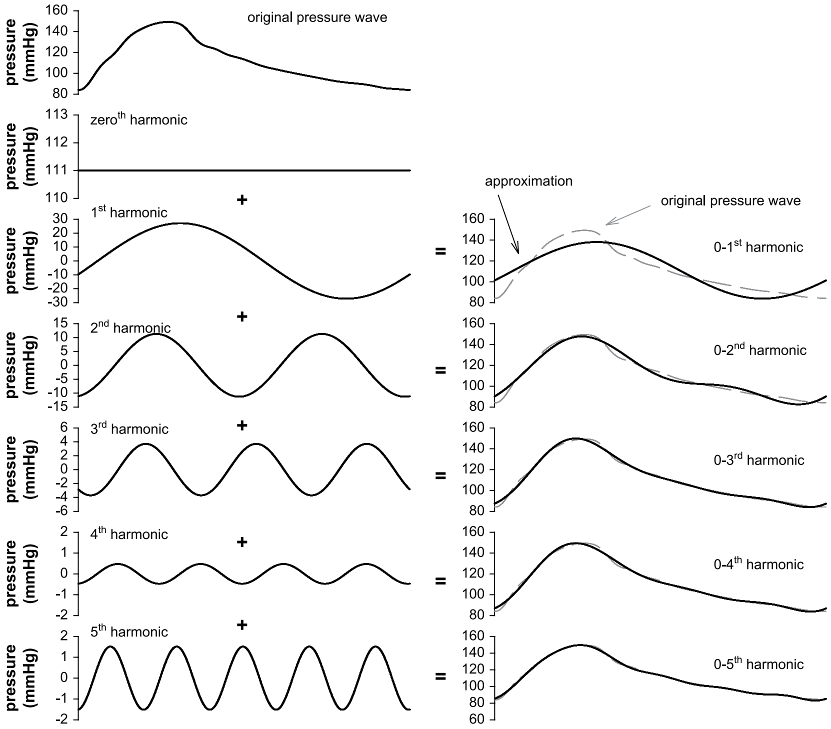

Figure 1.10: A waveform can be decomposed in a series of sinusoidal waves (harmonics) travelling at the same speed, each with its own amplitude and phase, period, frequency and wavelength. Image taken from [92].

pressure and flow, after these signals have been decomposed using the fast Fourier transform. The impedance phase angle is then estimated as their difference in phase angle. Although this measure has practical limitations from the clinical point of view, it has the potential to study the arterial system at a specific frequency, in order to improve the understanding of the arterial function [31].

1.4.1 Systemic vascular resistance

The systemic vascular resistance describes the resistance to the blood flow and equals the modulus of Z_{in} at the zeroth harmonic. SVR can also be approximated as the ratio of MAP to mean flow (Ohm's law) at the aortic root.

1.4.2 Total arterial compliance

Volume compliance (C) is defined as the ratio of the change in arterial volume ($\mathrm{d}V$) to the change in arterial pressure ($\mathrm{d}P$), $C = \mathrm{d}V/\mathrm{d}P$. A crude approximation of C is the ratio of stroke volume and pulse pressure. Alternative

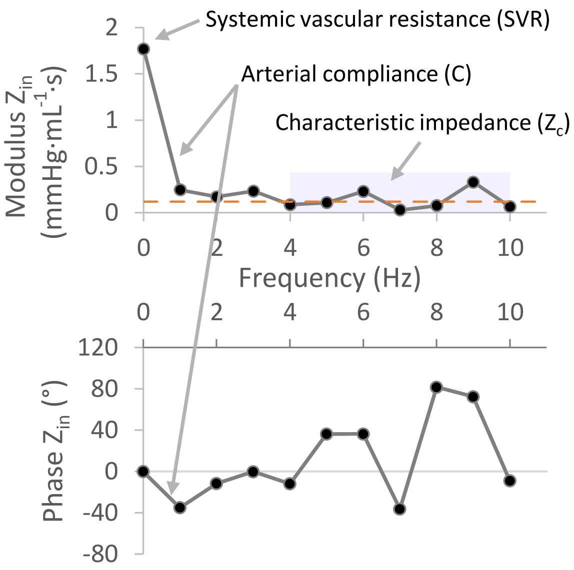

Figure 1.11: Modulus and phase of input impedance. SVR is determined as the modulus at zero frequency, compliance is determined at low frequencies, and Z_c is estimated at high frequencies as the average of the input impedance modulus for harmonics 4-10 (shaded area). Data from the Asklepios population.

methods to estimate volume compliance are based on Windkessel model approximations of the arterial system (see further Section 2.1.1). One can then either use a method indirectly based on a 2-element windkessel model assumption (decay time method [93], area method [94], pulse pressure method (PPM) [95]) or directly fit the parameters of a given Windkessel model to measured arterial pressure and flow. Refer to [31, 93] for a more detailed discussion on the different methods for estimating volume compliance.

1.4.3 Characteristic impedance

In contrast to input impedance, the characteristic impedance is the impedance that would be observed in absence of wave reflections. Since wave reflections vanish at high frequencies, Z_c is usually derived as the average of the modulus of Z_{in} from harmonics 4th to 10th (dashed orange line in Figure 1.11). Z_c can also be related to PWV starting from the water hammer equation;

$$Z_c = \frac{\rho \cdot \mathrm{PWV}}{A} \tag{1.11}$$

thus Z_c is inversely proportional to the vessel geometry.

1.5 PRESSURE AND FLOW WAVE PROPAGATION

With each ejection, the heart generates pressure and flow waves that propagate towards the periphery due to the distensibility of the arteries, leading to a finite wave speed [31]. The morphology of the waves varies with the location; with increasing distance from the heart, flow waveforms are reduced and pressure waveforms are amplified (see Figure 1.12). The waves also exhibit an increase in the slope of the wavefront and a time delay. Amplification of pressure waveforms are associated with reflections throughout the arterial network [96].

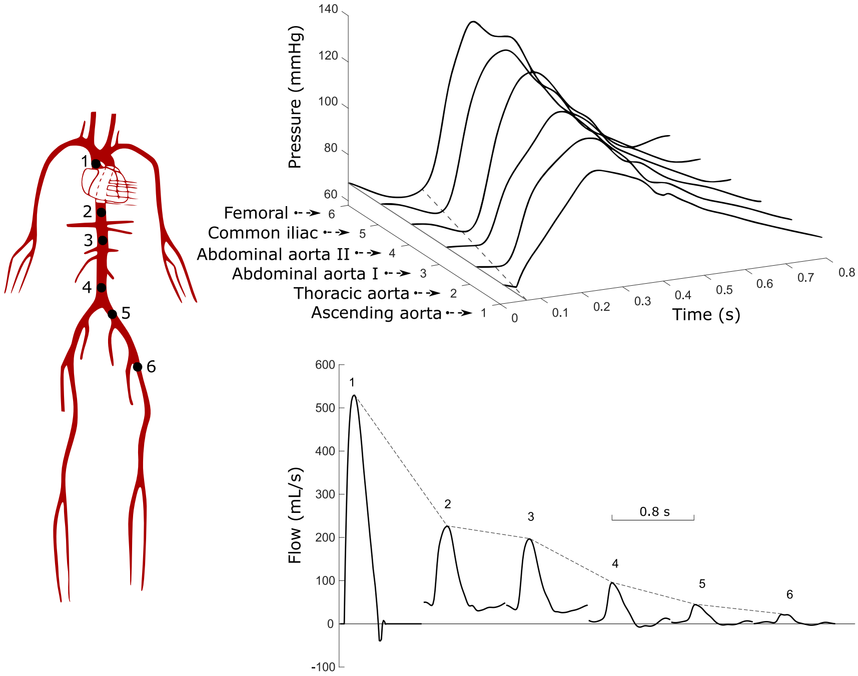

Figure 1.12: Example of wave propagation along the arterial tree from computer simulated data. From central to peripheral arteries pressure waveforms are amplified (top) and flow waveforms amplitudes are reduced (bottom). There is also a time delay in the arterial pulse.

1.5.1 Wave reflections

Due to changes in impedance along the arterial network, which may occur at bifurcations or with diameter variations or variations in mechanical properties, running waves get reflected [97]. In fact, each measured pressure and flow waveform is a superposition of a travelling forward wave (propagation from the heart to the periphery) and a travelling backward wave (reflection from the periphery to the heart) [6]. Wave reflections explain the changes in arterial pressure, leading to differences between central and peripheral pressures, and may even be involved in the pathophysiology of heart failure [98]. Furthermore, without reflections in the arterial system, the pressure and flow would have the same wave shape [31] (see Figure 1.13). The occurrence of wave reflections is not constricted to a single site or a limited number of sites [99]. On the contrary, reflections are distributed along the arterial network, turning them into a complex physiological process that is not easy to comprehend or quantify. Determining the reflection sites may be almost impossible, considering that in the arterial tree re-reflections are continuously occurring.

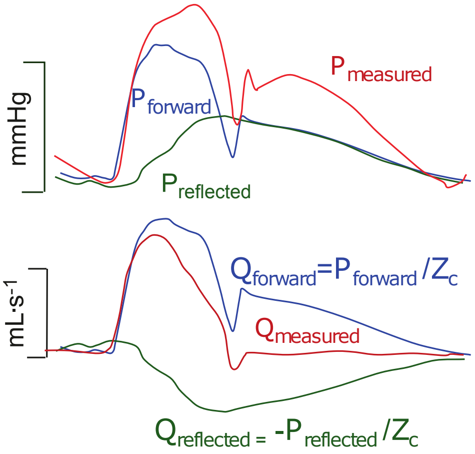

Figure 1.13: The measured pressure and flow waveforms are the sum of forward and reflected (backward) waves. Forward (or reflected) pressure and flow are related by the characteristic impedance. Reflections of pressure and flow are equal in magnitude but inverted. Image adapted from [31].

Wave reflections may also explain the differences in the pressure waveforms as observed with ageing [96]. For a young subject, reflected waves arrive during diastole, which increases diastolic perfusion. For an older subject, compliance decreases and PWV is increased, therefore reflected waves arrive earlier in systole, causing a rise in the systolic pressure peak and pulse pressure. These two characteristic phenotypes of the pressure waveform are known as C-type and A-type, respectively [96] (Figure 1.14).

1.5.2 Pressure waveform analysis

Analysis of the pressure wave shape is used, for instance, to determine the moment of arrival of the reflected pressure wave. Pressure waveforms typically show fiducial points that have been associated to reflections, such as the inflection point (T_{inf}) and the shoulder point (T_{sho}), which can be derived from the second and fourth derivative, respectively (see panels A-C in Figure 1.15). Using the fiducial point the augmentation index (AIx) is defined,

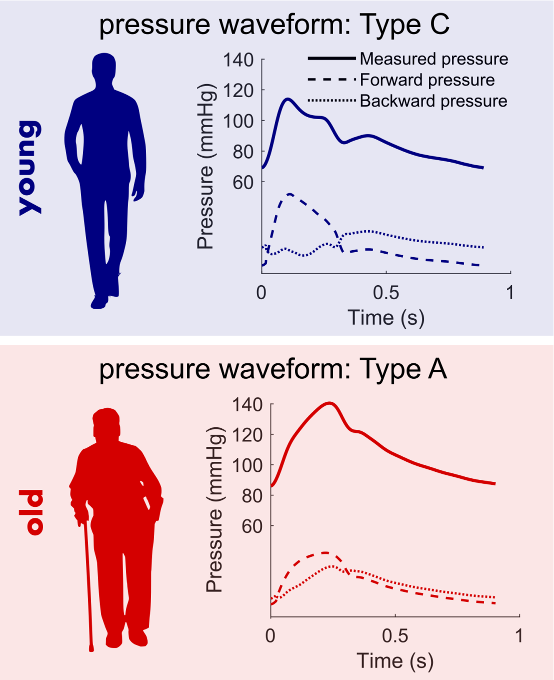

Figure 1.14: Carotid pressure waveforms type C and type A, measured in a young (top) and old (bottom) subject from the Asklepios population, respectively. Pressure waves decomposed in the forward and backward component show an arrival of reflected waves in diastole for the young, and in systole for the old subject.

AIx = AP/PP, with PP the pulse pressure and AP the augmented pressure, derived as the difference between SBP and the pressure at the fiducial point [82]. AIx is positive for type A waves, and negative for type C, since the reflected wave does not add to SBP. Although AIx is used as a measure of wave reflection, it has been shown to be a composite measure, influenced by several factors other than wave reflection, therefore not the most suitable index of wave reflection [82].

The inflection or shoulder points have been used to define the reflected wave transit time (RWTT) [100]. RWTT can also be derived from wave separation analysis (WSA), as the time delay between the zero crossing of the forward and backward pressure waves (see panel D in Figure 1.15). The timing of the inflection and shoulder points differ from each other, and from the RWTT estimated by WSA [100, 101]. In a recent work, RWTT estimated by WSA was found to be more reliable than T_{inf} [102].

The effective reflection distance (L), which is the distance travelled by the waves to an assumed effective reflection site, can be estimated from the combination of RWTT and the local PWV [100]. Since the wave would travel

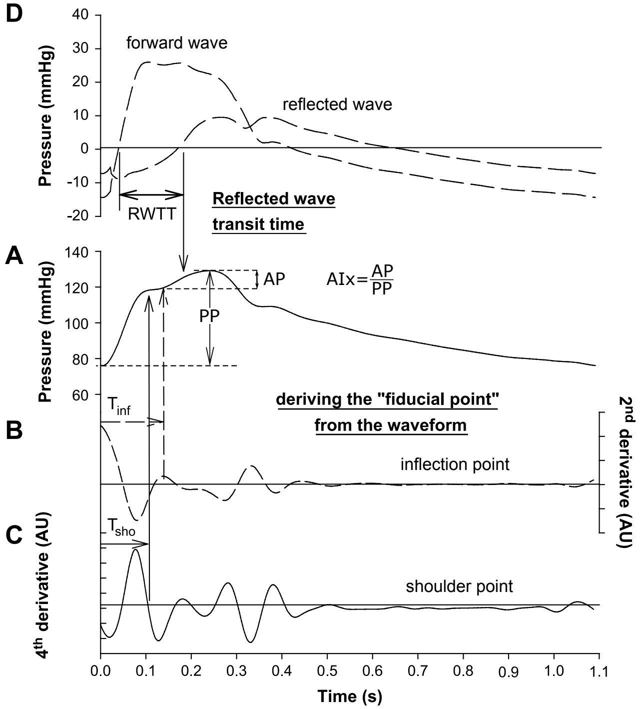

Figure 1.15: Pressure waveform analysis. Panel A: Measured pressure waveform type A, with indication of pulse pressure (PP) and augmented pressure (AP). Panels B and C: Determination of the inflection (T_{inf}) and shoulder (T_{sho}) points using 2nd and 4th order derivatives, respectively. Panel D: Wave separation analysis and determination of RWTT. Image adapted from [82].

twice the same distance, the final distance results in:

$$L = \frac{\text{PWV} \cdot \text{RWTT}}{2} \tag{1.12}$$

1.5.3 Wave separation analysis

There are two major methods for the separation of the waves when studying wave reflections: the classic method, based on the analysis of pressure and flow in the frequency-domain and through impedance analysis (see section 1.4) [6], and wave intensity analysis (WIA), which analyses the pressure and flow waveforms in the time-domain [103]. The first is a more complex method that decomposes the waves in sinusoidal harmonics using Fourier theory, and only allows to analyse the net effect of the waves. On the other hand, WIA is a simpler and more intuitive method, that allows to analyse the contribution of each wave separately. The wave separation analysis (WSA) by either the frequency or time domain produces similar results [92, 104]. The methods are sensitive to the derivation of characteristic impedance or wave speed, respectively.

1.5.3.1 Wave separation in the frequency-domain

Having determined Z_c from the impedance analysis in the frequency domain, as described in section 1.4, waves can be separated into their forward (subscript f) and backward (subscript b) components for each harmonic i [6]. For the pressure signal the equations become;

$$P_{f_i} = \frac{1}{2}(P_i + Z_c \cdot Q_i) \tag{1.13}$$

$$P_{b_i} = \frac{1}{2}(P_i - Z_c \cdot Q_i) \tag{1.14}$$

where P_i and Q_i represent the Fourier transformed pressure and flow signals for each harmonic i. The zeroth harmonic is not considered for WSA because it represents the steady component of the signal. The temporal forward and backward pressure components (P_f and P_b) can then be obtained by summing up all forward and backward harmonics, or by applying the inverse transform. The reflection coefficient, which is the relative amount of the reflective wave, can be estimated for each harmonic:

$$\Gamma_i = \frac{Z_{\text{in}} - Z_c}{Z_{\text{in}} + Z_c} = \frac{P_{b_i}}{P_{f_i}} \tag{1.15}$$

As the reflection coefficient is a complex number depending on each harmonic, in practice, Γ is reported as the absolute value at the fundamental heart frequency, the first harmonic, which normally contributes most to the amplitude of the waveform. The equations are similar for flow; Γ is the same for pressure and flow waves but the sign is opposite (Γ=-Q_{b_i}/Q_{f_i}). The reflection magnitude (RM) is the ratio of the amplitudes of the temporal forward and backward wave.

$$\text{RM} = \frac{\max(P_b) - \min(P_b)}{\max(P_f) - \min(P_f)} = \frac{|P_b|}{|P_f|} \tag{1.16}$$

1.5.3.2 Wave separation in the time-domain

Wave separation in the time domain was introduced by Parker and Jones [103], linked to wave intensity analysis. Rather than decomposing pressure and flow waveforms in sinusoidal signals, the method proposes the decomposition of the waveforms as a sequence of small wavefronts. These wavefronts are defined as the change in pressure (or flow velocity) during a sampling period Δt:

$$\begin{aligned} \mathrm{d}P &= P(t + \Delta t) - P(t) \\ \mathrm{d}U &= U(t + \Delta t) - U(t) \end{aligned} \tag{1.17}$$

This methodology was first developed using the method of characteristics, which is based on the one-dimensional equations of conservation of mass and momentum, and describes the propagation of the changes in pressure ($\mathrm{d}P$) and flow velocity ($\mathrm{d}U$) caused by any small perturbation. These small wavefronts propagate with speed $U \pm c$ in the forward (+) and backward (-) directions, with c the wave speed given by the Bramwell-Hill equation, and can be located in time and space. The analysis is further simplified by assuming constant wave speed at a specific location, and by making the linearising assumptions that the changes in pressure and flow velocity in the forward and backward waves are additive when they intersect, via:

$$\mathrm{d}P = \mathrm{d}P_+ + \mathrm{d}P_- \tag{1.18}$$

$$\mathrm{d}U = \mathrm{d}U_+ + \mathrm{d}U_- \tag{1.19}$$

By combining equations 1.18 and 1.19 with the water hammer equations for the forward and backward wavefronts ($\mathrm{d}P_\pm = \pm\rho c \mathrm{d}U_\pm$), the changes in pressure and flow velocity for the forward and backward wavefronts can be solved in terms of the measured wavefronts:

$$\mathrm{d}P_+ = \frac{1}{2}(\mathrm{d}P + \rho c \mathrm{d}U) \tag{1.20}$$

$$\mathrm{d}P_- = \frac{1}{2}(\mathrm{d}P - \rho c \mathrm{d}U) \tag{1.21}$$

$$\mathrm{d}U_+ = \frac{1}{2}(\mathrm{d}U + \frac{\mathrm{d}P}{\rho c}) \tag{1.22}$$

$$\mathrm{d}U_- = \frac{1}{2}(\mathrm{d}U - \frac{\mathrm{d}P}{\rho c}) \tag{1.23}$$

The sum of the forward and backward components of the change in pressure results in the total forward and backward pressure signals:

$$P_+ = P_{\text{dias}} + \sum_{t=0}^{t} \mathrm{d}P_+ \tag{1.24}$$

$$P_{-} = \sum_{t=0}^{t} \mathrm{d}P_{-} \tag{1.25}$$

where P_{dias} is the DBP. Similarly for flow velocity,

$$U_{+} = \sum_{t=0}^{t} \mathrm{d}U_{+} \tag{1.26}$$

$$U_{-} = \sum_{t=0}^{t} \mathrm{d}U_{-} \tag{1.27}$$

The reflection magnitude in the time domain is equivalent to equation (1.16) in the frequency domain.

1.5.4 Wave intensity analysis

Wave intensity ($\mathrm{d}I$) is defined as the product of the changes in pressure and flow velocity [103, 105],

$$\mathrm{d}I = \mathrm{d}P \cdot \mathrm{d}U \tag{1.28}$$

Wave intensity can be separated in the wave intensity due to the forward and the backward propagating waves:

$$\mathrm{d}I_{+} = \mathrm{d}P_{+} \cdot \mathrm{d}U_{+} \tag{1.29}$$

$$\mathrm{d}I_{-} = \mathrm{d}P_{-} \cdot \mathrm{d}U_{-} \tag{1.30}$$

By substituting equations 1.20-1.23, the forward and backward wave intensity can be derived as a function of the measured pressure and flow velocity changes.

$$\mathrm{d}I_{\pm} = \pm \frac{1}{4\rho c} (\mathrm{d}P \pm \rho c \mathrm{d}U)^2 \tag{1.31}$$

The sum of the forward and backward wave intensity represents the net wave intensity:

$$\mathrm{d}I = \mathrm{d}I_{+} + \mathrm{d}I_{-} \tag{1.32}$$

Wave intensity is expressed in units of ($\mathrm{W/m^2}$). WIA allows determining the nature and magnitude of the wave, and the type of wave dominating at a certain moment, provided that the local wave speed is known and pressure and flow velocity have been measured simultaneously at the same position. When $\mathrm{d}P$ is positive waves are called compression waves, and when $\mathrm{d}P$ is negative waves are called expansion or suction waves. Similarly, a positive $\mathrm{d}U$ means acceleration while negative $\mathrm{d}U$ deceleration. Thus, there are four possible types of waves: forward compression wave

(FCW), forward expansion wave (FEW), backward compression wave (BCW), and backward expansion wave (BEW). When dI is positive, forward travelling waves are dominant and when dI is negative, backward travelling waves are the dominant waves. Figure 1.16 gives an overview of the relationships for forward and backward waves and the travelling directions and origin. An example of WIA performed on simulated pressure and flow velocity waveforms, at the level of the ascending aorta, is shown in Figure 1.17.

direction	dP	dU	dI	
+	+	+	+	FCW
+	-	-	+	FEW
-	+	-	-	BCW
-	-	+	-	BEW

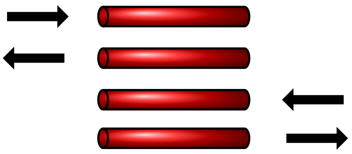

Figure 1.16: Scheme of the types of waves and the travelling direction. F: forward, B: backward, C: compression, E: expansion, W: wave.

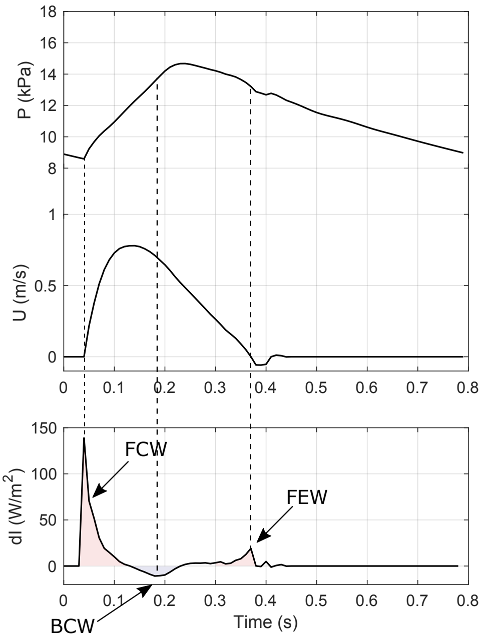

Figure 1.17: Example of wave intensity analysis for computer simulated data in the ascending aorta. Pressure and flow velocity waveforms (top) were used to derive wave intensity (bottom).

1.5.5 Wave power analysis

Wave intensity analysis has increased in popularity compared to frequency domain analysis, as its application in the time domain makes the interpretation of wave dynamics more intuitive. Nevertheless, wave intensity is not a conserved quantity since it is based on flow velocity rather than flow rate, being sensitive to vessel diameter variations. To overcome these difficulties, Mynard and Smolich [106] proposed a novel approach called wave power analysis (WPA), which is also entirely developed in the time domain and is closely related to WIA.

Using the method of characteristics, wave power ($d\pi$) was defined as the product of the changes in pressure (dP) and flow (dQ).

$$d\pi = dP \cdot dQ \tag{1.33}$$

Wave power can be separated into its forward (+) and backward (-) components, which by assuming linear separation can be written as;

$$d\pi = d\pi_{+} + d\pi_{-} \tag{1.34}$$

where,

$$d\pi_{+} = dP_{+} \cdot dQ_{+} \tag{1.35}$$

$$d\pi_{-} = dP_{-} \cdot dQ_{-} \tag{1.36}$$

By assuming constant characteristic impedance, with $Z_c = \rho c/A$, Mynard and Smolich [106] showed that the forward and backward wave power can be solved as a function of the measured changes in pressure and flow.

$$d\pi_{+} = \frac{1}{4Z_c}\left(dP + Z_c dQ\right)^2 \tag{1.37}$$

$$d\pi_{-} = -\frac{1}{4Z_c}\left(dP - Z_c dQ\right)^2 \tag{1.38}$$

Since linear flow conditions were assumed, $Z_c dQ = \rho c dU$, thus wave power and wave intensity are found to be related as $d\pi = A dI$.

The concept of wave power is analogous to wave intensity, with $d\pi > 0$ indicating dominant forward waves and $d\pi < 0$ indicating dominant backward waves. Wave power equals the energy carried by the wave and is given in units of (W). Contrary to wave intensity, wave power is conserved at junctions (see Figure 1.18), and has also been shown to be insensitive to diameter variations [106].

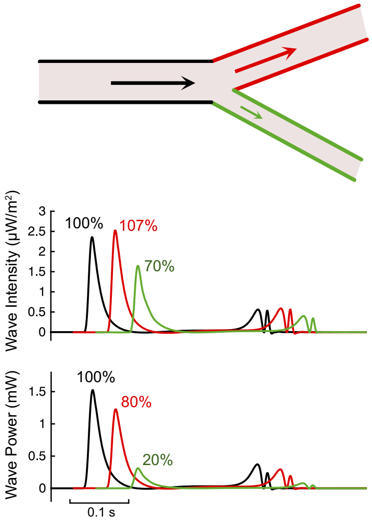

Figure 1.18: The comparison of wave intensity and wave power in the three branches of a bifurcation, shows that wave power is conserved at junctions; wave power of the parent vessel equals the sum of wave power of the daughters. Image adapted from [106].

Chapter 2

Modelling the cardiovascular system: Mathematical background on the one-dimensional model of the arterial tree

In the present chapter, a brief overview of relevant models of the cardiovascular system is first provided. The rest of the chapter focuses on the description of the 1D mathematical model of the arterial circulation, used throughout this thesis. This particular model was published and validated by Reymond *et al.* [12, 107], based on an earlier work by Stergiopulos *et al.* [108]. The model has gained great acceptance in the scientific community, and it has served as a base for many studies. This chapter accounts for the main physical and mathematical principles of the 1D model, which has been subsequently adapted to meet the need of the different studies undertaken.

2.1 Models of the arterial tree

The cardiovascular system has been studied not only from the clinicians point of view, but also by researchers from different disciplines, trying to unravel complex hemodynamic phenomena. Computational models have evolved from relatively simple lumped (0D) or one-dimensional (1D) models, to more complex three-dimensional (3D) models [24]. 3D models allow for comprehensive studies of complex hemodynamic phenomena, for instance through fluid-structure interaction approaches; however, due to the difficulty of defining a detailed 3D geometry of the arterial tree, and the computational cost associated with these models, they are usually restricted to simulations at specific locations of pathophysiological interest in the CV system [109]. 1D models on the contrary, are commonly used to investigate wave propagation of pressure and flow along the systemic arterial network, offering a simplified solution in one spatial direction with reasonable accuracy and computational cost [12, 110, 111].

Models of the cardiovascular circulation allow for a better understanding of the relationships of arterial flow and pressure, and how arterial properties influence the shape of the pressure and flow waveforms. Knowledge of the distribution of pressure and flow in the arterial tree is important for diagnostic and treatment planning [112]. *In silico* studies allow to investigate several pathophysiological conditions by varying the model parameters, without the ethical or technical limitations of *in vivo* studies. Moreover, models of the CV system can also be used in cardiac studies to simulate physiological as well as pathological conditions.

Modelling the CV system is challenging due to the complexity of the anatomy. Therefore, models are usually restricted to specific parts of the arterial tree, which requires the definition of boundary conditions at the distal ends where the smaller arteries and microcirculation must be described; while at the inlet of the aortic root the ventricular-arterial interaction has to be accounted for. The mechanical properties of the circulation also make the modelling task difficult, since blood vessels have nonlinear viscoelastic walls, while the flow is highly pulsatile and blood is, in essence, a fluid with a complex rheology. The description of the CV system adaptability, with its autoregulation mechanism, is also challenging.

2.1.1 Windkessel models

Windkessel models are lumped parameters models (also called 0D), which are based on an analogy to the Windkessel fire engine, and can be also represented as electric circuits. These models, when expressed at the proximal aorta, give a lumped representation of the entire arterial tree. Their main advantage is that they require only a few global parameters to represent the main properties of the arterial tree in consideration [113].

The first lumped arterial model was the 2-element Windkessel model introduced in 1899 by Frank [8], consisting of a resistance and a capacitor in parallel (see panel A in Figure 2.1). The resistance element accounts for the total peripheral resistance, which is the summation of all parallel resistances in the vascular bed. On the other hand, the compliance element (capacitor) is mainly determined by the large elastic arteries, and is considered to be the summation of the compliances of all vessels in the arterial tree, and is therefore called the total arterial compliance. The 2-element Windkessel model mimics pressure and flow well in diastole, but not in systole. The limitations of this model, observed from the calculation of input impedance in the frequency domain (see panel D in Figure 2.1), were improved by adding a third element (the characteristic impedance represented by a resistor) in series with the 2-element Windkessel model [114] (panel B in Figure 2.1). However, this leads to errors in the low frequencies range, and therefore to inaccurate estimates of total arterial compliance. This difficulty was overcome with a fourth element [115], where an inductance was incorporated in parallel with the characteristic impedance, representing the total arterial inertance (see panel C in Figure 2.1). In this way, the model approximates the 2-element model for low frequencies, and the 3-element model for high frequencies.

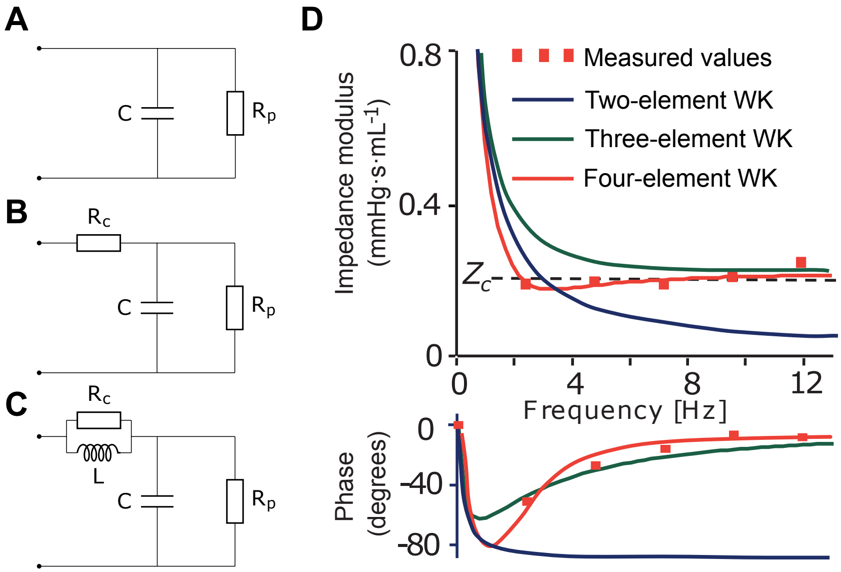

Figure 2.1: Analogy of Windkessel models to an electric circuit, for the two- (A), three- (B) and four-element (C) Windkessel models, respectively. R_c and R_p: characteristic and peripheral resistance. C: total arterial compliance. L: inertance. (D) Comparison of measured aortic input impedance with impedances predicted by the Windkessel models. Adapted from [31].

Windkessel models have been used to estimate pressure and flow, to estimate compliance [94, 116], and as a load to the heart in ventricular-arterial interaction studies [117, 118], as well as a peripheral load for 1D models [12, 108]. Despite being a good approximation to study the behaviour of the arterial system as a whole, they are very simplified models that do not account for the pressure and flow wave propagation phenomenon and reflection, thereby limiting the accuracy of the pressure wave shape.

2.1.2 1D or distributed model

Distributed models (or 1D models) decompose the arterial network in segments, connected by nodes, with known geometrical and mechanical properties (see Figure 2.2). For each of these segments, the wave transmission theory may be characterized through the oscillatory flow theory of Witzig-Womersley, the electrical transmission line theory, or by solving the 1D formulation of the Navier-Stokes equations of conservation of mass and momentum [24]. 1D models are usually used to predict pressure and flow waveforms at specific locations in the arterial system, because the 1D equations appropriately describe the wave propagation phenomenon [119]. The ability of the 1D formulation to capture the main features of pressure and flow waveforms in large human arteries has been verified by comparing with *in vivo* data [12, 107, 120–122], *in vitro* data [123–127], or with *in silico* 3D models [128, 129].

One-dimensional models have been used in several studies to investigate the cardiovascular physiology [130], or pathologies such as stenosis [108, 131, 132], abdominal aortic aneurysm [133], hypertension [17, 134], or diastolic dysfunction [135]. These models have increased their value in the last years, since they can be also used as boundary condition for more complex 3D models [136, 137]. Furthermore, patient-specific models can be a useful tool to support clinical decisions and surgical planning [107, 138], although progress within this topic is hampered due to the complexity of noninvasively measuring all the parameters used in the models.

2.2 MODEL ASSUMPTIONS

The governing equations of the 1D model described below, are based on the 1D equations of conservation of mass and momentum that result from integrating the Navier-Stokes equations, coupled with a constitutive relation that describes arterial wall elasticity [12]. Arteries are simulated as tapered or straight cylindrical segments connected by nodes, with circular cross-section. Structural arterial properties are assumed to be constant for the segment, with the same functional dependence of wall elasticity on pressure for all arterial locations. Blood is assumed to be a Newtonian and incompressible fluid (typical values of dynamic viscosity, μ = 0.004 Pa·s, and density, ρ = 1050 kg/m^3). The Witzig-Womersley theory is used to account for the pulsatile effects on the velocity profile, which is needed to calculate convective acceleration and wall shear stresses in the momentum equation. For the boundary conditions at each distal end, 3-element Windkessel models are used; whereas at the proximal end, the arterial-ventricular interaction is accounted for with a varying elastance model of the left ventricle. The modelled human arterial system includes the left heart, the aorta and its main branches, as well as a description of the cerebral artery network and major coronary arteries. The scheme of the arterial system comprising 103 arterial segments (Figure 2.2) and the geometrical and mechanical parameters used as model input (Table 2.1), are directly reproduced from Reymond *et al.* [12]. The data of the main systemic arterial tree were based on the model of Stergiopulos *et al.* [108] and the preceding work of Westerhof *et al.* [114], while the data of the main cerebral arteries were obtained from averaged literature data and completed by real patient scans.

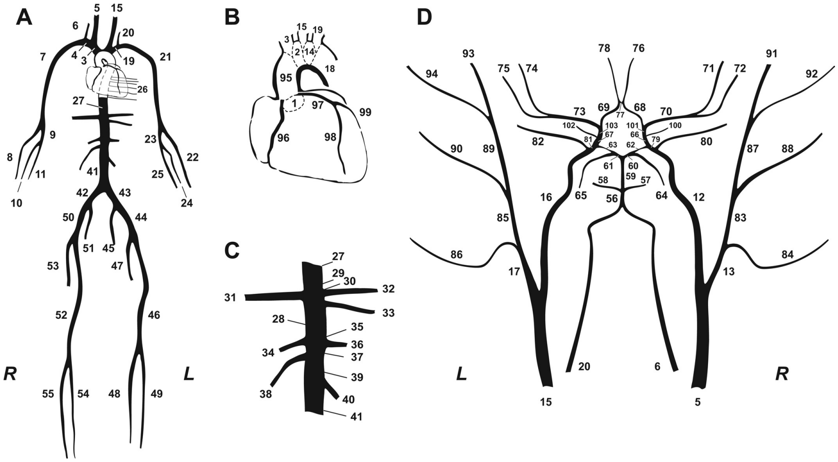

Figure 2.2: Scheme of the modelled human arterial tree. (A) Main systemic arteries; (B) Detail of the aortic arch and the coronary network; (C) Detail of the main abdominal aortic branches. (D) Detail of the cerebral artery network. R: right; L: left. Figure reproduced from [12].

Table 2.1: Initial geometric and mechanical properties for the 103-segments arterial system. Data from [12].

Arterial segment name	Arterial segment no. (right/left)	Length (mm)	Proximal diameter (mm)	Distal diameter (mm)	Distensibility (10^{-3} 1/mmHg)	Terminal resistance (mmHg·s/mL)	Terminal compliance (10^{-5} mL/mmHg)
Ascending aorta 1	1	5	29.4	29.3	5.46		
Aortic arch A	2	20	25.1	24	4.9		
Brachiocephalic	3	34	20.2	18	4.22		
Subclavian A	4/19	34	11.5/11	9/8.5	2.9/2.81		
Common carotid	5/15	94/139	13.5/12	7/6	2.93/2.68		
Vertebral	6/20	149/148	3.7	2.8	1.46		
Subclavian B, axillary, brachial	7/21	422	8.1	4.7	2.19		
Radial	8/22	235	3.7/3.5	3.1/2.8	1.49/1.43	39.7	702.9
Ulnar A	9/23	67	3.7/4.3	3.4/4.3	1.53/1.72		

Continued on Next Page…

Table 2.1: (Continued)

Arterial segment name	Arterial segment no. (right/left)	Length (mm)	Proximal diameter (mm)	Distal diameter (mm)	Distensibility (10^{-3} 1/mmHg)	Terminal resistance (mmHg·s/mL)	Terminal compliance (10^{-5} mL/mmHg)
Interosseous	10/24	79	2.1/1.8	1.8	1.08/1.03	633.8	44
Ulnar B	11/25	171	3.2/4.1	2.8/3.7	1.39/1.62	39.7	702.9
Internal carotid	12/16	178	5.7/5.3	4.3/4.1	1.89/1.82		
External carotid 1	13/17	41	5/4.7	4.5/4.3	1.83/1.77		
Aortic arch B	14	39	21.4	20.8	4.48		
Thoracic aorta A	18	52	20	18.9	4.26		
Intercostals	26	80	12.6	9.5	3.04	10.5	2670.1
Thoracic aorta B	27	104	16.5	12.9	3.6		
Abdominal aorta A	28	53	12.2	12.2	3.22		
Celiac A	29	20	7.8	6.9	2.38		
Celiac B	30	20	5.2	4.9	1.9		
Hepatic	31	66	5.4	4.4	1.87	27.3	1022.5
Gastric	32	71	3.2	3	1.42	40.7	686.1
Splenic	33	63	4.2	3.9	1.66	17.4	1599.8
Superior mesenteric	34	59	7.9	7.1	2.41	7	3991
Abdominal aorta B	35	20	11.5	11.3	3.09		
Renal	36/38	32	5.2	5.2	1.93	8.5	3284.6
Abdominal aorta C	37	20	11.8	11.8	3.16		
Abdominal aorta D	39	106	11.6	11	3.07		
Inferior mesenteric	40	50	4.7	3.2	1.64	51.7	539.5
Abdominal aorta E	41	20	10.8	10.4	2.96		
Common iliac	42/43	59	7.9	7	2.39		
External iliac	44/50	144	6.4	6.1	2.15		
Inner iliac	45/51	50	4	4	1.65	59.7	467.7
Femoral	46/52	443	5.2	3.8	1.77		
Deep femoral	47/53	126	4	3.7	1.61	35.9	778.1
Posterior tibial	48/54	321	3.1	2.8	1.38	35.9	778.1
Anterior tibial	49/55	343	2.6	2.3	1.24	42	664
Basilar artery 2	56	20	4	3.6	1.6		
Superior cerebellar	57/58	10	1.7	1.4	0.93	200.8	3.6
Basilar artery 1	59	5	3.1	2.7	1.36		
Posterior cerebral 1	60/61	2	1.9	1.9	1.05		
Posterior communicating	62/63	4	1.2	1.2	0.78		
Posterior cerebral 2	64/65	59	2	1.8	1.12	80.5	5.8
ICA distal 1	66/67	2	3.9	3.8	1.62		
Anterior cerebral 1	68/69	12	2.1	2	1.1		
MCA 1	70/73	8	3	2.8	1.36		
MCA 2 superior branch	71/74	71	2	1	0.92	75.2	2.8
MCA 2 inferior branch	72/75	70	2	1	0.92	75.2	2.8
Anterior cerebral 2	76/78	24	1.8	1.7	0.99	80.5	4.7
Anterior communicating	77	2	1.3	1.3	0.84		
ICA sinus	79/81	11	4.3	3.9	1.67		
Ophthalmic	80/82	11	1	0.5	0.6	200.8	0.4
External carotid 2	83/85	61	4	3.5	1.59		
Superior thyroid ascending pharyngeal lingual facial occipital	84/86	101	2	1	0.92	225.6	5.9
Superficial temporal	87/89	61	3.2	3	1.42		
Maxillary	88/90	91	2.2	1	0.95	188	5

Continued on Next Page...

Table 2.1: (Continued)

Arterial segment name	Arterial segment no. (right/left)	Length (mm)	Proximal diameter (mm)	Distal diameter (mm)	Distensibility (10^{-3} 1/mmHg)	Terminal resistance (mmHg·s/mL)	Terminal compliance (10^{-5} mL/mmHg)
Superficial temporal frontal branch	91/93	100	2.2	1.4	1.02	188	8.2
Superficial temporal parietal branch	92/94	101	2.2	1.4	1.02	188	7.6
Ascending aorta 2	95	35	29.3	28.8	5.42		
Right coronary artery	96	53.7	3.6	2.6	1.42	55.6	26.6
Left main coronary artery	97	5	4.9	4.7	1.84		
Left anterior descending coronary	98	47	3.8	1.5	1.29	45.1	26.6
Left circumflex coronary	99	26	3.5	3.1	1.47	45.1	26.6
Anterior choroidal	100/102	36	1.5	1.3	0.88	150.4	15.4
ICA distal 2	101/103	2	3.85	3.8	1.6		

ICA: internal carotid artery; MCA: middle cerebral artery.

2.3 GOVERNING EQUATIONS OF THE 1D MODEL

The conservation of mass principle states that in every continuum body, the mass (m) is unchanged during motion [139]. Hence, the mass of a fluid particle for instance, is the same in a reference configuration and during motion. The mass is characterized by the product of the density (ρ) and the volume (V), such that in differential form $\mathrm{d}m = \rho \mathrm{d}V$. By integrating over the entire region, and considering the material time derivative, the principle can be expressed mathematically in the continuity form as [139],

$$\frac{\partial \rho}{\partial t} + \nabla \rho \cdot \mathbf{u} = 0 \tag{2.1}$$

where $\mathbf{u}$ is the vector of fluid velocity, and the gradient of a function is defined as: $\nabla f = \frac{\partial f}{\partial x} + \frac{\partial f}{\partial y} + \frac{\partial f}{\partial z}$. Assuming an incompressible fluid, the density is constant and the equation simplifies to:

$$\nabla \cdot \mathbf{u} = 0 \tag{2.2}$$

The conservation of linear momentum (Newton's second law of motion) states that the rate of change of linear momentum equals the net applied forces. The balance of momentum in vector form can be written as [139]:

$$\rho \frac{\mathrm{d}\mathbf{u}}{\mathrm{d}t} = \nabla \cdot \boldsymbol{\sigma} + \rho \mathbf{b} \tag{2.3}$$

where $\mathbf{b}$ is the body force, and the Cauchy stress tensor ($\boldsymbol{\sigma}$), for the case of Newtonian fluids, is expressed by a constitutive equation depending on pressure and viscous forces. The first attempt to formulate the mathematical model for incompressible flow in an arterial segment was made by Euler in the 18th century, but his equation neglected the viscosity effects. Generalization of Euler's equation for viscous fluids were made initially by Navier in 1827 and later improved by Stokes in 1845 [8], and the equation can take the form:

$$\rho \frac{\mathrm{d}\mathbf{u}}{\mathrm{d}t} = -\nabla P + \mu \nabla^2 \mathbf{u} + \rho \mathbf{b} \tag{2.4}$$

where P is the fluid pressure and μ is the viscosity. Applying the chain rule in the material acceleration term the equation can be written as:

$$\rho \left(\frac{\partial \mathbf{u}}{\partial t} + \mathbf{u} \cdot \nabla \mathbf{u} \right) = -\nabla P + \mu \nabla^2 \mathbf{u} + \rho \mathbf{b} \tag{2.5}$$

These equations, known as the Navier-Stokes equations for the motion of viscous fluids, along with the continuity equation (2.2) can be used to describe the blood flow through the arterial system. The conservation of mass and momentum equations are further simplified for the one-dimensional case and by integrating over the cross section of the artery, yielding the following governing equations:

$$\frac{\partial A}{\partial t} + \frac{\partial Q}{\partial x} + \psi = 0 \tag{2.6a}$$

$$\frac{\partial Q}{\partial t} + \frac{\partial}{\partial x} \left(\int_A u^2 dA \right) = -\frac{A}{\rho} \frac{\partial P}{\partial x} - 2\pi R \frac{\mu}{\rho} \frac{\partial u}{\partial r} \bigg|_{r=R} + A\mathrm{b}_x \tag{2.6b}$$

These equations form a nonlinear system for the primary variables pressure $P(x,t)$, flow rate $Q(x,t)$, and the cross-sectional area $A(x,t)$. To close the system of equations, a constitutive relation between pressure and area is typically used. ψ is the arterial wall seepage, $R(x,t)$ is the lumen radius and $u(r,x,t)$ the component of the longitudinal velocity. Further assumptions consider the arterial wall to be impermeable ($\psi = 0$), and the action of any body force, such as gravity, is neglected in most cases ($\mathrm{b}_x = 0$). Other derivations of the equations can be found in [24, 111, 120, 137].

2.4 Arterial wall modelling: nonlinear elasticity

A constitutive equation is needed to account for the properties of the arterial wall, relating intra-arterial pressure with the cross-sectional area. In the work of Reymond *et al.* [12], the arterial wall behaviour includes a nonlinear elastic component and a viscoelastic component. For simplicity reasons, during this dissertation the effects of viscoelastic wall properties are neglected.

The nonlinear elastic behaviour of the arterial wall is described via the local area compliance (C_A), which is normally a function of distending pressure and of the position in the vascular network, accounted for by making C_A dependent on the reference/mean diameter ($\overline{d}$). Thus, vessels of the same size in different vascular territories are assigned similar properties.

$$C_A(\overline{d}, P) = \frac{\partial A}{\partial P} \tag{2.7}$$

As assumed by Reymond *et al.* [12], C_A is expressed as the product of a diameter-dependent function, $C_d(\overline{d}, P_{\text{ref}})$, and a pressure-dependent function, $C_P(P)$.

$$C_A(\overline{d}, P) = C_d(\overline{d}, P_{\text{ref}}) \cdot C_P(P) \tag{2.8}$$

The pressure dependency of the compliance is described based on the Langewouters model [140, 141],

$$C_P(P) = a_1 + \frac{b_1}{1 + \left[\frac{P - P_{\text{maxC}}}{P_{\text{width}}}\right]^2} \tag{2.9}$$

and fitting of the parameters in thoracic and abdominal aortas resulted in $a_1 = 0.4$, $b_1 = 5$, $P_{\text{maxC}} = 20$ mmHg, and $P_{\text{width}} = 30$ mmHg. These values were retained for the entire arterial tree, assuming the same functional dependence for every location.

The diameter-dependent function of the compliance, gives the compliance for a given local mean arterial lumen diameter ($\overline{d}$) at a given reference pressure value ($P_{\text{ref}} = 100$ mmHg), and it was derived as:

$$C_d(\overline{d}, P_{\text{ref}}) = \frac{A}{\rho \cdot \text{PWV}^2(\overline{d}, P_{\text{ref}})} \tag{2.10}$$

Taking into account the relation between PWV and the distensibility coefficient (D_w) given by the Bramwell-Hill equation (1.4), the equation for the local area compliance finally results in:

$$C_A(\overline{d}, P) = A \cdot D_w \left(a_1 + \frac{b_1}{1 + \left[\frac{P - P_{\text{maxC}}}{P_{\text{width}}}\right]^2} \right) \tag{2.11}$$

An example of the compliance curve obtained from this equation, for a segment of the abdominal aorta in the pressure range 0-200 mmHg, as well

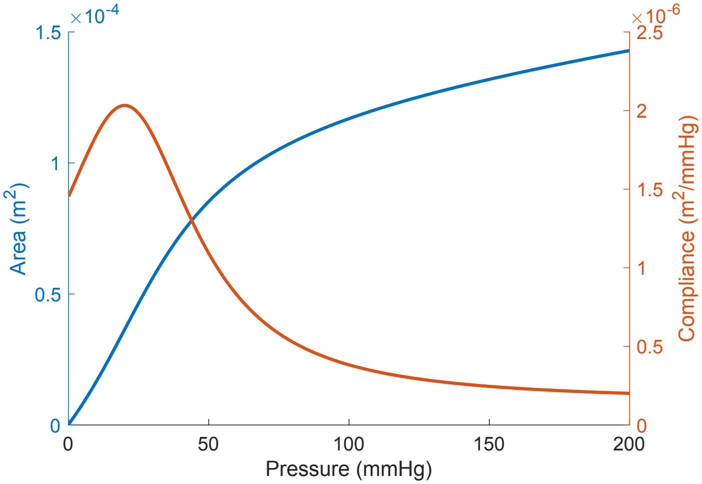

Figure 2.3: Example of the model pressure dependency of compliance and cross-sectional area for a segment of the abdominal aorta, over the pressure range 0-200 mmHg. Substitution of different parameter values in equation (2.11) gives a different relationship of compliance (or area) as a function of pressure.

as the area-pressure relationship (derived by integrating equation (2.11) over the pressure), is shown in Figure 2.3.

To estimate PWV and consequently the distensibility of the vessel, Reymond *et al.* [12] fitted an empirical inverse power curve for PWV as a function of the local diameter, from human data reported in the literature,

$$\mathrm{PWV}(\overline{d}) \approx \frac{a_2}{\overline{d}^{\,b_2}} \tag{2.12}$$

with the coefficients resulting in $a_2 = 13.3$ and $b_2 = 0.3$.

By considering the relation (2.7), the continuity equation (2.6a) can be rewritten as:

$$\frac{\partial P}{\partial t} = -\frac{1}{C_A}\frac{\partial Q}{\partial x} \tag{2.13}$$

with the local area compliance given by equation (2.11).

2.5 VELOCITY PROFILE

The formulation of the momentum equation (2.6b) contains the convective acceleration term $\left(\frac{\partial}{\partial x}\int_A u^2 dA\right)$, as well as the wall friction term $\left(\tau = \mu \frac{\partial u}{\partial r}\Big|_{r=R}\right)$, both depending on the local velocity profile (u). Velocity profiles are generally approximated and assumed to be symmetric to the longitudinal axis. Several approximations have been used to model the velocity profile; from

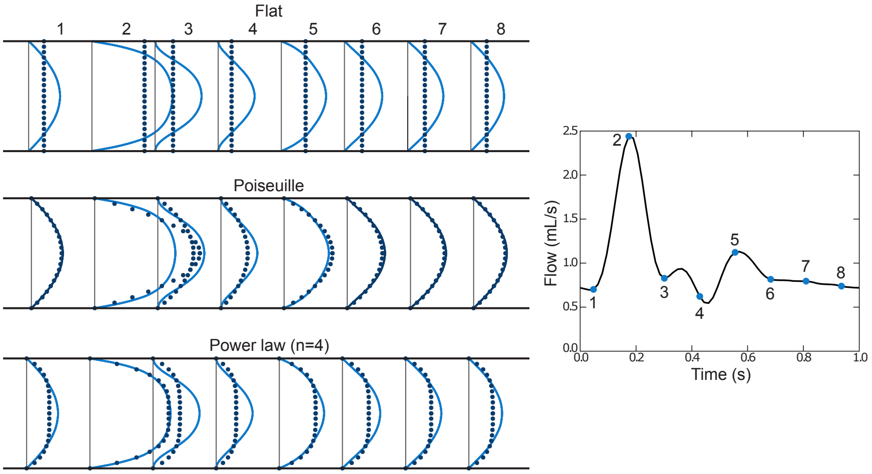

Figure 2.4: Comparison of different velocity profiles (dotted lines) with the Womersley velocity profiles (solid lines), for the carotid flow pulse on the right, at eight time instants. Figure adapted from [24].

the more simple ones such as the assumed shape profiles (flat, Poiseuille's law, power law), to more complex such as the profiles periodic in time (Witzig-Womersley theory), or the approximated velocity profiles (see Figure 2.4 and refer to [24] for more details).

The velocity profile depends on the Womersley parameter (α, defined further in section 2.5.1) [142, 143]. *In vivo* observations under normal conditions have shown that in the large arteries the velocity profile is relatively flat [8, 28]. In the periphery with small vessels ($\alpha < 3$) and more steady flow, the velocity profile has a more parabolic shape [8, 28]. In the model, to approximate the velocity profile the Witzig-Womersley theory (or oscillatory flow theory) is used, to model as best as possible the pulsatile effects on the velocity profile.

2.5.1 The Witzig-Womersley theory

The Witzig-Womersley theory [142, 143] describes the effect of flow pulsatility and inertia on the velocity profile. The oscillatory flow theory is of great importance especially for the calculations of wall shear and local flow profiles [31]. The relation for the velocity profile takes the form:

$$u(r,t) = \frac{2}{\pi R^2}\left(1-\frac{r^2}{R^2}\right)Q_1 + \sum_n \text{Real}\left\{\frac{Q_n}{\pi R^2}\left[\frac{1-\frac{J_0\left(\alpha i^{3/2}\frac{r}{R}\right)}{J_0\left(\alpha i^{3/2}\right)}}{1-\frac{2J_1\left(\alpha i^{3/2}\right)}{\alpha i^{3/2}J_0\left(\alpha i^{3/2}\right)}}\right]e^{i\omega t}\right\} \tag{2.14}$$

Derivative of the velocity profile given by this relation, allows for the deduction of the wall friction term (τ) for the oscillatory theory as:

$$\tau(t) = -\frac{4\mu}{\pi R^3} Q_1 + \sum_n \text{Real}\left\{ \frac{\mu}{\pi R^3} Q_n \alpha i^{3/2} \left[\frac{\frac{J_1\left(\alpha i^{3/2}\right)}{J_0\left(\alpha i^{3/2}\right)}}{1 - \frac{2 J_1\left(\alpha i^{3/2}\right)}{\alpha i^{3/2} J_0\left(\alpha i^{3/2}\right)}} \right] e^{i\omega t} \right\} \quad (2.15)$$

The velocity profile and the wall friction term are calculated as a Fourier series with harmonics (n) and depend on the harmonic-specific Womersley's number ($\alpha = R\sqrt{\rho 2\pi f/\mu}$); R is the artery radius and f the frequency, r/R is the relative radial position, Q_n is the n$^{\text{th}}$ harmonic of the flow pulse, $i = \sqrt{-1}$, and J_0 and J_1 are the Bessel functions of first kind of order 0 and 1, respectively. An overview of the derivation of these equations can be found in Appendix A. Note that if only the first term in the sum is considered, the equations reduce to Poiseuille's law (steady flow component), with a parabolic profile.

The Witzig-Womersley theory, obtained in the frequency domain, requires the knowledge of the local flow profile across the arterial lumen over the entire heart cycle, which is a priori unknown in the 1D model. This difficulty is overcome by assuming that the solution is periodic; the flow waveform from the previous heart cycle is used to calculate the velocity profile and the wall shear stress in equations (2.14) and (2.15), respectively.

2.6 PROXIMAL BOUNDARY CONDITIONS

A model of the left ventricle (LV) can be coupled to the arterial system at its proximal end (root of the ascending aorta), simulating the blood flow pumped out of the LV. Alternatively, a typical aortic flow profile (or pressure) may be used as the input condition in the proximal end of the arterial network. This approach presents more limitations to be used in a study where different heart conditions need to be simulated.

2.6.1 Heart model

The LV model is based on the time-varying elastance model originally suggested by Sagawa [144, 145], which was adapted by Reymond *et al.* [12] as follows. The time-varying elastance ($E(t)$) model describes the variation of LV pressure (P_{LV}) and volume (V_{LV}) during a cardiac cycle, where V_0 is the dead volume:

$$E(t) = \frac{P_{\text{LV}}(t)}{V_{\text{LV}}(t) - V_o} \quad (2.16)$$

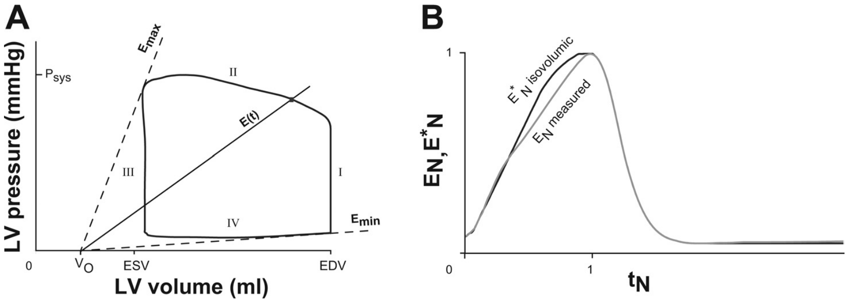

Figure 2.5: (A) Representation of the pressure-volume loop of the left ventricle, with indication of the four cardiac phases and the heart model parameters. (B) Normalized time varying elastance (E_N, E_N^*) as function of normalized time (t_N). E_{max} and E_{min}: maximal and minimal elastance; $E(t)$: time varying elastance; EDV and ESV: end-diastolic and end-systolic volume; V_0: dead volume; P_{sys}: systolic pressure. Reproduced from [12].

Under physiological conditions (no leaky valves), the interaction between the LV and the arterial tree occurs only during ejection (phase II in Figure 2.5A). The difference between ventricular pressure of an ejecting heart (P_{LV}), and the ventricular pressure during an isovolumic contraction (P_{LV}^*) (phase I in Figure 2.5A), can be explained by an internal resistance R_{int} as:

$$P_{LV} = P_{LV}^* - R_{int}(t)Q(t) \tag{2.17}$$

The internal resistance was found to be proportional to P_{LV}^*:

$$R_{int}(t) = \kappa P_{LV}^* \tag{2.18}$$

By substituting equation (2.18) into equation (2.17),

$$P_{LV} = P_{LV}^* \left(1 - \kappa Q(t)\right) \tag{2.19}$$

then considering the above equation, the varying elastance of an ejecting heart was expressed by Reymond *et al.* [12] as:

$$E(t) = E^*(t) \left(1 - \kappa Q(t)\right) \tag{2.20}$$

where E^* is the elastance that would be measured during a nonejecting isovolumic contraction, and κ a constant relating the internal resistance of the LV to the ventricular pressure during the same cardiac phase. By substituting equation (2.16) into equation (2.20), the equation can be then written in terms of the primary variables P and Q. Equation (2.20) allows to derive a normalized isovolumic elastance, E_N^*, by using the global normalized elastance curves, E_N, reported by Senzaki *et al.* [146] (see Figure 2.5B), and from aortic flow waves measured in vivo. The varying elastance curve for any individual is fully determined by only three cardiac parameters; the maximal elastance ($E_{\max}$), the minimal elastance ($E_{\min}$) and the time to maximum elastance ($t_{\max}$).

The heart model simulates the four main phases of the cardiac cycle as indicated in the pressure-volume loop of Figure 2.5. The loop starts at the onset of the isovolumic contraction phase, where the volume in the LV equals EDV (derived in the simulation from equation (2.16), for a LV pressure equal to the end-diastolic pressure ($P_{\text{end-dias}}$)). With the contraction, the pressure in the ventricle rises over the aortic pressure, which causes the opening of the aortic valve and the start of the ejection phase. During this period, the ventricle-arterial interaction is described by the combination of equations (2.16) and (2.20). When the flow becomes negative, end systole is reached (aortic valve closes) and the relaxation phase takes place. The filling phase is set when the pressure in the ventricle drops below the initially assumed $P_{\text{end-dias}}$, and the filling flow is modelled from the internal resistance of the LV (R_{ven}). The parameters of the heart model as given by Reymond *et al.* [12] are summarized in Table 2.2. The solution of the heart model is periodic; at the start of every cardiac cycle, EDV takes the value derived from the previous cardiac cycle.

Table 2.2: Parameters of the heart model. Data from [12].

Parameter	Value	Unit
Dead volume (V_0)	15	mL
Maximal elastance ($E_{\max}$)	2.6	mmHg/mL
Minimal elastance ($E_{\min}$)	0.08	mmHg/mL
Time to maximum elastance ($t_{\max}$)	0.34	s
End-diastolic pressure ($P_{\text{end-dias}}$)	14	mmHg
Venous resistance (R_{ven})	0.003	$\text{mmHg}\cdot\text{s}\cdot\text{mL}^{-1}$
Constant of proportionality (κ)	0.0005	s/mL
Heart rate (HR)	75	bpm

2.7 CORONARY MODEL

Coronary arteries were modelled by Reymond *et al.* [12], assuming that the changes induced by myocardial contraction in wall distensibility (D_{w}) and terminal compliance (C_{T}) and resistance (R_1, R_2), are proportional to ventricular time varying elastance:

$$D_{\text{w}}(E(t)) \approx D_{\text{w}}^{\text{ref}} - \varepsilon D_{\text{w}}^{\text{ref}} E(t)/E_{\max} \tag{2.21}$$

$$C_{\mathrm{T}}(E(t)) \approx C_{\mathrm{T}}^{\mathrm{ref}} - \alpha C_{\mathrm{T}}^{\mathrm{ref}} E(t)/E_{\max} \tag{2.22}$$

$$R_1(E(t)) \approx R_1 + \beta R_1 E(t)/E_{\max} \tag{2.23}$$

$$R_2 \approx \delta R_1 \tag{2.24}$$

where ε, α, β and δ are constants of proportionality. For the right coronary artery, an additional assumption was made, that the effect of the right ventricle (RV) contraction is smaller by a factor proportional to the relation of maximal pressure in both ventricles, taken as $P_{\mathrm{LV,max}}/P_{\mathrm{RV,max}} \approx 6$.

2.8 Distal boundary conditions

For the terminal arterial segments a 3-element Windkessel model was used (see section 2.1.1), to account for the cumulative effect of all distal vessels beyond the terminal sites [12, 108]. The equation takes the form:

$$\frac{\partial Q}{\partial t} = \frac{1}{R_1}\frac{\partial P}{\partial t} + \frac{P}{R_1 R_2 C_{\mathrm{T}}} - \left(1 + \frac{R_1}{R_2}\right)\frac{Q}{R_1 C_{\mathrm{T}}} \tag{2.25}$$

where R_1 is the proximal resistance, R_2 is the distal resistance, and C_{T} is the terminal compliance. Total peripheral resistances $R_{\mathrm{T}} = R_1 + R_2$, were estimated based on measured mean flow distribution in the major arterial beds. The values of R_1 were estimated assuming minimal reflection at high frequencies, with the condition $R_1 = Z_{\mathrm{c}}$, where $Z_{\mathrm{c}} = \rho \cdot \mathrm{PWV}/A$ is the characteristic impedance of the arterial segment proximal to the terminal site. Distal resistance was then obtained as $R_2 = R_{\mathrm{T}} - R_1$. Terminal compliance of each terminal vessel, C_{T_i}, was estimated by assuming it to be proportional to the area compliance, C_{A_i}, of the terminal vessel at its distal end:

$$C_{\mathrm{T}_i} \cong C_{\mathrm{T}} \frac{C_{A_i}}{\sum C_{A_i}} \tag{2.26}$$

with $C_{\mathrm{T}} = \sum C_{\mathrm{T}_i}$ the part of the total volume compliance attributed to peripheral vessels not included in the arterial tree model. The total systemic vascular compliance was derived by adding volume compliance of all vessels and compliance of the terminal beds, so that:

$$C_{\mathrm{V}} = \sum_i^n C_{\mathrm{V}_i} + \sum_i^m C_{\mathrm{T}_i} \tag{2.27}$$

where $n = 103$ is the total number of arterial segments and $m = 47$ is the number of terminal segments. To obtain volume compliance of each segment, the area compliance given by equation (2.11) is integrated over the segment length. The sum of compliances of the terminal beds was assumed to be in the order of 20% of the total systemic compliance. More details can be found in [12].

2.9 ARTERIAL BIFURCATIONS

Continuity of pressure and flow is imposed throughout the arterial network at bifurcations. These conditions may be expressed as (see Figure 2.6):

$$P_i = P_j = P_k \tag{2.28}$$

$$Q_i = Q_j + Q_k \tag{2.29}$$

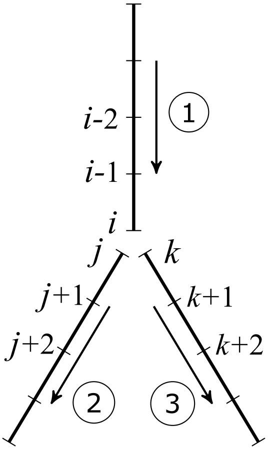

Figure 2.6: Scheme of an arterial bifurcation in the model, with one parent vessel and two daughters vessels. In the nodes i, j and k continuity of flow and pressure is assumed. The arrows indicate the positive direction of the axial coordinate.

The forward wave reflection coefficient at a bifurcation is calculated as:

$$\Gamma = \frac{Z_{\text{parent}}^{-1} - \sum Z_{\text{daughter}}^{-1}}{Z_{\text{parent}}^{-1} + \sum Z_{\text{daughter}}^{-1}} \tag{2.30}$$

where Z is the characteristic impedance of the parent and daughter vessels. Forward wave reflections were minimized by adapting the characteristic impedance of the downstream branches so that the absolute value of the reflection coefficient was < 0.1 at all bifurcations. This was achieved by slightly adjusting the cross sectional area of the daughter branches, while keeping the arterial wall distensibility unchanged.

2.10 NUMERICAL SOLUTION

To solve the system of governing equations along with the imposed boundary conditions and branching continuity models, an implicit finite difference scheme is used. Each vessel in the arterial network is discretized into a number of finite length elements (Δx) and nodes (N), so $i = (1, \dots, N)$ and the length of the vessel $L = (N-1)\Delta x$. As this is a non-stationary problem, the temporal variable has to be discretized as well, with Δt representing the time step. An example of a discretized three-segment arterial system is shown in Figure 2.6. For the human model each arterial segment was divided in 5 nodes as represented in Figure 2.6.

A second order accuracy scheme for the temporal and spatial domains, was implemented in the implicit finite difference scheme used to solve the system of partial differential equations (see Figure 2.7). The finite difference approximations equations were written in the form:

$$\frac{\partial v_i^k}{\partial t} \approx \frac{1}{2}\frac{v_i^{k-2}}{\Delta t} - 2\frac{v_i^{k-1}}{\Delta t} + \frac{3}{2}\frac{v_i^k}{\Delta t} \tag{2.31}$$

$$\frac{\partial v_i^k}{\partial x} \approx -\frac{3}{2}\frac{v_i^k}{\Delta x} + 2\frac{v_{i+1}^k}{\Delta x} - \frac{1}{2}\frac{v_{i+2}^k}{\Delta x} \quad \text{(proximal nodes)} \tag{2.32}$$

$$\frac{\partial v_i^k}{\partial x} \approx \frac{1}{2}\frac{v_{i-2}^k}{\Delta x} - 2\frac{v_{i-1}^k}{\Delta x} + \frac{3}{2}\frac{v_i^k}{\Delta x} \quad \text{(distal nodes)} \tag{2.33}$$

$$\frac{\partial v_i^k}{\partial x} \approx \frac{v_{i+1}^k - v_{i-1}^k}{2\Delta x} \quad \text{(middle nodes)} \tag{2.34}$$

where v_i^k denotes the value of the variable v at the node i and time k. In the model, v represents the primary unknown variables in the system of equations, i.e. P and Q. In equation (2.31), an approximation of backward difference for the first derivative of time is used. To approximate the spatial derivative, a forward difference is used for the proximal nodes (equation (2.32)),

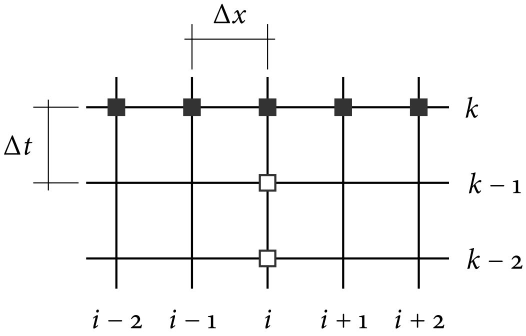

Figure 2.7: Representation of the implicit finite difference scheme for five nodes. The positions in the node i in the previous time level $(k-1)$ and $(k-2)$ are the only positions where the value of the function is known, whereas the five nodes of the time level k are the positions where the function is unknown.

a backward difference for distal nodes (equation (2.33)), and a central difference for the middle nodes (equation (2.34)).

Once the system of equations with the boundary conditions is discretized following the finite difference method described above, a matrix equation is obtained in the form:

$$\mathbf{AX} = \mathbf{B} \tag{2.35}$$

where **A** is the matrix of coefficients, **B** is the independent terms vector, and **X** is the vector of unknown P and Q. The implicit scheme requires simultaneous solution of the whole system of equations for all nodes, which can be achieved more efficiently if the matrix of coefficients has a band structure. For a simple arterial segment the system has dimensions $2N \times 2N$, N being the number of nodes in the segment. An example of the matrix equation for an arterial segment containing N=5 nodes is shown below.

$$\begin{bmatrix} * & * & & * & & * & & & & \\ & * & & & & & & & & \\ & * & * & & & * & & & & \\ * & * & & * & * & * & & & & \\ & & & * & * & & & * & & \\ & & * & * & & * & * & * & & \\ & & & & & * & * & & & * \\ & & & & * & * & & * & * & * \\ & & & & & * & & * & * & * \\ & & & & & & & & * & * \end{bmatrix}_{2N\times 2N} \begin{Bmatrix} P_1 \\ Q_1 \\ P_2 \\ Q_2 \\ \\ \vdots \\ \vdots \\ \\ P_N \\ Q_N \end{Bmatrix}_{2N\times 1} = \begin{Bmatrix} b_{11} \\ b_{12} \\ b_{21} \\ b_{22} \\ \\ \vdots \\ \vdots \\ \\ b_{N1} \\ b_{N2} \end{Bmatrix}_{2N\times 1} \tag{2.36}$$

The symbol ($*$) in the matrix represents the coefficients different from zero. In this system there are two equations that depend on the imposed boundary conditions. Rows 3, 4 ... 2(N-1) correspond to the central nodes, for which the continuity and momentum equations are discretized using the central formula in the spatial derivative.

The system matrix (**A**) for the whole arterial tree consists of submatrixes describing each arterial segment individually. The number of submatrixes equals the total number of arterial segments in the arterial tree. The integration of the submatrixes in only one system of equations is possible due to the continuity conditions imposed at the bifurcations or branching points of the arterial tree. The obtained matrix for the three-segments arterial tree in Figure 2.6 is represented in Figure 2.8. The isolated nodes correspond to the continuity conditions at the bifurcation.

The discretized system of equations is iteratively solved for pressure and flow at each time step over an entire cardiac cycle. The solution algorithm has

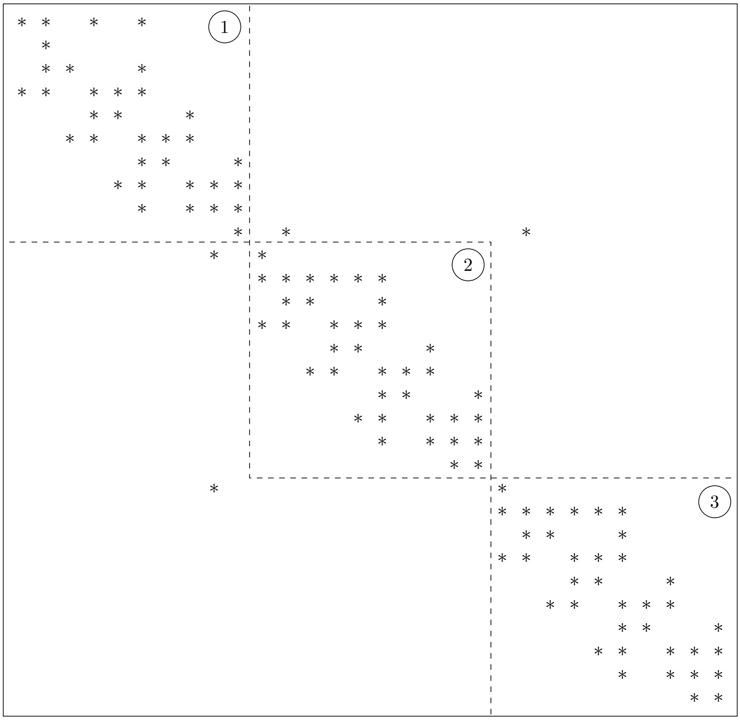

Figure 2.8: Matrix of coefficients for the arterial tree of three arterial segments. $\ast$-non zero entry.

been implemented in MatLab (Mathworks, Natick, MA, USA). Nonlinear terms are iteratively solved at each time step using the Newton-Raphson method. The arterial system is initialized with an arbitrary pressure of 100 mmHg and a flow of 1 ml/s in each artery. To ensure convergence, more than 8 consecutive cardiac cycles are typically simulated.

II

Applications of the one-dimensional model of the systemic arterial tree

CHAPTERS

CHAPTER 3

HEMODYNAMIC IMPACT OF THE C-PULSE CARDIAC SUPPORT DEVICE

The C-Pulse is a novel extra-aortic counterpulsation device to unload the heart in patients with heart failure. Its impact on overall hemodynamics, however, is not fully understood. In this study, the function of the C-Pulse heart assist system is implemented in the 1D model of the arterial tree, and central and peripheral pressure and flow waveforms with the C-Pulse turned on and off were simulated. The results were studied using wave intensity analysis and compared with *in vivo* data measured noninvasively in three patients with heart failure and with invasive data measured in a large animal (pig). In all cases the activation of the C-Pulse was discernible by the presence of a diastolic augmentation in the pressure and flow waveforms. Activation of the device initiates a forward travelling compression wave, whereas a forward travelling expansion wave is associated to the device relaxation, with waves exerting an action in the coronary and the carotid vascular beds. We also found that the stiffness of the arterial tree is an important determinant of action of the device. In settings with reduced arterial compliance, the same level of aortic compression demands higher values of external pressure, leading to stronger hemodynamic effects and enhanced perfusion. We conclude that the 1D model may be used as an efficient tool for predicting the hemodynamic impact of the C-Pulse system in the entire arterial tree, complementing *in vivo* observations. This chapter is based on the paper published in *Artificial Organs* [147].

3.1 INTRODUCTION

With cardiovascular diseases remaining one of the main causes of death globally, new methods and technologies are continuously being developed to better diagnose and treat patients. Aortic counterpulsation is a mode of circulatory support that, in contrast with left ventricular assist devices (LVADs), acts to increase native cardiac function rather than replace it. One of the well-established counterpulsation therapies for temporary left ventricular support in acutely ill patients is the intraaortic balloon pump (IABP) [148]. This device is implanted in the descending aorta and is used to treat myocardial infarction, ventricular refractory arrhythmias, or high risk surgeries. Despite the clinical benefits of this device in patients with an acute need for cardiac support [149, 150], the IABP still has some inherent limitations because of its blood contacting nature, requiring an intravascular catheter which presents risks of infection, thromboembolic complications, and lower limb vascular insufficiency [151]. Also, long-term support with IABP is practically not feasible, as well as mobility of patients, and the paucity of data supporting the use of this device in certain populations with myocardial infarction has been highlighted in the literature [152, 153]. Some studies have also shown that diastolic counterpulsation at the level of the ascending aorta is equivalent or more effective than at the descending aorta [154], due to the proximity to the aortic valve.

Recently a novel implantable device (not contacting the blood) has been introduced aiming for chronic ambulatory use in patients with moderate to severe cardiac failure. The C-Pulse heart assist system (Sunshine Heart, Inc., Eden Prairie, MN, USA) consists of a cuff surrounding the aorta containing an inflatable balloon, and is based on the counterpulsation method with inflation and deflation of the balloon synchronized to the natural heartbeat. This device may be implanted through a minimally invasive surgical procedure, contrary to most LVAD implants, which are highly invasive procedures [34]. The device has been designed to reduce the workload of the heart, to provide the coronary arteries with more oxygenated blood and to improve the cardiac output. In previous small-size clinical studies [155–158], the use of the C-Pulse system has been demonstrated to be feasible and apparently safe, and it was able to improve the functional status and the quality of life of patients. The exact mode of action of the device is, however, still not fully understood and it is unclear whether the improvement in patients is due to a direct unloading effect of the device and/or via secondary mechanisms. It is evident that it is essential to fully understand and test the mechanism of this device before it can be used at a larger scale.

We recently acquired hemodynamic data in an attempt to better understand the impact of the C-Pulse on intra-arterial hemodynamics. In a small-sized study in patients, noninvasive pressure (applanation tonometry) and flow velocity waveforms (ultrasound) were measured at the level of the carotid artery. Pressure waveforms, both peripheral and central, demonstrated an augmentation of diastolic pressure, while an apparent increase in carotid diastolic flow velocities was also observed. The interpretation of these *in vivo* measured waveforms, however, is not straightforward as measurements are highly dependent on measuring protocol and data processing, subject to noise, and measurements are restricted to superficial arteries. Some more invasive data were recorded in the coronary and renal arteries of a pig, instrumented with the C-Pulse.

The aim of this study is to complement these clinical and animal study observations and to investigate the direct hemodynamic impact of the C-Pulse on arterial hemodynamics, through implementation of its function in a validated 1D model of the arterial system connected to a time-varying elastance model of the left heart. The mathematical model of the arterial system used in this work was originally presented by Stergiopulos *et al.* [108], and was later extended and validated by Reymond *et al.* [12] (see also Chapter 2). It has been used for the study of stenosis, aneurysms, and other cardiovascular diseases [17, 108, 133]. As the model does not incorporate any adaptation or (neurological) feedback mechanisms, we anticipate that the model reveals the – theoretical – direct hemodynamic impact of the device. The model was used to simulate pressure and flow waveforms in a normal arterial system and in an arterial system with the C-Pulse included. To assess wave dynamics, data were analysed using the wave intensity analysis (WIA) method [103]. The data were qualitatively compared with *in vivo* measurements to assess whether the numerical observations were supported by the measured data.

3.2 METHODS

3.2.1 C-Pulse heart assist system

The C-Pulse heart assist system is an implantable device, not in direct contact with blood, mounted on the ascending aorta. The system operates in a counterpulsation mode, which means that the balloon inflates and exerts an external pressure on the aorta in ventricular diastole when the heart is filling with blood, and passively deflates before aortic valve opening in systole (see Figure 3.1).

3.2.2 Modelling of the C-Pulse system

We used the 1D mathematical model [12] described in Chapter 2 to simulate the hemodynamic impact of the C-Pulse device. The modelled arterial system

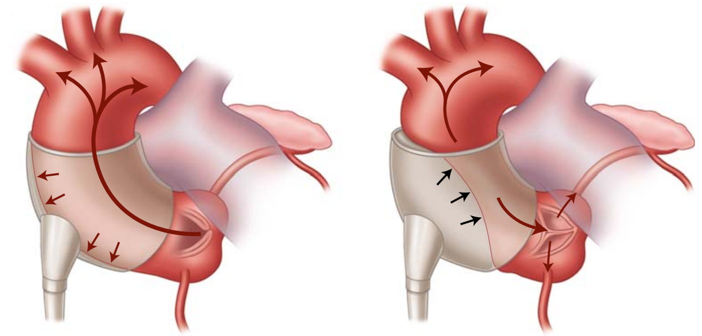

Figure 3.1: Schematic of the location of the C-Pulse cuff around the ascending aorta during deflation in systole (left) and inflation in diastole (right). Image taken from [159].

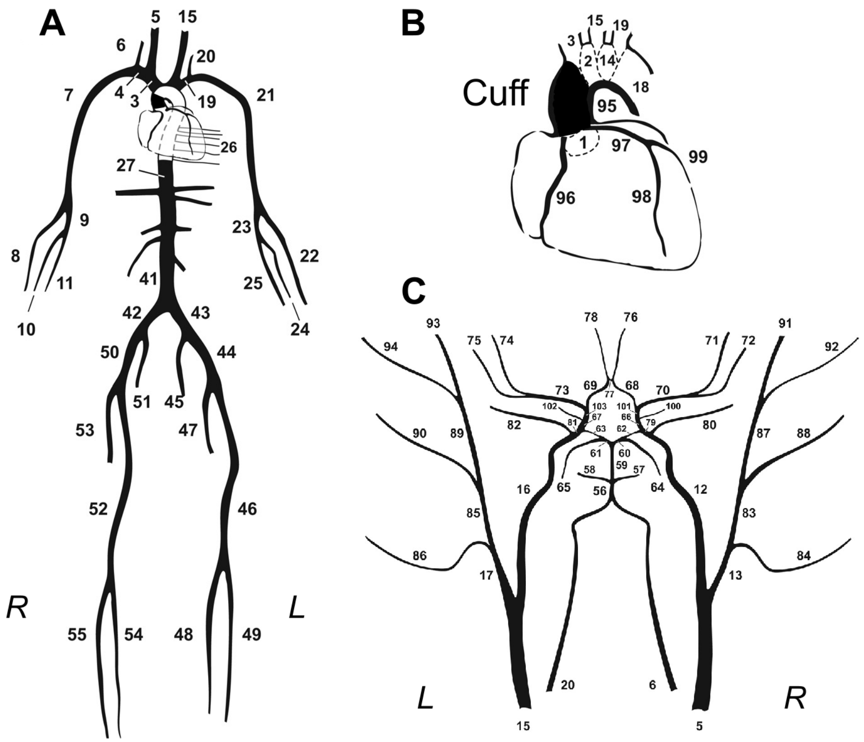

Figure 3.2: (A) Representation of the arterial tree modelled. (B) Detail of the aortic arch and the coronary network. The C-Pulse system is represented by a cuff in the ascending aorta. (C) Detail of the cerebral arterial tree. Adapted from Reymond *et al.* [12].

consists of 103 segments representing the main arteries of the arterial tree (Figure 3.2). At the proximal end of the arterial tree, a time varying elastance model of the heart is the source of aortic pressure and flow waves, while terminal segments are coupled to a 3-element Windkessel model, to account for the cumulative effect of all distal vessels and the microvasculature. Initial properties (arterial dimensions and properties and boundary conditions) are representative for the cardiovascular system of an average young healthy adult, and were taken from Reymond *et al.* [12] (see Table 2.1).

The squeezing action of the C-Pulse system was incorporated into the model as an external pressure source imposed on the ascending aorta segment in diastole (see Figure 3.2B). The inflation–deflation sequence was modelled as a Gaussian function (Figure 3.3) up to a maximal inflation pressure tuned with the arterial compliance, such that an aortic compression of 35% was obtained (reducing the cross-sectional area to 65% of the original value), similar to when the device is used in clinical practice. This value is the model of activation as advised by the company. The inflation and deflation timing was synchronized with the model of the left ventricle. Model simulations were performed with the device switched off and on to isolate the effects of the device; also a C-Pulse activation frequency of 1:2 was simulated to account for the impact in the subsequent cardiac cycle.

Pressure and flow waveforms were calculated (device on/off for three scenarios) at multiple locations throughout the arterial tree (ascending aorta, left coronary, right carotid, right brachial, right radial, left femoral, and renal artery). To assess the impact on perfusion of the C-Pulse throughout the arterial system, time-averaged flow rates were calculated at different locations as well as the peak diastolic flow velocity in the coronary arteries. Wave intensity analysis (see section 1.5.4 [103, 160]) was applied to the pressure and flow data to assess the impact of C-Pulse activation on the wave patterns observed at different locations throughout the arterial tree. To perform wave separation the pulse wave velocity (PWV) calculated by the theoretical equation, $PWV = 1/\sqrt{\rho \cdot D_w}$, was used, as well as a time step of 0.01 seconds.

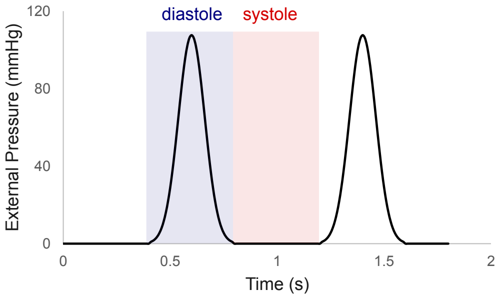

Figure 3.3: Representation of the inflation-deflation sequence modelled as a Gaussian function. Activation of the device occurs during diastole.

3.2.3 C-Pulse performance in a normal cardiovascular system and in heart failure

Three different scenarios were investigated, each characterized by a set of parameters for the arterial and cardiac model. In a first scenario, the default model settings representative for the cardiovascular system of a young healthy adult, were used. However, to mimic the action of the C-Pulse in more clinically realistic scenarios, two other simulations were performed better representing the patient with chronic heart failure (HF). In the C-Pulse trial performed by Abraham *et al.* [158], chronic HF patients were included with a left ventricular ejection fraction (EF) ≤ 35%, known as heart failure with reduced ejection fraction (HFrEF). This condition is characterized by a reduction in the stroke volume (SV) and a compensatory rise in preload (increase in ventricular end-diastolic volume (EDV) and pressure ($P_{\text{end-dia}}$)). With the reduction in the SV there is also an increase in the end-systolic volume (ESV), and a decrease in the maximal ventricular elastance $E_{\max}$ [23]. Therefore, we simulated HFrEF by decreasing the default value of $E_{\max}$ from 2.41 to 0.6 mmHg/mL in the heart model and increasing $P_{\text{end-dia}}$ from 17 to 24.1 mmHg. These values were based on the physiological ranges reported in [12, 146]. In a first heart failure scenario, only the cardiac parameters were modified without altering the arterial system parameters. For this reason, a final scenario was calculated where both, the cardiac parameters as well as the arterial system parameters were changed. Arterial compliance was decreased by a factor 2 over the complete arterial tree, while terminal resistance was increased by a factor 1.5, thus representing an older subject. The cardiac parameters were modulated to keep the EF ≤ 35%, which resulted in different values for both heart failure scenarios. Table 3.1 summarizes the model parameters used in each simulation; as compliance in the model is a nonlinear function of pressure, the values reported in the table correspond to total compliance, obtained from the calculated pressure.

Table 3.1: Cardiac and arterial system parameters in the different simulations.

Simulations	$E_{\max}$ (mmHg/mL)	$P_{\text{end-dia}}$ (mmHg)	Total resistance (mmHg · s/mL)	Total arterial compliance (mL/mmHg)
Healthy	2.41	17	0.64	1.41
HFrEF (younger)	0.6	24.1	0.64	2.19
HFrEF (older)	1.05	21.8	0.96	0.83

3.2.4 Dependence of C-Pulse performance on arterial stiffness

The effectiveness of the C-Pulse device is affected by the arterial stiffness. In practice the inflation pressure is adjusted regarding the arterial stiffness of the patient, keeping constant the aorta deflection. To further investigate this factor, extra simulations were performed changing arterial compliance to represent patients with different degrees of stiffness, while keeping the degree of deflection of the aorta approximately the same in each simulation. Thus, the external pressure required was variable from case to case. To simulate a constant deflection of the aorta with the activation of the C-Pulse in each patient, the cross-sectional area of the aorta was assumed to be 65% of the default value. Arterial compliance was changed multiplying the default value by a constant factor; consequently the values of the external pressure were altered as well.

3.2.5 Patient data

Noninvasive *in vivo* data were recorded in a small group of patients with heart failure and with a C-Pulse device implanted. The study group consisted of N=3 patients under treatment at the Cardio Centrum in Berlin, Erlangen University Hospital and Tübingen University Hospital (mean age 63 ± 6 years, 2 males/1 female). The measuring protocol consisted of (i) brachial cuff blood pressure measurement (brachial diastolic and systolic blood pressure); (ii) applanation tonometry at the right common carotid artery; (iii) ultrasound Doppler velocity measurements in the right common carotid artery. WIA was also performed to assess the timing and nature of wave reflections. It was practically not feasible to measure carotid pressure and flow velocity at the same time, with the presence of the ultrasound probe hampering the use of the pen tonometer, and *vice versa*. Instead, we measured both signals sequentially, verifying that the hemodynamic conditions remained more or less constant (heart rate change less than 5 bpm) and realigned the time-averaged signals in time upon post-processing in a graphical user interface written in Matlab. The protocol was approved by the local ethics committee and all patients provided written informed consent.

3.2.6 Porcine experiment

The protocol was approved by the Animal Care and Use Committee at Texas Heart Institute. The animal (20-30 kg) was fasted 18-24 hours prior to surgery and water provided *ad libitum*. The animal was sedated via an intramuscular injection of Telazol 4-6 mg/kg and Atropine Sulfate 0.02-0.05 mg/kg, intubated and ventilated with room air. Isoflurane (0.5-3.0%) was administered and the animal was placed in dorsal recumbency to allow surgical access to the neck and chest. A triple lumen catheter was placed in the right external jugular vein for fluid and drug administration. A 6Fr Millar catheter (Millar Instruments, Houston, TX, USA) was placed into the left carotid artery and advanced to the proximal aorta or abdominal aorta for systemic pressure measurements. Following placement, a midline sternal incision was made from the manubrium to the xiphoid process and a midline sternotomy performed. The pericardium was widely opened and the ascending aorta and brachiocephalic artery were dissected free. The C-Pulse cuff was passed around the aorta, and individual mattress sutures were placed through the opposing ends of the “open” cuff and using the cuff markings as guides for suture placement. An epicardial LV lead was sutured in place and connected to an electrocardiogram (ECG) output lead and then attached to the C-Pulse system. Transit time ultrasonic flow probes (Transonic Inc, Ithaca, NY, USA) were placed on the left anterior descending artery (approximately at the level of the mitral annulus) and the left renal artery. Measurements were made at steady state with C-Pulse turned off and on. All data were digitized at 1 kHz and stored for offline analysis; the tracings were aligned according to the ECG signal.

3.3 RESULTS

3.3.1 Computer model simulations

3.3.1.1 Scenario 1: Simulated impact of C-Pulse in the healthy person

Figure 3.4 shows the pressure and flow waveforms simulated using the computational model, with the C-Pulse device disabled and activated. The represented locations are the middle nodes of the ascending aorta (proximal to the location of the C-Pulse), the left main coronary artery, and the right common carotid. The simulation was performed for a maximal cuff external pressure of 53.8 mmHg. The simulation clearly demonstrates a diastolic pressure augmentation upon C-Pulse activation which pertains to all peripheral locations up to the femoral artery (data not shown). A comparison of the flow waveforms with the C-Pulse system turned off and on demonstrates an increase in diastolic flow at each location. Interestingly, C-Pulse lowers arterial end-diastolic pressure by about 2.1 mmHg, leading to an overall reduction in blood pressure levels. Table 3.2 demonstrates an overall increase in flow in all investigated vascular territories, except for the coronary artery. The EF was 64% in the C-Pulse off simulation, and increased with the device activation to 65%. The mean value of the peak diastolic coronary flow velocity was 0.24 m/s with the device off, increasing to 0.26 m/s with the activation of the C-Pulse.

3.3.1.2 Scenario 2: Simulated impact of C-Pulse in the younger HFrEF patient

Figure 3.4 also depicts the pressure and flow waveforms simulated representing a younger HFrEF patient. The EF was 33% and increased to 34% with the device switched on, for an external pressure of 53.8 mmHg. Comparing the waveforms in this scenario (younger HFrEF) with the waveforms for the healthy person, a decrease in pressure and flow can be detected, as a result of

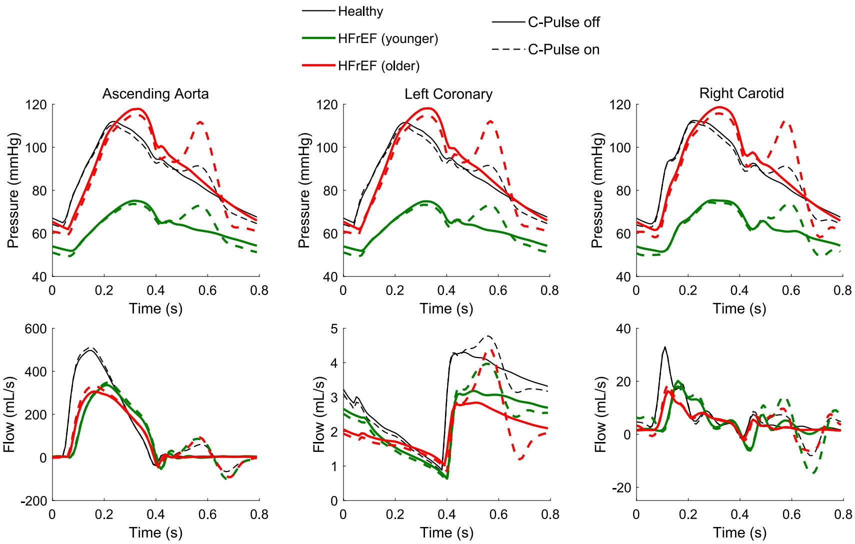

Figure 3.4: Comparison of simulated pressure and flow waveforms of a healthy subject, a younger subject with HFrEF, and an older subject with HFrEF, in the ascending aorta, the left main coronary artery, and the right carotid artery, with the device off and on. Inflation pressure: healthy and HFrEF younger (53.8 mmHg) and HFrEF older (107.6 mmHg).

Table 3.2: Mean flow (mL/s) in different arteries for the three scenarios, and percent of mean flow increase with the C-Pulse activation.

	Healthy			HFrEF (younger)			HFrEF (older)		
Arteries	C-Pulse off	C-Pulse on	Increase %	C-Pulse off	C-Pulse on	Increase %	C-Pulse off	C-Pulse on	Increase %
Ascending aorta	126.85	128.77	1.51	90.07	93.95	4.3	86.73	90.9	4.81
Left coronary	2.92	2.89	-1.07	2.26	2.26	-0.18	2.06	2.05	-0.43
Right carotid	6.14	6.23	1.42	4.41	4.68	6.08	4.3	4.5	4.6
Right brachial	6.1	6.27	2.82	4.31	4.55	5.54	4.19	4.39	4.77
Right radial	2.87	2.89	0.53	2.05	2.09	1.97	1.99	2.01	1.1
Left femoral	4.79	4.96	3.52	3.42	3.58	4.61	3.54	3.78	6.79

the heart failure (with pressure values within the hypotension range). Again, the waveforms obtained with the C-Pulse on show the more pronounced diastolic peak. A drop in end-diastolic pressure (about 2.5 mmHg) and overall blood pressure is again noticed. The increase in the mean flow caused by the device (Table 3.2) was in this case greater than in scenario 1. The mean value of the peak diastolic flow velocity in the coronary artery with the C-Pulse off was 0.18 m/s, increasing with the device on to 0.22 m/s.

3.3.1.3 Scenario 3: Simulated impact of C-Pulse in the older HFrEF patient

Finally, Figure 3.4 shows the pressure and flow waveforms of the simulated HF case when the heart model parameters were altered, as well as the arterial system parameters (terminal resistance and compliance), representing an older subject, with a corresponding external pressure of 107.6 mmHg. In this case the values of the arterial pressure are within normal range. Again, the diastolic augmentation in the pressure and flow signals caused by the device activation can be observed. Compared to scenario 2, the gain in flow is higher for the aorta and femoral segments, as well as the reduction of the end diastolic pressure and the overall pressure lowering effect. The EF with the device off was 35% and increased with the device on to 37%. Table 3.2 summarizes the calculated mean flow of different arteries and the increase in the mean flow caused by the activation of the device. The increase in the mean flow caused by the device was in general lower in this scenario than the increase obtained in scenario 2. For the coronary artery, there was a slight decrease in the mean flow caused by the C-Pulse in all simulations; nevertheless, the diastolic augmentation in the flow signals caused by the device activation is evident. The mean values of the peak diastolic coronary flow velocity were 0.16 m/s and 0.24 m/s with the device off and on respectively.

Figure 3.5 shows the aortic pressure and coronary flow signals in the simulation of 1:2 counterpulsation mode for the older HFrEF case. Systolic pressure was lower in the unassisted beat compared to the assisted beat. Peak coronary diastolic flow increased from 2.87 mL/s in the unassisted beat to 4.42 mL/s in the assisted beat. The activation caused a very small reduction (0.56%) in end-diastolic pressure, prior to the onset of systole in the subsequent cycle. Integrating the coronary flow profiles in the assisted and unassisted beats showed that the C-Pulse action increased diastolic coronary flow from 0.95 mL in the unassisted beat to 1.03 mL in the assisted beat. Diastolic coronary flow was about 62.4% from total coronary flow in the assisted beat compared to 60.8% in the unassisted beat.

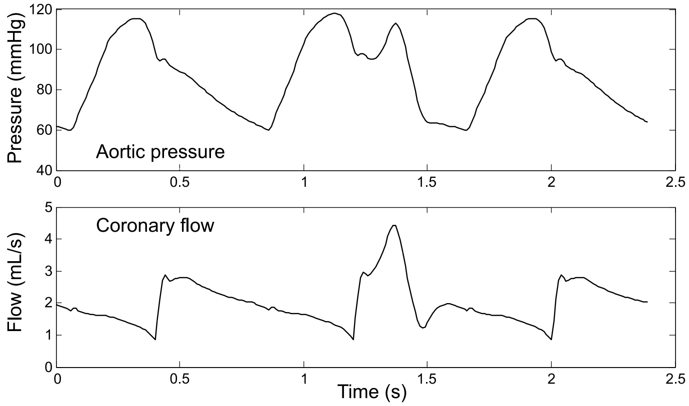

Figure 3.5: Aortic pressure and coronary flow in the simulation of the 1:2 counterpulsation mode, for a case of HFrEF in an older subject.

3.3.2 Effect of changing external pressure

Starting from the "baseline" parameters for scenario 2 (young patient with HFrEF) and 3 (older patient with HFrEF), we varied total arterial compliance by increasing and decreasing the values in a 20% range while the deflection in the aorta was kept constant by modulating the external pressure. It is observed from Figure 3.6 that the stiffer the vessels, the higher the external pressure that is needed to achieve the same level of aortic compression. This leads to higher increase in the mean flow and peak diastolic coronary flow velocity. Also the left ventricular ejection fraction increases moderately for stiffer vessels from 1 to 2%.

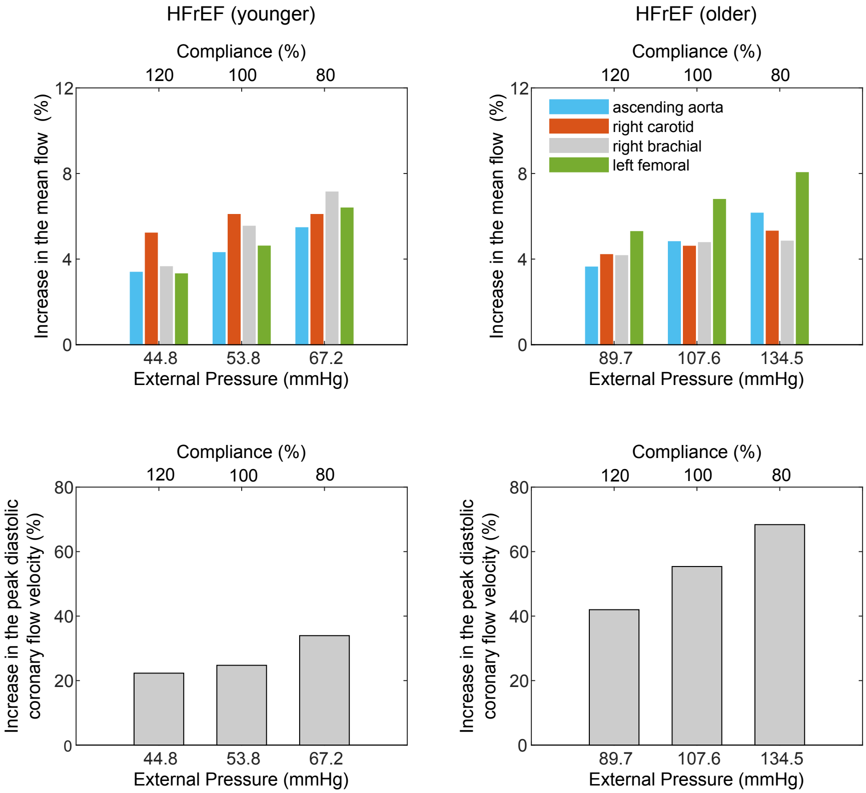

Figure 3.6: Improvement in the C-Pulse performance with increasing external pressure and decreasing arterial elasticity (compliance) for both simulations of heart failure with reduced ejection fraction (HFrEF). Top: Increase in the mean flow for different arteries caused by the device activation with increasing external pressure and decreasing compliance. Bottom: Increase in the peak diastolic coronary flow velocity caused by the device activation with increasing external pressure and decreasing compliance.

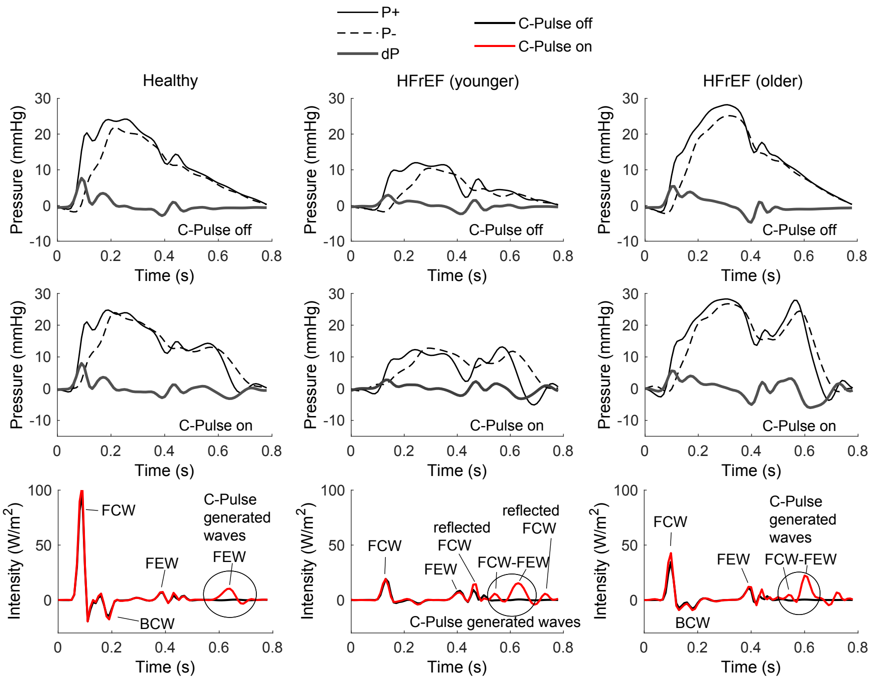

Figure 3.7: Wave intensity analysis at the location of the right common carotid artery for the healthy and both heart failure with reduced ejection fraction (HFrEF) simulations. Top: change in pressure (dP), forward and backward pressure components ($P+$ and $P-$) with the C-Pulse off. Middle: dP, $P+$ and $P-$ with the C-Pulse on. Bottom: WIA with the C-Pulse turned on and off. FCW and BCW: forward and backward compression waves; FEW: forward expansion wave.

3.3.3 Results of the wave intensity analysis

Figures 3.7 and 3.8 show the wave intensity data for the carotid and coronary arteries, respectively, for the three scenarios and with the device switched off and on. Wave intensity patterns are more complex than in the aorta due to the proximity of distal reflection sites and open-end re-reflection of backward waves at the junction of the vessel with the aorta. When the C-Pulse is disabled, the most prominent peaks in the signals are: (i) the forward compression wave (FCW) caused by the ejection of the heart; (ii) a backward compression wave (BCW) resulting from the peripheral wave reflection (coming from the head or distal coronary bed); (iii) a forward expansion wave (FEW) generated by the slowing of ventricular contraction; and (iv) the backward expansion wave (BEW) in the coronary artery. Note that the observed BCWs originate from impedance mismatches along the arterial tree and reflections on distal boundaries, and might not always be found *in vivo* (to that extent). In the carotid signal there is also a secondary

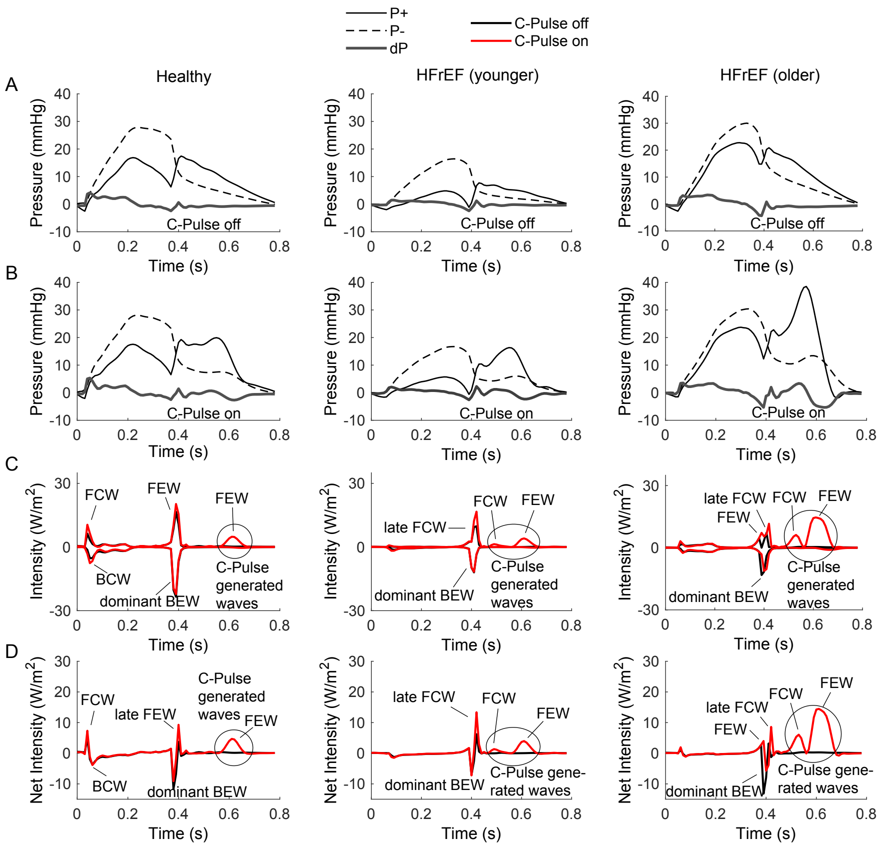

Figure 3.8: Wave intensity analysis at the location of the left main coronary artery for the healthy and both heart failure with reduced ejection fraction (HFrEF) simulations. Panel A: change in pressure (dP), forward and backward pressure components ($P+$ and $P-$) with the C-Pulse off. Panel B: dP, $P+$ and $P-$ with the C-Pulse on. Panel C and D: separated wave intensity and net wave intensity, respectively, with the C-Pulse turned on and off. FCW and BCW: forward and backward compression waves; FEW and BEW: forward and backward expansion waves.

FCW that we attribute to re-reflection of the FEW at the open-end aortic junction. When the C-Pulse system is switched on the presence of two new waves in diastole can be noticed (Figures 3.7 and 3.8); a FCW caused by the squeezing action of the cuff and a FEW attributed to the device relaxation. For the carotid artery (Figure 3.7), it seems that the diastolic FCW is more apparent with depressed cardiac function (scenario 1 vs. scenario 2 and 3). Similar observations can be made for the diastolic FEW in the carotid artery, with the strongest FEW observed in scenario 3. In presence of a strong FEW (scenario 2 and 3), a third small forward (compression) wave is visible, which we again ascribe to re-reflection. The impact of device activation on the heart-related early and late systolic forward compression and expansion waves, respectively, is fairly limited.

Figure 3.8 shows the separated wave intensity curves (panel C) for the coronary artery and also the net wave intensity (panel D). The analysis in the coronary artery, besides of the typical peaks, indicates a dominant BEW (stronger than the FEW), which is initiated by the decrease in the resistance of the microcirculation and the pressure at the distal artery, produced in turn by the ventricular relaxation. In the coronary simulations, the FEW generated by the slowing of LV contraction is not apparently visible since its effect is overruled by the BEW. With the incorporation of the C-Pulse system, there is a new FCW attributed to the device inflation. From the timing in the figures, one can observe that this wave is causing the augmentation peak in the pressure signal as well as the peak in flow. The slowing of the cuff inflation creates a suction effect at the proximal end of the artery giving rise to the second FEW. As we may note, the FEW originated by the relaxation of the C-Pulse is in all cases stronger than the FCW caused by the compression of the device.

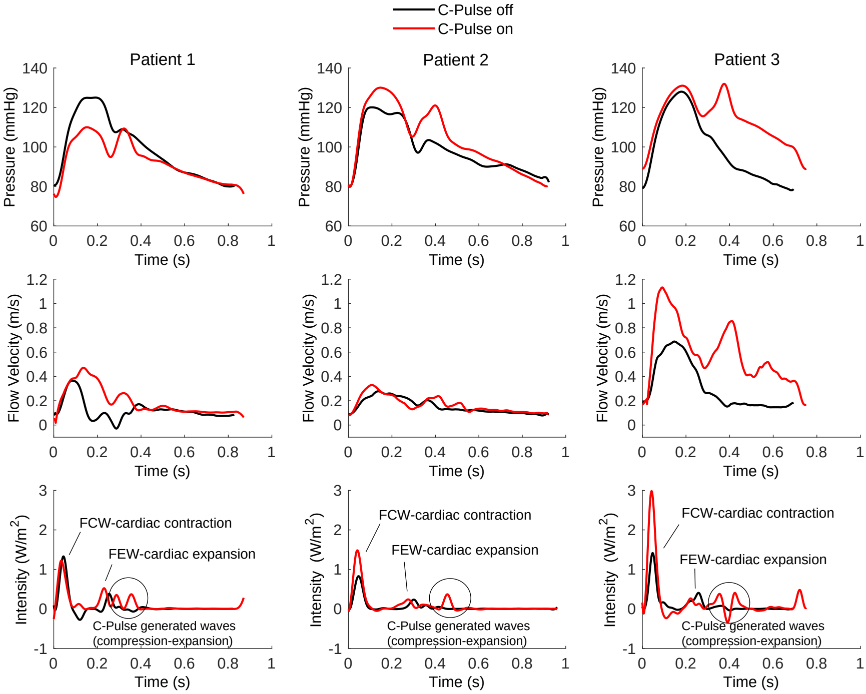

Figure 3.9: *In vivo* measurements performed on the right common carotid artery of three patients, with the C-Pulse off and on. Top: pressure waveforms. Middle: flow waveforms. Bottom: wave intensity. FCW and FEW: forward compression and expansion waves.

3.3.4 *In vivo* results

Figure 3.9 (top and middle) depicts the impact of the C-Pulse in the right carotid pressure and flow for each patient. In all patients, the flow and pressure waveforms are clearly modified in diastole, with the appearance of a (more) pronounced secondary peak in early diastole. The wave intensity patterns (bottom) indicate that activation of the C-Pulse induces wave activity in diastole: a FCW that increases pressure (and flow), and a FEW likely caused by the relaxation of the device.

Figure 3.10 shows the impact of the C-Pulse in the aortic pressure and the coronary and renal flow of a pig. Also here, the flow and pressure waveforms are altered in diastole with the activation of the C-Pulse. The coronary flow waveforms in systole differ a little from the simulations; nevertheless, diastole presents the higher peak with the device switched on, which is qualitatively comparable to the model. A slight decrease in systolic and end-diastolic pressure of the aorta can be detected in the porcine data as well as in simulations. The *in vivo* renal data and the simulated renal data for the case of a young patient with HFrEF (last column in Figure 3.10), present the diastolic peak caused by the device, with an increase in the peak diastolic flow of 52% in the pig data compared to an increase of 21% in the simulation. In this artery the effect of C-Pulse is clearly visible even when it is fairly distal from the location of the cuff in the aorta.

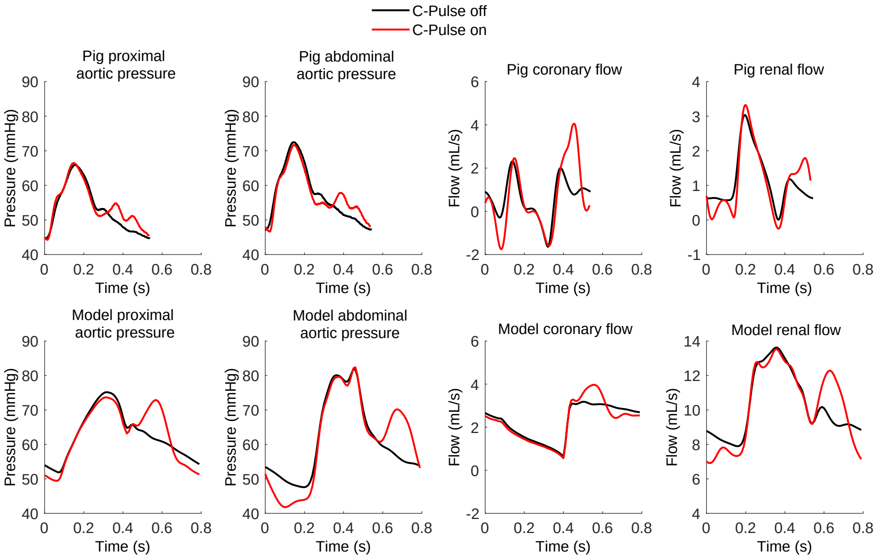

Figure 3.10: *In vivo* measurements performed on the aorta, coronary and renal arteries of a pig, with the C-Pulse off and on, compared with model simulations for the younger HFrEF scenario.

3.4 Discussion

In this chapter, we have presented the results of a 1D arterial model simulation of an extra-aortic counterpulsation device as a tool to complement *in vivo* animal and clinical observations. Besides the anticipated diastolic pressure augmentation, some other observations can be made. In all simulations, we found a slight decrease in systolic and end-diastolic pressure, as well as an increase in flow, that is obtained when the C-Pulse is activated. The logical explanation for this phenomenon is that when the aorta is squeezed upon cuff inflation, the pressure increases (second peak in pressure waveform), and the blood volume displaced also increases (second peak in flow waveform). The significant volume displacement and the action of the cuff deflation cause a decrease in aortic end-diastolic pressure and, as a consequence, the aortic systolic pressure also decreases. For this reason, the $P_{\text{end-dia}}$ with the cuff activated is lower than the $P_{\text{end-dia}}$ without the cuff. The ejection phase in the left ventricle begins when the aortic valve opens, thus happens at a lower end-diastolic pressure, with the device unloading the heart. This also results in an (albeit modest) increase in stroke volume and ejection fraction.

3.4.1 Impact of the C-Pulse device on coronary hemodynamics

Besides unloading of the heart, counterpulsation devices also intend to augment organ perfusion, particularly the heart. We therefore analyzed coronary hemodynamics. It is easily observed from simulations (Figures 3.4-3.6) and *in vivo* data (Figure 3.10) that C-Pulse activation leads to an increase in coronary blood flow in diastole. This observation has been also pointed out by Davies *et al.* [154], where a more efficient improvement in diastolic coronary blood flow by C-Pulse compared with IABP was reported. Note that, in the Davies' study, the prototype used is different from the final C-Pulse device. Intriguingly, averaged over the complete cardiac cycle, left coronary blood flow in the model simulations remained virtually unchanged (Table 3.2), and this is in contrast to other vascular territories. Such result is a consequence of the early deflation process, assumed in this study by means of a Gaussian function, which produces a reversal of flow in late diastole. This is consistent with observations made by Davies *et al.* [154]. One important aspect in counterpulsation therapy is synchronization of cuff inflation-deflation sequence with the cardiac cycle. Comparing the timing of inflation in patients with the timing of inflation in the simulations and porcine data, one can observe a slight difference with respect to the dicrotic notch. Extra simulations in the older HFrEF case, with the C-Pulse activation in late systole (25 ms shifted) revealed lower EF (-2.8%) and aortic mean flow (-26.9%) compared with inflation in the dicrotic notch, while the peak diastolic coronary flow experienced an increase (2%). The reduction in left ventricular afterload is rather limited in this study, as we can observe from the simulated data in 1:2 counterpulsation frequency (Figure 3.5). We should stress that the results depend on the selected inflation pulse; hence further studies are required to deepen in this issue.

3.4.2 Importance of arterial stiffness

Interestingly, the increase in the coronary peak diastolic flow velocity due to the C-Pulse activation was higher in the older HFrEF simulation (55%) than the younger HFrEF simulation (25%), and the gain in perfusion of the aorta was higher in the older subject. In addition, the increase in the LVEF in the younger HFrEF simulation was only of 1% compared to an increase of 2% in the older HFrEF simulation. The main difference between both scenarios is the fact that arterial system properties were modified to mimic vascular ageing, with a loss in arterial compliance and an increase in peripheral resistance. Since in practice higher activation pressures are required for systems with reduced arterial compliance to keep constant the aorta deflection, we speculate that the arterial compliance combined with the inflation pressure is the major factor explaining these results. For this reason, we performed the extra simulations reported in Figure 3.6, where arterial compliance and external pressure were changed while keeping constant the aorta deflection - as in practice. In these simulations higher values of mean flow, peak diastolic coronary flow velocity, and ejection fraction with the C-Pulse switched on were found for stiffer arteries. It is, however, important to highlight that this finding relates to the choice of maintaining a constant degree of aortic compression. Opposite results are found when changing compliance while maintaining the same external pressure, as a more compliant aorta will then undergo a higher degree of compression.

Nevertheless, all patients receiving C-Pulse and the vast majority of all HF patients have stiff arterial systems and advanced arterial disease including aortic calcifications. Therefore, based on our simulations, we could conclude that the *theoretical* benefits with the use of the C-Pulse system (or probably any device based on counterpulsation principle) are more evident in HF patients with stiffer arteries. We stress that the above should be interpreted as the potential theoretical direct hemodynamic benefit of a device in patients with a stiffer aorta. This does not imply a better clinical outcome in patients, where better outcomes with ventricular assist devices in younger patients have been reported [161].

3.4.3 Comparison of simulated and *in vivo* data

Our main motivation for the computer model study was to complement and provide a basis to better understand noninvasively recorded *in vivo* data (ultrasound and applanation tonometry). These measurements can be technically challenging and are restricted to superficial arteries (carotid, radial, femoral). Because of the relatively crude calibration of tonometry data based on brachial cuff measurements, small changes in blood pressure are not easily detected. Furthermore, measuring noise complicates the use of wave intensity analysis for the apprehension of arterial wave dynamics. Overall, we found a satisfactory qualitative agreement between carotid pressure and flow waveforms measured in patients (Figure 3.9) and generated by the computer model (Figures 3.4 and 3.7). In contrast, also a good qualitative agreement between coronary and renal flow waveforms and aortic pressure waveforms simulated and measured in the pig (Figure 3.10) was found (where it should be kept in mind that the model represents human anatomy and physiology and not porcine). The model is clearly capable of reproducing the main features of the C-Pulse activation, presenting a diastolic augmentation in pressure and flow waveforms comparable in shape to the *in vivo* measurements. Nevertheless, an increase in the peak diastolic coronary flow due to the C-Pulse activation was much higher in the *in vivo* porcine data (102%) than in the simulations (25% and 55% for the younger and older HFrEF cases, respectively). The same occurred for the renal blood flow as was previously analyzed, and also the increase in the carotid mean flow velocity for patients was higher compared with simulations, with maximum values of 89% in patients against 6% in the simulations. All this suggests that there are other mechanisms present *in vivo* and not considered in the model, playing a main role in the benefits caused by the C-Pulse. The peak diastolic arterial pressure caused by the device activation was comparable to the peak systolic arterial pressure in the simulation of a young patient with HFrEF, and in patient 3 (Figure 3.9) was even greater, which is consistent with data reported by Hayward *et al.* [156]. Model simulations predicted a modest decrease in systolic and end-diastolic pressure, which was also observed in the invasive porcine data. In patients, a decrease was noted only in patient 1 but we doubt whether such small changes can be detected noninvasively with calibration based on cuff sphygmomanometric data. Nevertheless, a similar phenomenon has been reported in previous studies for the C-Pulse and the IABP, which is also based on the counterpulsation technology [154, 159]. On the contrary, an increase in systolic pressure was experienced by the other two patients, which could be the result of different clinical conditions in patients. This aspect cannot be determined without further studies.

Observing the intensity waveforms for the HF patient simulations (Figures 3.7 and 3.8), we can note that the first FCW and also the reflected wave are less strong than the waves in the healthy subject simulation. This is associated with a weak ejection of blood from the ventricle caused by the systolic dysfunction. In the coronary circulation, the myocardial contraction generates an early-systolic BCW shortly before the FCW resultant from ventricular ejection, and then a late-systolic BCW shows up as a consequence of the FCW reflection. In our simulations (Figure 3.8), the early-systolic BCW is not present, given that the coronary model used does not include the effect of myocardial contraction on vessels. Davies *et al.* [162] reported that in the coronary arteries, the greatest waves occur during ventricular relaxation (consistent with the dominant BEW, Figure 3.8), thus causing a greater coronary flow in diastole. They also reported a late FCW generated by the closure of the aortic valve. This wave, which appears in our simulations, is responsible for a brief interruption of the dominant BEW. The wave intensity analysis reveals two new strong waves in diastole when the C-Pulse system is incorporated, in both simulations and *in vivo* data: a FCW caused by the action of the cuff, and a stronger FEW attributed to the relaxation of the cuff. The compression wave counteracts the "natural" decrease in pressure in diastole, but the relaxation of the cuff is in synergy with the otherwise decaying pressure, thus generating a steeper pressure gradient and hence a stronger signal in the WIA. For the IABP, the diastolic augmentation in the ascending aorta has been associated to a BCW rather than to a FCW [163]. This obviously has to do with the position of the IABP in the descending aorta.

3.4.4 Limitations

It is clear that a computer model study has some inherent limitations and does not account for adaptive mechanisms due to autoregulation or sympathetic/parasympathetic modulation. The latter mechanism may be important since the relatively moderate hemodynamic effects predicted from the model and observed in patients, has resulted in improved clinical outcomes in terms of improvement in ejection fraction [164]. The results obtained therefore represent a theoretical acute hemodynamic effect of the C-Pulse. We should also point out that the model used to simulate the effect of the cuff is simple, and its limitations need to be investigated in detail. The coronary model used lacks the effects of myocardial contraction on vessels. The impact of variation in the cuff deflation timing position has not been accounted for in this study; further studies are required. The limited *in vivo* data (3 patients and one pig) only allow a qualitative comparison with the outcomes of the computer model, based on a generic dataset. A more quantitative comparison between *in vivo* data and simulations would require a tuned and personalized model, which implies an extensive amount of anatomical and physiological data, which is practically not feasible.

3.5 CONCLUSIONS

The function of the C-Pulse system was implemented in a numerical model of the arterial tree. This device was designed to improve the function of the heart in three different ways: decreasing cardiac afterload, increasing coronary blood flow, and increasing cardiac function with more blood being pumped from the heart to the rest of the body. Computer model simulations demonstrate that activation of the C-Pulse system generates a diastolic forward compression-expansion wave sequence, augmenting diastolic pressure and flow, while at the same time, diminishing end-diastolic pressure by a few mmHg. The numerical results are in qualitative accordance with *in vivo* data (patients and pig). Our data indicate that the potential beneficial effect of the device is dependent on the arterial stiffness, with more important effects in less compliant aortas, which is closely related with the inflation pressure of the cuff.

CHAPTER 4

NUMERICAL ASSESSMENT AND COMPARISON OF LOOP-BASED LOCAL PULSE WAVE VELOCITY METHODS OVER THE HUMAN ARTERIAL TREE

Local pulse wave velocity (PWV) can be estimated from the water hammer equation and is an essential component of wave separation analysis. However, previous studies have demonstrated inaccuracies in the estimations of local PWV due to the presence of reflections. In this study we compared the estimates of local PWV from the PU-loop, ln(D)U-loop, QA-loop and ln(D)P-loop methods along the complete human arterial tree, and analysed the impact of the estimations on subsequent wave separation analysis. Estimated values were derived from the numerical outputs (pressure, flow, flow velocity, area and diameter waveforms) of the 1D model of the human circulation, and compared against a reference PWV obtained from the Bramwell–Hill equation in a reference configuration, and in a configuration with lower distensibility representing ageing. When including all nodes, the overall performance of the methods was poor (correlations and mean differences of $R^2 < 0.4$ and 3.0±4.1 m/s for the PU-loop, $R^2 < 0.07$ and −0.7±2.3 m/s for the ln(D)U-loop, and $R^2 < 0.06$ and −0.4±2.3 m/s for the QA-loop). Focusing on specific sites, the ln(D)U- and QA-loop methods yielded acceptable results in the thoracic aorta and iliac arteries, while the PU-loop method was acceptable at the aortic arch. The reflection-insensitive ln(D)P-loop method performed

well over the complete network (R^2 = 0.9 and 0.3±0.3 m/s), as did a previously proposed reflection-correction method for most vascular sites. Large errors in PWV estimation are attenuated in subsequent wave separation analysis, but the errors are site-dependent. We conclude that the performances of the PU-loop, ln(D)U-loop and QA-loop methods are highly site-specific. The results should be interpreted with caution at all times. This chapter is based on the paper published in *Physiological Measurement* [165].

4.1 INTRODUCTION

The local mechanical properties of a blood vessel, expressed in terms of local distensibility or PWV, are intrinsic to the assessment of arterial wave dynamics. Local PWV is a co-determinant of the characteristic impedance of blood vessels, and hence of the relation between forward pressure and flow (velocity) waves. It is also an essential component of wave separation analysis (WSA), splitting total pressure (or flow) into their forward and backward travelling components. Furthermore, since PWV is recognized as a clinically useful measure of arterial stiffness in the arterial tree with prognostic power [45], several noninvasive methods have been developed to assess PWV: either transit time methods (such as the carotid-femoral PWV, brachial-ankle PWV, cardio-ankle PWV or finger-toe PWV [74, 76, 77, 166]), or in a single position (local methods such as PU-loop, ln(D)U-loop or QA-loop [87, 89, 90]). Transit time methods give a global or regional measure of the stiffness of the arterial system, with PWV calculated as the ratio of the distance between two measuring locations and the time it takes for the waves to travel from one location to the other (section 1.3.2). Single-location methods provide an estimate of PWV at the measurement site, based on a linear relation between measured quantities (the water hammer equation), assuming an absence of reflected waves in early systole (section 1.3.3).

Despite the increasing use of these methods (mainly because of their non-invasive applicability to MRI or ultrasound data), local estimates of PWV have been shown to present incorrect values in cases of strong local reflections [167–169], which may lead to wrong estimates of wave speed, with errors propagating into the assessment of forward and backward waves. In general, it has been shown that the PU-loop overestimates PWV in strong local positive reflections, while the ln(D)U-loop or QA-loop methods underestimate in the same conditions; the opposite happens in the case of strong local negative reflection. In a theoretical paper from our group [168], it was demonstrated that the degree of over- and underestimation is directly linked to the magnitude of the local reflection coefficient. In that same work, a frequency-domain method that allows to correct for the effect of reflection was introduced. Recently, Kowalski *et al.* [91] also highlighted that the use of measured peak velocity (as is typically achieved from pulsed Doppler ultrasound measurements) rather than the (spatial) mean flow velocity introduces additional error into velocity-based methods (i.e. the ln(D)U- and PU-loop methods). Also, inaccuracies in the noninvasive estimation of the local pressure wave arising from calibration of distension waveforms based on oscillometric pressure data propagate into estimates of local PWV [91]. They introduced the ln(D)P-loop method which no longer relies on velocity. The ln(D)P method is mathematically equivalent to the Bramwell-Hill equation, which does not require unidirectional wave travel, and the method is therefore expected to be insensitive to wave reflections.

The vast majority of studies on local PWV have been performed mainly on experimental setups [88, 169], or for the carotid and femoral arteries using computational analysis and *in vivo* data [167, 168, 170]. To the best of our knowledge, the first study addressing the performance of local PWV estimation methods at several locations along the arterial tree was performed by Alastruey [171], who demonstrated that the errors of local PWV estimation methods decreased at locations where visco-elastic effects were small and near to junctions that were well-matched for forward-travelling waves. The recent work of Kowalski *et al.* [91] also considered testing loop methods in the aorta in an *in vivo* study, and at four different locations in the arterial tree of a virtual patient cohort. The impact of an error in PWV on subsequent wave separation analysis, however, was not addressed in these studies.

The primary aim of this study is to compare the estimates of PWV from the PU-loop, ln(D)U-loop, ln(D)P-loop and QA-loop methods throughout the human arterial tree, and quantify the impact of possible over- or underestimation on subsequent WSA. For this purpose, the output data of a previously validated 1D model of the human systemic circulation [12] was used, to simulate the physiological signals needed for the estimations of local PWV methods and for configurations representing a young and an aged individual. The second aim of the study was to verify the performance of a previously proposed (frequency-domain) method [168] to correct for the effects of wave reflection.

4.2 METHODS

4.2.1 Numerical simulations

We used the 1D model of the human systemic arterial circulation, including the aorta and its main branches [12], to simulate hemodynamic (physiological) signals of pressure (P), flow (Q), flow velocity (U), cross-sectional area (A) and diameter (D). Data were generated using the 103-segments (each having five nodes) configuration of the model [12] with: i) the standard parameters representative of a young healthy adult and, ii) decreasing the distensibility by a factor of 5 (PWV increases by a factor of 2.24) throughout the entire arterial tree to mimic the effect of ageing. Diameters were calculated assuming a circular cross-sectional area, and flow velocity was derived as $U = Q/A$; A being the cross-sectional area as a function of time (obtained by integration of equation (2.11)). Single-location PWV methods (see section 1.3.3.1) were applied for each of the 515 nodes of the arterial tree. Reference values of PWV for each node were calculated using the Bramwell-Hill equation [47] $\mathrm{PWV_{BH}} = \sqrt{(A/\rho)(\mathrm{d}P/\mathrm{d}A)}$, with ρ being the blood density (1050 kg/m^3). Local $\mathrm{PWV_{BH}}$ was taken as the average of values at the working pressure of the loop-based methods.

Reference characteristic impedance, $Z_{\text{c-BH}}$, was calculated as $Z_{\text{c-BH}} = \rho \cdot \mathrm{PWV_{BH}}/\overline{A}$, with $\overline{A}$ being the local cross-sectional area at a reference transmural pressure of 100 mmHg. The reflection coefficient, $\Gamma_{\mathrm{BH}-k}$, was derived for each node from the frequency-domain method as $\Gamma_{\mathrm{BH}-k} = \frac{Z_{\mathrm{in}} - Z_{\text{c-BH}}}{Z_{\mathrm{in}} + Z_{\text{c-BH}}}$, with Z_{in} being the ratio of the harmonics pressure and flow. We only report the values of the real part of the reflection coefficient at the heart frequency.

4.2.2 Loop-based local PWV methods

The loop-based local PWV methods compared in this study were previously described in section 1.3.3.1. The methods based on pressure such as PU-loop [87] and ln(D)P-loop [91] methods, are derived directly from the water hammer equation 1.7 and the Bramwell-Hill equation 1.4, respectively; whereas the QA-loop [90] and the ln(D)U-loop [89] methods are obtained by combining the Bramwell-Hill and the water hammer equations. For each node of the arterial tree and for each method, the linear part of each loop was determined by linear regression analysis on a selected data portion (by eye) during early systole.

4.2.3 Correcting for wave reflection using a frequency-domain analysis

Besides applying conventional analysis on the PU-loop, ln(D)U-loop, ln(D)P-loop and QA-loop, we performed the frequency-domain analysis as proposed by Segers *et al.* [168] for the correction of the PU-loop and QA-loop methods. The method makes use of the following equation for the PU-loop:

$$\frac{P_k}{U_k} = \frac{P_{k+} + P_{k-}}{U_{k+} + U_{k-}} = \frac{(1 + \Gamma_k)}{(1 - \Gamma_k)}\rho c = \beta_k \rho c \tag{4.1}$$

and for the QA-loop:

$$\frac{Q_k}{A_k} = \frac{\overline{A} U_k}{A_k} = \frac{\overline{A}(U_{k+} + U_{k-})}{A_{k+} + A_{k-}} = \rho c^2 \frac{U_{k+}(1 - \Gamma_k)}{P_{k+}(1 + \Gamma_k)} = \frac{c}{\beta_k} \tag{4.2}$$

where β is a coefficient that depends on the reflection coefficient $\beta_k = (1 + \Gamma_k)/(1 - \Gamma_k)$, k refers to the harmonics number, $P_{k+}/U_{k+} = \rho c$ and the subscripts (+) and (-) denote the forward and backward directions, respectively. The ratio between equations (4.1) and (4.2) can be used to estimate the correction coefficient (β):

$$\frac{P_k/U_k}{Q_k/A_k} = \rho\frac{(1+\Gamma_k)^2}{(1-\Gamma_k)^2} = \rho \cdot \beta^2 \tag{4.3}$$

which can be further used to correct either the PU-loop or QA-loop through equations (4.1) or (4.2). PWV_{1-5} is then derived by averaging the first five harmonics after applying the correction. As harmonics are superimposed on the mean pressure, reference values of the wave speed for this method are derived using the Bramwell-Hill equation, with values corresponding to the local mean pressure ($\mathrm{PWV}_{\mathrm{BHmp}}$, to distinguish from the reference of the loop methods).

4.2.4 Data analysis

We first analysed conventional loops at the middle nodes of four locations in the arterial tree commonly sampled in arterial research (ascending aorta (AAO), right common carotid artery (CA), brachial artery (BR) and femoral artery (FE)). Estimates of PWV for the AAO and CA were also reported as the mean ± standard deviation, averaging over the five nodes in the arterial segments. We then analysed how the methods perform over the complete arterial tree (five nodes per 103 arterial segments) by comparing reference and estimated data using Bland-Altman analysis and the coefficient of determination (R^2). Cerebral arteries of the circle of Willis and coronary arteries were not included, as it was impossible to identify a linear segment in the loops, which resulted in data for a total of 446 nodes. Differences between the young and aged configurations were assessed using the paired t-test.

Finally, we quantified the effect of using conventional loop estimates of PWV on derived indices from WSA (amplitude of forward (AFW) and backward waves (ABW) and reflection magnitude (RM)) by calculating the error with respect to the reference PWV for all locations of the arterial tree. $\mathrm{PWV}_{\mathrm{BH}}$ was used to obtain reference wave separation indices; in the same way wave separation was performed from each of the loop-based estimates of PWV, and the relative error was calculated. The same process was followed for the correction method PWV_{1-5}. Errors were calculated as (estimate − reference)/reference and reported in percent. Wave separation analysis was performed using the time-domain method [92, 103]. This theory relates the propagation of disturbances (change in pressure ($\mathrm{d}P$) and flow velocity ($\mathrm{d}U$)) along the vessels with a wave speed (PWV), which in turn can be separated into the forward (+) and backward (-) components; summation of these components results in the composite forward (P_+) and backward (P_-) pressure signals (see also section 1.5.3.2). The RM can then be calculated as $\mathrm{RM} = \frac{\max(P_-)-\min(P_-)}{\max(P_+)-\min(P_+)}$. All data were processed in Matlab (Mathworks, Natick, MA, USA).

4.3 Results

4.3.1 Assessment of local PWV methods from conventional analysis

A comparison of the PU-loop, ln(D)U-loop, ln(D)P-loop and QA-loop for the young and aged arterial tree and for different locations of interest (AAO, right CA, BR and FE), is presented in Figure 4.1. Note the overall large disparity of estimates for local PWV; except for the ln(D)P method, none of the methods provides consistent results at these four locations.

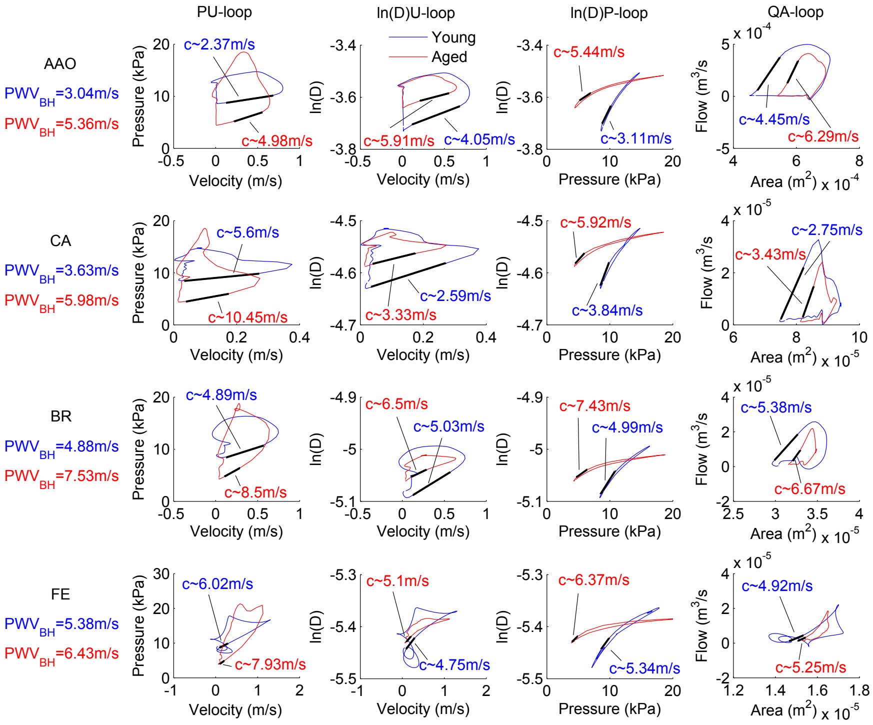

Figure 4.1: PU, ln(D)U, ln(D)P and QA single-location PWV measurement techniques for the young (blue) and aged (red) configurations in the middle node of the AAO, right CA, BR and FE. $\mathrm{PWV_{BH}}$ is the reference wave speed, and *c* is the wave speed estimated from the slope of the loops.

To compare the performance of the tested methods in each node of the arterial tree, we plotted the Bland-Altman analysis comparing estimated values versus the reference $\mathrm{PWV}_{\mathrm{BH}}$, for both the young and aged model (Figure 4.2). The correlation of $\mathrm{PWV}_{\mathrm{BH}}$ with $\mathrm{PWV}_{\ln(D)U}$ or PWV_{QA} was almost non-existent ($R^2 < 0.06$), whereas the correlation with PWV_{PU} was moderate ($R^2 < 0.4$). In contrast, the mean differences for the PU-loop method were 3.0 ± 4.1 m/s for the young case and 6.0 ± 6.2 m/s for the aged case; which was higher compared to a mean difference for the ln(D)U-loop of −0.7 ± 2.3 m/s and −2.6 ± 2.7 m/s, and for the QA-loop of −0.4 ± 2.3 m/s and −2.4 ± 2.8 m/s, for the young and aged cases, respectively. The ln(D)P-loop method showed the best correlations ($R^2 \sim 0.91$ and 0.99 for the young and aged cases, respectively) and the smallest mean differences with $\mathrm{PWV}_{\mathrm{BH}}$ (0.3 ± 0.3 m/s young model, and −0.0 ± 0.2 m/s aged model), as was expected given their mathematical equivalence. The correlation between $\mathrm{PWV}_{\mathrm{BHmp}}$ and the correction method PWV_{1-5} was $R^2 = 0.80$ for the young situation and $R^2 = 0.75$ for the aged situation. Differences were small for the young case (−0.1 ± 0.8 m/s), but were much higher for the simulations in the aged arterial tree (−4.5 ± 2.0 m/s). In every case, the correlations were slightly lower for the young tree compared to the stiffer tree, except for PWV_{1-5}; whereas the differences tended to increase with ageing for every method, except for the ln(D)P-loop method.

To topologically map the deviation of local PWV estimates from the reference, we visualized the error (in %) for every location in the arterial tree with a color map (Figure 4.3), where segments in the white range indicate regions with acceptable errors (± 5%), and red and blue colors indicate over- and underestimation, respectively. The figure reveals that the ln(D)U-loop and QA-loop methods deviate from the reference in a similar way, while the PU-loop method deviates in the opposite direction overestimating in regions where the other two methods underestimate, and *vice versa*. Overall, in the young configuration, locations with an acceptable range of errors are limited for the PU-loop, the ln(D)U-loop and QA-loop methods, in concordance with the differences discussed above. Nonetheless, in some locations, the ln(D)U- and QA-loop methods seem to show lower deviations than the PU-loop method (for a guide on the names of the different segments in the arterial tree refer to Table 2.1). As is already obvious from Figure 4.2, the ln(D)P method showed the smallest discrepancies across the arterial tree. The discrepancies increased with ageing in most of the arterial tree for every studied method (except the ln(D)P method), showing a severe over- and underestimation with respect to the reference $\mathrm{PWV}_{\mathrm{BH}}$. The correction method, for the young configuration, yields lower values than the reference $\mathrm{PWV}_{\mathrm{BHmp}}$ in more central arteries, showing an overestimation in the limb arteries. Interestingly, errors on the estimates for cerebral arteries were close to zero. With ageing, there is a severe underestimation in most of the arterial tree, except for tibial arteries.

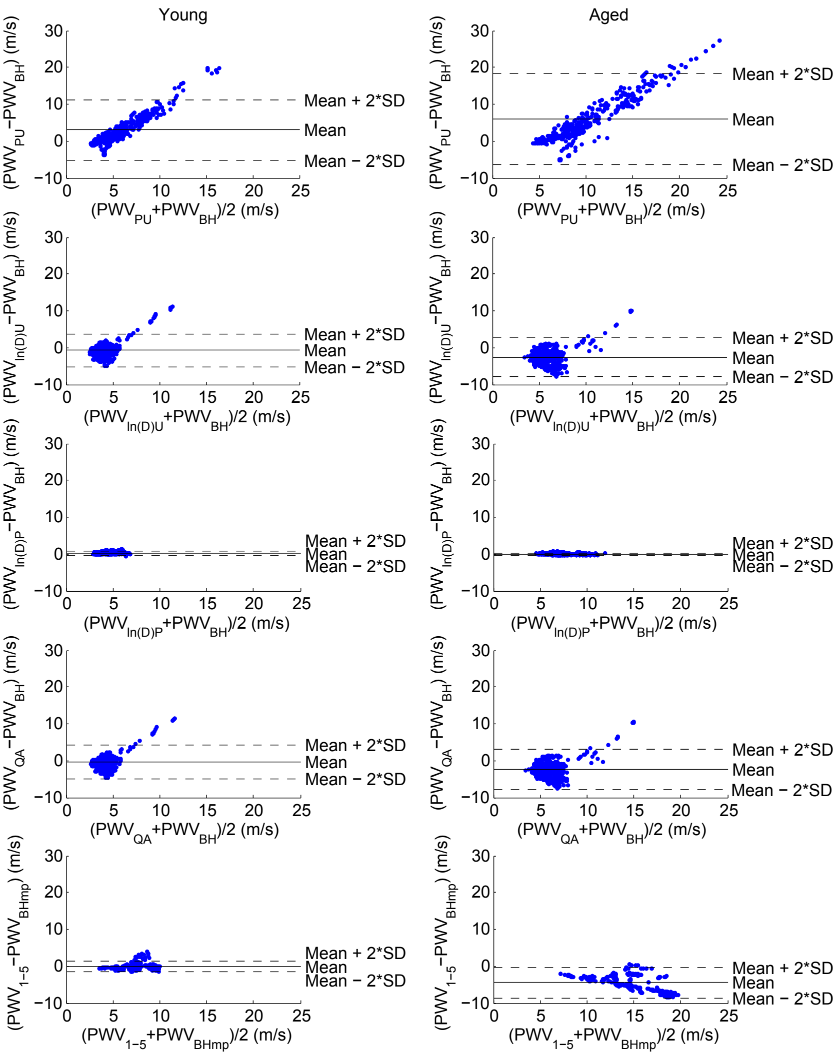

Figure 4.2: Bland-Altman plots between the different tested methods and their respective references, for each node of the arterial tree (n=446). Left column: young arterial system. Right column: aged arterial system. From top to bottom: PWV_{PU} versus PWV_{BH}, $\text{PWV}_{\ln(D)U}$ versus PWV_{BH}, $\text{PWV}_{\ln(D)P}$ versus PWV_{BH}, PWV_{QA} versus PWV_{BH}, and PWV_{1-5} versus PWV_{BHmp}.

4.3.2 Comparison of the methods for the ascending aorta and common carotid artery

When estimating the slope of the PU-, ln(D)U-, ln(D)P- and QA-loop, discrepancies are found for the AAO and CA (Figures 4.1 and 4.4). For the young aorta, the QA method results in the highest PWV value (4.4 ± 0.3 m/s)

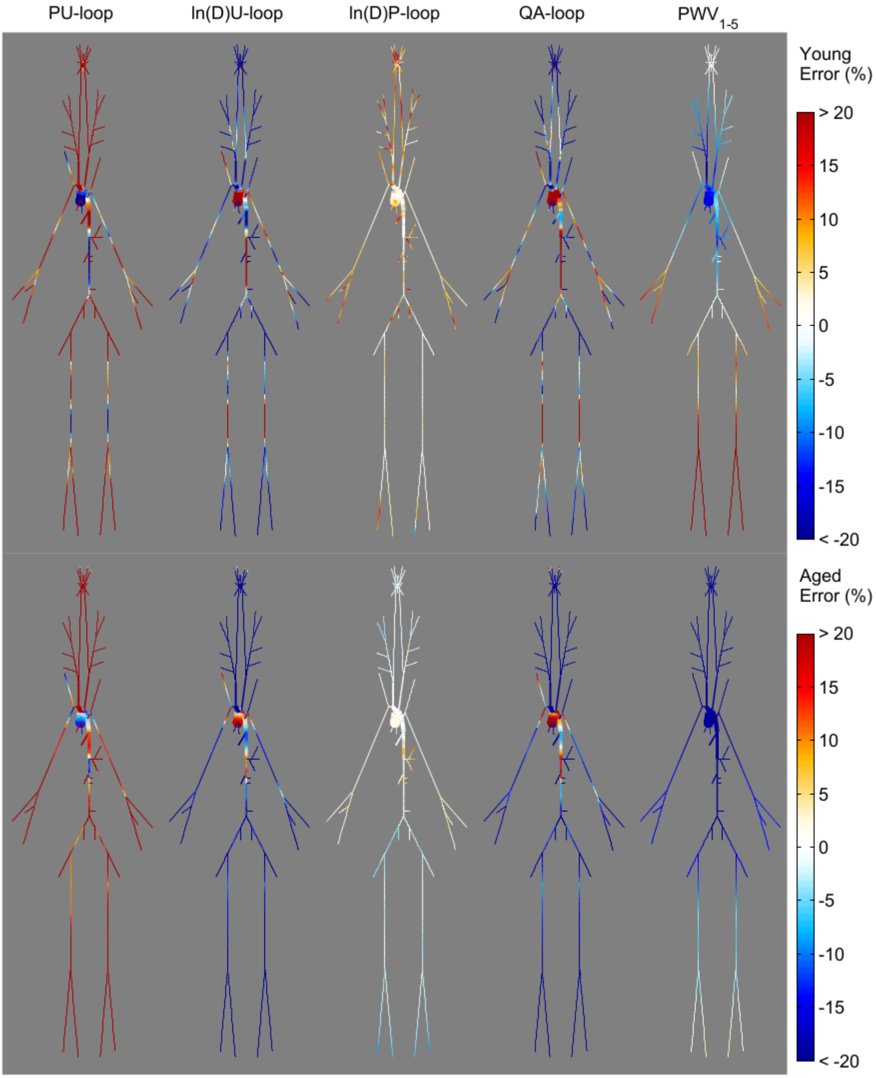

Figure 4.3: Deviation of the loop-based estimates of PWV (PU-, ln(D)U-, ln(D)P- and QA-loops) and the correction method (PWV$_{1-5}$) from their respective references (PWV$_{BH}$ and PWV$_{BHmp}$, respectively), for every location of the arterial tree in the young and aged configurations. Red and blue colors indicate over- and underestimation, respectively.

followed by the ln(D)U method (4.0 ± 0.3 m/s); these values overestimate the reference value of 3.1 ± 0.1 m/s. In the aged arterial tree, both methods overestimate again but with mean values closer to the range of variation of the reference (5.3 ± 0.2 m/s). In contrast, the PU-loop method underestimates, with estimated PWV of 2.5 ± 0.0 m/s and 5.0 ± 0.1 m/s for the young and aged cases, respectively. The opposite occurs for the carotid artery, where the PU method yields values higher than the reference PWV (4.9 ± 0.6 m/s and 9.7 ± 1.2 m/s compared to a reference of 3.5 ± 0.1 m/s and 6.0 ± 0.5 m/s for the young and aged configurations, respectively; shaded area in Figure 4.4). On the other hand, the ln(D)U and QA methods underestimate the reference in both configurations; however, the deviation is higher for the aged case. In each case, the ln(D)P method is within the range of variation of the reference. These data are summarized in Table 4.1, along with the estimations of the reflection coefficient for both arteries in each case.

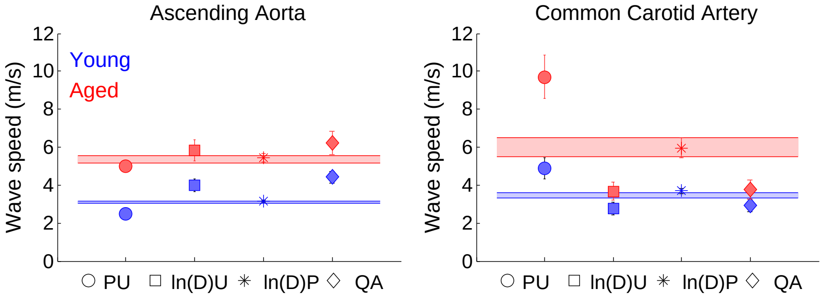

Figure 4.4: A comparison of the loop-based estimates of local PWV assessed from the four measuring methods (PU, ln(D)U, ln(D)P and QA), with the reference (PWV_{BH}, rectangular shaded area), in the ascending aorta and the common carotid artery. PWV values were averaged over five nodes in the arterial segment and their standard deviation is shown.

Table 4.1: An overview of local PWV estimated by different methods, for the young and aged configurations in the aorta (AAO) and carotid (CA) arteries. PWV_{PU}, $PWV_{\ln(D)U}$, $PWV_{\ln(D)P}$ and PWV_{QA}: estimates based on the slopes of the linear segment in the conventional loops. PWV_{BH} and PWV_{BHmp}: estimates based on the Bramwell-Hill equation corresponding to the working pressure of the loop methods and to mean pressure, respectively. PWV_{1-5}: estimates based on the correction method averaged for the first five harmonics. Re(Γ): real part of the reflection coefficient at the heart frequency. All data are reported as the average over five nodes in the arterial segment ± the standard deviation.

		PWV_{BH} (m/s)	**PWV_{PU} (m/s)**	**$PWV_{\ln(D)U}$ (m/s)**	**$PWV_{\ln(D)P}$ (m/s)**	**PWV_{QA} (m/s)**	**PWV_{BHmp} (m/s)**	**PWV_{1-5} (m/s)**	**Re(Γ)**
AAO	Young	3.07 ± 0.06	2.47 ± 0.19	4.0 ± 0.33	3.14 ± 0.05	4.42 ± 0.31	3.88 ± 0.01	3.29 ± 0.04	0.54 ± 0.02
	Aged	5.34 ± 0.19	5.01 ± 0.08	5.83 ± 0.58	5.42 ± 0.22	6.21 ± 0.61	8.27 ± 0.03	6.16 ± 0.02	0.71 ± 0.01
CA	Young	3.48 ± 0.14	4.89 ± 0.56	2.78 ± 0.33	3.69 ± 0.14	2.92 ± 0.32	5.93 ± 0.34	4.73 ± 0.17	0.91 ± 0.04
	Aged	6.0 ± 0.53	9.69 ± 1.15	3.67 ± 0.47	5.96 ± 0.53	3.78 ± 0.49	11.34 ± 0.36	8.36 ± 0.06	0.91 ± 0.04

4.3.3 Impact of PWV estimates on wave separation analysis

Figure 4.5 shows the impact of loop-based estimates of PWV on derived indices of WSA, such as the AFW and ABW, and on the RM for the young

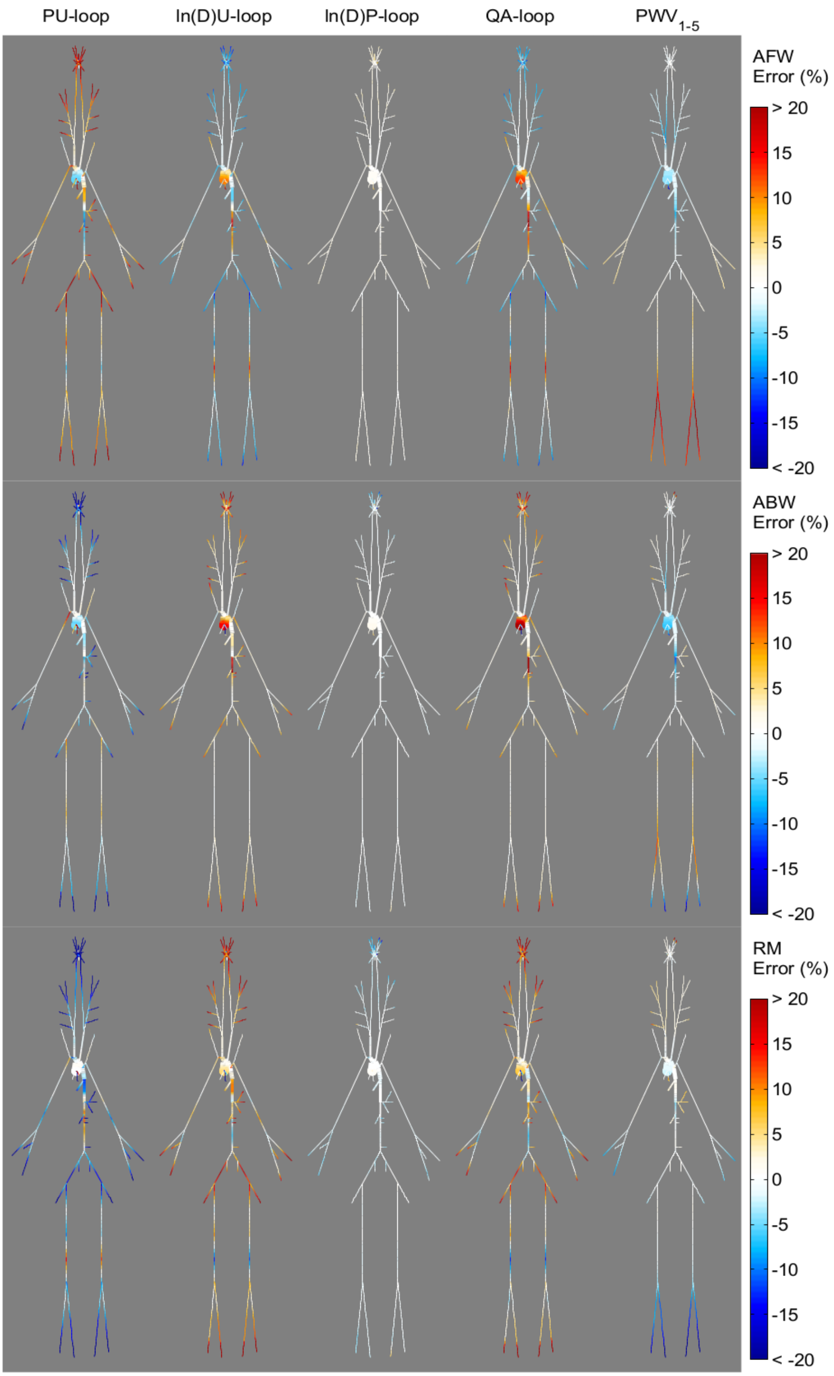

Figure 4.5: The effect of using the loop-based estimates of PWV and the correction method (PWV_{1-5}), on the resultant AFW and ABW, and on the RM for every location in the young arterial tree. Red and blue colors indicate over- and underestimation, respectively.

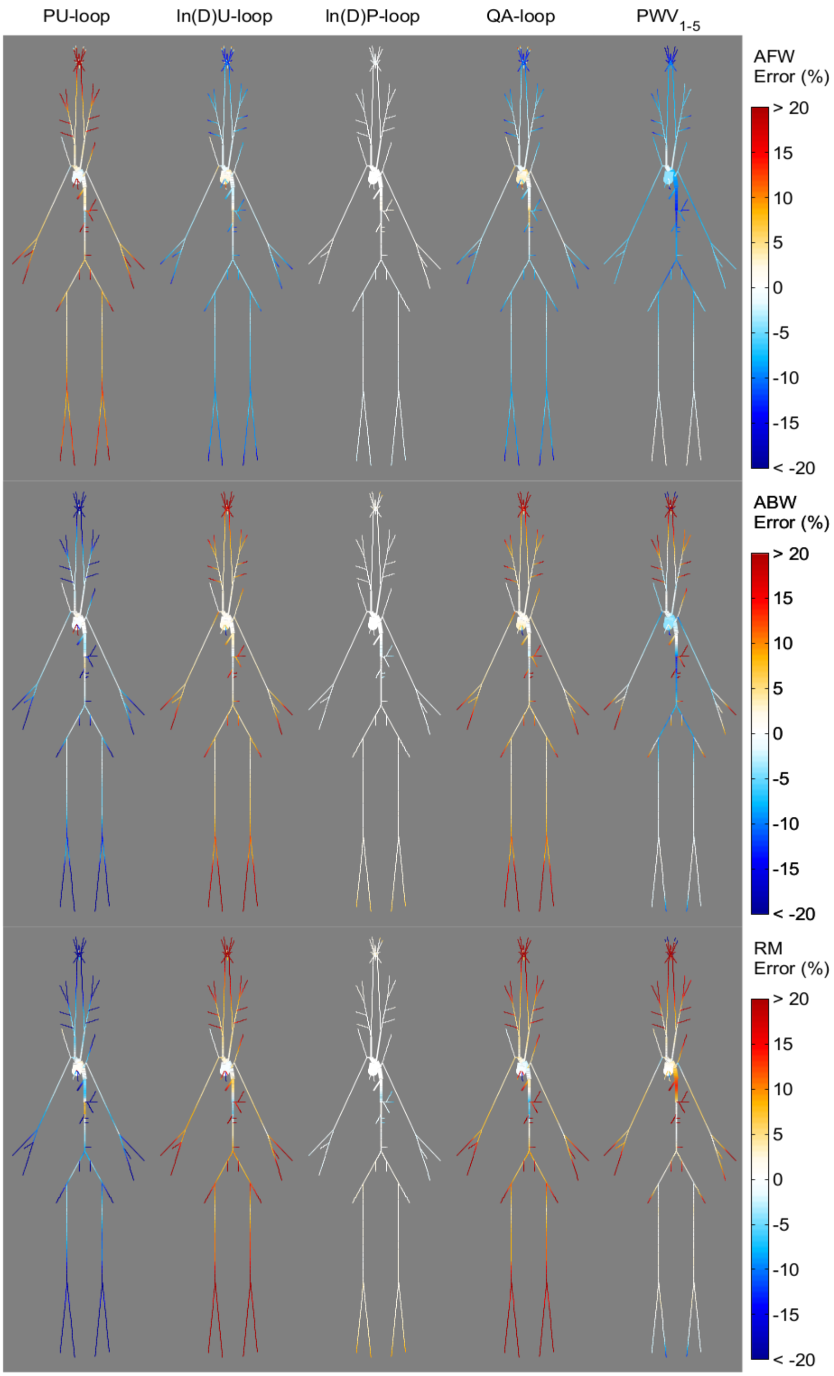

Figure 4.6: The effect of using the loop-based estimates of PWV and the correction method (PWV_{1-5}), on the resultant AFW and ABW, and on the RM for every location in the aged arterial tree. Red and blue colors indicate over- and underestimation, respectively.

arterial tree. Again, the degree of error (in %), along the whole arterial tree, is represented in a color-map graph. PWV as estimated by the ln(D)U and QA methods, mainly decreases the AFW in most of the arterial tree, concomitantly leading to an increase in the ABW and, logically, in the RM. The opposite happens for the estimates of PWV by the PU-loop in a similar scale throughout the arterial tree. The ln(D)P-loop provides the lowest errors with respect to the reference showing the whiter arterial trees (white color representing zero difference with the reference).

When focusing on the proximal aorta, errors in the AFW and ABW (top and middle in Figure 4.5) in the AAO and aortic arch were positive for the ln(D)U- and QA-loop estimates and negative for the PU-loop estimates (opposite to the behaviour of most of the arterial tree). The errors in the RM (bottom in Figure 4.5) at the same sites, however, were in a lower range for the PU-loop than for the ln(D)U- and QA-loop methods. Overall, the errors were somewhat lower at the CAs with similar performances for the three methods.

The performance of the PWV method correcting for wave reflections (PWV_{1-5}) on derived indices of WSA is presented in the last column of Figure 4.5. For the three indices analysed, one observes a trend to low errors in most of the arterial tree, with nonetheless larger deviations from the reference in tibial arteries, where an increase in the AFWs was produced while the RM decreased with respect to the reference. When analysing the aged arterial tree (Figure 4.6), the same patterns as presented for the young case were found in each tested loop method, but deviations from the reference were higher for each of the wave separation indices studied. Interestingly, the deviations for the proximal aorta and CAs remained very low. The corrected PWV_{1-5} also experienced higher deviations with ageing, except for the tibial arteries that in this case showed low deviations.

4.4 Discussion

In this study, we used a 1D arterial network model to investigate the performance of single-location methods to estimate local PWV in different locations of the human arterial tree. In the discussion, we will first focus on the PU-loop, ln(D)U-loop and QA-loop methods, known to be prone to reflections, and subsequently discuss the performance of the ln(D)P-loop method and the reflection-correction method.

4.4.1 The PU-loop, ln(D)U-loop and QA-loop methods

Pooling all nodes of the arterial system, there seemed to be no linear relation between the reference PWV and the ln(D)U-loop or QA-loop methods ($R^2 <$

0.06). Nevertheless, the Bland-Altman analysis, for all locations in the arterial tree and for the young data (similar occurs with ageing, Figure 4.2), revealed less discrepancies in these methods with the reference than in the PU-loop method, with an approximated range of the limits of agreement for the ln(D)U and QA methods between -5 and 4 m/s compared to a wider range (from -5 to 11 m/s) for the PU method, that in contrast showed a better linear relation ($R^2 \approx 0.4$) with the reference method. The Bland-Altman plot reveals a trend of overestimation of PU-loop as the wave speed increases, whereas the ln(D)U-loop and QA-loop tend to underestimate showing a less consistent variability.

Alastruey [171] also performed a similar study using also a 1D numerical model, where in addition to the single location methods considered here, two other methods (D^2P-loop and $\sum^2$-methods) were also compared at different sites of the arterial system (along the aorta, iliac, femoral and tibial arteries). Despite the study having included several locations of the arterial network, only individual arterial sites were reported. Alastruey [171] reported values of loop-based estimates of PWV for the middle node of the thoracic aorta in an elastic configuration, with the PU-loop underestimating the reference by -16.3%, while the ln(D)U and QA loop methods overestimated by 20.3% and 21%. The study thus confirms the opposing behaviour of the QA- and ln(D)U-loop methods on the one hand, and the PU-loop method on the other. In our study, however, the ln(D)U- and QA-loop method underestimated by -18.1 and -5.5%, while the PU loop method overestimated by 23%. Note that the differences in our outcomes might be explained since the tube law in the 1D model used by Alastruey [171], differs from the one in the 1D model of our study [12]. Moreover, the reference PWV is derived by an approximation of the Bramwell-Hill equation for the tube law, while we directly use the Bramwell-Hill equation.

The PWV estimates determined in our study were also within the ranges reported in previous studies using the ln(D)U-loop method on *in vivo* data, for the AAO [172], CAs and FEs [170]. Rabben *et al.* [90] reported an acceptable correlation between the reference PWV (derived from the distensibility coefficient) and the QA method measured in human carotid arteries, however, with a rather wide range of the limits of agreement (between -2.39 and 2.10 m/s); for our simulations the mean difference between PWV_{BH} and the QA-loop method for the CA was of the same order, but with a narrower range of the limits agreement (between -1.45 and 1.08 m/s). In the recent study by Kowalski *et al.* [91], reported mean values for the PU and ln(D)U methods measured from MRI data in the aorta were also close to our data; the reference Bramwell-Hill (approximated also from the distensibility coefficient) was a bit lower though (2.45 versus 3.05 m/s).

The poor correlation for the loop methods discussed above, together with the discrepancies with respect to PWV_{BH} may be influenced because we consider all nodes in the model, while previous comparisons have been reported for isolated locations. As can be seen from the topological color maps, the disparity between the tested method and the reference is highly dependable on the location, with non-systematic over- or underestimation over the entire network resulting in a lack of correlation when pooling all data points. Also, the (non)validity of a given method cannot be tied down to a given artery; in longer segments such as the upper leg arteries, zones of over- and underestimation alternate, suggesting an effect of constructive/destructive interference of waves over these segments depending on the distance to reflection sites and the prevailing PWV. When focusing on the AAO (Figure 4.4 and Table 4.1), the PU-loop estimates were lower than the reference, while the ln(D)U-loop and QA-loop methods yielded values higher than the reference. In the carotid arteries on the other hand, the PU-loop method overestimated PWV_{BH} and the ln(D)U- and QA-loop methods underestimated PWV_{BH}, the errors being lower for the diameter-based methods (see also Figure 4.1). This is in line with what was reported in [168] for this same artery and the study published in [169], and the same observations were done by Kowalski *et al.* [91]. The performances of the PU-, ln(D)U- and QA-loop methods thus have a strong relation with the location in the arterial tree.

The performances of methods were significantly different for the young and aged arterial tree for all methods when analysing all nodes in a global way ($p < 0.01$), visualized in Figure 4.3, where there is a marked over- and underestimation of PWV for the bulk of the locations. When focusing on specific locations, the errors increased in the aged model for the AAO and CAs ($p < 0.001$). At other locations, such as the BRs and FEs, the errors were similar for the methods in both configurations, consistent with what was reported in [170].

Practical implications can be derived from these results, where under the assumption of a maximum tolerance of ±10% error in the estimation of PWV, we grouped the arterial locations that are well represented for the different local PWV methods. Table 4.2 shows an overview of our recommendations according to this analysis for measurements performed in the middle nodes of the arterial segments. It is clear that neither the PU-loop nor the ln(D)U- or QA-loop method perform well over the complete arterial tree.

4.4.2 Eliminating the effect of reflections: correction method and the ln(D)P method

Even though single-location methods are being extensively used in practical applications [90, 170, 172, 173], previous studies have demonstrated inaccuracies in these estimations induced by wave reflections [167–169], where

Table 4.2: Locations where the local PWV methods succeed (✓) and fail (×) in this model, assuming a maximum tolerance of ± 10% error on the estimation of PWV.

Locations	**PU-loop**	**ln(D)U-loop**	**ln(D)P-loop**	**QA-loop**	**PWV_{1-5}**
Ascending aorta	×	×	✓	×	×
Aortic arch	✓	✓	✓	×	✓
Thoracic aorta	×	✓	✓	✓	✓
Abdominal Aorta	×	×	✓	×	✓
Common carotid	×	×	✓	×	×
Brachial	×	×	✓	×	✓
Radial	×	×	✓	×	✓
Common iliac	×	✓	✓	✓	✓
Femoral	×	×	✓	×	×
Tibial arteries	×	×	✓	×	×

the appearance of a linear segment in the loops does not always guarantee the absence of reflected waves [88, 167]. As a solution to this Segers *et al.* [168] proposed a coupled time-frequency domain method, which leads to estimates of PWV corrected for the presence of these reflections. This method was also applied in our study and was compared with the reference PWV_{BHmp}. When analysing the overall performance of the PWV methods over the entire arterial tree (Figure 4.2), the corrected PWV based on harmonics (PWV_{1-5}) had a good correlation with the reference PWV_{BHmp} ($R^2 \sim 0.8$). The method also showed a very low mean difference of -0.13 ± 0.76 m/s for the young case; however, the differences increased for the aged case, having a tendency to a severe underestimation as revealed by the Bland-Altman plot (bottom in Figure 4.2), with a mean difference of -4.46 m/s and a corresponding wide range of the limits of agreement (from -8.6 to -0.3 m/s). On the other hand, PWV_{1-5} also showed a very good performance looking at individual locations, only behind the ln(D)P method (see Table 4.2), and presented lower deviations from its reference in the WSA compared with errors in the PU, ln(D)U and QA methods. At the same time, PWV_{1-5} does not provide an overall solution as the estimate was poor in some areas in the arterial tree (most distal segments in the arms and legs). In the aged arterial tree, PWV_{1-5} displayed higher deviations from the reference, similar to what was found for the other tested loop methods. The correction method thus seems to perform less well when PWV (and the wavelength) is high.

Alastruey [171] proposed to use the average of the PWV estimated by the PU- and ln(D)U-loops. We tested this approach (for the young model data) by analysing all nodes in a global way and examining specific locations. In the overall analysis including all nodes, the correlation with PWV_{BH} was $R^2 = 0.45$, which is substantially lower than the correlation achieved by

PWV_{1-5}. The method also showed a higher mean difference with PWV_{BH} than the correction method with PWV_{BHmp} (~ 1 m/s); the range of the limits of agreement was also wide (-2.13 to 4.13 m/s), with which the method is not interchangeable with the reference PWV_{BH}. However, the use of an average between the PU- and ln(D)U-loops is indeed an improvement compared with simply using the loop methods (with the exception of ln(D)P). Segers *et al.* [168] reported the best performance by PWV_{1-5} compared with the estimates of the PU and QA methods, from *in vivo* data of the human carotid artery, but in that study PWV as approximated by the distensibility coefficient was used as a reference ($PWV_{DC} = \sqrt{\frac{1}{\rho D_w}} = \sqrt{\frac{A_{min}(P_{max}-P_{min})}{\rho(A_{max}-A_{min})}}$). If we compare our results with this variant of the Bramwell-Hill equation (more used in practice) instead of the theoretical equation used in our study, a very good performance of PWV_{1-5} is also obtained, with a correlation of $R^2 = 0.9$ and a mean difference of 0.48 ± 0.53 m/s (see Figure 4.7). Moreover, the performance of PWV_{1-5} is closer to PWV_{DC} than the ln(D)P method. Nonetheless, as stated in [168], the correction method PWV_{1-5} lacks practical applicability because of the necessity of simultaneously measuring pressure, flow velocity and diameter, with which one could simply apply the Bramwell-Hill equation rather than correcting.

As expected, since the ln(D)P method is mathematically equivalent to the Bramwell-Hill equation, it is insensitive to the presence of reflections and performs equally well along the arterial tree. The correlation with PWV_{BH} was excellent ($R^2 > 0.9$), and the mean difference was 0.29 m/s for the young case and -0.028 m/s for the aged case, with the lowest limits of agreement comparing with the other tested methods (maximum range between both cases of -0.4 to 0.9 m/s). Moreover, the ln(D)P method had a very good performance analysing the results for individual locations of the arterial bed, as can be seen in Table 4.2. Lastly, the ln(D)P method had the lowest deviations from the reference in the wave separation analysis, as can be visually confirmed from Figure 4.5. These deviations were even lower in the aged arterial tree, contrary to the performance of the other methods. However, since the ln(D)P method makes use of both pressure and diameter, and given its equivalence to the Bramwell-Hill equation, its practical added value over simply using the Bramwel-Hill equation appears limited.

4.4.3 Effect of error in PWV estimation on wave separation analysis

The large errors in PWV estimates do not fully propagate into the resulting wave separation. For example, in the carotid artery, a large error of -20% on the estimation of PWV by ln(D)U or QA methods only implies a small error (less than ± 2%) in the subsequent WSA. The major impacts occur at the level of the abdominal aorta, tibial and cerebral arteries, as well as in the

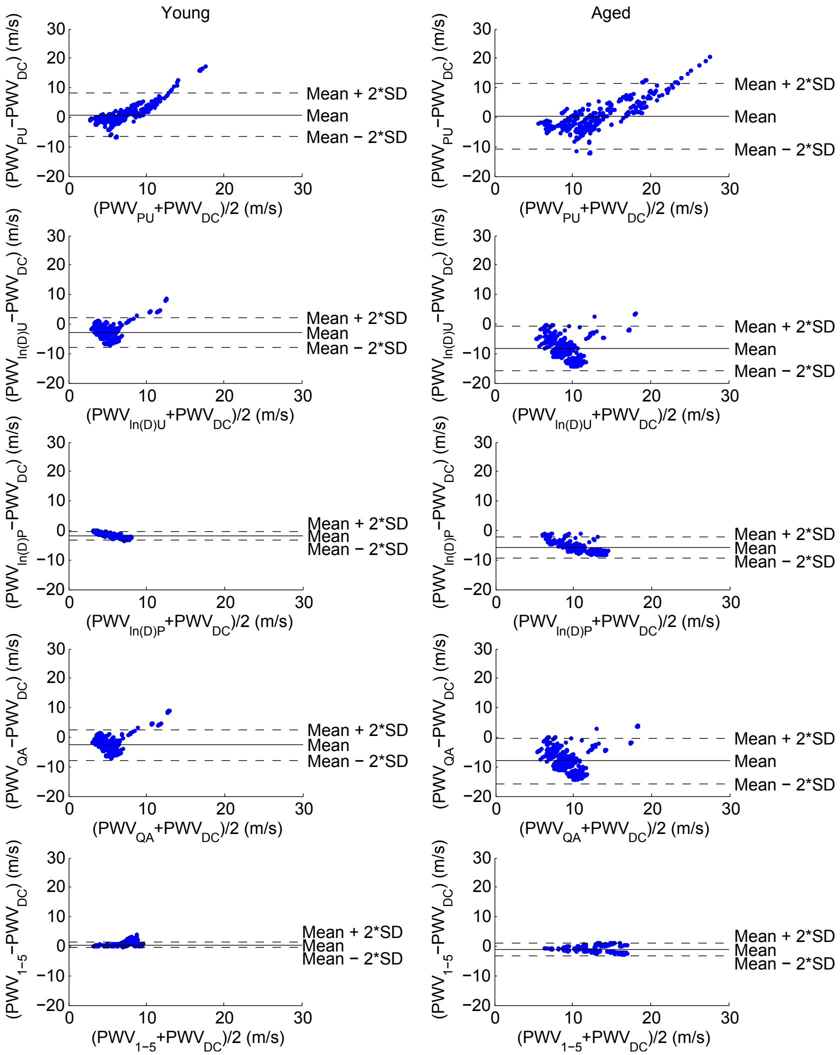

Figure 4.7: Bland-Altman plots between the different methods and the reference PWV$_{\mathrm{DC}}$, for each node of the arterial tree (n=446). Left column: young arterial system. Right column: aged arterial system. From top to bottom: PWV$_{PU}$ versus PWV$_{\mathrm{DC}}$, PWV$_{\ln(D)U}$ versus PWV$_{\mathrm{DC}}$, PWV$_{\ln(D)P}$ versus PWV$_{\mathrm{DC}}$, PWV$_{QA}$ versus PWV$_{\mathrm{DC}}$, and PWV$_{1-5}$ versus PWV$_{\mathrm{DC}}$.

iliac and femoral arteries, and (in general) for all the terminal beds of the arterial network considered. Khir *et al.* [87] stated that the wave separation process is not highly dependent on the accuracy of the determination of the wave speed, and we agree that this is true in certain locations although exceptions may apply to many sites in the arterial tree (see the dark coloured regions in Figure 4.5). As for PWV, the errors are somewhat higher in the aged configuration (Figure 4.6).

4.4.4 Limitations

One of the limitations of the 1D model used for this study is that it does not include the entire circulation of the vascular system, and a Windkessel model was prescribed at the terminal ends. Overall, these terminal ends presented critical points with the highest deviations of PWV estimates from the reference, as can be expected since these distal ends constitute reflection points. Although the use of numerical simulations reduces errors derived from measurements and the alignment of signals, there are still some inaccuracies that may result from the estimation of the linear region in the loop, determined by eye. As we could not identify a linear segment in loops calculated in the circle of Willis and coronary arteries, these were excluded from the analysis. It is also a limitation of the study that the aged configuration was obtained by simply changing the distensibility over the complete arterial tree to the same extent. Clearly, the effect of age on the arterial tree in humans is much more complex, with accelerated ageing in large elastic vessels and relatively little changes in the stiffness of the more muscular vessels and alterations in arterial dimensions. As such, the results obtained in the aged configuration should be interpreted as an illustration of the sensitivity of the method to an alteration in arterial stiffness, rather than as a prediction of the accuracy of the tested methods in the elderly.

4.5 CONCLUSIONS

Single-location PWV methods were tested using 1D numerical modelling in the human systemic arterial tree. The accuracies of the PU-, ln(D)U- and QA-loop methods to assess local PWV was highly dependent on the location in the arterial network, with the PU-loop behaving opposite to the ln(D)U-loop and QA-loop methods. Including all network nodes in the analysis, the ln(D)U-loop and QA-loop methods performed significantly better than the PU-loop, although the correlation of these methods with the reference PWV_{BH} was close to zero. When focusing at specific sites, the methods performed best in the aortic arch rather than the AAO, and the ln(D)U- and QA-loop methods also performed well in the thoracic aorta and iliac arteries. However, the best results were obtained when we applied a loop method based on diameter and pressure (ln(D)P-loop). The estimates of PWV corrected for wave reflections (PWV_{1-5}) also had a good agreement with the wave speed derived from the theoretical Bramwell-Hill equation at mean pressure, although this method did not outperform the ln(D)P-loop method. Overall, methods were very sensitive to the reference chosen, even for approximations of the same equation. Interestingly, WSA was not highly dependent on the accuracy of the PWV estimates for locations such as the AAO or CA. We conclude that results obtained from local PWV loop-based methods require cautious interpretation.

CHAPTER 5

A ONE-DIMENSIONAL MODEL OF THE ARTERIAL CIRCULATION IN HORSES

Arterial rupture in horses has been observed during exercise, after phenylephrine administration or during parturition (uterine artery). In human pathophysiological research, the use of computer models for studying arterial hemodynamics and understanding normal and abnormal characteristics of arterial pressure and flow waveforms is very common. The objective of this research was to develop a computer model of the equine arterial circulation, in order to study local intra-arterial pressures and flow dynamics in horses. Morphologically, large differences exist between human and equine aortic arch and arterial branching patterns. Development of the present model was based on *post-mortem* obtained anatomical data of the arterial tree (arterial lengths, diameters and branching angles); *in vivo* collected ultrasonographic flow profiles from the common carotid artery (CCA), external iliac artery (EIA), median artery (MA) and aorta; and invasively collected pressure curves from carotid artery and aorta. These data were used as input for a previously validated (in humans) 1D arterial network model. Data on terminal resistance and arterial compliance parameters were tuned to equine physiology. Given the large arterial diameters, Womersley theory was used to compute friction coefficients, and the input into the arterial system was provided via a scaled time-varying elastance model of the left heart. Outcomes showed plausible predictions of pressure and flow waveforms throughout the considered arterial tree. The simulated flow waveform morphology was in line with measured flow profiles. Consideration of gravity further improved model

based predicted waveforms. Derived flow waveform patterns could be explained using wave power analysis (WPA). The model offers possibilities as a research tool to predict changes in flow profiles and local pressures as a result of strenuous exercise or altered arterial wall properties related to age, breed or gender. This chapter is based on the paper published in *PLoS One* [174].

5.1 Introduction

A wide range of one dimensional (1D) computer models of the human arterial circulation is available. Such models allow the computation of pressure and flow waveforms throughout the whole arterial network, and hence allow researchers to study the normal and abnormal physiology of the cardiovascular system, without the need of in vivo measurements [108, 111, 131, 175–178]. 1D models are well balanced between complexity and computation costs, making them relevant for many (bio)medical applications. Due to their capability of involving extensive arterial segments, 1D models can provide useful information about characteristics of blood flow at the level of individual branches or even in patient-specific situations [179, 180]. These models can also be used as a non-invasive diagnostic tool, helping physicians to understand observed changes in routine clinical blood pressure measurements and their possible physiological origin and to predict surgical operation results [122, 180, 181].

Due to technical limitations, difficult arterial accessibility, and ethical concerns, in-depth pathophysiological research of the equine arterial tree remains challenging and could be facilitated by the application of a model. Because of large differences between human and equine arteries regarding dimensions and branching patterns, especially of the aortic arch, a horse-specific 1D model of the arterial circulation is needed.

The aim of this study was therefore to develop a 1D computer model of the equine arterial circulation. Providing reference data on equine arterial hemodynamics and physiology, this model might contribute to a better understanding of some clinical findings, such as the origin of the more oscillatory flow patterns in horses, the higher prevalence of aortic rupture in Friesians compared to Warmblood horses [182, 183], the occurrence of sudden death during exercise due to arterial rupture [184–187], the higher chance on uterine artery rupture in older mares [188, 189], or the higher chance on arterial rupture after phenylephrine administration in older horses [190]. In order to develop a reliable model, several anatomical data of the main equine arterial tree were collected *ex vivo* and combined both with *in vivo* invasive blood pressure measurements and noninvasively determined ultrasonographic flow profiles.

5.2 METHODS

5.2.1 Arterial tree

The arterial tree was based mainly on dedicated *ex vivo* measurements. Five Warmblood horses were investigated, mean age 18 ± 3 years and mean body weight 648 ± 47 kg. All horses were scheduled for euthanasia because of non-cardiovascular reasons. Necropsy of 4 out of 5 horses was performed within 12 hours after euthanasia. A dissection was completed on the aorta and the most important (left sided) side branches and morphometric data (length, diameter and branching angle) were recorded. Arterial length was measured using a tape measure, and diameters were measured in the middle of each segment by introducing custom-made iron rods of different diameters into the explored arterial lumen. Subsequently, *post-mortem* diameters were scaled to the *in vivo* diameters, using the *in vivo* ultrasound measurements of CCA, EIA and MA as a reference (see further section 5.2.3). The arterial segments were projected on the horse median plane, and their orientation was defined by the angle between the longitudinal axis of the artery and a reference horizontal axis. Angles of the different arterial segments were measured using anatomical images of the equine arterial tree [191]. Lengths of terminal segments were only measured in one horse. Right sided circulation was assumed to be the same as the left sided arterial circulation, except for the right sided subclavian circulation (as the branching pattern is different), which was measured separately in one of the horses. All investigated arterial branches and their corresponding average length and diameter are displayed in Table 5.1. The main branches of the equine arterial tree were divided into 117 interconnected straight cylindrical arterial segments and inserted in the mathematical model (Figure 5.1). Note that in the mathematical model vessel tapering will be included, meaning that average segment diameters will be adjusted to minimize forward reflections (see further section 5.2.2.3).

All procedures were approved by the Ethical Committee of the Faculty of Veterinary Medicine, Ghent University (EC 2016/104). One horse was privately owned (informed owner consent was obtained), the remaining four horses were experimental horses owned by the Faculty of Veterinary Medicine, Ghent University.

5.2.2 Adapting the cardiovascular 1D model from the human to the equine setting

The mathematical model is based on the previously published and validated 1D arterial network model in humans [12, 107], detailed in Chapter 2. Main differences between the human and the adapted equine model are described below. The system of nonlinear equations is solved using in-house MatLab code. For the solution, an implicit finite difference scheme was chosen, with

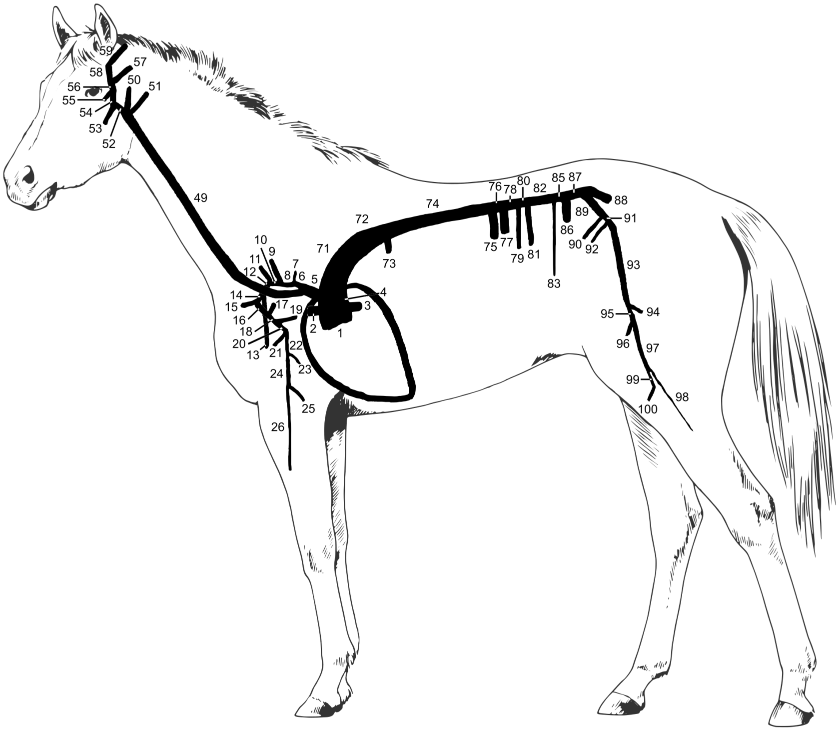

Figure 5.1: Schematic representation of the left sided arterial tree of the horse. Numbers agree with the numbers displayed in Table 5.1.

Table 5.1: Anatomical data of the equine arterial tree.

Arterial segment name	Arterial segment number	Angle in the 1D plane (degrees)	Mean length (mm)	SD	Mean diameter (mm)	SD	Tapering		Distensibility (10^{-3} 1/mmHg)
							Proximal diameter (mm)	Distal diameter (mm)	
Aorta ascendens 1	1	90	18	9	68	6	68.18	67.39	6.85
A. coronaria sinistra	2	180	20		19	6	23.638	12.1	3.17
A. coronaria dextra	3	0	20		19	6	23.638	12.1	3.17
Aorta ascendens 2	4	90	64	9	67	6	67.22	66.82	6.8
Truncus brachiocephalicus 1	5	160	38	26	39	9	38.882	38.88	4.9
A. subclavia sinistra 1	6	155	39	24	26	11	25.332	25.33	3.79
Truncus costocervicalis sinister	7	90	10		11	5	12.102	10.5	2.34
A. subclavia sinistra 2	8	155	19	13	24	8	24.11	24.11	3.68
A. cervicalis profunda sinistra	9	115	70		3	1	2.82	2.82	0.87
A. subclavia sinistra 3	10	155	14	8	24	8	24.11	24.11	3.68

Continued on Next Page…

Table 5.1: (Continued)

							Tapering		
Arterial segment name	**Arterial segment number**	**Angle in the 1D plane (degrees)**	**Mean length (mm)**	**SD**	**Mean diameter (mm)**	**SD**	**Proximal diameter (mm)**	**Distal diameter (mm)**	**Distensibility (10^{-3} 1/mmHg)**
A. vertebralis sinistra	11	135	95		12	5	14.17	9.98	2.45
A. subclavia sinistra 4	12	240	40	6	23	6	22.89	22.89	3.57
A. thoracica interna sinistra	13	280	137		12	4	12.11	12.11	2.44
A. subclavia sinistra 5	14	240	7	8	23	6	22.89	22.89	3.57
A. cervicalis superficialis sinistra	15	180	80		8	2	10.31	4.79	1.9
A. axillaris sinistra 1	16	310	62	25	21	6	21.5	20.37	3.38
A. suprascapularis sinistra	17	70	15		6	0	7.68	3.52	1.59
A. axillaris sinistra 2	18	310	58	45	20	8	19.9	19.9	3.28
A. subscapularis sinistra	19	10	10		17	7	16.8	16.8	2.96
A. axillaris sinistra 3	20	310	23	18	18	5	18.02	18.02	3.09
A. circumflexa humeri cranialis sinistra	21	230	30		5	2	6.11	2.79	1.39
A. axillaris sinistra 4	22	270	70	28	17	3	17.05	17.05	2.99
A. profunda brachii sinistra	23	325	5		11	5	11.281	9.6	2.23
A. axillaris sinistra 5	24	270	82	11	14	1	15.35	12.79	2.67
A. collateralis ulnaris sinistra	25	320	5		6	2	8.6	4.92	1.75
A. mediana sinistra	26	270	145		7	3	10.01	5.3	1.9
Truncus brachiocephalicus 2	27	160	50	91	39		38.88	38.88	4.9
Truncus costocervicalis dexter	28	90	10	59	11	6	14.38	7.07	2.34
Truncus brachiocephalicus 3	29	160	10		39		38.88	38.88	4.9
A. cervicalis profunda dextra	30	115	70		3	2	2.81	2.81	0.87
Truncus brachiocephalicus 4	31	160	10		39		38.88	38.88	4.9
A. vertebralis dextra	32	135	95		12	5	16.95	7.12	2.54
Truncus brachiocephalicus 5	33	160	20		26		26.96	25	4.24
A. subclavia dextra 1	34	240	30		26	11	25	25	3.76
A. thoracica interna dextra	35	280	137		11	5	12.12	12.1	2.44

Continued on Next Page…

Table 5.1: (Continued)

							Tapering		
Arterial segment name	**Arterial segment number**	**Angle in the 1D plane (degrees)**	**Mean length (mm)**	**SD**	**Mean diameter (mm)**	**SD**	**Proximal diameter (mm)**	**Distal diameter (mm)**	**Distensibility (10^{-3} 1/mmHg)**
A. cervicalis superficialis dextra	36	180	80		3	1	8.07	8.02	1.9
A. axillaris dextra 1	37	310	62	25	21	6	20.95	20.94	3.38
A. suprascapularis	38	70	15		6	0	6.43	5.47	1.59
A. axillaris dextra 2	39	310	58	45	20	8	19.9	19.9	3.28
A. subscapularis dextra	40	10	10		17	7	16.8	16.8	2.96
A. axillaris dextra 3	41	310	23	18	18	5	18.02	18.02	3.09
A. circumflexa humeri cranialis dextra	42	230	30		5	2	6.115	2.79	1.39
A. axillaris dextra 4	43	270	70	28	17	3	17.05	17.05	2.99
A. profunda brachii dextra	44	325	5		11	5	10.47	10.47	2.23
A. axillaris dextra 5	45	270	82	11	14	1	17.05	10.42	2.67
A. collateralis ulnaris dextra	46	320	5		6	2	8.6	4.92	1.75
A. mediana dextra	47	270	145		7	3	10	5.3	1.9
Truncus bicaroticus	48	165	78	91	22	19	22.06	21.26	3.45
A. carotis communis sinistra	49	110	710	59	12	1	13.45	10.35	2.42
A. carotis interna sinistra	50	90	120		4	1	4.43	3.53	1.25
A. occipitalis sinistra	51	60	45		5	2	4.94	4.13	1.35
A. carotis externa sinistra 1	52	130	65	41	10	3	10.04	10.04	2.18
Truncus linguofacialis sinister	53	180	80		6	3	6.54	5.5	1.6
A. carotis externa sinistra 2	54	90	41	11	9	2	9.22	8.83	2.04
Ramus massetericus sinister	55	255	20		2	1	2.51	1.21	0.82
A. carotis externa sinistra 3	56	90	13	3	9	2	8.56	8.55	1.98
A. auricularis caudalis sinistra	57	55	10		3	2	3.953	1.74	1.07
A. carotis externa sinistra 4	58	90	23	3	7	3	8.56	5.15	1.76
A. temporalis superficialis sinistra	59	60	20		2	2	3.44	2.48	1.05
A. carotis externa sinistra 5	58b*	90	5		5.15		5.15	5.15	1.46

Continued on Next Page…

Table 5.1: (Continued)

							Tapering		
Arterial segment name	**Arterial segment number**	**Angle in the 1D plane (degrees)**	**Mean length (mm)**	**SD**	**Mean diameter (mm)**	**SD**	**Proximal diameter (mm)**	**Distal diameter (mm)**	**Distensibility (10^{-3} 1/mmHg)**
A. carotis communis dextra	60	110	710	59	12	1	13.45	10.35	2.42
A. carotis interna dextra	61	90	120		4	1	4.43	3.53	1.25
A. occipitalis dextra	62	60	45		5	2	4.94	4.13	1.35
A. carotis externa dextra 1	63	130	65	41	10	3	10.04	10.04	2.18
Truncus linguofacialis dexter	64	180	80		6	3	6.54	5.5	1.6
A. carotis externa dextra 2	65	90	41	11	9	2	9.22	8.83	2.04
Ramus massetericus dexter	66	255	20		2	1	2.51	1.21	0.82
A. carotis externa dextra 3	67	90	13	3	9	2	8.56	8.55	1.98
A. aurocularis caudalis dextra	68	55	10		3	2	3.95	1.74	1.07
A. carotis externa dextra 4	69	90	23	3	7	3	8.56	5.15	1.76
A. temporalis superficialis dextra	70	60	20		2	2	3.44	2.48	1.05
A. carotis externa dextra 5	69b*	90	5		5.15		5.15	5.15	1.46
Arcus aortae (lig. Art Botalli)	71	45	77	26	54	10	58.07	49.53	5.97
Aorta descendens 1	72	45	105	5	45	11	48.21	40.62	5.32
A. broncho-oesophagea	73	270	66		11	2	13.71	6.31	2.26
Aorta descendens 2	74	0	486	69	36	1	38.44	32.28	4.64
A. coeliaca	75	270	20		15	3	19.31	9.24	2.78
Aorta descendens 3	76	0	48	26	29	6	28.7	28.7	4.09
A. mesenterica cranialis	77	270	20		11	7	13.48	7.56	2.29
Aorta descendens 4	78	0	30	35	29	10	28.7	28.7	4.09
A. renalis dextra	79	270	30		11	2	13.26	7.21	2.26
Aorta descendens 5	80	0	20	19	29	5	28.7	28.7	4.09
A. renalis sinistra	81	270	30		11	2	13.26	7.21	2.26
Aorta descendens 6	82	0	104	60	29	6	28.7	28.7	4.09
A. ovarica sinistra	83	270	300		3	1	2.76	2.76	1
A. ovarica dextra	84	270	300		3	1	2.76	2.76	1
Aorta descendens 7	85	0	40	27	29	6	28.7	28.7	4.09
A. mesenterica caudalis	86	270	10		8	3	9.78	4.63	1.85
Aorta descendens 8	87	0	63	12	29	6	28.7	28.7	4.09

Continued on Next Page…

Table 5.1: (Continued)

							Tapering		
Arterial segment name	**Arterial segment number**	**Angle in the 1D plane (degrees)**	**Mean length (mm)**	**SD**	**Mean diameter (mm)**	**SD**	**Proximal diameter (mm)**	**Distal diameter (mm)**	**Distensibility (10^{-3} 1/mmHg)**
A. iliaca interna sinistra	88	330	30	10	18	6	20.19	15.12	0.92
A. iliaca externa sinistra 1	89	315	30		17	2	16.93	16.24	0.88
A. circumflexa iliumprofunda sinistra	90	240	160		6	2	7.58	3.66	0.48
A. iliaca externa sinistra 2	91	280	29	19	16	3	15.99	15.54	0.86
A. uterina sinistra	92	260	200		3	2	3.19	3.19	0.33
A. iliaca externa sinistra 3	93	280	230	54	15	3	15.3	15.3	0.84
A. profunda femoris sinistra	94	335	30		8	2	7.93	7.23	0.55
A. femoralis sinistra 1	95	280	51	14	15	3	15.26	14.27	0.82
A. circumflexa femoris lateralis sinistra	96	240	30		6	3	7.69	3.62	0.48
A. femoralis sinistra 2	97	280	180	56	11	1	10.78	10.78	0.68
A. saphena sinistra	98	285	625		3	3	2.59	2.59	0.29
A. femoralis sinistra 3	99	280	25	26	10	1	10.78	9.71	0.66
A. genus descendens sinistra	100	260	25		3	1	4.46	3.47	0.38
A. femoralis sinistra 4	99b*	280	5		9.71		9.71	9.71	0.64
A. iliaca interna dextra	101	330	30	10	18	6	20.19	15.12	0.92
A. iliaca externa dextra 1	102	315	30		17	2	16.98	16.19	0.88
A. uterina dextra	103	260	200		6	2	3.19	3.19	0.33
A. iliaca externa dextra 2	104	280	29	19	16	3	15.97	15.56	0.86
A. circumflexa iliumprofunda dextra	105	240	160		3	2	7.52	3.77	0.48
A. iliaca externa dextra 3	106	280	230	54	15	3	15.3	15.3	0.84
A. profunda femoris dextra	107	335	30		8	2	7.93	7.23	0.55
A. femoralis dextra 1	108	280	51	14	15	3	15.26	14.27	0.82
A. circumflexa femoris lateralis dextra	109	240	30		6	3	7.69	3.62	0.48
A. femoralis dextra 2	110	280	180	56	11	1	10.78	10.78	0.68
A. saphena dextra	111	285	625		3	3	2.59	2.59	0.29
A. femoralis dextra 3	112	280	25	26	10	1	10.78	9.71	0.66

Continued on Next Page…

Table 5.1: (Continued)

Arterial segment name	Arterial segment number	Angle in the 1D plane (degrees)	Mean length (mm)	SD	Mean diameter (mm)	SD	Tapering: Proximal diameter (mm)	Tapering: Distal diameter (mm)	Distensibility (10^{-3} 1/mmHg)
A. genus descendens dextra	113	260	25		3	1	4.46	3.47	0.38
A. femoralis dextra 4	112b*	280	5		9.71		9.71	9.71	0.64

SD: standard deviation. * An additional terminal segment, which was not measured on necropsy, with an artificial length of 5 cm was implemented in the model.

second order of accuracy for the temporal and spatial domains. Forward, central and backward difference approximations of the spatial derivative were used for the proximal, middle and distal nodes in each segment, respectively. The arterial tree was initialized with a pressure of 100 mmHg and a flow of 1 mL/s. The solution was found over 8 cardiac cycles yielding pressure and flow waveforms over the entire arterial tree.

5.2.2.1 Governing equations: including gravity

The integrated forms of the continuity and momentum equations of the Navier-Stokes equations were solved in each of these segments for pressure (P), flow (Q) and cross-sectional area (A),

$$\frac{\partial A}{\partial t} + \frac{\partial Q}{\partial x} = 0 \tag{5.1}$$

$$\frac{\partial Q}{\partial t} + \frac{\partial}{\partial x}\left(\int_A u^2 dA\right) = -\frac{A}{\rho}\frac{\partial P}{\partial x} - 2\pi R \frac{\mu}{\rho}\frac{\partial u}{\partial r}\bigg|_{r=R} + Ag\cos\theta \tag{5.2}$$

where x and t are the spatial and temporal variables, u is the longitudinal velocity component, and R is the lumen radius. Given that measurements in animals, used as input into the model, were acquired in standing, awake animals, as well as in anaesthetized and dorsal recumbent animals, we expect effects of gravity to be important given the height of the animal. We therefore accounted for the effects of gravity including the body forces term in the momentum equation, with $g = 9.81$ m/s^2, the gravitational acceleration constant, and θ, the projection angle on the vertical axis. Results will be further reported for both situations, considering the effects of gravity and neglecting gravitational body forces. Blood was assumed to be an incompressible Newtonian fluid with density $\rho = 1050$ kg/m^3 and dynamic viscosity $\mu = 0.004$ Pa·s.

Given the large arterial diameters in horses, the Witzig-Womersley correction (see previous section 2.5.1) was used to approximate the convective acceleration term ($\frac{\partial}{\partial x}(\int_A u^2 \mathrm{d}A)$) and the wall friction term ($\tau = \mu \frac{\partial u}{\partial r}|_{r=R}$), both present in the momentum equation. The oscillatory flow theory is taken into account for vessels with $\alpha > 3$ (75% of the total number of arterial segments in the horse model), where the wall friction and convective acceleration are related as independent terms in the 1D momentum equation; the solution described by Stergiopulos *et al.* [108] is considered otherwise. The solution is found solving in time a number of repeating cycles until convergence.

5.2.2.2 *Modelling of the arterial wall*

A constitutive equation is needed to account for the elastic properties of the arterial wall, relating the dependency in intra-arterial pressure with the cross-sectional area (see previous section 2.4). The nonlinear elastic behaviour of the arterial wall is assumed with an expression of area compliance (C_A), as the product of a location-dependent function and a pressure-dependent function (see also equation (2.11)) [12]:

$$C_A(\overline{d}, P) = \frac{A}{\rho \cdot \mathrm{PWV}^2(\overline{d}, P_{\mathrm{ref}})} \left(a_1 + \frac{b_1}{1 + \left[\frac{P - P_{\mathrm{maxC}}}{P_{\mathrm{width}}}\right]^2} \right) \tag{5.3}$$

As described in [12] (and section 2.4), the parameters of the pressure-dependent function are fitted based on the Langewouters model [141]; whereas, PWV for each arterial segment is estimated by fitting an empirical inverse power curve (equation (2.12)) of PWV plotted against lumen diameter, for human data reported in the literature.

To the best of our knowledge, measurements of the pressure and diameter dependency of the compliance in horses are lacking in literature but it can be assumed that the intrinsic building blocks (elastin, collagen, smooth muscle cells, proteoglycans) and their organization, and hence the overall mechanical behaviour, is similar as in humans. Initially, following Reymond *et al.* [12], we used the fitted values on humans for the pressure dependency of the compliance. However, these parameters were subsequently adapted to obtain values of pulse pressure (PP) close to the value reported by Boegli *et al.* [192] for healthy horses, resulting in $a_1 = 0.76$, $b_1 = 5$, $P_{\mathrm{maxC}} = 10$ mmHg and $P_{\mathrm{width}} = 21$ mmHg. We also applied the fit obtained from human data to describe the relation between local diameter and compliance (for $a_2 = 13.3$ and $b_2 = 0.3$). Nonetheless, we did tune the arterial distensibilities to the equine physiology, by multiplying the distensibilities of all vessels of the 1D model by a common factor with value 0.75. That factor was determined such that in resting conditions, we obtained a value of PWV close to the PWV computed from invasive blood pressure measurements over the abdominal aorta of an anaesthetized horse; keeping in mind that differences may arise between an anaesthetized and a conscious animal.

5.2.2.3 *Distal boundary conditions and bifurcations*

For the terminal nodes a 3-elements Windkessel model was used, to account for the cumulative resistance and compliance of all distal vessels beyond the terminal sites (equation (2.25)) [12, 108]. Total peripheral resistances $R_T = R_1 + R_2$, were estimated for the equine physiology in an approximate way, taking into account both the distribution of flow described in the literature [193, 194] and our own measurements of flow at specific locations from ultrasound data. The systemic vascular resistance was 0.14 mmHg·s/mL based on *in vivo* data. The values of the proximal (R_1) and distal (R_2) resistances, as well as terminal compliance (C_{T_i}), were derived as in the human model (see section 2.8).

The total systemic vascular compliance was assumed to be the sum of the volume compliance of all vessels and compliance of the terminal beds, so that $C_V = \sum_i^n C_{V_i} + \sum_i^m C_{T_i}$, where $n = 117$ is the total number of arterial segments and $m = 62$ is the number of terminal segments. C_{V_i} is obtained by integrating C_A over the segment length. Following Reymond *et al.* [12], we assumed that 20% of the total systemic compliance lies in the terminal beds. All values of terminal resistance and compliance can be found in Table 5.2.

Continuity of pressure and flow was imposed throughout the arterial network at bifurcations. Forward wave reflections were minimized by adapting the characteristic impedance of the tributaries so that the absolute value of the reflection coefficient was < 0.2 at all bifurcations. The cross-sectional area of the vessels was therefore slightly adjusted resulting in tapered-structure segments. Cross-sectional areas were determined by minimizing the reflection coefficient, subject to three conditions: (i) measured area is the average between the input and output areas (A_{in} and A_{out} respectively); (ii) A_{in} of tributaries is lower or equal to A_{in} of the parent, and (iii) for each segment $A_{\text{out}} \leq A_{\text{in}}$. Initial searching points were obtained by assuming linear tapering. The forward wave reflection coefficient is calculated in equation (2.30).

5.2.2.4 *Heart and coronary models*

The heart was modelled using the time-varying elastance model of the LV as described previously (see section 2.6.1). Assuming that the elastance curve (when normalized with respect to its peak value) is similar in shape for all mammals, a normalized isovolumic elastance, E^*, can be derived from equation (2.20) using the global normalized elastance curves, E, reported by Senzaki *et al.* [146]. The constant κ was derived iteratively by minimizing the difference between the elastance curve resultant from the 1D model and the original elastance curve reported by Senzaki *et al.* [146]. The value of κ obtained was 55E-06 s/mL. Due to the lack of detailed horse data in current literature, assumptions needed to be made to set most of the input

Table 5.2: Terminal impedance data.

Arterial Segment Number	Terminal resistance (mmHg·s/mL)	Terminal compliance (10^{-2} mL/mmHg)
2	7.22	14.36
3	7.22	14.36
7	32.80	7.97
9	29.82	0.05
11	10.98	7.53
13	32.80	11.01
15	55.44	1.34
17	55.44	0.61
19	55.44	25.80
21	55.44	0.33
23	55.44	6.34
25	67.61	1.31
26	64.46	1.65
28	32.80	3.62
30	29.82	0.05
32	10.98	3.98
35	55.44	11.00
36	55.44	3.78
38	55.44	1.46
40	55.44	25.80
42	55.44	0.33
44	61.60	7.55
46	67.61	1.31
47	64.46	1.65
50	1.10	0.48
51	8.55	0.71
53	8.55	1.50
55	8.62	0.04
57	8.92	0.10
58b	9.00	1.19
59	9.08	0.20
61	1.10	0.48
62	8.55	0.71
64	8.55	1.50
66	8.62	0.04
68	8.92	0.10
70	9.08	0.20
73	3.55	2.78
75	1.96	7.34
77	3.03	4.04
79	1.80	3.62
79b	9.00	1.20
81	1.80	3.63
83	22.55	0.24
84	22.55	0.24
86	3.51	1.22
88	5.52	21.68
90	47.31	0.66
92	23.13	0.12
94	47.31	2.97
96	47.31	0.65
98	47.31	0.07
99b	57.70	6.21
100	57.70	0.47
101	5.52	21.68
103	23.13	0.12
105	55.02	0.70
107	47.31	2.97
109	47.31	0.65
111	47.31	0.07
112b	57.70	6.21
113	52.57	0.47

parameters necessary for the heart model. The value of end-diastolic pressure was taken as, $P_{\text{end-dias}} = 16$ mmHg, according to the value reported by Brown and Holmes [195] for a normal horse and well within the standard range (12-24 mmHg) reported in the literature for horses [196], whereas the end-systolic pressure was 113 mmHg [195]. The value of the dead volume of the LV was set to $V_0 = 0$ mL. Initial reference values for stroke volume (SV = 900 mL) and ejection fraction (EF = 60%) were used to estimate the end-diastolic volume (EDV) and the end-systolic volume (ESV), wherewith initial values of minimal (E_{min}) and maximal (E_{max}) elastance were derived considering equation (2.16). These values were further tuned to obtain a close match between the simulated aortic flow velocity and the aortic flow velocity measured from ultrasound imaging, which resulted in final values of $E_{\text{min}} = 0.01$ mmHg/mL and $E_{\text{max}} = 0.26$ mmHg/mL. The standard heart rate was set to 40 bpm, a normal physiological value for the horse at rest, whereas systolic duration was set to 478 ms [197]. The internal resistance of the LV was assumed as 0.003 mmHg·s·mL^{-1}.

Coronary arteries were modelled following Reymond *et al.* [12], assuming that changes in compliance, distensibility and resistance are proportional to the local time varying elastance of each vessel. For the right coronary, it was additionally assumed that the effect of the right ventricular contraction is smaller by a factor proportional to the ratio of maximal pressure in the two ventricles ($P_{\text{LV,max}}/P_{\text{RV,max}} \approx 3$ [196]).

5.2.3 In vivo measurements

5.2.3.1 Ultrasound

Ultrasound imaging was performed (Vivid IQ, GE Healthcare) on all 5 standing, non-sedated horses. Different regions along the arterial tree were examined: the aorta from a left and right parasternal position, the right CCA 15 cm cranial to the thoracic inlet, the right EIA from the inguinal region and the right MA just proximal to the carpus on the medial side of the leg. 2D B-mode images were collected, using a 9 MHz linear transducer (9L-RS, GE Healthcare) for the CCA and the MA, a 6 MHz phased array probe (6S-RS,GE Healthcare) for the EIA, and a 5 MHz phased array probe (M5Sc-RS, GE Healthcare) for the aorta. Mean values were obtained from 3 consecutive cardiac cycles at a heart rate between 35-45 beats per minute. Measurements were performed, offline (Echopac version 201, GE Healthcare). Diastolic diameters were measured from a transverse image for the CCA and EIA, and from a longitudinal image for the aorta and the MA. Pulsed wave Doppler images were collected at every location, using a 6 MHz phased array probe (6S-RS,GE Healthcare) for the CCA and the EIA, a 5 MHz phased array probe (M5Sc-RS GE Healthcare) for the aorta, and a 9 MHz linear probe

(9L-RS,GE Healthcare) for the MA. Angle correction was set at 45 degrees for every image at all locations. Using this fixed angle correction, images were optimised to align with the flow direction.

5.2.3.2 *Invasive blood pressure*

In all 5 horses, the blood pressure at the level of the CCA was measured invasively in the standing, awake animal. The right CCA was punctured aseptically under ultrasound guidance (Vivid IQ, GE Healthcare; 9L-RS, GE Healthcare), using an 18 gauche 90 mm needle (Terumo® spinal needle, Terumo) placed in the middle of the lumen and kept in place for at least 20 consecutive heart cycles. The needle was connected with a fluid filled pressure transducer (MLT0699 Disposable BP Transducer®, ADInstruments) interfacing with a digital acquisition station (PowerLab 8, ADInstruments), and blood pressure curves were recorded for offline analysis (LabChart, ADInstruments). For each horse the systolic, diastolic, and mean arterial pressure was calculated automatically as the mean of 20 consecutive heart beats (HR between 35-45 bpm).

In one horse, scheduled for euthanasia, invasive blood pressure measurements over the whole length of the thoracic and abdominal aorta were performed under general anaesthesia (pre-medication: detomidine 0.02 mg/kg; induction: combination of ketamine 2.2 mg/kg I.V. and midazolam 0.04 mg/kg I.V.) with the horse in the dorsal recumbent position. After chirurgical exposure of the right CCA, a 72 cm steerable 8.5 Fr sheath (Zurpaz, Boston Scientific) was introduced using the Seldinger technique. Under transthoracic ultrasound guidance (Vivid IQ, GE Healthcare; M5Sc-RS, GE Healthcare) the sheath was introduced retrogradely through the brachiocephalic trunk, into the ascending part of the aorta. Once in place, a custom-made pressure tip catheter (Gaeltec) was introduced and advanced to the most caudal end of the aorta under transrectal ultrasound guidance. Blood pressures were recorded (PowerLab 8, ADInstruments) at the most caudal site and subsequently at every 10 cm during step-wise pulling back of the catheter until the ascending part of the aorta was reached. An ECG was recorded simultaneously. At each location, an ensemble-averaged waveform was constructed from at least 5 cardiac cycles. The ensemble-average was aligned in time relative to the peak of the R-wave of the ECG. PWV was calculated from the relation between inter-measurement distance and time delay. The time delay was calculated from delays in the peak of the 2nd derivative of pressure, assumed to represent the foot of the pressure wave. After the procedure the horse was euthanized while still under general anaesthesia with 6 mL/kg T61 (Intervet International GmbH, Unterschleissheim, Germany), containing 24 mg/kg embutramide, 6 mg/kg mebezoniumjodide and 0.6 mg/kg tetracaïnehydrochloride.

5.2.4 Hemodynamic and wave reflection analysis using wave power

WPA [106] was applied in different locations to study the dynamics of the waves. The method defines the wave power, dπ, as the product of the changes in pressure (dP) and flow (dQ), and equals the energy carried by the wave which is conserved at junctions. Wave power was separated into its forward and backward components (see section 1.5.5). The distance travelled by the waves to their assumed reflection points can be estimated as the product of the transit time between a wave and its reflection and the local theoretical PWV. Since the wave travels twice the same distance, the final distance can be computed as $L = (\Delta t \cdot \mathrm{PWV}_{\mathrm{theor}})/2$.

5.3 RESULTS

5.3.1 General physiological parameters

Running the model without including gravity revealed a CO of 33 L/min, EF of 65% and SV of 820 mL. Systolic/diastolic pressure in the aortic root was 114/70 mmHg, with PP of 44 mmHg and MAP of 93 mmHg. Taking gravity into account, CO was reduced to 30 L/min, with an EF of 59% and SV of 740 mL, whereas systolic/diastolic pressure increased to 131/88 mmHg, resulting in an almost unaltered PP of 43 mmHg and an increased MAP of 111 mmHg. The distribution of CO derived from the model for both configurations is summarized in Table 5.3. Table 5.4 shows the values of the Womersley number, maximum shear stress, mean values of the convective acceleration approximation and the Reynolds number, derived from the model at different locations in the arterial network, including and neglecting gravity. On the other hand, the total vascular resistance resulted in a value of 0.17 mmHg·s/mL for the model without gravity, and 0.22 mmHg·s/mL for the model with gravity.

Table 5.3: Distribution of cardiac output in the model.

	Cardiac output distribution (%)		
Body parts	Model without gravity	Model with gravity	Reference [193]
Heart	4.2	5.4	5
Brain	15.4	10.5	10
Muscle	7.7	11.3	15
Kidney	18.2	20.7	20
Splanchnic	28.3	32.6	30
Other	26.2	19.5	20

Table 5.4: Womersley number, maximum shear stress, mean convective acceleration and Reynolds numbers, derived from the model with and without gravity at different locations along the equine arterial tree.

Artery		Prox Ao	Dist Ao	CCA	MA	EIA
Womersley number α		35.47	15.05	6.02	3.78	8.02
Maximum shear stress ($\tau_{\max}$ in Pa)	with gravity	2.72	2.89	2.28	1.74	1.5
	without gravity	3.05	3.11	2.09	1.79	1.7
Mean convective acceleration ($\frac{\partial}{\partial x}(\int_A u^2 \mathrm{d}A)\ 10^{-5}$ in $\mathrm{m^3/s^2}$)	with gravity	57.32	-27.75	-0.12	0.27	-1.02
	without gravity	68.67	-31.55	6.79	0.06	-1.32
Reynolds number	with gravity	2404	870	1160	98	278
	without gravity	2660	749	2312	68	195

5.3.2 Effects of gravity

To assess the importance of considering gravity in the model, the distribution of pressure and flow velocity was plotted all over the arterial tree, both with and without taking gravity into account (see Figure 5.2). Considerable differences in pressure were most evident in the limb arteries, carotid arteries and the arteries of the head. Because of pressure amplification, systolic pressures were relatively high in the front and hind legs (>160 mmHg) when gravity was neglected, while mean pressures were almost unaltered over the whole arterial tree. Considering gravity, systolic pressures in the front legs became even higher, whereas systolic pressures in the arteries of the head became low (<100 mmHg) and mean pressures increased from the head to the legs. Mean flow velocity distribution was similar for both configurations, with higher values for vessels in the splanchnic region and toward the head. A more direct comparison on the features of waveforms is displayed in Figure 5.3, with evident discrepancies in flow waveforms of the CCA and in pressure waveforms for the proximal aorta, CCA and MA.

5.3.3 Model predictions versus *in vivo* measurements

Table 5.5 presents peak blood flow velocities and pressure data estimated from the 1D model in both situations, including and neglecting gravity, along with available *in vivo* measurements. Of note is the higher PP predicted by both models, in combination with the amplification of PP towards the periphery. Moreover, both models reveal an amplification in pressure along the aorta. An increase in SBP from the ascending aorta to the EIA of ~ 54% was found for the model neglecting gravity, while it was reduced to ~ 34% when gravitational forces are included.

Figure 5.4 displays the modelled blood flow velocity waveforms, both with and without including gravitational forces, for the ascending aorta, CCA and the main limb arteries (MA and EIA), compared with the measured waveforms in standing horses, derived using pulsed wave Doppler ultrasound.

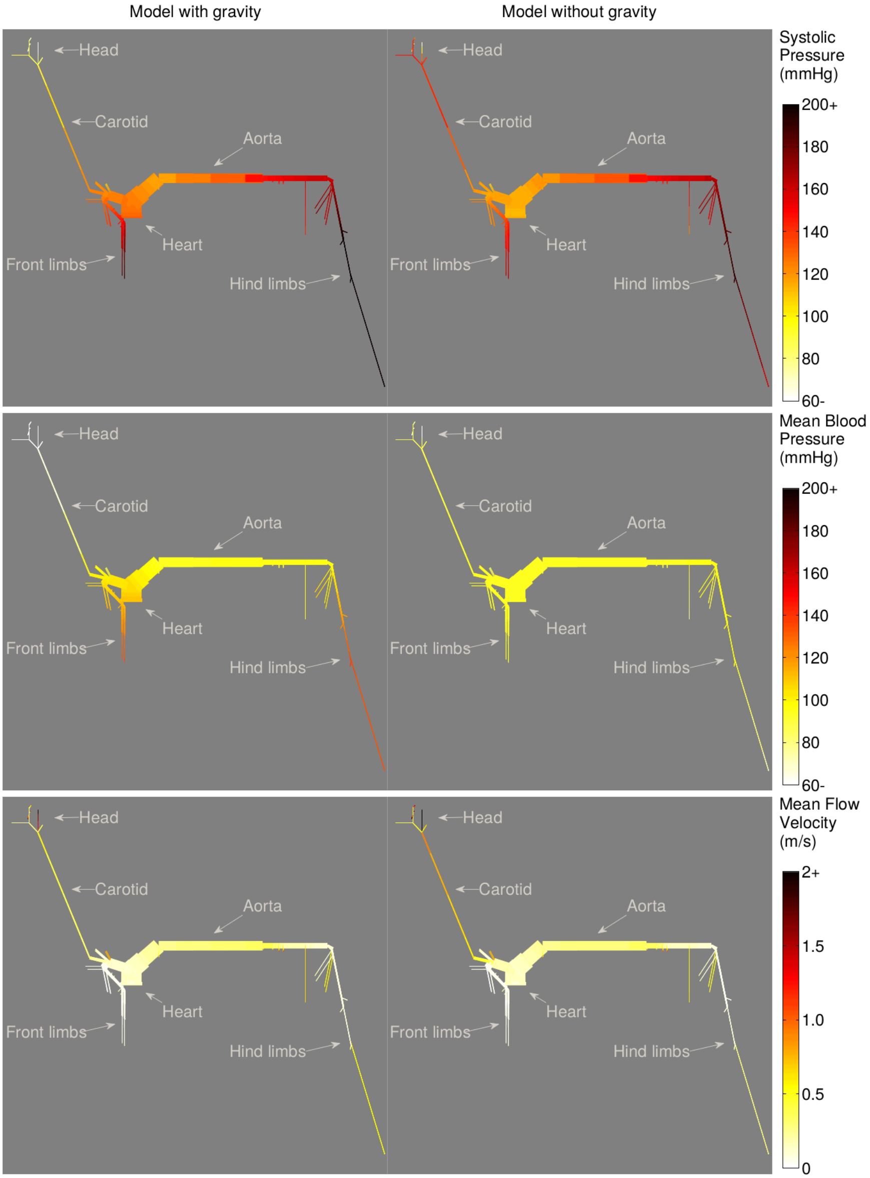

Figure 5.2: Distribution of systolic pressure, mean blood pressure and mean flow velocity over the complete arterial tree, comparing the model including gravity with the model neglecting gravity. Lower and higher values are indicated with colours varying from light to dark tones, respectively.

A relatively good similarity in waveform shape and their amplitude was found at all arterial locations, with relative errors for peak flow velocity between *in vivo* data, in the standing awake animal, and simulations without including gravitational forces of 29% for the ascending aorta, 82% for the CCA, 15% for

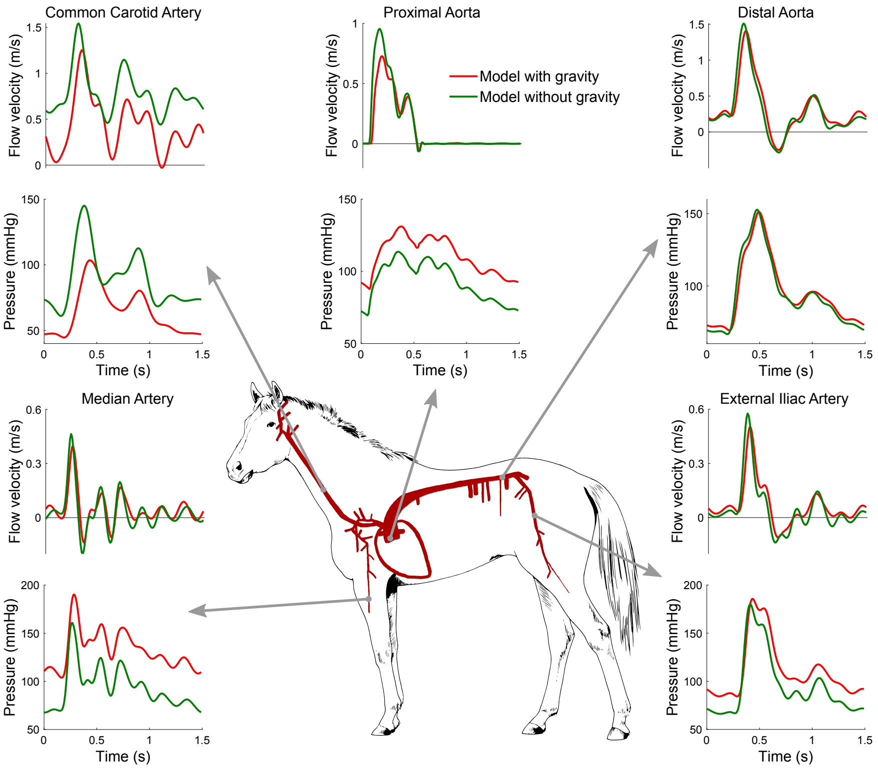

Figure 5.3: Model results with and without gravity of pressure and flow waveforms at various arterial locations: common carotid artery, proximal aorta, distal aorta, median artery and external iliac artery.

the EIA and 40% for the MA. When gravitational forces are included, relative errors improved to 2%, 48%, 2% and 23%, respectively.

Figure 5.5 compares *in vivo* invasively measured pressure waveforms along the thoracic and abdominal aorta (horse under general anaesthesia in dorsal recumbent position), with modelled pressure waveforms at the same locations (simulations resemble a non-anaesthetised horse), with and without considering gravitational forces. The effect of wave propagation is well captured by the model. Modelled mean, systolic and diastolic arterial pressures in the proximal aorta and neglecting the gravitational forces, showed relative errors of 11%, 3% and 25%, respectively, compared to the invasively recorded pressure measurements. When gravitational forces are included relative errors changed to 6% for MAP, 12% for SBP and 5% for DBP. For the distal aorta relative errors were slightly higher, 21% for MAP, 20% for SBP and 40% for DBP. Including gravity had almost no influence on the derived pressures and thus the relative errors. Aortic PWV determined from the simulation was 5.3 m/s when gravity is neglected, changing to 5.2 m/s

Table 5.5: Pressure and blood flow velocity predictions derived from the model with and without gravity and corresponding *in vivo* measurements at different locations along the equine arterial tree.

Artery		Prox Ao	Dist Ao	CCA	MA	EIA
Segment number		1	87	49	26	93
Peak flow velocity (m/s)	*In vivo*	0.742*	NA	0.846*	0.403*	0.457*
	Model without gravity	0.968	1.079	1.213	0.556	0.536
	Relative error (without gravity)°	0.3	NA	0.43	0.38	0.18
	Model with gravity	0.8	0.98	1.227	0.392	0.394
	Relative error (with gravity)°	0.06	NA	0.45	0.03	0.14
MAP (mmHg)	*In vivo*	104.5**	119.7**	123.7*	NA	NA
	Model without gravity	96.5	96.6	95.7	96.6	96.7
	Relative error (without gravity)°	0.08	0.19	0.23	NA	NA
	Model with gravity	112	96.1	83.6	128.6	105.9
	Relative error (with gravity)°	0.07	0.2	0.32	NA	NA
SBP (mmHg)	*In vivo*	116.7**	134.4**	133.3*	NA	NA
	Model without gravity	129.1	158.5	138.9	167.1	182.1
	Relative error (without gravity)°	0.11	0.18	0.04	NA	NA
	Model with gravity	143.9	156.1	146.7	179.6	182.1
	Relative error (with gravity)°	0.23	0.16	0.1	NA	NA
DBP (mmHg)	*In vivo*	92.2**	109.8**	111.4**	NA	NA
	Model without gravity	75.1	71	73.8	74.6	71.1
	Relative error (without gravity)°	0.19	0.35	0.34	NA	NA
	Model with gravity	90.9	72.5	61.7	106.4	82
	Relative error (with gravity)°	0.01	0.34	0.45	NA	NA
PP (mmHg)	*In vivo*	24.0**	24.2**	22.0**	NA	NA
	Model without gravity	54	87	65	92	111
	Relative error (without gravity)°	1.25	2.59	1.95	NA	NA
	Model with gravity	58	83.6	85	72	100
	Relative error (with gravity)°	1.41	2.48	2.86	NA	NA

Prox Ao: proximal aorta; Dist Ao: distal aorta; CCA: common carotid artery; MA: median artery; EIA: external iliac artery; NA: not applicable. *Measured in standing, non-sedated horses; mean of all investigated horses. **Measured in the anesthetised horse in dorsal recumbency; values of only 1 horse °Relative error was calculated as |(*in vivo* measured value–Modelled value)|/*in vivo* measured value.

considering gravity, whereas the value obtained from *in vivo* data was 5.27 m/s (difference of ~ 0.6% when comparing with the model neglecting gravity, and ~ −1.3% when comparing with the model including gravity).

5.3.4 Results of the wave power analysis

WPA is shown in Figure 5.6 for the proximal aorta, CCA, MA and EIA. Models with and without including gravitational forces are compared. In both situations, the proximal aorta shows the three typical peaks: i) a forward compression wave (FCW) generated by the systolic ejection, ii) a backward compression wave (BCW) as the result of peripheral reflection, and iii) a forward expansion wave (FEW) due to the slowing of ventricular contraction. Besides these normal peaks, a small FEW can be visible at the different locations in mid-systole. The timing of occurrence of this wave coincides with the drop in flow signals for the median and iliac arteries. For all the considered

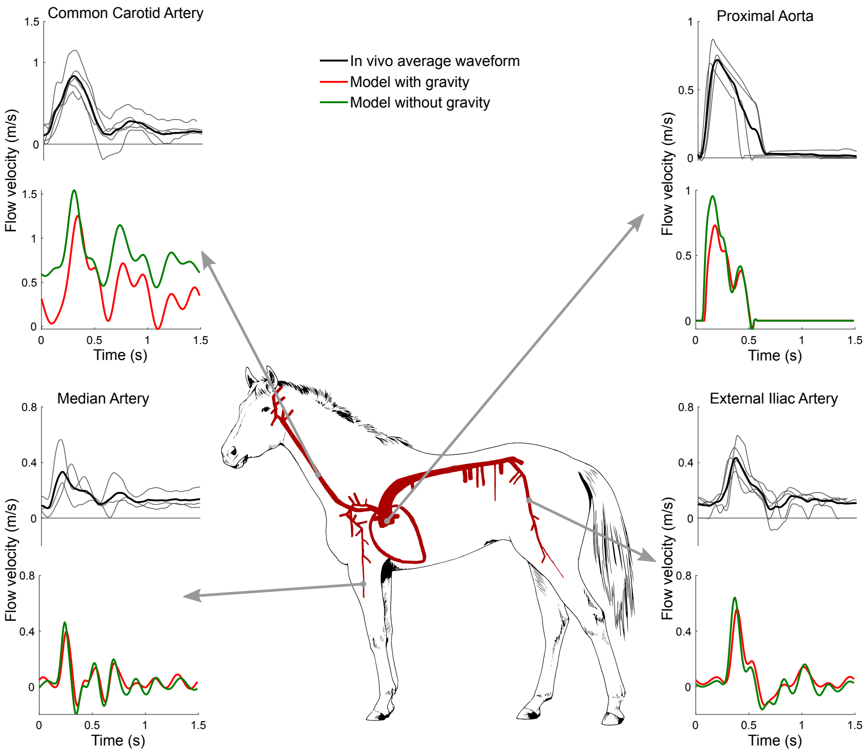

Figure 5.4: Model results with and without gravity (bottom) compared with the averaged *in vivo* measurements of flow velocity in all investigated horses (top) at various arterial locations: common carotid artery, ascending aorta, median artery and external iliac artery.

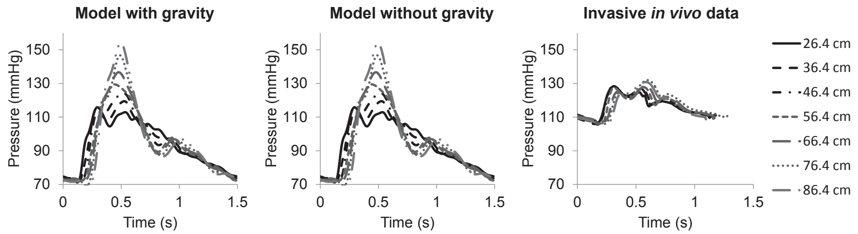

Figure 5.5: *In vivo* pressure waveforms compared with simulations, at seven locations along the aorta. Distances are expressed in centimetres distal from the aortic root.

locations, wave power was lower when gravitational forces were included. The largest difference between both situations is observed at the CCA, where for the configuration without gravity, a mid-systolic FEW combines with the typical FEW from the ventricular contraction, resulting in a wide FEW; and this in a more drastic drop in the carotid SBP of the model without gravity than the model with gravity (see Figure 5.3).

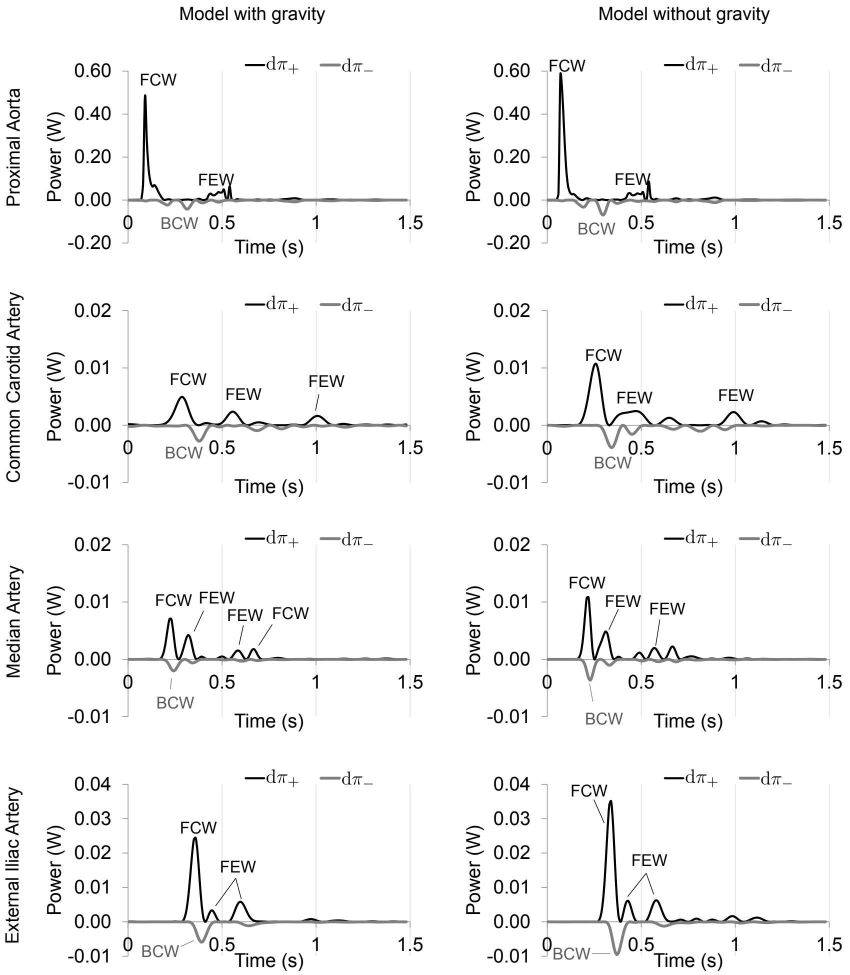

Figure 5.6: Wave power analysis at several locations of the arterial tree, comparing the model including gravity, with the model neglecting gravity. (FCW and FEW: forward compression and expansion waves; BCW and BEW: backward compression and expansion waves; $d\pi_+$ and $d\pi_-$: forward and backward components of wave power, respectively).

5.4 Discussion

Current literature provides only limited information on arterial hemodynamics in horses. In-depth fundamental research into equine intra-arterial pressures and flows is therefore expected to increase the understanding of aortic and arterial rupture in this species [184–187]. Today, due to technical limitations it is difficult to assess pressure and flow in the centrally located arteries and therefore peripheral measurements are usually extrapolated to the rest of the vascular network. The present study aimed to develop a 1D computer model for the equine arterial circulation comprising all major vessels of the arterial tree. The original 1D human model on which this equine model is based, has been validated and is used as a research tool in many studies [17, 19, 133, 147, 178]. Recently, it formed the basis for the development of a 1D model in mice [198]. As aortic branching pattern of horses is completely different compared to humans, arterial segments needed to be redefined. *Ex vivo* measurements (diameter, length and branching angle) of each arterial segment along the equine arterial tree resulted in a unique dataset of the equine arterial anatomy (Table 5.1). Dimensions (lengths and diameters) of the equine arterial tree are much bigger than those of humans. Moreover, equine HR is lower at rest (28-45 bpm in horses and 60-100 bpm in humans) and the heart mass is much larger compared to humans (> 1% of the body mass in horses and ~ 0.5% of the body mass in humans [193]). Both elements imply a much higher CO in horses (~ 35 L/min compared with ~ 7 L/min in humans). Of note is the higher Womersley number in the horse, implying a considerably higher impact of inertia on the flow velocity profile, leading to flatter velocity profiles with steeper velocity gradients near the wall than those predicted by Poiseuille flow. As this leads to an improved estimation of viscous friction, it was important to include the Witzig-Womersley correction factor in the momentum equation.

5.4.1 Importance of gravity

Existing 1D models usually ignore the effects of gravity, because most physiological measurements in humans are performed in supine position, with the heart being at the same level as the rest of the arterial tree. In horses most blood flow velocity and pressure measurements are performed on standing patients, and therefore the effect of gravity was incorporated in the present model. The arterio-venous pressure gradients, which causes flow, do not fluctuate considerably for the body in the supine position compared with that in the standing position; thus overall flow is similar in both situations. The transmural pressures on the contrary, are strongly different. Given the nonlinear pressure dependency of arterial stiffness, gravity was expected to exert an effect on wave propagation and wave morphology. This was indeed confirmed by our results.

In order to assess the impact of gravitation, two configurations of the model (with and without gravity) were compared (Figures 5.2 through 5.6). Taking into account gravity generally improved predicted peak flows. Relative errors improved from 15-82% for the model without gravity to 2-48% for the model including gravity. While peak flow predictions improved when including gravity into the model, relative error for MAP, DBP and SBP did not improve when gravity was included, with relative errors ranging from 3-40% without gravity and 5-56% with gravity included. Figure 5.2 shows that, when gravity is neglected, MAP is practically the same in all conduit arteries. As was expected, including gravity into the model revealed more variability in MAP throughout the arterial tree, with lower values toward the head and higher values toward the limbs. Figure 5.5 clearly shows the similarities in pressure waveforms of the descending aorta with and without gravity. These similarities in pressure waveforms are due to the assumption of a horizontal motion of blood (angle = 0°) in the descending aorta, causing no influence of gravity.

5.4.2 Wave power analysis

As changes in arterial pressure waves are associated with alterations in the contour of the arterial flow profiles [199], the pronounced oscillations during flow wave measurements at different arteries in horses probably indicate pressure waves returning from the periphery at multiple reflection sites, starting during systole and continuing during diastole. WPA performed at several locations revealed important wave reflections mainly during systole. Wave power patterns were most complex for the CCA, which also displayed the biggest delay between the first FCW and its peripheral reflection (BCW) coming from the head. This was somewhat expected considering that the wave has to travel forth and back along the carotid artery. The reflection of the first forward peak at the peripheral site in the head was higher when gravity was included in the model (~ 56% with gravity versus ~ 36% without gravity). The presence of a mid-systolic FEW immediately after the first peak generated by the heart ejection (Figure 5.6), was responsible for the drop of pressure and flow velocity that resulted in narrow systolic peaks in pressure and flow waveforms of the investigated vessels. In order to understand the origin of this suction wave, we estimated the distance travelled by the wave to the site of re-reflection. By combining the time difference measured from the foot of the waves with the local theoretical PWV in the involved segments, very short distances were derived. These re-reflections might be occurring locally in the network rather than at the heart level, and may be related to a mismatch of junctions in the peripheral branches. Higher efforts to minimize forward wave reflections at these sites are needed.

5.4.3 Limitations and future work

In general, flow waveform patterns (morphology) are well captured by the model, especially by the one including gravity while discrepancies in amplitude are quite obvious (Figure 5.4), this is probably due to several limitations of this model, which will be explained clearly in this section.

Since the present model is based on averaged data, it enables us to predict generic local pressures and flow profiles in all investigated arterial segments. A fully quantitative validation, however, would require a detailed horse-specific approach, tuning of all input parameters that define the model to each specific animal (such as geometry, elastic properties, peripheral resistance, and cardiac parameters) and comparing the outcomes of the model with *in vivo* measurements in that specific animal. Such an approach is technically challenging and almost impossible. Therefore, even if we consider the present model to be representative for the average healthy horse, waveforms should only be compared qualitatively and not quantitatively to individual measurements.

The lack of literature data on equine hemodynamics was the major challenge to develop an equine 1D model. Tuning the model parameters was based on plausible assumptions and scaling factors between human and equine patients. Further fine-tuning of the input parameters to equine physiology will be necessary to obtain a closer match with *in vivo* flow profiles. Branching patterns and dimensions of the arterial tree, both largely defining flow wave patterns, are well integrated in this model. However, branching patterns and arterial dimensions can vary significantly between individual horses. Other important parameters, influencing flow velocity and pressure waves morphology are arterial elasticity and peripheral resistance. Both, arterial elasticity and peripheral resistance largely defines diastolic flow [200] and PP [17], two parameters still showing large differences between measured values and modelled ones, with relative errors for DBP ranging from 5 to 60% and for PP ranging from 81 to 288%. Equine arterial elasticity and peripheral vascular resistance are therefore interesting criteria to further unravel in the future. In addition, in our simulations the compliance distribution and peripheral resistances remain the same for both, the model with gravity and the model without gravity. Neglecting the autoregulation mechanisms that lead to a cardiovascular response to control blood flow and pressure levels during postural changes, can also partially explain the differences found in our simulations and *in vivo* data.

The limited research possibilities in equines form another restrictive factor in the development of the equine 1D model. Due to ethical concerns, invasive aortic BP was only collected in one horse, which is a limitation of this study. Moreover these aortic BP were collected in anaesthetized, dorsally recumbent animals, while ultrasound and pressure measurements at the carotid artery were performed in non-sedated, standing horses. This complicates comparison between *in vivo* measurements and modelled findings. The present model does not yet account for the changes in physiological parameters due to anaesthesia or dorsal recumbent position. Anaesthesia tends to slow down HR, reduce both CO and PP and likely leads to modulations in resistance of vascular beds and mechanical properties of arteries. Changes in smooth muscular tone modulate distensibility and stiffness. The recumbent position of the horse has a huge effect on intrathoracic and arterial transmural pressure, modulating stiffness and leading to important volume shifts of blood affecting cardiac filling and preload and, via the Frank-Starling mechanism, cardiac contractility. In addition, the model does not include physiological control mechanisms such as the baroreflex that neurologically modulates cardiovascular function via sympathetic/parasympathetic mechanisms. When a body changes from the supine to the standing position, these baroreceptor control mechanisms are activated to limit MAP decrease to only a few mmHg. The restoring mechanisms include an increase in CO (mainly an increase in HR), as well as an increase in SVR.

Next to this, discrepancies in pressure and flow waveforms between measured and obtained modelled values may be affected by angle correction. In order to obtain standardised images, angle correction was set at 45° when collecting flow velocity profiles in the standing horse. Measurements were optimized for alignment with the flow but this alignment was not always perfect and flow was probably not always captured in the centre of the artery, which implies that captured flow velocities are only an approximation of the true flow profiles.

Discrepancies in pressure and flow waveforms may also be affected by the exclusion of the entire systemic and pulmonary circulation, making the model an open-loop system that requires boundary conditions: a cardiac time-varying elastance model at the inlet, and the Windkessel model at the terminal ends. Moreover, the cerebral arterial tree is not included in detail in the equine model, only a simplified representation containing the major vessels that supply the cerebral circulation. A more detailed description of the cerebral arterial tree may provide better predictions of pressure and flow waveforms in the carotid artery and smaller vessels of the head circulation, as has been previously shown for the human [12] and murine models [198]. Furthermore, in the present design, the model used for coronary arteries is simplistic. Last but not least, development of the present model was based on data obtained on a limited number of horses, without accounting for cardiovascular variations due to age or gender.

Nevertheless, despite individual differences in absolute values of flow velocities and arterial pressures, flow wave morphology is well captured by the model as shown in Figure 5.4. Figure 5.5 evidences the effect of wave propagation along the aorta both in the measured and the modelled pressure profiles. This indicates the added value of the model for studying trends in arterial flow dynamics in horse populations.

In the future this computer model may be useful to predict changes in flow profiles and local pressures under specific circumstances or conditions (age, exercise). During high-intensive exercise, HR may rise up to 8 times above the resting rate and total aerobic capacity can reach a 40-fold increase, which is much greater compared to human athletes. By altering input parameters of the horse-specific model, this model might predict local pressures and flow profiles during these extreme circumstances and contribute to the understanding of the relatively high incidence of sudden death during exercise due to arterial rupture [184–187]. As increasing age increases the risk of arterial disorders (arterial rupture during exercise, during parturition or after phenylephrine administration) [184, 188–190], it might also be interesting to use the present model to study the effect of age on arterial hemodynamics. Moreover, the development and adjustment of this kind of computer models could lead to a better understanding of some intensively studied, but poorly understood clinical situations such as exercise induced pulmonary haemorrhage.

5.5 CONCLUSIONS

A 1D computer model for the equine arterial circulation has been developed and this provided a unique anatomical dataset for horses. *Ex vivo* anatomical measurements were combined both with literature data and physiological information from ultrasound analysis in order to predict pressure and flow waveforms in the equine arterial tree by means of 1D modelling. The qualitative validation of the model was carried out by comparing the results with average flow velocities and pressures measured *in vivo* in horses. Despite its generic character and limitations, outcomes from the model showed plausible predictions of pressure and flow waveforms throughout the considered arterial tree. Simulated flow waveforms reproduce important features observed in ultrasound Doppler images, especially the oscillating pattern (most pronounced at the external iliac artery, median artery and common carotid artery). Adapting the model by taking into account gravity further improved predicted waveforms. Thanks to wave power analysis, the contours of the arterial flow profiles could be explained. Despite the shortcomings of *in vivo* measured pressures (aortic pressures measured under general anaesthesia with the horse in dorsal recumbent position), modelled pressure data seem in line with invasive measurements. We believe that the present model may be useful, not only to explain flow wave patterns in horses, but also to predict changes in flow profiles and local pressures as a result of strenuous exercise or altered arterial wall properties related to age, breed or gender.

III

Arterial ageing, hemodynamics and stiffness in middle-aged individuals: insights from the Asklepios study

Chapters

Chapter 6

Longitudinal changes of pulse wave velocity, input impedance parameters, and wave reflection indices: ten years of ageing in middle-aged subjects

The changes experienced by the arterial system due to the ageing process have been extensively studied but are incompletely understood. Within-subject patterns of changes in regards to input impedance and wave reflection parameters have not been assessed. The Asklepios study is a longitudinal population study including healthy (at onset) middle-aged subjects, with 974 males and 1052 females undergoing two rounds of measurements of applanation tonometry and ultrasound, 10.15 ± 1.40 years apart. Carotid-femoral pulse wave velocity (PWV), aortic input impedance, and wave reflection parameters were assessed, and linear mixed-effects (LME) models were used to evaluate their longitudinal trajectories and determinants. Overall, the effective 10-year increase in PWV was less than expected from first round cross-sectional data, and PWV was found to accelerate more in women than in men. Interestingly, the increase in PWV was not paralleled by a decrease in arterial volume compliance, particularly in younger males. The aortic root characteristic impedance decreased with age in younger subjects while it increased for the older subjects in the study. These changes suggest that

aortic dilation and elongation may play an important role determining the longitudinal age-related changes in impedance parameters in middle-age. Wave reflection decreased with ageing, whereas resistance increased in women and decreased in men. We conclude that the effective impact of ageing on arterial system properties, in a middle-aged population, is not well reflected by cross-sectional studies. Future studies should assess the interaction between geometric remodelling and wall stiffening as determinants of pulsatile hemodynamics. The content in this chapter has recently been published in *Hypertension* [201].

6.1 INTRODUCTION

The changes exhibited by the arterial system due to the ageing process have been extensively studied [7, 10, 38, 57, 202–205] but are incompletely understood. With advancing age, the aorta and major arteries of the arterial tree may endure a loss/degradation of elastin resulting in wall stiffening on one hand, and geometric remodelling on the other. Ageing has been reported to have a profound impact on aortic stiffness, dilatation and elongation, arterial input impedance, and pulsatile hemodynamics. Adverse pulsatile hemodynamic changes associated with ageing and various disease states play a central role in the pathogenesis of various cardiovascular diseases (CVDs) [2–4, 44, 53, 84, 206–208].

Most of what is known about the impact of age on arterial hemodynamics and arterial system properties is based on cross-sectional studies performed over the past few decades [10, 14, 209–212]. These studies have shown that arterial stiffness increases with age [10, 56, 58, 59, 213], and that stiffening is accelerated by CV risk factors [45, 210, 214] (diabetes and hypertension being the most important). Arterial stiffness is considered to quantify the cumulative impact of exposure of the CV system to risk factors and is a strong predictor of CV mortality and morbidity [45, 54].

Although valuable, cross-sectional analyses do not account for cohort effects, which could arise in people born at different times, and could exert an impact on arterial phenotypes independent of age. Cohort effects may occur due to early and mid-life exposures, survival bias, and epidemiological transitions affecting life trajectories of morbidity through lifestyle, environmental, and epigenetic changes [215]. If arterial stiffness is indeed an integrative marker of CV risk, the effective evolution of arterial stiffness within an individual or within the population may be quite different from what one would expect on the basis of historical cross-sectional data. Such data can only be obtained in longitudinal studies, where repeated measurements are acquired over time from the same subjects. Reference longitudinal studies, such as the Framingham Heart Study (FHS) [54, 60], the Baltimore Longitudinal Study of Ageing (BLSA) [61, 62], or the SardiNIA study [63], have previously reported on the impact of ageing on arterial stiffness (mainly PWV) and its association with CV risk factors.

Our group previously reported and documented cross-sectional data on arterial input impedance, PWV and wave reflection in 2026 seemingly healthy middle-aged individuals (age 35-55), free from overt CVD at study initiation (Asklepios study [65]). For both sexes, we found an increase with age in PWV, systemic vascular resistance (SVR), and parameters of wave reflection. Marked differences in aortic input impedance were found between men and women, while total aortic compliance was found as the main determinant of carotid pulse pressure (PP). The age-related increase in carotid-femoral PWV was not accompanied by an increase in arterial impedance, suggesting age-dependent mechanisms modulating the aortic cross-sectional area. After a period of about 10 years, follow-up measurements were repeated on the same individuals. The major aims of this study are (1) to examine the 10-year longitudinal evolution of aortic input impedance, carotid-femoral PWV and wave reflection indices within the same cohort; (2) to assess how these effective changes compare to what was anticipated from the cross-sectional perspective.

6.2 METHODS

6.2.1 Study population

This is a substudy of the Asklepios cohort study, which has been previously described in detail [15]. Between 2002 and 2004, noninvasive measurements of carotid blood pressure (BP; applanation tonometry) and aortic flow (ultrasound) were performed on 2524 apparently healthy, middle-aged subjects aged 35-55 years. Baseline cross-sectional data from this cohort were previously reported in 2026 subjects (1052 women and 974 men; visit 1) [65], who met the requirements to be included into the analysis. The same individuals, now aged 45-65 years old, were invited from 2013 to 2017 for a follow-up exam (visit 2; same single operator). To this call, 2252 returning volunteers (91% of the surviving subjects) had their second visit. On average, subjects were 10.15 ± 1.40 years older upon the second visit. The primary analyses in this study were performed on a sample of 2026 subjects included in the baseline study [65]. Basic analyses were limited to 1757 subjects (920 women and 837 men) with analysable data sets on both occasions (complete case analysis). The study protocol was approved by the ethical committee of the Ghent University Hospital, and all subjects gave written informed consent.

Exclusion criteria at baseline included antihypertensive and/or lipid lowering drug treatment, and incomplete data sets because of missing flow data,

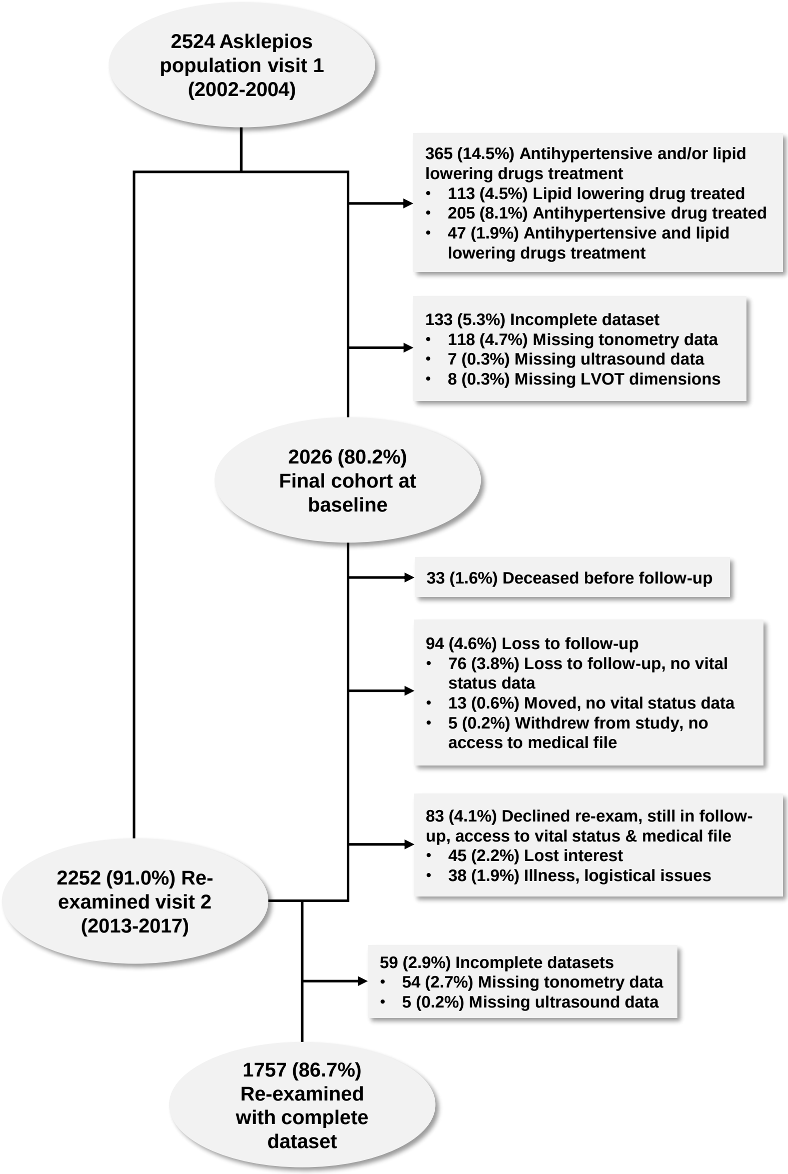

Figure 6.1: Flowchart of the Asklepios study – baseline and follow-up.

left ventricular outflow tract (LVOT) dimensions or noninvasive pressure measurements [65]. Of the 2026 subjects that formed the baseline cohort for our study on arterial hemodynamics and impedance, 33 died before follow-up, 94 were lost to follow-up, moved or withdrew from follow-up, and 83 declined re-exam because of loss of interest, illness, or logistical difficulties; an additional 59 presented incomplete data sets (n=54 inability and/or technical failure to accurately assess carotid tonometry, and n=5 missing flow data). Figure 6.1 shows a detailed flowchart of participants with available data at baseline and follow-up.

6.2.2 Measured and derived variables

The data acquisition protocol and methods for data processing have been previously described [65] (see also Figure 6.2). Briefly, anthropometric measurements of height, weight, distances from sternal notch to carotid, radial and femoral arteries were performed, and body mass index (BMI) and body surface area (BSA) were derived. To allow for direct comparison with the round 1 data and values published earlier, carotid-femoral PWV was estimated using the subtracted distance method, with the time delay obtained from the measured flow waveforms at these locations, as described previously in section 1.3.2.1. Before examinations, subjects were allowed 10-15 minutes of rest in a temperature-controlled environment.

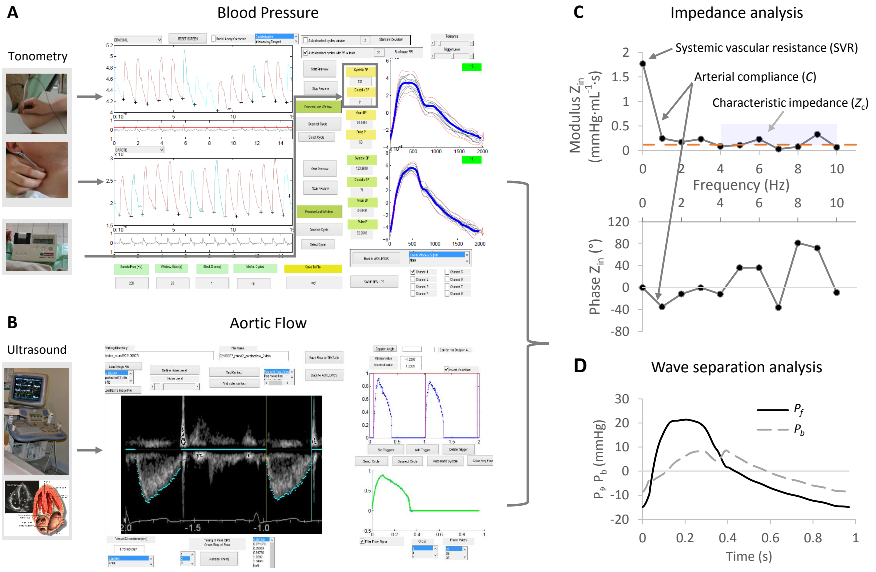

Figure 6.2: Scheme of the measurement protocol and data processing in a dedicated Matlab software interface. (A) Carotid artery pressure waveform is obtained from calibrated brachial and carotid applanation tonometry. (B) Pulsed Doppler measurement of blood flow velocity in the left ventricular outflow tract, together with LVOT cross-sectional area, yields central blood flow waveform. (C) From the time-aligned pressure and flow signals input impedance modulus and phase angle are derived. (D) Linear wave separation theory allows to separate the pressure wave into a forward (P_f) and a backward (P_b) component.

6.2.2.1 *Noninvasive assessment of blood pressure and aortic flow*

Blood pressure waveforms were acquired noninvasively at the left brachial artery by using applanation tonometry (SPT 301, Millar Instruments, Houston, Texas, USA), and the signal was calibrated based on oscillometric brachial systolic (SBP) and diastolic (DBP) blood pressure. Mean arterial pressure (MAP) was derived as the numerical average of the calibrated brachial pressure waveform. Tonometry was also performed at the left common carotid artery. Further calibration was based on brachial pressure, assuming that DBP and MAP remain approximately constant in the whole body.

Aortic flow velocity waveforms and LVOT dimensions were assessed using ultrasound (Vivid 7 for the baseline visit; Vivid E9 for the follow-up visit, GE Vingmed Ultrasound, Horten, Norway). LVOT area was calculated assuming circularity. Flow velocity images were processed off-line within a dedicated software interface written in Matlab (Mathworks, Natick, MA, USA), and were combined with the LVOT cross-sectional areas to obtain the aortic flow waveforms (Q). Stroke volume (SV) was derived by integration of Q, and cardiac output (CO) as the product of SV and HR. Signals of pressure (P) and Q were carefully time-aligned.

6.2.2.2 *Derivation of input impedance and wave reflection parameters*

Input impedance (Z_{in}) was derived from the time-aligned pressure and flow waveforms after decomposing in harmonics, with the modulus being estimated as the ratio of both signals harmonics and the phase angle as their difference (section 1.4). Characteristic impedance (Z_{c}) was then assessed by averaging the modulus of harmonics 3 to 10, with exclusion of values higher than 3 times the median value of Z_{in} over that range of harmonics. The modulus of Z_{in} at 0 Hz equals SVR. Total arterial compliance was estimated using the pulse pressure method (C_{PPM}) [116]. The reflection coefficient was calculated as $\Gamma = \frac{(Z_{\text{in}} - Z_{\text{c}})}{(Z_{\text{in}} + Z_{\text{c}})}$ and reported as the amplitude at the heart frequency ($|\Gamma_1|$). The pressure signal was separated into its forward and backward components ($P_f = (P + Z_{\text{c}} \cdot Q)/2$ and $P_b = (P - Z_{\text{c}} \cdot Q)/2$, respectively), and the reflection magnitude was derived from the ratio of the amplitudes of P_b and P_f ($|P_b|/|P_f|$). Reflected wave transit time (RWTT) was derived from wave separation analysis (WSA), as the time delay between the zero crossings of the reflected and forward pressure waves.

6.2.3 Statistical methods

General characteristics of the study population are presented as mean ± standard deviation (SD) for normally-distributed variables, median (interquartile range) for non-normally distributed variables, and counts (percentages) for categorical variables. In the figures with observed data, standard errors of the mean (SEM) are displayed. Subjects were classified into half-decades of age (35-40, 41-45, 46-50, and 51-56 years) based upon age at baseline. Differences between sex and examination visits were tested from t-tests in the basic analysis. Moreover, analyses of variance (ANOVA) and covariance (ANCOVA) were performed for all the variables of interest, accounting for the repeated measures by subjects. The categorical variables age, sex, visit, and their interaction terms were included in the models. Height, weight and MAP were considered as covariates when applicable.

In addition, for a better comprehension of the longitudinal relationships among variables, LME analyses were performed [216]. LME models are regression models that account for fixed as well as random effects. The random effects term allows to take into account the non-independence in the data, as occurs in longitudinal studies where there are repeated measurements per subject over time. LME analyses make use of the full dataset to model the population-average variability in the response variable while accounting for group-specific variability. These models are also flexible to accommodate unbalanced data. A random intercept structure of the random effects allows to model group-specific deviations from the average, whereas a random slope structure accounts for different effects of a covariate on different groups.

Data were assumed to be missing at random, and consequently the analyses also included those participants with only baseline observations. Mixed-effects models in combination with the missing at random assumption have been shown to provide robust estimates, even when data are actually missing not at random [216, 217]. A comparison of baseline characteristics between the group with complete dataset and the group with missing data at follow-up can be seen in Table 6.1. Models describing the effects on PWV, BP variables, impedance, and wave reflection parameters were constructed. Age at baseline (Entry-Age) and follow-up time (Time), are considered as fixed effects in all models [218], and as random effects, we had random intercepts for subjects in simpler models, as well as by-subject random slopes for the effect of time in more complex models. In these models, baseline and follow-up measurements were used for the dependent as well as the independent variables. Time and its interaction terms in mixed-effects models, account for the longitudinal changes on the response variable. Correlation analysis was used to identify significant relationship among variables of interest that were further considered as potential covariates in the mixed-effects models (see the correlation matrix in Figure B.1 of the Appendix B). Sex, HR, height, weight, and the previously mentioned dependent variables (when applicable), were included as potential covariates. Age-squared terms were also added to models to better capture the observed differences associated with older age, with age terms centered to reduce collinearity. The estimated variance inflation factor was lower than 10. Selection of significant independent factors was obtained by likelihood ratio test. Sex-specific models were considered when the factor sex was found significant. Residual plots were visually inspected to check for deviations from homoscedasticity or normality, and the correlation between predicted and observed data was used as a measure of model quality (see Figures B.2-B.8 in Appendix B). An estimation of the explained variance (R^2) for mixed-effects models was derived as described in [219, 220]. As an alternative to assuming a normal distribution of the dependent variable, generalized LME models were also considered assuming a gamma distribution and the logarithmic function as the link function. P-values < 0.05 were considered statistically significant. All analyses were done using Matlab (Mathworks, Natick, MA, USA). In the results and figures, observed data (and ANOVA or ANCOVA) as well as data predicted from the mixed-effects model analysis will be presented side by side when relevant.

Table 6.1: Baseline characteristics of subjects with complete dataset and subjects with missing data at follow-up.

	Complete dataset (N=1757)	Missing data (N=269)	P-value
Women, %	52.36	49.07	0.3143
Age, years	45.13 (40.6-49.8)	45.06 (40.1-50.8)	0.6043
Height, cm	169.47 ± 8.75	169.21 ± 9.15	0.6489
Weight, kg	71.1 (62.1-81.4)	72.9 (63.7-84.2)	0.0144
BMI, kg/m^2	24.7 (22.5-27.1)	25.5 (22.8-28.3)	0.0005
BSA, m^2	1.83 ± 0.20	1.85 ± 0.21	0.1252
SBP_{CA}, mmHg	129 ± 16.07	132 ± 15.43	0.0244
DBP, mmHg	76 ± 10.73	79 ± 10.16	0.0010
MAP, mmHg	99 ± 11.82	102 ± 11.41	0.0027
PP_{CA}, mmHg	53 ± 11.30	53 ± 10.87	0.9325
HR, bpm	63.28 ± 9.07	66.13 ± 10.47	2.94E-06
SV, mL	78.21 ± 18.09	78.85 ± 19.33	0.5923
CO, L/min	4.89 ± 1.10	5.15 ± 1.22	0.0006
LVOT area, cm^2	3.27 ± 0.69	3.28 ± 0.71	0.7426
Diabetes, %	0.74	1.49	0.2110
Obesity, %	9.39	17.84	2.56E-05
Overweight, %	36.99	36.06	0.7671
Active smoker, %	18.33	31.23	8.56E-07
Ex-smoker, %	27.26	24.54	0.3476
Weekly alcohol intake, u/week	10 (5-21)*	12 (6-24)*	0.0189
Education beyond secondary school, %	39.61*	30.86*	0.0226

Data are expressed as mean ± SD, median (interquartile range) or percent. BMI: body mass index; BSA: body surface area; DBP: diastolic blood pressure; MAP: mean arterial pressure; SBP_{CA} and PP_{CA}: carotid systolic and pulse pressure; HR: heart rate; SV: stroke volume; CO: cardiac output; LVOT: left ventricular outflow tract. P<0.05 significant differences comparing groups by using Student t-test for continuous variables and a chi-square test for categorical variables. *Missing values.

6.3 RESULTS

6.3.1 Basic clinical data and hemodynamic parameters

Basic clinical data and hemodynamic parameters of the study cohort at baseline and follow-up, stratified by sex and age group, are shown in Table 6.2. Females exhibited lower height, weight, BMI and BSA than males. BMI increased from one examination visit to the other, both in men and in women. SV and CO were also significantly lower in women ($P < 0.001$), whereas HR was higher in women than in men. None of these three hemodynamic variables varied with age over the studied ranges (cross-sectional observations), but CO and SV increased or tended to increase, comparing baseline data with measurements at follow-up (10-year period). LVOT cross-sectional area increased significantly between examination visits for both females and males; the area was lower for females compared to males and showed a decrease from younger to older groups, as observed from the cross-sectional studies.

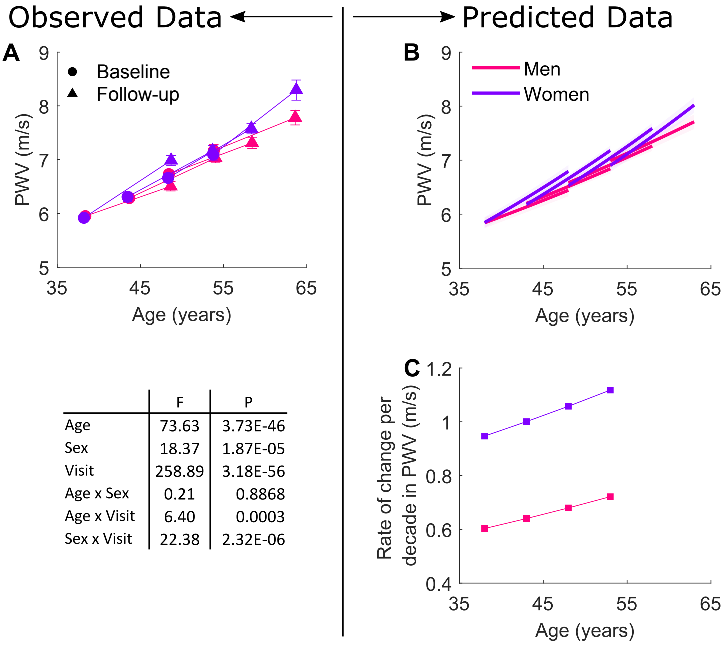

	F	P
Age	73.63	3.73E-46
Sex	18.37	1.87E-05
Visit	258.89	3.18E-56
Age x Sex	0.21	0.8868
Age x Visit	6.40	0.0003
Sex x Visit	22.38	2.32E-06

Figure 6.3: Observed (A) and predicted (B) longitudinal trajectories in PWV per sex and age strata. Shaded area represents the nonsimultaneous 95% CIs. (C) Model-predicted rate of change per decade in PWV for men and women. The plots of the predictions refer to models in Table 6.4. The P and F values in the table indicate the statistical significance of the factors age, sex, visit, and their interaction in the ANCOVA, where PWV was adjusted for MAP. Values of the observations are mean ± SEM.

Table 6.2: Basic clinical data and hemodynamic parameters of the complete case cohort at baseline (V1) and follow-up (V2). A1, A2, A3, and A4 indicate the age groups 35-40, 41-45, 46-50, and 51-56 years, respectively.

Parameter	Men (N=837)				Women (N=920)			
	A1	A2	A3	A4	A1	A2	A3	A4
N	226	230	212	169	269	256	214	181
Follow-up time, y	9.8 (9.1–11.1)	10 (9.3–11.2)	9.6 (8.9–10.5)	9.6 (9–10.3)	10.1 (9–11.8)	9.9 (9.2–11)	9.7 (9–10.6)	9.8 (9.1–10.6)
Age, y								
V1	38.4 (37–39.9)	43.7 (42.4–45)	48.4 (47.1–49.5)	53.9 (52.3–55.3)	38.4 (36.9–39.7)	43.4 (42–44.8)	48.3 (47.1–49.6)	53.5 (52.2–55)
V2	48.7 (46.9–50.2)*	54.1 (52.4–55.3)*	58.2 (56.8–59.6)*	63.7 (61.9–65.1)*	48.8 (47–50.4)*	53.6 (52–54.9)*†	58.2 (56.9–59.6)*	63.9 (62–65.2)*
Height, cm								
V1	177.6±6.63	175.9±6.10	175.4±6.73	174.5±6.23	164.8±5.89†	164.3±6.15†	162.8±5.65†	161.7±5.47†
V2	177.0±6.55*	175.4±5.98*	174.7±6.55*	173.5±6.28*	164.6±5.81*†	163.7±6.14*†	161.9±5.55*†	160.7±5.49*†
Weight, kg								
V1	79.5 (72.2–87)	80 (71.8–87)	81 (72.5–88.7)	79.2 (74.1–84.3)	63.2 (58–70)†	62.9 (57.8–69.5)†	63.4 (58.4–70.5)†	63.3 (56.7–71.1)†
V2	82.9 (74.6–90.5)*	82.5 (75–89.7)*	82.1 (75.2–91.6)*	80.7 (74.4–87.2)*	68.3 (60.5–76.6)*†	66.6 (60.3–73.7)*†	66.1 (59.8–73.9)*†	66 (59.6–73.3)*†
BMI, kg/m²								
V1	25 (23.2–27.1)	25.6 (23.6–27.7)	26.2 (24.1–28.6)	26 (24–27.8)	23 (21–25.7)†	23.3 (21.5–25.6)†	23.9 (22.3–26.1)†	24 (22.2–27.2)†
V2	26.2 (24.1–28.6)*	26.5 (24.4–29)*	26.9 (24.9–29.1)*	26.6 (24.6–29.1)*	24.5 (22.3–28.2)*†	24.8 (22.3–27.2)*†	24.7 (22.6–28.3)*†	25.4 (22.9–28)*†
BSA, m²								
V1	1.98±0.15	1.96±0.15	1.97±0.15	1.94±0.13	1.71±0.14†	1.70±0.15†	1.70±0.14†	1.69±0.14†
V2	2.01±0.17*	1.99±0.15*	1.99±0.16*	1.95±0.14	1.76±0.16*†	1.74±0.15*†	1.72±0.14*†	1.70±0.14*†
SBP, mmHg								
V1	130 (123–137)	132 (124–140)	134 (124–143)	134 (124.8–144.3)	121 (114–132)†	125 (116–135)†	128 (120–138)†	134 (123–146)
V2	132 (124–143.6)*	136 (128–146)*	137 (128–145.5)*	136 (128–144)	132 (119.8–146)*	132 (120.7–145)*†	137 (124–147.8)*	139 (126–151.5)*
DBP, mmHg								
V1	74±9.39	77±10.7	79±9.82	79±12.1	74±10.9	75±10.7†	76.0±10.1†	78±10.9
V2	82±10.6*	84±10.2*	82±10.6*	79±9.44	81±10.2*	80±9.96*†	81±9.09*	79±10.0*
MAP, mmHg								
V1	97±9.29	100±11.3	102±10.9	103±13.6	95±11.7	98±11.8	100±11.5†	103±12.6
V2	103±12.0*	105±12.3*	104±12.2*	102±11.0	103±12.5*	102±12.2*†	104±11.8*	104±12.3

Continued on Next Page…

Table 6.2: (Continued)

Parameter	Men (N=837)				Women (N=920)			
	A1	A2	A3	A4	A1	A2	A3	A4
SBP_{CA}, mmHg								
V1	126±11.6	129±13.9	131±13.9	134±17.9	123±14.8†	127±16.4	131±16.4	137±19.7
V2	132±16.1*	136±18.0*	136±16.5*	136±16.8	133±18.6*	133±18.8*	138±18.9*	140±20.5†
PP_{CA}, mmHg								
V1	52.0±9.93	51.5±8.50	51.8±9.49	55.1±11.8	49.3±9.15†	51.7±11.0	54.9±12.4†	59.1±15.6†
V2	50.1±10.6	52.3±12.6	54.3±10.8*	56.3±12.8	51.8±12.4*	52.8±13.2	57.2±14.1†	61.7±17.2†
HR, bpm								
V1	60.8±8.39	60.2±8.68	62.5±9.49	61.1±9.33	65.1±9.24†	65.9±8.93†	64.7±8.46†	65.1±7.94†
V2	61.8±9.51	60.9±8.66	62.1±9.28	60.6±9.52	65.4±8.55†	64.5±8.86*†	63.1±7.91*	63.7±7.72*†
SV, mL								
V1	87.0±17.8	87.8±19.4	85.6±17.7	86.7±18.1	70.5±13.0†	70.8±14.4†	70.5±13.0†	69.5±15.3†
V2	91.6±18.6*	92.4±18.9*	91.6±20.5*	90.6±20.2	74.5±14.8*†	73.2±15.7*†	72.3±15.3†	73.3±17.2*†
CO, L/min								
V1	5.23±1.04	5.23±1.17	5.30±1.13	5.26±1.16	4.55±0.91†	4.65±1.07†	4.53±0.90†	4.49±0.98†
V2	5.59±1.13*	5.58±1.14*	5.66±1.44*	5.44±1.31	4.83±0.98*†	4.68±1.01†	4.54±1.02†	4.63±1.07†
LVOT area, cm^2								
V1	3.80±0.60	3.73±0.60	3.70±0.59	3.70±0.59	2.87±0.44†	2.85±0.49†	2.82±0.42†	2.82±0.43†
V2	4.02±0.63*	3.91±0.67*	3.86±0.69*	3.79±0.62*	3.05±0.47*†	2.99±0.49*†	2.98±0.49*†	2.99±0.48*†

Data are expressed as mean ± SD or median (interquartile range). BMI indicates body mass index; BSA, body surface area; CO, cardiac output; DBP, diastolic blood pressure; HR, heart rate; LVOT, left ventricular outflow tract; MAP, mean arterial pressure; SBP, brachial systolic blood pressure; SBP_{CA} and PP_{CA}, carotid systolic and pulse pressure; and SV, stroke volume.

*P<0.05 testing whether the difference between visits was statistically significant per sex and age category.

†P<0.05 testing whether the difference between sexes was statistically significant per visit and age category.

Table 6.3: Generalized LME model of the longitudinal effects on PWV for the entire cohort. The correlation coefficient between observed and predicted values and the conditional R^2 are reported.

Variables	Estimate	SE	P-value
Intercept	1.8431	0.0074	0.0000
Sex (Men)	0.0059	0.0086	0.4933
Time	0.0140	0.0009	2.32E-51
Entry-Age	0.0115	0.0007	7.85E-54
$(\text{Entry-Age})^2$	0.0001	0.0001	0.2685
Sex (Men)×Time	-0.0028	0.0013	0.0256
Entry-Age×Time	-6.87E-05	0.0001	0.5177
$(\text{Entry-Age})^2$×Time	2.85E-05	1.78E-05	0.1092
Sex (Men)×Entry-Age×Time	0.0001	0.0001	0.3761
Sex (Men)×$(\text{Entry-Age})^2$× Time	-6.79E-05	2.42E-05	0.0050
R (Obs. vs. Pred.)		0.826	
R^2		0.880	

Table 6.4: Generalized LME model of the longitudinal effects on PWV for groups of men and women.

	Men			Women		
Variables	Estimate	SE	P-value	Estimate	SE	P-value
Intercept	1.8555	0.0060	0.0000	1.8448	0.0061	0.0000
Time	0.0098	0.0007	2.88E-46	0.0150	0.0007	4.06E-91
Entry-Age	0.0120	0.0009	7.40E-41	0.0111	0.0009	3.82E-36
Entry-Age×Time	-	-	-	-	-	-
R (Obs. vs. Pred.)		0.844			0.812	
R^2		0.865			0.886	

6.3.2 Pulse wave velocity and blood pressure indices

PWV, adjusted for MAP, increased significantly between examination visits with differences by age group and sex ($P<0.001$; Figure 6.3). Basic mixed-effects models for the effects on PWV were first constructed for all subjects, including entry-age, $(\text{entry-age})^2$, time, sex, and their interaction terms (see Table 6.3). The average effect of entry-age on PWV was sex-independent, but longitudinally there were significant differences by sex that accelerate at older age, as shown for the significant interaction term (Sex×$(\text{Entry-Age})^2$×Time). Models were then constructed for men and women separately (Table 6.4). From these models, the predicted longitudinal trajectories with 95% confidence intervals (CIs) and rates of change of PWV per decade were plotted by

Table 6.5: Generalized LME models of the longitudinal effects on PWV for men and women, including HR, height, weight, and SBP_{CA} as covariates.

	Men			**Women**		
Variables	Estimate	SE	P-value	Estimate	SE	P-value
Intercept	0.9766	0.0502	1.30E-76	0.9422	0.0507	4.18E-71
Weight	0.0005	0.0004	0.2821	0.0008	0.0004	0.0188
SBP_{CA}	0.0040	0.0003	8.44E-51	0.0050	0.0002	3.35E-97
HR	0.0052	0.0004	3.00E-32	0.0031	0.0006	2.45E-07
Time	-0.0011	0.0043	0.8053	-0.0032	0.0053	0.5412
Entry-Age	-0.0015	0.0056	0.7916	0.0069	0.0009	3.25E-14
SBP_{CA}×Entry-Age	8.67E-05	4.24E-05	0.0412	-	-	-
Weight×Time	0.0001	5.16E-05	0.0438	-	-	-
HR×Time	-	-	-	0.0002	8.02E-05	0.0036
Entry-Age×Time	-	-	-	0.0002	0.0001	0.0467
R (Obs. vs. Pred.)		0.836			0.806	
R^2		0.928			0.941	

Table 6.6: Generalized LME models of the longitudinal effects on PWV for men and women, including HR, height, weight, and DBP as covariates.

	Men			**Women**		
Variables	Estimate	SE	P-value	Estimate	SE	P-value
Intercept	1.1419	0.0469	2.71E-113	1.1630	0.0468	2.19E-118
Weight	0.0002	0.0005	0.6863	-	-	-
DBP	0.0057	0.0004	3.12E-42	0.0077	0.0004	5.40E-72
HR	0.0041	0.0005	3.08E-19	0.0015	0.0006	0.0215
Time	-0.0019	0.0043	0.6676	-0.0024	0.0054	0.6562
Entry-Age	0.0096	0.0009	5.41E-25	0.0093	0.0009	9.01E-23
$(\text{Entry-Age})^2$	-	-	-	0.0001	0.0002	0.3568
Entry-Age×Time	0.0003	0.0001	0.0078	0.0003	0.0001	0.0130
$(\text{Entry-Age})^2$×Time	-	-	-	3.19E-05	1.90E-05	0.0927
HR×Time	-	-	-	0.0002	8.18E-05	0.0121
Weight×Time	0.0001	0.0001	0.0376	-	-	-
R (Obs. vs. Pred.)		0.836			0.810	
R^2		0.922			0.932	

sex and age group at baseline (Figure 6.3B and 6.3C); the predicted rate of change in PWV for subjects between 35 and 55 years increased around 18%, with higher values for women in all age categories. In women, the 10-year change in PWV increases from 0.95 m/s per 10 yr in the youngest group to 1.12 m/s per 10 yr in the oldest group.

Tables 6.5-6.8 show the estimates for final fitted generalized LME models of the effects on PWV after the inclusion of potential covariates (HR, weight,

Table 6.7: Generalized LME models of the longitudinal effects on PWV for men and women, including HR, height, weight, and PP_{CA} as covariates.

	Men			Women		
Variables	Estimate	SE	P-value	Estimate	SE	P-value
Intercept	1.1483	0.0446	1.92E-124	1.2188	0.0554	6.09E-96
Weight	0.0017	0.0004	4.09E-06	0.0019	0.0004	7.33E-07
PP_{CA}	0.0033	0.0004	1.64E-18	0.0040	0.0005	2.47E-18
HR	0.0064	0.0005	2.25E-43	0.0045	0.0006	4.43E-12
Time	0.0088	0.0007	1.43E-39	-0.0092	0.0067	0.1693
Entry-Age	0.0009	0.0034	0.8019	0.0085	0.0008	8.75E-26
PP_{CA}×Entry-Age	0.0002	6.23E-05	0.0034	-	-	-
PP_{CA}×Time	-	-	-	0.0002	5.46E-05	0.0053
HR×Time	-	-	-	0.0002	8.47E-05	0.0069
R (Obs. vs. Pred.)		0.835			0.803	
R^2		0.914			0.930	

Table 6.8: Generalized LME models of the longitudinal effects on PWV for men and women, including HR, height, weight, and MAP as covariates.

	Men			Women		
Variables	Estimate	SE	P-value	Estimate	SE	P-value
Intercept	0.9700	0.0437	1.46E-96	1.0018	0.0475	3.13E-89
Weight	0.0007	0.0004	0.0657	-	-	-
MAP	0.0059	0.0004	8.08E-55	0.0076	0.0003	1.13E-98
HR	0.0039	0.0004	4.16E-18	0.0014	0.0006	0.0219
Time	0.0075	0.0006	1.43E-30	-0.0013	0.0052	0.7971
Entry-Age	0.0092	0.0009	1.58E-23	-0.0014	0.0055	0.8007
Entry-Age×Time	0.0003	0.0001	0.0178	0.0002	0.0001	0.0296
HR×Time	-	-	-	0.0002	7.97E-05	0.0083
MAP×Entry-Age	-	-	-	9.38E-05	5.41E-05	0.0830
R (Obs. vs. Pred.)		0.837			0.814	
R^2		0.928			0.940	

height, and BP variables). There was a cross-sectional independent association of carotid systolic blood pressure (SBP_{CA}), DBP, or MAP with PWV, but longitudinal associations were not significant. However, carotid pulse pressure (PP_{CA}) was associated with the longitudinal increase in PWV over time in women. Additional models (Tables 6.9-6.12) explore the effects of PWV on the longitudinal changes of BP indices. Higher PWV was associated with lower longitudinal trajectories in all BP variables except for PP_{CA}, for both men and women.

Table 6.9: LME models of the longitudinal effects on SBP_{CA} for groups of men and women, with PWV, HR, weight and height as covariates.

	Men			Women		
Variables	Estimate	SE	P-value	Estimate	SE	P-value
Intercept	153.4416	10.9147	1.24E-42	133.7518	12.5086	5.73E-26
Height	-0.4048	0.0648	5.16E-10	-0.3170	0.0740	1.90E-05
Weight	0.2310	0.0339	1.23E-11	0.1986	0.0352	1.85E-08
PWV	4.5068	0.3291	1.22E-40	5.6991	0.3333	3.72E-61
HR	-	-	-	-0.0421	0.0508	0.4076
Time	0.8875	0.2988	0.0030	2.0918	0.4823	1.52E-05
Entry-Age	0.0628	0.0748	0.4010	0.3483	0.0813	1.92E-05
$(\text{Entry-Age})^2$	0.0034	0.0120	0.7786	-	-	-
Entry-Age×Time	-0.0105	0.0099	0.2894	-0.0276	0.0098	0.0050
$(\text{Entry-Age})^2\times$Time	-0.0032	0.0016	0.0489	-	-	-
PWV×Time	-0.0933	0.0418	0.0257	-0.1371	0.0379	0.0003
HR×Time	-	-	-	-0.0163	0.0070	0.0189
R (Obs. vs. Pred.)		0.938			0.927	
R^2		0.672			0.668	

Table 6.10: LME models of the longitudinal effects on DBP for groups of men and women, with PWV, HR, weight and height as covariates.

	Men			Women		
Variables	Estimate	SE	P-value	Estimate	SE	P-value
Intercept	72.1116	7.5564	4.42E-21	64.9088	7.0789	1.18E-19
Height	-0.2476	0.0433	1.29E-08	-0.2163	0.0421	3.05E-07
Weight	0.1957	0.0224	4.86E-18	0.2131	0.0199	3.86E-26
PWV	3.3439	0.2438	9.42E-41	3.3234	0.2073	1.99E-54
HR	0.1920	0.0250	2.59E-14	0.1682	0.0251	2.75E-11
Time	1.2637	0.1868	1.81E-11	1.1286	0.1530	2.39E-13
Entry-Age	0.6096	0.1724	0.0004	0.3456	0.1395	0.0133
Entry-Age×Time	-0.0215	0.0064	0.0007	-0.0163	0.0059	0.0058
PWV×Time	-0.1547	0.0270	1.13E-08	-0.1421	0.0218	8.56E-11
PWV×Entry-Age	-0.0950	0.0257	0.0002	-0.0642	0.0203	0.0016
R (Obs. vs. Pred.)		0.963			0.97	
R^2		0.747			0.770	

6.3.3 Input and characteristic impedance, systemic vascular resistance, and total arterial compliance

Figure 6.4 shows the modulus (logarithmic scale) and phase angle of Z_{in}, divided by age category and sex. Comparing between visits, women that entered the study at a younger age (35 to 45 years), had a significant decrease in the modulus of Z_{in} in the high-frequency range (harmonics 4 and 5 for A1 and 4 to 7 for A2). Men had also a significant decrease in the modulus of Z_{in} for the youngest group, in the low and high frequency range (harmonics 1, 3-5 and 7), and for subjects that entered the study in their forties in harmonics 4-5, while there was a significant increase in harmonics 9-10 only for A2. In the oldest group of males and females, differences between examination visits were mostly non-significant. After correcting for height and weight, the age and sex effects had significant effects on the modulus of Z_{in} for harmonics 1 to 7, while visit and the interaction term between age and sex were significant for harmonics 1 to 5. The phase angle also showed higher differences between examination visits mainly for high frequencies (Figure 6.4B and 6.4D).

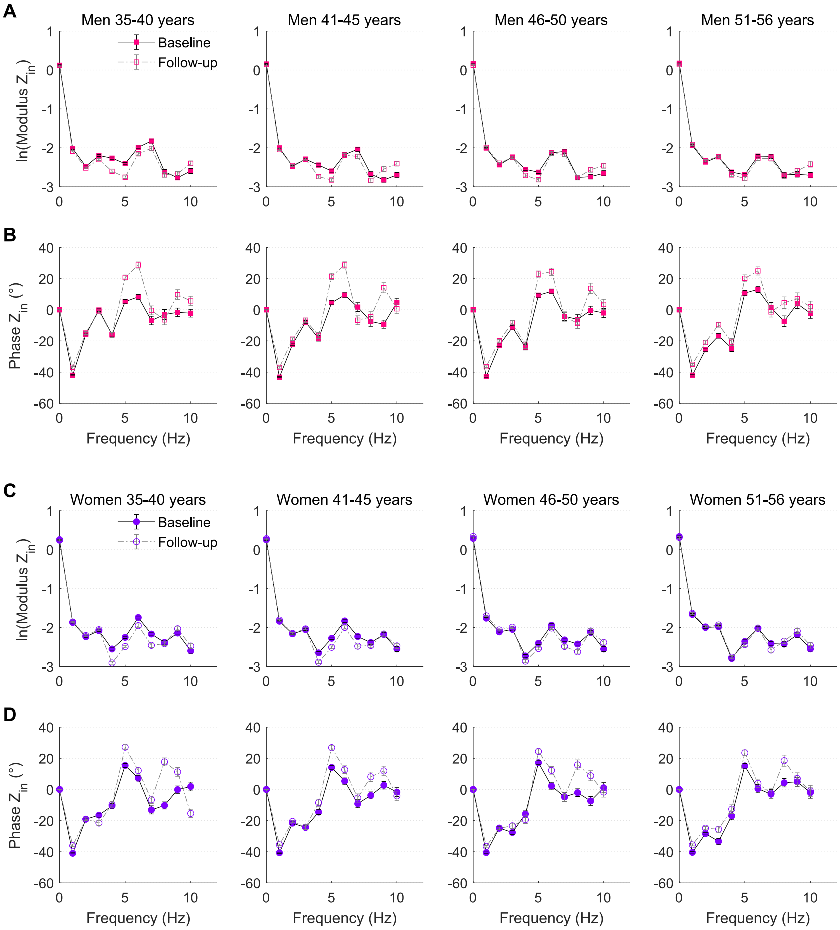

Figure 6.4: Logarithmic transformed modulus (A and C) and phase angle (B and D) of Z_{in} for males (top) and females (bottom) at both visits. Data are presented in stratum per age category.

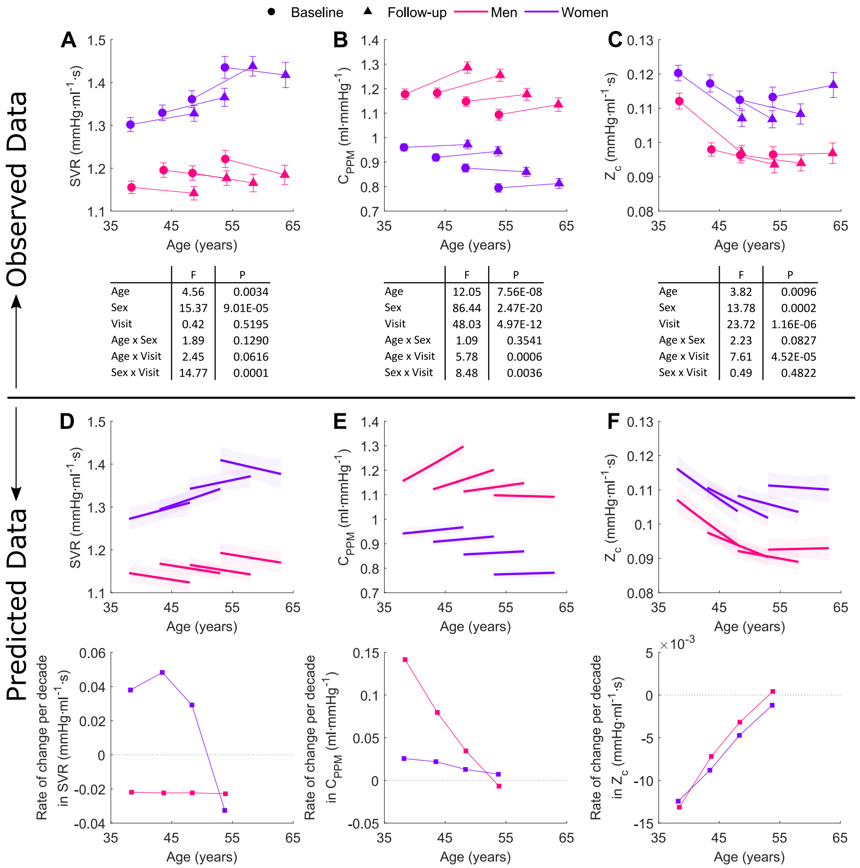

	F	P
Age	4.56	0.0034
Sex	15.37	9.01E-05
Visit	0.42	0.5195
Age x Sex	1.89	0.1290
Age x Visit	2.45	0.0616
Sex x Visit	14.77	0.0001

	F	P
Age	12.05	7.56E-08
Sex	86.44	2.47E-20
Visit	48.03	4.97E-12
Age x Sex	1.09	0.3541
Age x Visit	5.78	0.0006
Sex x Visit	8.48	0.0036

	F	P
Age	3.82	0.0096
Sex	13.78	0.0002
Visit	23.72	1.16E-06
Age x Sex	2.23	0.0827
Age x Visit	7.61	4.52E-05
Sex x Visit	0.49	0.4822

Figure 6.5: Top: Observed changes between baseline and follow-up measurements in SVR (A), C_{PPM} (B), and Z_c (C) per sex and age strata. Values are mean ± SEM. The P and F values in the table indicate the statistical significance of the factors age, sex, visit, and their interaction in the ANCOVA, where the three parameters were adjusted for height and weight; C_{PPM} and Z_c additionally for MAP. Bottom: Model-predicted longitudinal trajectories and rates of change per decade in SVR (D), C_{PPM} (E), and Z_c (F) per sex and age strata. Shaded area represents the non-simultaneous 95% CIs. The plots refer to models in Tables 6.13, 6.14 and 6.15.

The observed changes between examination visits, of parameters describing the impedance patterns (ie., C_{PPM}, SVR and Z_c) are shown in Figure 6.5A through 6.5C. Basic analysis of the complete dataset showed that SVR, adjusted for height and weight, was significantly different for men and women (P<0.001), with women presenting higher values per visit (Figure 6.5A). In males, and females in the oldest category, there was a longitudinal decrease in SVR rather than an increase. C_{PPM} showed an unexpected increase from baseline to follow-up (Figure 6.5B), with significant differences of visit by

Table 6.11: LME models of the longitudinal effects on PP_{CA} for groups of men and women, with PWV, HR, weight and height as covariates.

	Men			**Women**		
Variables	Estimate	SE	P-value	Estimate	SE	P-value
Intercept	80.6319	8.0216	3.72E-23	58.4179	11.1176	1.65E-07
Height	-0.1490	0.0430	0.0005	-0.0439	0.0635	0.4891
PWV	1.8778	0.1991	1.22E-20	2.6654	0.1831	1.16E-45
HR	-0.2274	0.0289	5.71E-15	-0.2438	0.0427	1.30E-08
Time	-0.0732	0.0441	0.0975	3.7871	1.3272	0.0044
Entry-Age	0.0296	0.0600	0.6211	0.3591	0.0555	1.19E-10
$(\text{Entry-Age})^2$	-	-	-	0.0193	0.0087	0.0264
Entry-Age×Time	0.0180	0.0073	0.0142	-	-	-
Height×Time	-	-	-	-0.0185	0.0076	0.0143
HR×Time	-	-	-	-0.0132	0.0056	0.0178
R (Obs. vs. Pred.)		0.756			0.786	
R^2		0.332			0.430	

Table 6.12: LME models of the longitudinal effects on MAP for groups of men and women, with PWV, HR, weight and height as covariates.

	Men			**Women**		
Variables	Estimate	SE	P-value	Estimate	SE	P-value
Intercept	101.881	8.2611	1.39E-33	92.1053	8.2579	4.80E-28
Height	-0.3024	0.0476	2.60E-10	-0.2717	0.0493	4.00E-08
Weight	0.2208	0.0246	7.07E-19	0.2233	0.0232	1.67E-21
PWV	3.5366	0.2436	3.38E-45	3.9987	0.2204	4.43E-68
HR	0.1893	0.0271	4.17E-12	0.1657	0.0288	1.03E-08
Time	0.8710	0.2005	1.48E-05	1.0480	0.1691	6.98E-10
Entry-Age	0.0332	0.0549	0.5451	0.0642	0.0548	0.2418
$(\text{Entry-Age})^2$	-0.0170	0.0080	0.0333	-	-	-
Entry-Age×Time	-0.0243	0.0067	0.0003	-0.0221	0.0061	0.0003
PWV×Time	-0.1164	0.0287	5.17E-05	-0.1456	0.0238	1.10E-09
R (Obs. vs. Pred.)		0.931			0.916	
R^2		0.690			0.670	

age and sex ($P<0.01$). Z_c on the other hand, decreased significantly between examination visits, with less pronounced changes and even a slight increase for the oldest (Figure 6.5C), but the changes between visit were not different by sex.

Generalized LME models of the longitudinal effects on SVR, C_{PPM}, and Z_c for men and women can be found in Tables 6.13 through 6.15, with plots of residuals and correlations in the Appendix B (Figures B.2-B.4). In men,

Table 6.13: Generalized LME models of the longitudinal effects on SVR for men and women, including covariates.

	Men			**Women**		
Variables	Estimate	SE	P-value	Estimate	SE	P-value
Intercept	1.7469	0.1745	5.30E-23	2.1644	0.1720	5.38E-35
Height	-0.0061	0.001	2.38E-09	-0.0074	0.0010	1.18E-12
Weight	-0.0020	0.0005	0.0001	-0.0031	0.0006	4.88E-08
HR	-0.0056	0.0006	9.96E-24	-0.0073	0.0006	2.52E-33
Time	-0.0019	0.0008	0.0101	-0.0075	0.0042	0.0723
Entry-Age	0.0150	0.0059	0.0107	0.0042	0.0011	0.0002
(Entry-Age)^2	-	-	-	0.0003	0.0002	0.1220
Entry-Age×Time	-	-	-	-0.0003	0.0001	0.0165
(Entry-Age)^2×Time	-	-	-	-5.13E-05	2.09E-05	0.0142
Weight×Time	-	-	-	0.0002	6.07E-05	0.0076
HR×Entry-Age	-0.0002	9.41E-05	0.0152	-	-	-
R (Obs. vs. Pred.)		0.887			0.892	
R^2		0.360			0.406	

Table 6.14: Generalized LME models of the longitudinal effects on C_{PPM} for men and women, including covariates.

	Men			**Women**		
Variables	Estimate	SE	P-value	Estimate	SE	P-value
Height	0.0036	0.0004	6.64E-17	0.0031	0.0004	3.85E-13
Weight	0.0062	0.0006	5.73E-25	0.0080	0.0005	3.64E-46
MAP	-0.0061	0.0006	5.69E-21	-0.0089	0.0006	1.62E-47
HR	-0.0065	0.0007	4.43E-22	-0.0040	0.0007	3.31E-09
Time	0.0396	0.0086	4.83E-06	0.0449	0.0079	1.38E-08
Entry-Age	-0.0149	0.0075	0.0475	0.0094	0.0078	0.2299
(Entry-Age)^2	-	-	-	-0.0005	0.0002	0.0096
Entry-Age×Time	-0.0007	0.0002	8.96E-06	-	-	-
MAP×Time	-0.0003	8.40E-05	5.96E-05	-0.0004	7.73E-05	4.19E-08
MAP×Entry-Age	-	-	-	-0.0002	7.66E-05	0.0172
Weight×Entry-Age	0.0002	9.20E-05	0.0573	-	-	-
R (Obs. vs. Pred.)		0.872			0.815	
R^2		0.400			0.314	

SVR decreased with time independent of the entry-age. Women showed a nonlinear pattern in the longitudinal changes in SVR over time, with an accelerated decrease at older age. The average rates of change in SVR over 10 years increased for females in the younger groups and had a steeper decrease in older women. For males, it decreased with ageing at a constant rate over the entire entry-age range (Figure 6.5D).

Table 6.15: Generalized LME models of the longitudinal effects on Z_c for men and women, including covariates.

	Men			Women		
Variables	Estimate	SE	P-value	Estimate	SE	P-value
Intercept	-2.0366	0.1041	1.87E-77	-1.7509	0.1031	1.84E-60
Weight	-0.0041	0.0007	4.29E-08	-0.0055	0.0007	6.69E-14
MAP	0.0001	0.0009	0.9134	0.0006	0.0009	0.5028
HR	-	-	-	-0.0024	0.0010	0.0141
Time	-0.0549	0.0123	8.31E-06	-0.0640	0.0117	5.35E-08
Entry-Age	-0.0101	0.0019	5.40E-08	-0.0330	0.0110	0.0028
(Entry-Age)^2	0.0009	0.0003	0.0005	0.0007	0.0002	0.0075
Entry-Age×Time	0.0008	0.0002	0.0005	0.0005	0.0002	0.0229
MAP×Time	0.0005	0.0001	5.81E-05	0.0006	0.0001	7.72E-07
MAP×Entry-Age	-	-	-	0.0003	0.0001	0.0093
R (Obs. vs. Pred.)		0.843			0.805	
R^2		0.249			0.209	

Total arterial compliance increased between visits mainly among men, particularly among those who were younger at entry (significant negative Entry-Age×Time interaction; Table 6.14). The predicted average rate of change in C_{PPM} was thus mainly positive for men, decreasing as age increased. Women, on the other hand, had less variation in the rate of change, with slight differences by age group (Figure 6.5E).

The fitted model for Z_c evidenced, on average, a longitudinal decrease over time in both men and women, which however was dependent on the entry-age, with older subjects (particularly men) having an increase. Predicted rates of change over 10 years for both sexes (Figure 6.5F), decrease for entry ages between 35 and 50 years and show a slight increase for entry ages older than 50 years.

6.3.4 Indices of wave reflection: RWTT, $|\Gamma_1|$, and $|P_f|$ and $|P_b|$

Observed longitudinal changes for $|\Gamma_1|$, RWTT, and $|P_f|$ and $|P_b|$ are shown in Figure 6.6A through 6.6D. Both reflection measures, $|\Gamma_1|$ and the reflection magnitude ($|P_b|/|P_f|$, data not shown), decreased between examination visits for all age categories and both sexes, showing an opposite trend as observed from cross-sectional data; and changes in $|\Gamma_1|$ were steeper in men and in the oldest group for men and women. RWTT also decreased between visits, and was shorter, with steeper and more uniform decreases in women (P<0.01). $|P_f|$ differed by sex and age (P<0.001), with women showing higher values than men only for the oldest subjects, but the changes between visits were overall not found significant, except when depending on the age group

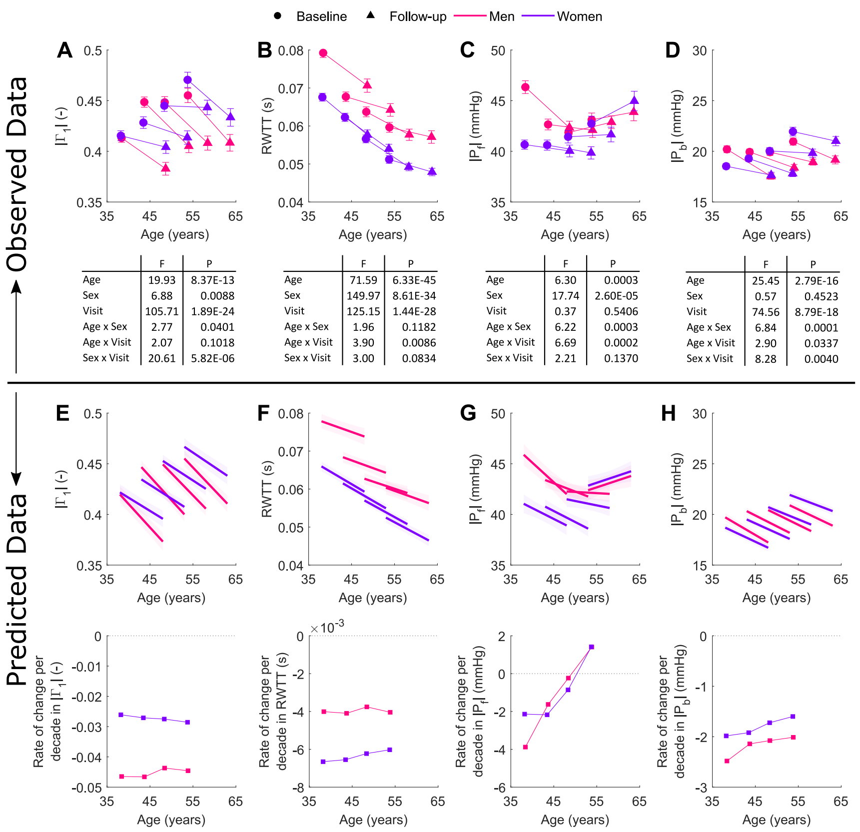

	F	P
Age	19.93	8.37E-13
Sex	6.88	0.0088
Visit	105.71	1.89E-24
Age x Sex	2.77	0.0401
Age x Visit	2.07	0.1018
Sex x Visit	20.61	5.82E-06

	F	P
Age	71.59	6.33E-45
Sex	149.97	8.61E-34
Visit	125.15	1.44E-28
Age x Sex	1.96	0.1182
Age x Visit	3.90	0.0086
Sex x Visit	3.00	0.0834

	F	P
Age	6.30	0.0003
Sex	17.74	2.60E-05
Visit	0.37	0.5406
Age x Sex	6.22	0.0003
Age x Visit	6.69	0.0002
Sex x Visit	2.21	0.1370

	F	P
Age	25.45	2.79E-16
Sex	0.57	0.4523
Visit	74.56	8.79E-18
Age x Sex	6.84	0.0001
Age x Visit	2.90	0.0337
Sex x Visit	8.28	0.0040

Figure 6.6: Top: Observed changes between baseline and follow-up measurements in the wave reflection coefficient derived from impedance analysis, $|\Gamma_1|$ (A), RWTT (B), $|P_\mathrm{f}|$ (C), and $|P_\mathrm{b}|$ (D), per sex and age strata. The P and F values indicate the statistical significance of the factors age, sex, visit, and their interaction in the ANOVA. Bottom: Model-predicted longitudinal trajectories and rates of change per decade in $|\Gamma_1|$ (E), RWTT (F), $|P_\mathrm{f}|$ (G) and $|P_\mathrm{b}|$ (H) per sex and age strata. The plots refer to models in Tables 6.16- 6.19.

(P<0.001). $|P_b|$ on the contrary, decreased between visits for men and women, and there were significant differences by age category. Although the overall effect of sex was not significant, values of $|P_b|$ differed between men and women by age (P<0.001) and by visit (P<0.01) as seen from the ANOVA, with men in age groups A1 and A2 having higher values than women, and the opposite happening for A3 and A4.

Figure 6.6E through 6.6H and Tables 6.16 through 6.19 show the LME models for $|\Gamma_1|$, RWTT, $|P_f|$ and $|P_b|$, modelled using height, weight, HR and MAP as potential covariates. $|P_b|$ decreased with ageing for both sexes; the longitudinal change in $|P_b|$ was associated with height in men

Table 6.16: LME models of the longitudinal effects on $|\Gamma_1|$ for men and women, including HR, height, weight and MAP as covariates.

	Men			Women		
Variables	Estimate	SE	P-value	Estimate	SE	P-value
Intercept	0.7319	0.0865	5.25E-17	0.8479	0.0753	1.64E-28
Height	-0.0009	0.0005	0.0684	-0.0016	0.0004	0.0003
Weight	-0.0006	0.0003	0.0244	-0.0007	0.0003	0.0088
MAP	0.0017	0.0003	1.18E-10	0.0017	0.0002	1.62E-18
HR	-0.0040	0.0002	1.27E-63	-0.0042	0.0003	1.65E-34
Time	0.0254	0.0113	0.0241	-0.0198	0.0035	2.06E-08
Entry-Age	0.0017	0.0004	1.06E-05	0.0019	0.0004	4.89E-06
(Entry-Age)^2	-0.0002	6.32E-05	0.0018	-	-	-
Height×Time	-0.0002	6.35E-05	0.0021	-	-	-
MAP×Time	-0.0001	3.30E-05	0.0393	-	-	-
Weight×Time	0.0001	3.41E-05	5.17E-05	0.0001	3.05E-05	0.0037
HR×Time	-	-	-	0.0002	4.52E-05	0.0002
R (Obs. vs. Pred.)		0.704			0.699	
R^2		0.361			0.310	

Table 6.17: LME models of the longitudinal effects on the RWTT for men and women, including HR, height, weight and MAP as covariates.

	Men			Women		
Variables	Estimate	SE	P-value	Estimate	SE	P-value
Intercept	0.0509	0.0166	0.0022	0.1219	0.0047	9.14E-127
Height	0.0004	9.15E-05	1.42E-05	-	-	-
Weight	0.0001	4.93E-05	0.1040	0.0001	3.36E-05	4.55E-05
MAP	-0.0004	4.63E-05	1.66E-17	-0.0005	4.06E-05	5.12E-32
HR	-0.0003	6.39E-05	8.54E-08	-0.0003	4.54E-05	3.33E-14
Time	-0.0018	0.0006	0.0036	-0.0022	0.0006	9.07E-05
Entry-Age	-0.0026	0.0006	1.44E-05	-0.0039	0.0006	1.17E-09
(Entry-Age)^2	5.76E-05	1.50E-05	0.0001	-	-	-
HR×Entry-Age	1.85E-05	7.81E-06	0.0178	-	-	-
HR×Time	2.26E-05	9.85E-06	0.0218	-	-	-
MAP×Time	-	-	-	1.53E-05	5.44E-06	0.0050
MAP×Entry-Age	-	-	-	1.91E-05	5.14E-06	0.0002
Weigh×tEntry-Age	1.94E-05	7.18E-06	0.0070	-	-	-
R (Obs. vs. Pred.)		0.856			0.800	
R^2		0.494			0.455	

and with MAP in both men and women. On the contrary, $|P_f|$ differed by sex and showed a nonlinear dependence with age. Body weight, MAP, and HR in women, also determined the longitudinal changes in $|P_f|$ over time.

Table 6.18: LME models of the longitudinal effects on $|P_\mathrm{f}|$ for men and women, including HR, height, weight and MAP as covariates.

	Men			**Women**		
Variables	Estimate	SE	P-value	Estimate	SE	P-value
Intercept	20.5095	8.1615	0.0121	15.1044	7.2268	0.0367
Height	0.0881	0.0442	0.0463	0.0821	0.0407	0.0439
Weight	0.0444	0.0289	0.1248	-0.0261	0.0251	0.2980
MAP	0.0714	0.0289	0.0135	0.2132	0.0239	9.03E-19
HR	-0.0696	0.0261	0.0078	-0.1118	0.0321	0.0005
Time	-1.7437	0.4030	1.59E-05	-1.1839	0.3919	0.0026
Entry-Age	-1.1478	0.3511	0.0011	-0.9551	0.2855	0.0008
(Entry-Age)^2	0.0256	0.0073	0.0005	0.0128	0.0079	0.1053
Entry-Age×Time	0.0291	0.0069	2.29E-05	0.0152	0.0061	0.0128
(Entry-Age)^2×Time	-	-	-	0.0022	0.0010	0.0276
Weight×Time	-0.0097	0.0032	0.0029	-0.0060	0.0029	0.0394
HR×Time	-	-	-	-0.0115	0.0043	0.0072
MAP×Time	0.0238	0.0036	3.28E-11	0.0214	0.0031	7.38E-12
MAP×Entry-Age	0.0092	0.0035	0.0083	0.0100	0.0028	0.0004
R (Obs. vs. Pred.)		0.740			0.741	
R^2		0.302			0.379	

Table 6.19: LME models of the longitudinal effects on $|P_\mathrm{b}|$ for men and women, including HR, height, weight and MAP as covariates.

	Men			**Women**		
Variables	Estimate	SE	P-value	Estimate	SE	P-value
Intercept	21.1319	4.6381	5.56E-06	15.6762	1.3687	1.91E-29
Height	-0.0201	0.0238	0.3982	-	-	-
Weight	-	-	-	-0.0493	0.0089	3.37E-08
MAP	0.1146	0.0140	5.16E-16	0.1825	0.0121	8.78E-49
HR	-0.1456	0.0122	1.06E-31	-0.1659	0.0123	6.18E-40
Time	0.2100	0.5631	0.7093	-1.1234	0.1551	6.31E-13
Entry-Age	-0.3501	0.1644	0.0333	-0.0696	0.1886	0.7121
Height×Time	-0.0069	0.0029	0.0191	-	-	-
MAP×Time	0.0076	0.0017	7.74E-06	0.0093	0.0015	1.14E-09
MAP×Entry-Age	0.0039	0.0016	0.0142	0.0089	0.0014	5.71E-10
HR×Entry-Age	-	-	-	-0.0067	0.0021	0.0015
Weight×Entry-Age	-	-	-	-0.0036	0.0015	0.0153
R (Obs. vs. Pred.)		0.910			0.921	
R^2		0.554			0.643	

6.3.5 Effects of antihypertensive and lipid-lowering medications

An important factor that might have influenced the observed longitudinal patterns is the start of medication use between visits. From baseline to follow-up, 165 subjects started taking antihypertensive medications only, 281 lipid-lowering medications only, and 133 both drug treatments. Further analyses were performed after exclusion of these subjects, which resulted in a population of N=1447 (54% women, 59% of excluded subjects were from A3 and A4). Besides excluding data, we also followed a second approach where the starting use of medication was controlled for in the statistical models, allowing their interaction with time and entry-age. A comparison of the modelled rates of change of the original cohort with both approaches, in average subjects not on medications, is shown in Figure 6.7. Models were adjusted for time, entry-age, (entry-age)^2, HR, weight, height, and MAP when applicable. Overall, longitudinal trajectories in PWV, C_{PPM}, and Z_c were minimally affected when accounting for medication use. Women showed slight differences in the patterns of change, with a steeper increase in PWV for older subjects, and a slower decrease in Z_c for younger. In these models, the use of lipid-lowering drugs had a decreasing effect on PWV and Z_c that reduces over time. As for SVR, analysis of the reduced cohort (excluding subjects who started medication) removed the decrease in older women (although the trend remained) while for men, this analysis resulted in a minimal decrease in the annual rate of change.

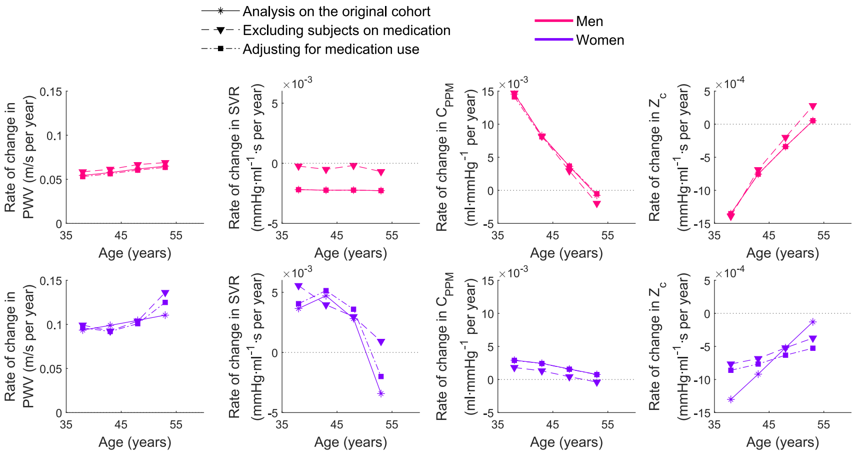

Figure 6.7: Annual rate of change of PWV and impedance parameters for average subjects (men and women) not on medications and per age group, in the analysis of the original cohort, after excluding subjects taking antihypertensive and lipid-lowering medications, and in models adjusting for the use of medications. Models included entry-age, time, HR, height, weight, MAP, and interaction terms with time and entry-age, as possible covariates.

6.3.6 Association of impedance parameters with cardiovascular risk factors

At the end of the second round of measurements, there were 82 diabetic subjects (84.1% diagnosed during follow-up). We performed extra analyses testing for the association between PWV, impedance or wave reflection parameters and traditional CV risk factors. Diabetes, smoking, obesity, weekly alcohol intake, lipid-lowering medications use, hypertension, entry-age, time, HR and education, were considered as potential covariates in the models (see Figures 6.8 and 6.9, and Tables C.1 through C.7 in Appendix C). Hypertension was defined as SBP ≥ 140 mmHg, or DBP ≥ 90 mmHg, or use of antihypertensive medications. Compared to normal weight subjects, obese and overweight subjects had higher C_{PPM} and lower SVR and Z_{c}, but there were no longitudinal associations. In women, the use of lipid-lowering treatment had a decreasing effect on Z_{c} that was lower over time. In men, subjects that never smoked and ex-smokers over time had higher C_{PPM} and lower $|\Gamma_1|$ than active smokers. Diabetic women had lower SVR and lower compliance for the older than nondiabetic women, whereas diabetic men had lower C_{PPM}, and higher Z_{c} depending on the entry age, but none of these associations were longitudinal. Interestingly, men with lower education level showed lower SVR, $|\Gamma_1|$, and PWV compared to men with higher education level.

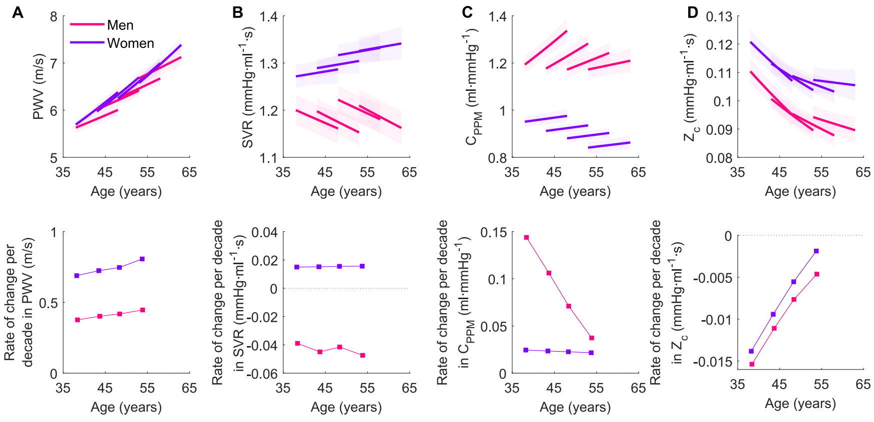

Figure 6.8: Model-predicted longitudinal trajectories (top) and rate of change per decade (bottom) in PWV (A), SVR (B), C_{PPM} (C), and Z_{c} (D) for average subjects (men and women) without cardiovascular risk factors and per age group. Shaded area represents the non-simultaneous 95% CIs. The plots refer to models in Tables C.1, C.2, C.3, and C.4.

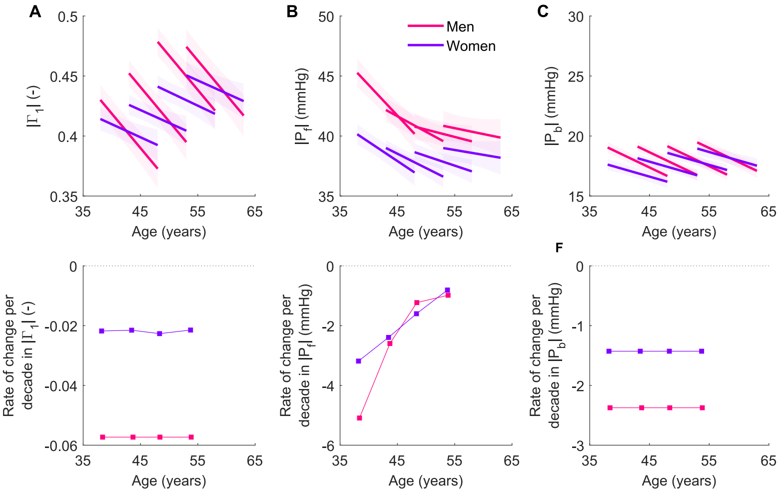

Figure 6.9: Model-predicted longitudinal trajectories (top) and rate of change per decade (bottom) in $|\Gamma_1|$ (A), $|P_f|$ (B), and $|P_b|$ (C) for average subjects (men and women) without CV risk factors and per age group. Shaded area represents the non-simultaneous 95% CIs. The plots refer to models in Tables C.5, C.6, and C.7.

6.3.7 Comparison of subjects of the same age but distinct generation controlling for lifestyle factors

For some of the studied parameters, statistically significant differences were observed when comparing subjects of a certain age at baseline with subjects that reached the same age during follow-up. E.g. women that were about 50 years old at the beginning of the study, had on average a volume compliance 9% lower than women that were about the same age 10 years later. An extra analysis was performed to test whether the observed differences between two groups of subjects in the same age range but a decade apart, were associated with lifestyle and social factors. In a subsample of subjects (n=1427, 48.5% second-generation) with age between 44 and 57 years old, we first fitted regression models using a group indicator variable and controlling for age, sex, obesity, smoking status, education level and weekly alcohol intake. Then, we tested the null hypothesis that the effects of these factors were not different across both groups. We found statistically significant differences of the effects of education, obesity and smoking status on the reflection coefficient across the first- and second-generation groups. Subjects with an education level beyond secondary school had higher $|\Gamma_1|$ in the first generation group, while the opposite occurred for the second group. The effect of smoking status on $|\Gamma_1|$ differed between the two groups, with higher values for active smokers in the group 2, in comparison to ex-smokers and subjects that never smoked. Subjects with normal weight showed higher mean values in group 1 but lower mean values in group 2, while overweight or obese subjects presented similar characteristics. Table 6.20 shows other group interaction effects that resulted statistically significant for parameters that differed between the two groups. For other parameters that also showed statistically significant differences when comparing both generation groups (e.g. C_{PPM}, SVR, LVOT area or SV), we did not find enough evidence to support the hypothesis that these differences may be also influenced by lifestyle or socio-economic factors.

Table 6.20: Differences between two groups of subjects with the same mean age but from distinct decade, explained by lifestyle- and social-related factors.

Variables	F	P-value
$\lvert\Gamma_1\rvert$**:**		**<0.001***
Group × Education	5.09	0.02
Group × Obesity	3.38	0.03
Group × Smoker	3.10	0.04
RWTT:		**0.001***
Group × Obesity	3.23	0.04
$\lvert P_b\rvert$**:**		**<0.001***
Group × Education	3.79	0.05

*P<0.05 t-unpaired test determining whether the difference between the mean of both groups was statistically significant. Regression models included terms shown, sex, age, and weekly alcohol intake (units/week); all group interaction terms were evaluated. Only significant (P<0.05) group interaction terms in the hypothesis tests are reported.

6.4 Discussion

In this study, we have shown the effective impact of ageing on the arterial system properties and dynamics in the middle-aged. To our knowledge, this is the first study to report and analyse the longitudinal evolution of impedance and wave reflection parameters (besides BP and arterial stiffness) over a span of about a decade. A major observation to notice from our longitudinal data is that impedance and wave reflection parameters have a different evolution, and in some cases even opposed, from results of cross-sectional analyses. Indeed, while cross-sectional data show a decrease with age in total arterial compliance and an increase in resistance, our longitudinal data demonstrate an increase in C_{PPM} and a decrease in SVR, mainly for men and for the older age groups. Similar opposite behaviour is found for wave reflection parameters, such as the reflection coefficient and the reflection magnitude. Although PWV increased with age, concordant with cross-sectional analyses, it increased more rapidly than expected in women, while the opposite was true for men; besides it was not paralleled by a decrease in arterial compliance, mainly in younger subjects.

6.4.1 Longitudinal trajectories of PWV and BP variables: a puzzling relationship

While the overall consensus is that PWV increases with age, the modelled age-dependency of the relation between PWV and time is more complex than this and depends on the chosen models. Our results, as well as previously published results [62, 63], show no baseline differences in PWV between men and women in the age range of study. In the models accounting only for entry-age and time (Figure 6.3 and Table 6.4), the longitudinal trajectories of PWV over time were independent of the baseline age and their rates of change, although higher for women, showed a similar increasing pattern with age for both sexes, in agreement with reports from the SardiNIA longitudinal study [63]. However, in models including covariates (Tables 6.5 through 6.8), the longitudinal increase in PWV over time was associated with higher entry-age mainly in women, thus implying that the older the subject entering into the study, the higher was the increase in PWV in ten years. Similarly to the present study, in the BLSA [62], sex differences in PWV arise and accelerate with ageing; however, in contrast to our study, men had a steeper longitudinal increase in PWV than women. Controversial results when referring to sex differences in PWV values with age have been previously reported [205, 221–223], with a lack of consensus on whether PWV is higher in women or in men, which may be influenced by study design factors such as the age range of participants, ethnicity, body weight, the variety of methods used when calculating PWV, or whether the data are cross-sectional or longitudinal. It has been also suggested that this divergence may be associated to menopause [223, 224], a factor not accounted for in our study.

Previous studies [60, 63] have shown a dissociation of BP variables with longitudinal changes in PWV. Our results are in line with these previous findings, where none of the BP variables was longitudinally associated with PWV trajectories over time (except PP_{CA} in women). *Vice versa*, PWV was inversely associated with the longitudinal changes in all BP variables except PP_{CA} for both sexes (Tables 6.5 through 6.12). Results from the FHS [60] and the BLSA [61] showed an association of higher PWV with the longitudinal increase in SBP, supporting the premise that accelerated arterial stiffness is one of the causes of hypertension in older adults and not *vice versa*. Our outcomes, on the contrary, show that the longitudinal increase in carotid systolic pressure over time is lower for higher PWV among middle-aged adults. However, when subjects taking medications were excluded from the analyses, increased carotid systolic pressure was associated with the longitudinal increase in PWV. Similar results were obtained in [62] with models adjusting for medications use. What is clear from these results is that medication has an impact on the relationship between BP and arterial stiffness, and that this relation is rather complex. Note that a direct comparison of our results with previous longitudinal studies is limited by differences in the statistical approaches, location where BP was measured, the age range and characteristics of the study population, and duration of the follow-up (the Asklepios study has the longest mean follow-up compared to [60, 61, 63]).

6.4.2 Longitudinal trajectories of impedance and wave reflection parameters

The longitudinal trajectories of Z_c decreased for the younger subjects (A1 to A3). On the contrary, C_{PPM} increased over the 10-year period and this increase declined with older age. Results obtained for total arterial compliance can be gleaned from the input impedance plots (Figure 6.4). The modulus of the first two harmonics of Z_{in} in men decreased from visit 1 to visit 2, this decrease between visits being more evident from the younger to the older group. This indicates an increase in total arterial compliance as it is confirmed from the C_{PPM} data. The change in women is less apparent and does not have a constant behaviour with age, which again reflects the results of C_{PPM}. In contrast, within the same visit, the modulus of the first two harmonics of Z_{in} systematically increases with age. This is consistent with the continuous cross-sectional decrease of C_{PPM} with increasing age.

Different factors may explain why age-related changes in volume compliance differ from previous reports [65, 225]. First, most reports are cross-sectional and when looking at our data from a cross-sectional perspective, compliance does decrease with age in both rounds. Second, we are studying a large cohort in a narrow age range that is not often considered. Our main rationale to include apparently healthy middle-aged subjects at baseline was to specifically start studying the CV system at a moment where, presumably, major CV adaptations still need to take place. The pattern of an increase in volume compliance concomitant with an increase in PWV suggests that aortic geometric remodelling (such as dilation and elongation) may be involved. Indeed, earlier studies report that the aorta undergoes marked changes with ageing, becoming more tortuous with increased elongation [38] and increased aortic root diameter which is larger in men compared with women [39]. The former may also explain the decrease in aortic Z_c for all but the oldest age category. Characteristic impedance is known to be very sensitive to aortic size, as quantified by the water hammer equation [46, 210]; therefore, aortic dilation may be able to overcome the hemodynamic impact of aortic stiffening. Besides, it has been already suggested that the effective cross-sectional area (A_{eff}) plays an important role in the arterial function, particularly as a determinant of aortic Z_{c} [210].

In the design of our population study, we did not account for a direct measure of change in aortic size (dilatation or elongation). In the previous report of the Asklepios study [65], a relation between age and the cross-sectional area of the LVOT (which can be seen as an indication of further changes in A_{eff}) could not be established. In contrast, in our present longitudinal study, LVOT cross-sectional area increased significantly between visits (see Table 6.2). In the younger middle-aged males, while PWV increased a 9% between visits, Z_{c} decreased a 13%, which suggest from the water hammer equation a 25% increase in A_{eff}. Total arterial compliance, via the distensibility coefficient, could be assumed to be proportional to $A_{\mathrm{eff}}/\mathrm{PWV}^2$, thus the increase in both parameters would imply an increase in arterial compliance of $\approx 5\%$, which corresponds with the order of magnitude of the increase observed in C_{PPM} for this group of subjects.

Contrary to what has been observed by cross-sectional studies including the baseline Asklepios study [10, 65, 226], in the transition from middle-aged to older of our sample population wave reflection did not increase but decreased with ageing for men and women. There was a nonlinear relation in $|\Gamma_1|$ with the cross-sectional age in men, but longitudinal trajectories over time were independent of the entry-age. The longitudinal trajectories in $|P_f|$ had a marked dependency with ageing, whereas $|P_b|$ decreased albeit with less age-dependency. The conventional understanding of wave reflection shows that with advancing age, increased aortic stiffness results in larger reflected waves returning earlier in the aorta and elevating BP [9]. On the contrary, Mitchell *et al.* [54, 227] have suggested that the increase in characteristic impedance due to increasing aortic stiffness with ageing, leads to an impedance matching between the aorta and large peripheral arteries, which in turn leads to a reduction in wave reflection. The patterns of change for the older subjects in our study are consistent with these findings. However, it is important to consider that impedance matching is also highly sensitive to the geometry of proximal and distal vessels. Future studies should examine the determinants of wave reflection in more detail, including the role of segmental stiffening and conduit artery geometry.

6.4.3 Cardiovascular risk factors do not fully explain the dissociation between baseline and follow-up observations

A major observation from our study is the dissociation between our longitudinal outcomes and what was expected based on our previous cross-sectional analysis [65]. We cannot exclude that secular trends due to a change of lifestyle, diet, socio-economic factors or environmental exposures may be affecting our results, since they are likely to occur in the long observation period. Such factors were not fully accounted for in our study and in general are considered a limitation of long period longitudinal studies. Nonetheless, we performed additional analyses testing for the association between the studied parameters and traditional cardiovascular risk factors such as obesity, diabetes, smoking status, alcohol intake, hypertension, use of lipid-lowering treatments, and the education level. Although the longitudinal effect of medication use was significant for some parameters, overall the patterns of change remained consistent (Figure 6.7). When accounting for the other CV risk factors, the patterns of change persisted in general (see Figures 6.8 and 6.9). Significant differences were also observed when comparing parameters in subjects of a certain age at baseline with subjects that reached the same age during follow-up. Speculatively, this may be an effect of subjects of a same age experiencing a different lifestyle history and different environmental exposures. It was also verified by a multiple regression analysis for the rate of change of some variables (data not shown), adjusting for age, sex, and the baseline measurement of the variable, that our results are not affected by regression to the mean.

6.4.4 Limitations

Our study has some limitations that should be discussed. Our noninvasive data of central pressure were estimated at the carotid artery as a surrogate for aortic pressure, this combined with central aortic flow might have influenced the derived impedance and reflection parameters. The evaluated population was narrowed down to white middle-aged subjects that transitioned to an older cohort in the span of the study, thus our results cannot be generalized to younger or elder subjects, or to other races and ethnicities. Besides, our longitudinal study includes only one follow-up measurement, limiting the detection power of complex interactions that may have occurred between both examination visits. Derived PWV at follow-up was not corrected for the changes in the path length between visits.

6.5 CONCLUSIONS

In middle-aged adults, the evolution of arterial parameters over a 10-year period differ from cross-sectional trends, leading to differences in subjects of similar ages but a decade apart. Overall, the arterial system of subjects that reached a certain age in the span of the study had higher compliance, body size measures, cardiac output, stroke volume, PWV (in women) than subjects that were the same age at baseline, but also presented lower wave reflection parameters, SVR, and characteristic impedance. These differences may be conditioned by different socio-economic factors, environmental exposures, and changes of subjects' lifestyle, rather than ageing alone. Although PWV rises with age indicating stiffening of the arterial tree, this increase was not paralleled by a decrease in volume compliance or by an increase in characteristic impedance. This suggests that dilation and elongation of the aorta plays an important role in determining impedance. Our results evidence the importance of performing longitudinal studies over cross-sectional studies, which do not properly reflect the effective impact of ageing on arterial system properties. More efforts are still needed to develop therapies aiming to influence directly arterial stiffness, whereas traditional risk factors together with socio-economic, genetic, and environmental factors, deserve greater consideration to reduce the risk of cardiovascular events and achieve healthy vascular ageing.

CONCLUSIONS

Pulse wave propagation in the CV system has become an important subject of study, as researchers have gained awareness of the influence of wave dynamics on pressure and flow patterns, and its potential for explaining many observed age and disease related changes in arterial hemodynamics and their effects on the CV system. Within this context, the research presented in this dissertation aimed to gain a deeper insight into arterial hemodynamics and pulse wave travel and reflection in the arterial system (in humans and the horse), and assess how they are affected by ageing.

KEY MESSAGES FROM THE THESIS

We studied arterial hemodynamics and wave propagation in the CV system in a number of selected applications, by making use of a previously validated 1D model of the systemic circulation [12]. We first applied the 1D model to investigate the hemodynamic impact of the C-Pulse heart assist system on the circulation (Chapter 3). Simulations of standard hemodynamic measurements were comparable to *in vivo* human (noninvasive) and pig (invasive) measurements, in terms of wave dynamics, as well as pressure and flow wave shape. Since pulse wave propagation may be a significant contributor to the efficacy of the device, we used wave intensity analysis to provide insight in the mechanisms by which the C-Pulse device produces hemodynamic benefits. We demonstrated that activation of the C-Pulse in diastole generates a sequence of forward compression-expansion waves, leading to the increase in diastolic arterial pressure and coronary flow. Nevertheless, the circulatory benefits of the heart assist device were more evident *in vivo* than in the simulations, suggesting the influence of neuro-modulating mechanisms, not accounted for in the computer model. A major observation of this study was that the potential beneficial effect of the device is dependent upon arterial compliance, with greater hemodynamics effects in diastole on stiffer aortas. This might constitute an important factor to take into account when selecting patients, for this or similar heart assist devices intended as a bridge-to-transplant or as destination therapy, since most of the patients are likely to have large-artery stiffening [46]. These results are in turn conditioned by the *modus operandi* of the device, which is programmed to achieve approximately the same degree of aorta compression in each patient, thus requiring higher cuff inflation pressures for less compliant vessels.

In Chapter 4, we studied several methods to estimate local PWV, based on the water hammer equation. By means of the 1D model, we were able to derive local PWV at each location in the arterial tree, and use these data to map the accuracy of the loop-based methods along the complete main systemic network. The numerical approach of the study offers an advantage compared to *in vivo* studies, where the hemodynamic signals needed to apply the methods are only available noninvasively at superficial arteries such as the carotid or femoral, limiting the estimation of local PWV to few isolated locations. We confirmed that the loop-based methods present inaccuracies compared to the reference Bramwell-Hill equation, and this largely depending on the location in the arterial tree, although with a non-systematic pattern. The PU-loop method overestimated the value of PWV by more than 20% for most arterial locations, whereas the ln(D)U-loop and QA-loop methods underestimated the value of PWV to the same extent at the very same locations. Discrepancies increased significantly in the aged model configuration for each of these methods. The error trends of these methods have been associated with the nature of wave reflections in previous studies [167–169]. In contrast, the ln(D)P-loop, which is insensitive to wave reflections, performed well over the complete network, as did the reflection-correction method proposed by Segers *et al.* [168] in most vascular sites. Nonetheless, the ln(D)P-loop is mathematically equivalent to the theoretical Bramwell-Hill equation, therefore this method does not really provide a practical alternative to it. On the other hand, the method correcting for wave reflections also lacks practical applicability since four signals have to be simultaneously measured. Accordingly, the Bramwell-Hill equation remains as the recommended method to estimate PWV at a single-location [71]. Because the knowledge of local PWV is essential to perform wave separation analysis (WSA), we later examined how the errors on PWV, obtained with the different methods, propagate on subsequent WSA. We again found that the errors are site-dependent, but overall WSA was not highly dependent on the accuracy of the PWV estimates, in particular for locations such as the ascending aorta or carotid artery, which are sites of interest in clinical practice. Although an important result of this study is that the performance of the different methods is highly site-specific, results are bounded to the two simulated cases. Further studies are thus required to deepen in this matter, which can be carried out by generating a virtual cohort dataset, for instance by varying cardiac and arterial parameters within healthy ranges [228]. A virtual dataset may be useful to further investigate the impact of using a surrogate pressure waveform, obtained from linear calibration of the local diameter waveform to brachial mean and diastolic pressures, as proposed by Kowalski *et al.* [91] for the ln(D)P method.

Another contribution of this thesis was the development in Chapter 5 of a 1D model of the equine arterial circulation, based on the human 1D model of the systemic arterial system. A major difficulty in developing the model was the lack of data to fit the model parameters. Due to the technical challenges of horse measurements, most of the parameters required as input in the model are not available in the literature; even our *in vivo* measurements of pressure and flow waveforms were performed only at few locations and in a limited number of horses. In view of this, several parameters, including the cardiac and terminal model parameters, were assumed and tuned to the equine physiology by scaling factors based on the human data. Further fine-tuning of these parameters to equine physiology will be necessary to obtain a closer match with *in vivo* flow profiles. The use of the Witzig-Womersley's oscillatory flow theory to compute the local velocity profile and the friction coefficient was of great relevance in the horse model. Horses have larger arteries calibre than humans, which is a factor determining the Womersley parameter, with higher alpha numbers indicating influence of inertial effects over viscous effects in the velocity profile, and therefore a flatter profile. Exclusion of the Womersley equations in the horse model led to non-physiological pressure and flow patterns in the large arteries. Overall, model predictions were in line with measured pressure and flow waveforms. Inclusion of gravity in the horse model improved predicted waveforms. Nevertheless, the results accounting for gravity are not completely accurate since the model does not include the necessary control mechanisms. Changes in posture from the lying to the standing position, lead to differences in the arterial and venous pressures since gravitational forces play a role [31]. In the lying position the mean pressures are similar for all the major arteries, while in the standing position mean pressures increase going from the head to the limbs. Autoregulation mechanisms are activated with the change in posture, increasing cardiac output (increased heart rate) and resistance (vasoconstriction), to maintain a normal arterial blood pressure [23]. The developed equine model has a generic character since it is based on averaged data. Therefore, predictions of pressure and flow waveforms can be made for the average healthy horse, and comparison between predicted and *in vivo* waveforms should only be considered qualitatively. A detailed horse-specific model would be the preferred option to study the pathophysiology in an individual animal, as we have observed that flow patterns differ considerable from one horse to the other, but this approach is challenging due to the large number of parameters required to develop such a per horse model. The horse model constitutes a promising tool to study various types of pathophysiological conditions in horses, as a result of strenuous exercise or changes due to ageing, breed or gender.

A second major goal of this PhD project was to investigate the effective impact of ageing on arterial system properties and arterial wave reflections, for which we made use of the longitudinal *in vivo* data of the Asklepios middle-aged population (Chapter 6). Concretely, we statistically analysed the 10-years longitudinal changes on PWV and BP indices, input impedance parameters, and wave reflections parameters, and compared them to the previous cross-sectional perspectives. We found that PWV increased with age, but to a lesser extent than predicted from cross-sectional data. The longitudinal age-related increase in PWV was besides steeper in women than in men. Another striking observation was that the increase in PWV was not paralleled by a decrease in arterial compliance. Moreover, longitudinal changes in global system parameters as arterial compliance, systemic vascular resistance, the reflection coefficient, and the reflected pressure wave, opposed to cross-sectional observations over the studied age range. Overall, discrepancies remained after exclusion of hypertensive subjects or when accounting for several CV risk factors such as diabetes, obesity, or smoking. Our data suggest that aortic remodelling (dilation and elongation), together with stiffening, play an important role determining the longitudinal age-related changes in PWV and impedance parameters for younger middle-aged subjects. These changes may contribute to impedance matching between the aorta and large peripheral arteries, reducing wave reflection in the studied age range. Our results may be conditioned by differences in socio-economic factors, environmental exposures, and changes of subjects' lifestyle, rather than ageing alone. If so, this implies that arterial stiffening is modifiable, but also that reference and normal values, typically obtained from cross-sectional studies, require frequent updates. Finally, the steeper increase in PWV in women warrants further attention, especially in view of ventricular-arterial interactions and the higher incidence of heart failure with preserved ejection fraction in women [229, 230]. We stress that longitudinal studies of ageing provide important information that cannot be gained by cross-sectional studies alone.

Limitations and future perspective

Our work with the 1D model has confirmed it as a powerful tool for understanding physiological changes occurring in the CV system under different circumstances, and their effect on pulse wave propagation. Nevertheless, modelling will always be an approximation of reality. An important complication and challenge for modelling the CV system, is to incorporate regulation and adaptation mechanisms in the constitutive relations. Some studies have simulated autoregulation mechanisms (vasodilatation and vasoconstriction) of the cerebral circulation by using time-varying resistance models [231, 232], but these effects are rarely included in 1D modelling studies. Accounting for adaptation mechanisms in the 1D model would be of relevance for the study of counterpulsation devices such as the C-Pulse, providing a more objective evidence of hemodynamic efficacy. The mechanism of counterpulsation, although long established as a therapy for heart failure [233], is still very controversial in terms of a purely mechanical effect or neural mediated effect. In this regard, the discrepancy between simulations and *in vivo* data shown in our study, may suggest that the hemodynamic effect of the C-Pulse is besides influenced by autoregulation or sympathetic/parasympathetic modulation mechanisms, and this apart from the limitations *per se* of the simple model used to simulate the action of the cuff.

The horse model would also benefit from the incorporation of regulation mechanisms, particularly to study the effects of gravity, which in turn is a feature that is not routinely implemented in 1D modelling in humans, and thus could also be considered in future work. The horse model can be used in future research to study various types of pathologies, or physiological changes in local pressure and flow profiles under different conditions, and without the need of invasive measurements. One of the applications of this model could be oriented to study the effects of extreme exercise on arterial hemodynamics, which may contribute to the understanding of the relatively high incidence of sudden death during exercise due to arterial rupture [184, 185]. During exercise the cardiac output of the horse increases considerably (about 8 to 13 times higher than the resting values [193]), which can be simulated by altering the cardiac parameters in the model. The flow distribution in the arterial system also changes from rest to exercise, with more than 80% of the cardiac output perfusing skeletal muscle during maximal exercise, in contrast to only 15% at rest [193]. Therefore, simulating this condition would imply a readjustment of the terminal impedance parameters. Nevertheless, validation of this case would be hampered since measurements in horses during exercise are difficult to obtain. For instance, to our knowledge, horse blood pressure has only been measured during exercise through very invasive approaches [234, 235]. As mentioned previously, the effect of ageing on the equine hemodynamics can also be investigated using the 1D model. As occurs for humans (shown in the longitudinal *in vivo* Asklepios dataset - Chapter 6), an increase in arterial stiffness (PWV) has also been observed with ageing in horses [236]; meaning that the ageing condition can be simulated by modifying the arterial compliance parameters in the model, albeit in simple models to some extent.

The current 1D model is an open-loop system, since it does not include the venous and pulmonary circulation. Inclusion of a model of the pulmonary circulation could be relevant to understand other clinical conditions in horses such as exercise-induced pulmonary haemorrhage [235]. Recent work improving the modelling capabilities of this particular 1D model has already been undertaken [135], with the inclusion of a simplified five-segment lumped parameters model of the pulmonary circulation (2-element Windkessel models connected in series). More importantly in that same study, which aimed to investigate the biomechanics of diastolic dysfunction, the time-varying elastance model of the left ventricle was upgraded to a lumped parameters model of the heart accounting for the four chambers and valves. The use of such an improved version of the heart model would favourably impact the results of the different studies presented in this thesis. Particularly, it could be useful to further unravel the effects on arterial hemodynamics of heart assist devices such as the C-Pulse, due to the importance of counterpulsation synchronization with the timing of the cardiac cycle.

The value of 1D modelling is increasing as the large amount of parameter data necessary to describe the circulation becomes more available, due to the continuous improvement of the noninvasive measuring techniques. In this way, computational models of the CV system are closer to becoming a reliable and useful tool for prediction and case studies in clinical practice. In our studies with the 1D model, we represented ageing by simply modifying the distensibility over the complete arterial tree, which appears to be a very simple solution for a phenomenon that is much more complex. Other studies with the 1D model have included more complexity when simulating ageing, by accounting for age-specific curves for the estimation of distensibility, and age-specific variations of terminal resistance and cardiac parameters [20]. On the other hand, the Asklepios dataset, based on longitudinal noninvasive measurements, provides a unique opportunity to study the effects of ageing on arterial hemodynamics in a large population. A major drawback of the study is that we did not measure aortic remodelling as a result of ageing, thus we can only presume about its role driving our results. Further studies are needed to evaluate in more detail age-related geometric remodelling and wall stiffening as determinants of pulsatile hemodynamics.

One aspect observed in the Asklepios population is the difference between men and women in the longitudinal evolution of some parameters, particularly arterial stiffness. Accordingly, it seems reasonable to further consider sex-specific 1D models when studying CV ageing. Changes due to menopause have been pointed out in some studies [223, 224, 237] as a potential factor determining the sex differences in arterial stiffness; therefore, considering the age range of women in the Asklepios study and the presumed change in the menstrual status during the study period, menopause becomes an interesting point to be elucidated in future research. Nonetheless, accounting for pre- and post-menopause effects is challenging, especially in middle-aged women where besides natural hormonal changes, hormone therapies may also be incorporated. Another research subject that may be even more relevant for future studies, is the role of environmental exposure, socio-economic and lifestyle factors such as exercise, as confounding in the cohort effects. We presume that these factors may have influenced our results, and led to differences in ageing related changes in subjects of distinct generations. Unfortunately, despite the extent of the database and the extensive cardiovascular phenotyping, the Asklepios database is too limited to assess a potential impact of environmental, socio-economic and lifestyle factors on arterial ageing. This highlights the need for well-designed longitudinal studies where lifestyle, socio-economic, genetic and environmental factors, together with traditional CV risk factors, are taken into account in order to assess them as determinants of the hemodynamic changes with ageing, in different populations and from different generations. A possible pathway to achieve this purpose is the application of novel computational techniques such as machine learning, by means of which insight from the raw data can be derived without a priori assumptions. For instance, machine learning could be applied to the Asklepios dataset in order to prospectively investigate and identify the factors associated with the prevalence of healthy vascular ageing during the follow-up period. Clear identification of these factors is important to reinforce cardiovascular prevention, influence the ageing process and improve individuals' quality of life.

APPENDIX

APPENDIX A: WITZIG-WOMERSLEY THEORY

Considering the flow of a viscous incompressible fluid in a straight, circular, sufficiently long tube, the velocity along the tube can be assumed to be independent of its axial direction. Then if the convective acceleration and body forces are neglected, the momentum equation (2.5) can be rewritten in the form (Womersley 1957 [143]):

$$\frac{\partial u}{\partial t} = -\frac{1}{\rho}\frac{\partial P}{\partial x} + \frac{\mu}{\rho}\left(\frac{\partial^2 u}{\partial r^2} + \frac{1}{r}\frac{\partial u}{\partial r}\right) \tag{A.1}$$

and assuming that the local pressure gradient is a sinusoidal wave with amplitude A and angular frequency ω,

$$\frac{\partial P}{\partial x} = \mathrm{A}e^{i\omega t} \tag{A.2}$$

we get to the expression:

$$\frac{\partial^2 u}{\partial r^2} + \frac{1}{r}\frac{\partial u}{\partial r} - \frac{\rho}{\mu}\frac{\partial u}{\partial t} = \frac{1}{\mu}\mathrm{A}e^{i\omega t} \tag{A.3}$$

By using the substitution $u = we^{i\omega t}$ in the above equation, and by cancelling the term $e^{i\omega t}$ throughout the equation, the following relation is derived:

$$\frac{\partial^2 w}{\partial r^2} + \frac{1}{r}\frac{\partial w}{\partial r} - \frac{\rho}{\mu}i\omega w = \frac{\mathrm{A}}{\mu} \tag{A.4}$$

This is a form of Bessel's equation, and its solution is [143]:

$$w = \frac{\mathrm{A}}{i\omega\rho}\left[1 - \frac{J_0\left(\alpha i^{3/2}\frac{r}{R}\right)}{J_0\left(\alpha i^{3/2}\right)}\right] \tag{A.5}$$

where J_0 is a Bessel function of the first kind of order zero, with complex argument, and $\alpha = R\sqrt{\rho\omega/\mu}$ is the dimensionless Womersley's alpha parameter. By converting the solution to the fluid velocity u, the equation for the fluid velocity takes the form:

$$u(r,t) = \text{Real}\left\{\frac{\mathrm{A}}{i\omega\rho}\left[1 - \frac{J_0\left(\alpha i^{3/2}\frac{r}{R}\right)}{J_0\left(\alpha i^{3/2}\right)}\right]e^{i\omega t}\right\} \tag{A.6}$$

where the amplitude A is unknown, R is the artery radius (assumed constant and equal to the local radius at mean pressure) and r/R is the relative radial position. The "Real" means that only the real part of the mathematically complex formula is taken [31]. As the flow profile depends on the velocity profile,

$$Q(t) = \int_0^R u(r,t)\mathrm{d}A \tag{A.7}$$

and considering $\mathrm{d}A = 2\pi r\mathrm{d}r$ we obtain:

$$Q(t) = 2\pi\int_0^R u(r,t)r\mathrm{d}r \tag{A.8}$$

By substituting the relation for the velocity u (equation (A.6)) in the above equation, and applying the commutation integral properties we obtain,

$$Q(t) = \text{Real}\left\{\frac{2\pi\mathrm{A}}{i\omega\rho}\left[\int_0^R r\mathrm{d}r - \int_0^R r\frac{J_0\left(\alpha i^{3/2}\frac{r}{R}\right)}{J_0\left(\alpha i^{3/2}\right)}\mathrm{d}r\right]e^{i\omega t}\right\} \tag{A.9}$$

Solving the first integral in equation (A.9):

$$\int_0^R r\mathrm{d}r = \frac{R^2}{2} \tag{A.10}$$

Solving the second integral in equation (A.9):

$$\int_0^R r\frac{J_0\left(\alpha i^{3/2}\frac{r}{R}\right)}{J_0\left(\alpha i^{3/2}\right)}\mathrm{d}r = \frac{1}{J_0\left(\alpha i^{3/2}\right)}\int_0^R rJ_0\left(\alpha i^{3/2}\frac{r}{R}\right)\mathrm{d}r \tag{A.11}$$

by applying the substitution $w = \alpha i^{3/2}\frac{r}{R}$, which implies $r = \frac{R}{\alpha i^{3/2}}w$ and $\mathrm{d}r = \frac{R}{\alpha i^{3/2}}\mathrm{d}w$, and rearranging:

$$\int_0^R r\frac{J_0\left(\alpha i^{3/2}\frac{r}{R}\right)}{J_0\left(\alpha i^{3/2}\right)}\mathrm{d}r = \frac{R^2}{(\alpha i^{3/2})^2 J_0\left(\alpha i^{3/2}\right)}\int_0^R wJ_0(w)\,\mathrm{d}w \tag{A.12}$$

By applying the property of Bessel functions [238]:

$$\int x^k J_{k-1}(x)\,\mathrm{d}x = x^k J_k(x) \tag{A.13}$$

where k is the order of the Bessel function and x its argument; the solution of the integral in function of w is:

$$\int_0^R r\frac{J_0\left(\alpha i^{3/2}\frac{r}{R}\right)}{J_0\left(\alpha i^{3/2}\right)}\mathrm{d}r = \frac{R^2}{\left(\alpha i^{3/2}\right)^2 J_0\left(\alpha i^{3/2}\right)} w J_1(w)\Big|_0^R \tag{A.14}$$

By converting the solution to the radius r and evaluating in the integration limits, the solution of the integral is finally:

$$\int_0^R r\frac{J_0\left(\alpha i^{3/2}\frac{r}{R}\right)}{J_0\left(\alpha i^{3/2}\right)}\mathrm{d}r = \frac{R^2}{\alpha i^{3/2} J_0\left(\alpha i^{3/2}\right)} J_1\left(\alpha i^{3/2}\right) \tag{A.15}$$

By substituting the results of equations (A.10) and (A.15) in equation (A.9), and rearranging, a final relation for the flow can be obtained [31]:

$$Q(t) = \mathrm{Real}\left\{\frac{\pi R^2 \mathrm{A}}{i\omega\rho}\left[1 - \frac{2J_1\left(\alpha i^{3/2}\right)}{\alpha i^{3/2} J_0\left(\alpha i^{3/2}\right)}\right] e^{i\omega t}\right\} \tag{A.16}$$

Taking into account equation (A.16), the velocity can be written as a function of the flow:

$$u(r,t) = \mathrm{Real}\left\{\frac{Q(t)}{\pi R^2}\left[\frac{1 - \frac{J_0\left(\alpha i^{3/2}\frac{r}{R}\right)}{J_0\left(\alpha i^{3/2}\right)}}{1 - \frac{2J_1\left(\alpha i^{3/2}\right)}{\alpha i^{3/2} J_0\left(\alpha i^{3/2}\right)}}\right] e^{i\omega t}\right\} \tag{A.17}$$

Since the heart generates a series of sine waves rather than a single one, the velocity profile is calculated as a Fourier series with harmonics (n):

$$u(r,t) = \sum_n \mathrm{Real}\left\{\frac{Q_n}{\pi R^2}\left[\frac{1 - \frac{J_0\left(\alpha i^{3/2}\frac{r}{R}\right)}{J_0\left(\alpha i^{3/2}\right)}}{1 - \frac{2J_1\left(\alpha i^{3/2}\right)}{\alpha i^{3/2} J_0\left(\alpha i^{3/2}\right)}}\right] e^{i\omega t}\right\} \tag{A.18}$$

where Q_n is the n^{th} harmonic of the flow pulse, and J_0 and J_1 are the complex Bessel functions of the first kind of zero and first order, respectively. For n= 1 and considering the property [238]:

$$J_k(x) = \sum_{n=0}^{\infty} \frac{(-1)^n (x/2)^{k+2n}}{n!(k+n)!} \tag{A.19}$$

the solutions for the Bessel functions in equation (A.18) are:

$$J_0\left(\alpha i^{3/2}\frac{r}{R}\right) = -\frac{\alpha^2 i^3 r^2}{4R^2} \tag{A.20}$$

$$J_0\left(\alpha i^{3/2}\right) = -\frac{\alpha^2 i^3}{4} \tag{A.21}$$

$$J_1\left(\alpha i^{3/2}\right) = -\frac{\alpha^3 i^{9/2}}{16} \tag{A.22}$$

By substituting the relations (A.20), (A.21) and (A.22) in equation (A.18) and simplifying, the equation for the velocity profile takes the form:

$$u(r,t) = \frac{2}{\pi R^2}\left(1-\frac{r^2}{R^2}\right)Q_1 + \sum_n \text{Real}\left\{\frac{Q_n}{\pi R^2}\left[\frac{1-\frac{J_0\left(\alpha i^{3/2}\frac{r}{R}\right)}{J_0\left(\alpha i^{3/2}\right)}}{1-\frac{2J_1\left(\alpha i^{3/2}\right)}{\alpha i^{3/2}J_0\left(\alpha i^{3/2}\right)}}\right]e^{i\omega t}\right\} \tag{A.23}$$

To derive an expression in the oscillatory theory for the wall friction term τ, the derivative of the velocity profile given by relation (A.23) is obtained.

$$\tau = \mu\frac{\partial}{\partial r}\left(\frac{2}{\pi R^2}\left(1-\frac{r^2}{R^2}\right)Q_1 + \sum_n \text{Real}\left\{\frac{Q_n}{\pi R^2}\left[\frac{1-\frac{J_0\left(\alpha i^{3/2}\frac{r}{R}\right)}{J_0\left(\alpha i^{3/2}\right)}}{1-\frac{2J_1\left(\alpha i^{3/2}\right)}{\alpha i^{3/2}J_0\left(\alpha i^{3/2}\right)}}\right]e^{i\omega t}\right\}\right)\Bigg|_{r=R} \tag{A.24}$$

By solving the derivative of the first term in the sum and evaluating in the limits we obtain:

$$\mu\frac{\partial}{\partial r}\left(\frac{2}{\pi R^2}\left(1-\frac{r^2}{R^2}\right)Q_1\right)\Bigg|_{r=R} = -\frac{4\mu}{\pi R^3}Q_1 \tag{A.25}$$

The derivative of the second term in the sum can be written as:

$$\mu\frac{\partial}{\partial r}\left(\sum_n \text{Real}\left\{\frac{Q_n}{\pi R^2}\left[\frac{1-\frac{J_0\left(\alpha i^{3/2}\frac{r}{R}\right)}{J_0\left(\alpha i^{3/2}\right)}}{1-\frac{2J_1\left(\alpha i^{3/2}\right)}{\alpha i^{3/2}J_0\left(\alpha i^{3/2}\right)}}\right]e^{i\omega t}\right\}\right)\Bigg|_{r=R} =$$
$$\sum_n \text{Real}\left\{\frac{\mu Q_n}{\pi R^2}\frac{e^{i\omega t}}{1-\frac{2J_1\left(\alpha i^{3/2}\right)}{\alpha i^{3/2}J_0\left(\alpha i^{3/2}\right)}}\left[-\frac{1}{J_0\left(\alpha i^{3/2}\right)}\frac{d}{dr}\left(J_0\left(\alpha i^{3/2}\frac{r}{R}\right)\right)\Bigg|_{r=R}\right]\right\} \tag{A.26}$$

To solve the term $\frac{\mathrm{d}}{\mathrm{d}r}\left(J_0\left(\alpha i^{3/2}\frac{r}{R}\right)\right)$, let's consider once more the substitution $w = \alpha i^{3/2}\frac{r}{R}$, with $r = \frac{R}{\alpha i^{3/2}}w$ and $\mathrm{d}r = \frac{R}{\alpha i^{3/2}}\mathrm{d}w$, then we obtain:

$$\frac{\mathrm{d}}{\mathrm{d}r}\left(J_0\left(\alpha i^{3/2}\frac{r}{R}\right)\right)\bigg|_{r=R} = \frac{w}{r}\frac{\mathrm{d}}{\mathrm{d}w}\left(J_0(w)\right) \tag{A.27}$$

By applying the property [238]:

$$x\frac{\mathrm{d}}{\mathrm{d}x}J_k(x) = kJ_k(x) - xJ_{k+1}(x) \tag{A.28}$$

the following equation is obtained:

$$\frac{\mathrm{d}}{\mathrm{d}r}\left(J_0\left(\alpha i^{3/2}\frac{r}{R}\right)\right)\bigg|_{r=R} = -\frac{w}{r}J_1(w) \tag{A.29}$$

Converting back the solution and evaluating in $r = R$, the derivative is finally calculated as:

$$\frac{\mathrm{d}}{\mathrm{d}r}\left(J_0\left(\alpha i^{3/2}\frac{r}{R}\right)\right)\bigg|_{r=R} = -\frac{\alpha i^{3/2}}{R}J_1(\alpha i^{3/2}) \tag{A.30}$$

By substituting this result in equation (A.26),

$$\mu\frac{\partial}{\partial r}\left(\sum_n \text{Real}\left\{\frac{Q_n}{\pi R^2}\left[\frac{1-\dfrac{J_0\left(\alpha i^{3/2}\frac{r}{R}\right)}{J_0\left(\alpha i^{3/2}\right)}}{1-\dfrac{2J_1\left(\alpha i^{3/2}\right)}{\alpha i^{3/2}J_0\left(\alpha i^{3/2}\right)}}\right]e^{i\omega t}\right\}\right)\Bigg|_{r=R} =$$
$$\sum_n \text{Real}\left\{\frac{\mu Q_n}{\pi R^2}\left[\frac{\dfrac{\alpha i^{3/2}}{R}\dfrac{J_1\left(\alpha i^{3/2}\right)}{J_0\left(\alpha i^{3/2}\right)}}{1-\dfrac{2J_1\left(\alpha i^{3/2}\right)}{\alpha i^{3/2}J_0\left(\alpha i^{3/2}\right)}}\right]e^{i\omega t}\right\} \tag{A.31}$$

Finally, by substituting the results of (A.25) and (A.31) in equation (A.24) and rearranging, we obtain a general equation for the wall shear stress as:

$$\tau = -\frac{4\mu}{\pi R^3}Q_1 + \sum_n \text{Real}\left\{\frac{\mu}{\pi R^3}Q_n\alpha i^{3/2}\left[\frac{\dfrac{J_1\left(\alpha i^{3/2}\right)}{J_0\left(\alpha i^{3/2}\right)}}{1-\dfrac{2J_1\left(\alpha i^{3/2}\right)}{\alpha i^{3/2}J_0\left(\alpha i^{3/2}\right)}}\right]e^{i\omega t}\right\} \tag{A.32}$$

APPENDIX B: SUPPLEMENTAL FIGURES

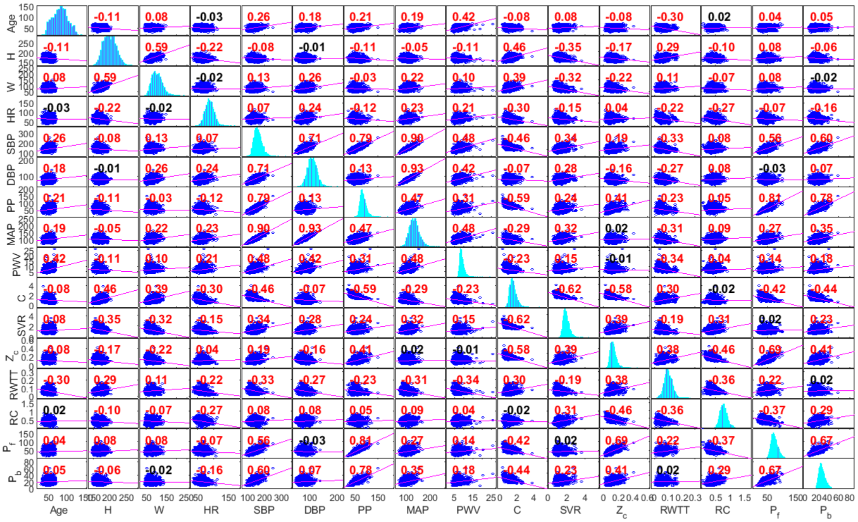

Figure B.1: Correlation matrix of key variables in the analyses. Values in red indicate significant correlation. H: height; W: weight; SBP: carotid systolic blood pressure; PP: carotid pulse pressure; C: volume compliance (C_{PPM}); RC: amplitude of the reflection coefficient at the heart frequency ($|\Gamma_1|$).

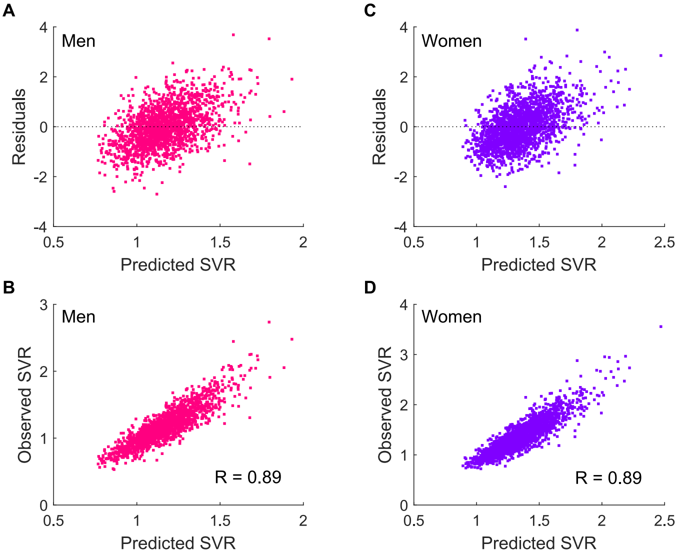

Figure B.2: Residuals versus predicted values of SVR for men and women (A and C). Correlation between observed and predicted values of SVR for men and women (B and D). The plots refer to model in Table 6.13.

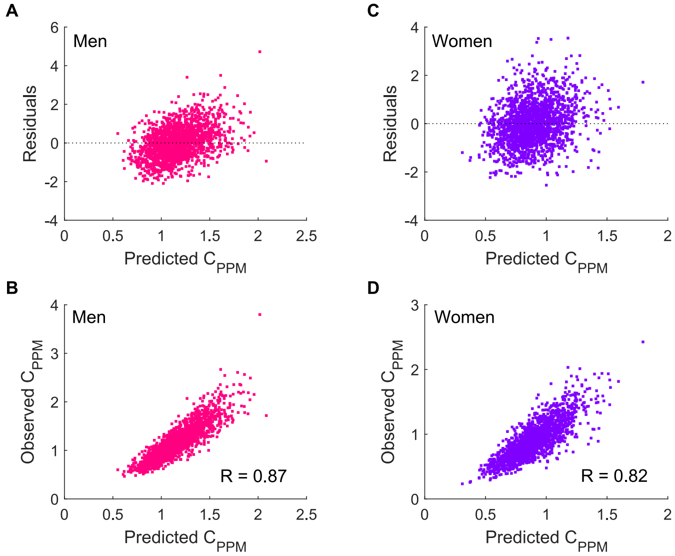

Figure B.3: Residuals versus predicted values of C_{PPM} for men and women (A and C). Correlation between observed and predicted values of C_{PPM} for men and women (B and D). The plots refer to models in Table 6.14.

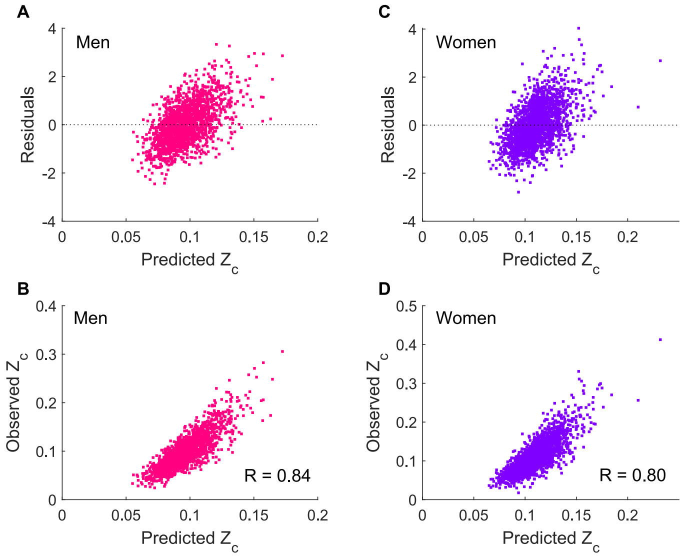

Figure B.4: Residuals versus predicted values of Z_c for men and women (A and C). Correlation between observed and predicted values of Z_c for men and women (B and D). The plots refer to models in Table 6.15.

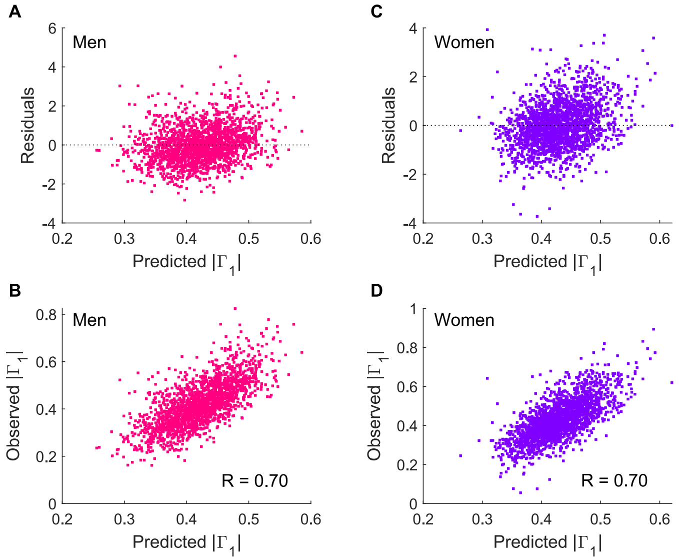

Figure B.5: Residuals versus predicted values of $|\Gamma_1|$ for men and women (A and C). Correlation between observed and predicted values of $|\Gamma_1|$ for men and women (B and D). The plots refer to the models in Table 6.16.

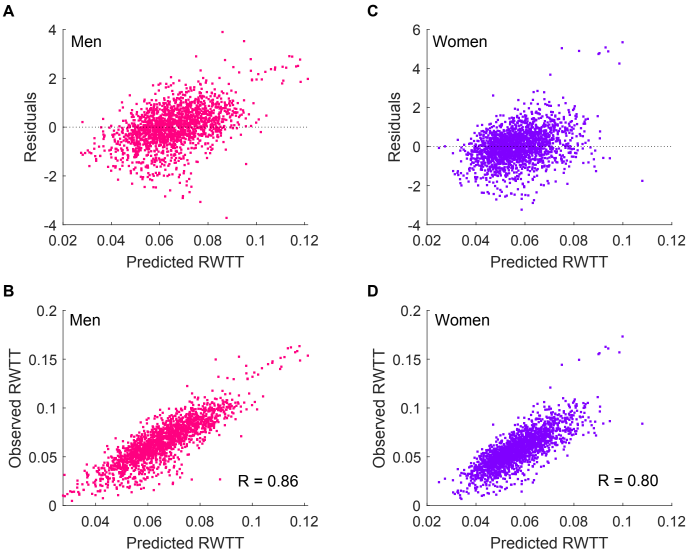

Figure B.6: Residuals versus predicted values of RWTT for men and women (A and C). Correlation between observed and predicted values of RWTT for men and women (B and D). The plots refer to the models in Table 6.17.

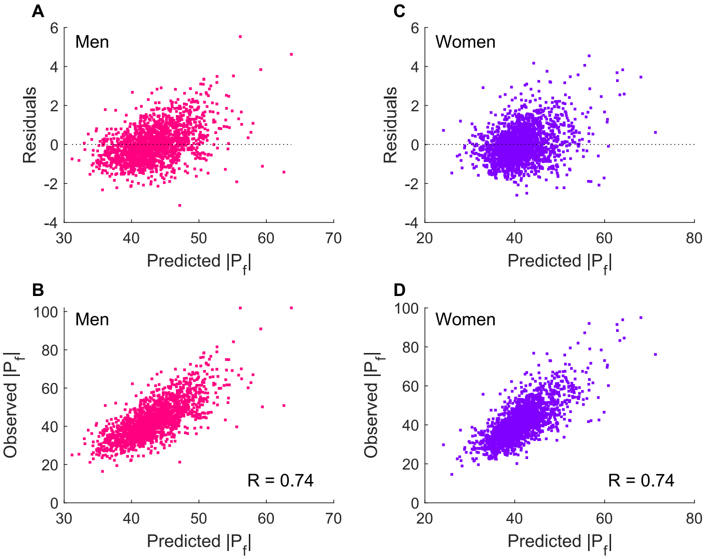

Figure B.7: Residuals versus predicted values of $|P_\mathrm{f}|$ for men and women (A and C). Correlation between observed and predicted values of $|P_\mathrm{f}|$ for men and women (B and D). The plots refer to the models in Table 6.18.

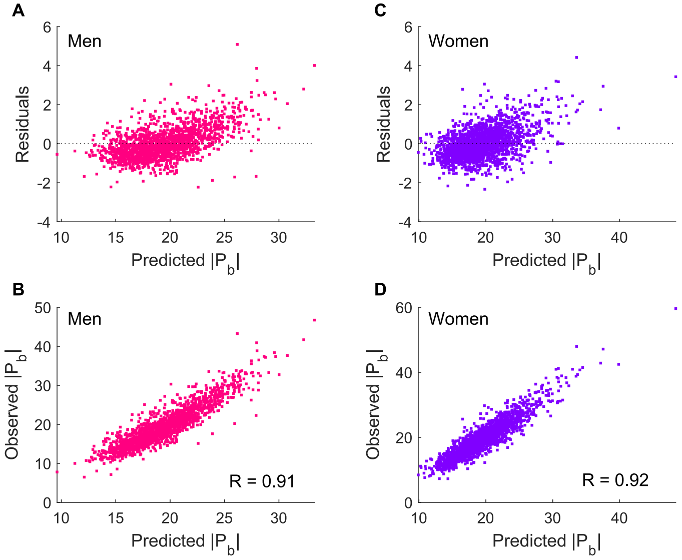

Figure B.8: Residuals versus predicted values of $|P_\mathrm{b}|$ for men and women (A and C). Correlation between observed and predicted values of $|P_\mathrm{b}|$ for men and women (B and D). The plots refer to the models in Table 6.19.

APPENDIX C: SUPPLEMENTAL TABLES

Table C.1: Generalized LME models examining the associations between PWV and traditional CV risk factors for men and women.

	Men			**Women**		
Variables	Estimate	SE	P-value	Estimate	SE	P-value
Intercept	1.5197	0.0286	0.0000	1.5855	0.0388	1.97E-264
Time	0.0065	0.0008	1.33E-15	-0.0033	0.0056	0.5583
Entry-Age	0.0098	0.0008	7.05E-32	0.0095	0.0008	9.46E-34
HR	0.0049	0.0005	4.87E-25	0.0034	0.0006	6.26E-09
HR×Time	-	-	-	0.0002	0.0001	0.0079
Obesity	0.0498	0.0142	0.0005	0.0373	0.0139	0.0073
Overweight	0.0147	0.0093	0.1141	0.0117	0.0093	0.2072
Diabetes (Yes)	-	-	-	-0.0374	0.0366	0.3071
Diabetes (Yes)×Entry-Age	-	-	-	0.0181	0.0069	0.0086
Hypertension (Yes)	0.1010	0.0092	4.18E-27	0.1334	0.0092	2.12E-45
Lipid-lowering drugs (Yes)	-0.4882	0.0902	7.17E-08	-0.4961	0.1039	1.94E-06
Lipid-lowering drugs (Yes)×Time	0.0471	0.0089	1.31E-07	0.0476	0.0103	4.04E-06
Lipid-lowering drugs (Yes)×Entry-Age	0.0045	0.0022	0.0364	-	-	-
Weekly alcohol intake	0.0006	0.0003	0.0270	-	-	-
Education (not beyond secondary school)	-0.0200	0.0092	0.0290	-	-	-
R (Obs. vs. Pred.)		0.897			0.887	
R^2		0.938			0.943	

Table C.2: Generalized LME models examining the association between SVR and traditional CV risk factors for men and women.

	Men			**Women**		
Variables	Estimate	SE	P-value	Estimate	SE	P-value
Intercept	0.4872	0.0410	2.03E-31	0.7013	0.0387	6.77E-68
Time	0.0065	0.0051	0.2050	0.0012	0.001	0.2278
Entry-Age	0.0149	0.0059	0.0112	0.0030	0.0010	0.0020
HR	-0.0051	0.0007	1.84E-14	-0.0068	0.0006	2.78E-30
HR×Time	-0.0002	0.0001	0.0363	-	-	-
HR×Entry-Age	-0.0002	0.0001	0.0187	-	-	-
Obesity	-0.0666	0.0172	0.0001	-0.0499	0.0167	2.82E-03
Overweight	-0.0411	0.0112	0.0003	-0.0265	0.011	0.0156
Diabetes (Yes)	-	-	-	-0.1048	0.0383	0.0063
Hypertension (Yes)	0.1198	0.0108	1.68E-27	0.1649	0.0141	1.54E-30
Hypertension (Yes)×Time	-	-	-	-0.0056	0.0017	0.0012
Education (not beyond secondary school)	-0.0327	0.0120	0.0063	-	-	-
R (Obs. vs. Pred.)		0.881			0.897	
R^2		0.194			0.419	

Table C.3: Generalized LME models examining the association between C_{PPM} and traditional CV risk factors for men and women.

	Men			Women		
Variables	Estimate	SE	P-value	Estimate	SE	P-value
Intercept	0.6022	0.0464	5.91E-37	0.3637	0.0478	4.43E-14
Time	0.0011	0.0028	0.6913	0.0025	0.0010	0.0128
Entry-Age	-0.0020	0.0014	0.1474	-0.0081	0.0014	3.14E-09
Entry-Age×Time	-0.0006	0.0002	0.0018	-	-	-
HR	-0.0083	0.0007	1.12E-32	-0.0073	0.0007	3.01E-23
Obesity	0.1367	0.0212	1.40E-10	0.1584	0.0205	1.63E-14
Overweight	0.0646	0.0140	4.14E-06	0.0771	0.0136	1.79E-08
Diabetes (Yes)	-0.0854	0.0346	0.0137	0.1017	0.0504	0.0439
Diabetes (Yes)×Entry-Age	-	-	-	-0.0170	0.0096	0.0771
Smoker (Ex-smoker)	0.0095	0.0213	0.6565	-	-	-
Smoker (Never smoked)	0.0431	0.0204	0.0351	-	-	-
Smoker (Ex-smoker)×Time	0.0063	0.0033	0.0617	-	-	-
Smoker (Never smoked)×Time	0.0061	0.0032	0.0539	-	-	-
Hypertension (Yes)	-0.1612	0.0138	2.89E-30	-0.2495	0.0134	1.64E-71
Hypertension (Yes)×Entry-Age	-	-	-	-0.0066	0.0021	0.0019
R (Obs. vs. Pred.)		0.870			0.867	
R^2		0.371			0.320	

Table C.4: Generalized LME models examining the association between Z_c and traditional CV risk factors for men and women.

	Men			Women		
Variables	Estimate	SE	P-value	Estimate	SE	P-value
Intercept	-2.4293	0.0571	1.32E-274	-2.1993	0.0151	0.0000
Time	-0.0100	0.0018	1.52E-08	-0.0072	0.0015	1.82E-06
Entry-Age	-0.0104	0.0019	2.46E-08	-0.0083	0.0019	2.36E-05
(Entry-Age)^2	0.0008	0.0003	0.0022	0.0005	0.0003	0.0365
Entry-Age×Time	0.0007	0.0002	0.0049	0.0007	0.0002	0.0038
HR	0.0017	0.0009	0.0624	-	-	-
Obesity	-0.1179	0.0277	2.24E-05	-0.1185	0.0268	1.04E-05
Overweight	-0.0401	0.0185	0.0302	-0.0799	0.0182	1.20E-05
Diabetes (Yes)	0.0515	0.0488	0.2912	-	-	-
Diabetes (Yes)×Entry-Age	0.0191	0.0081	0.0184	-	-	-
Hypertension (Yes)	0.0197	0.0247	0.4248	0.1206	0.0180	3.03E-11
Hypertension (Yes)×Time	0.0087	0.0031	0.0052	-	-	-
Hypertension (Yes)×Entry-Age	-	-	-	0.0100	0.0030	0.0008
Lipid-lowering drugs (Yes)	-	-	-	-0.5348	0.1928	0.0056
Lipid-lowering drugs (Yes)×Time	-	-	-	0.0490	0.0189	0.0096
R (Obs. vs. Pred.)		0.841			0.801	
R^2		0.247			0.208	

Table C.5: LME models examining the association between $|\Gamma_1|$ and traditional CV risk factors for men and women.

	Men			Women		
Variables	Estimate	SE	P-value	Estimate	SE	P-value
Intercept	0.6668	0.0155	1.59E-278	0.6703	0.0212	4.69E-177
Time	-0.0021	0.0012	0.0717	-0.0104	0.0032	0.0014
Entry-Age	0.0036	0.0006	4.05E-10	0.0025	0.0004	2.62E-09
(Entry-Age)^2	-0.0002	0.0001	0.0007	-	-	-
HR	-0.0036	0.0002	4.22E-55	-0.0035	0.0003	6.17E-29
HR×Time	-	-	-	0.0001	4.70E-05	0.0024
Obesity	-0.0027	0.0084	0.7466	-0.0131	0.0096	0.1745
Overweight	-0.0088	0.0053	0.0980	-0.0073	0.0062	0.2424
Obesity×Time	0.0030	0.0012	0.0120	0.0032	0.0012	0.0112
Overweight×Time	0.0013	0.0009	0.1241	0.0024	0.0009	0.0098
Diabetes (Yes)	-0.0024	0.0131	0.8534	-	-	-
Diabetes (Yes)×Entry-Age	-0.0047	0.0021	0.0253	-	-	-
Smoker (Ex-smoker)	0.0001	0.0069	0.9860	-0.0008	0.0085	0.9219
Smoker (Never smoked)	0.0068	0.0065	0.2995	-0.0092	0.0072	0.2029
Smoker (Ex-smoker)×Time	-0.0026	0.0012	0.0313	-0.0029	0.0014	0.0349
Smoker (Never smoked)×Time	-0.0036	0.0012	0.0018	-0.0011	0.0012	0.3749
Hypertension (Yes)	0.0303	0.0059	3.73E-07	0.0304	0.0065	3.23E-06
Hypertension (Yes)×Time	-0.0020	0.0008	0.0178	-0.0021	0.0009	0.0170
Lipid-lowering drugs (Yes)	-	-	-	0.1315	0.0582	0.0240
Lipid-lowering drugs (Yes)×Time	-	-	-	-0.0136	0.0058	0.0189
Education (not beyond secondary school)	-0.0031	0.0044	0.4827	-	-	-
Education (not beyond secondary school)×Time	-0.0020	0.0007	0.0071	-	-	-
R (Obs. vs. Pred.)		0.868			0.879	
R^2		0.519			0.471	

Table C.6: LME models examining the association between $|P_f|$ and traditional CV risk factors for men and women.

	Men			Women		
Variables	Estimate	SE	P-value	Estimate	SE	P-value
Intercept	44.4901	1.6067	1.28E-140	44.0198	1.5827	8.33E-144
Time	-0.1748	0.0681	0.0103	-0.2053	0.0472	1.44E-05
Entry-Age	-0.2809	0.0525	9.88E-08	-0.0905	0.0476	0.0574
(Entry-Age)^2	0.0323	0.0089	0.0003	0.0150	0.0062	0.0151
Entry-Age×Time	0.0270	0.0072	0.0002	0.0159	0.0063	0.0125
(Entry-Age)^2×Time	-0.0022	0.0012	0.0612	-	-	-
HR	-0.0545	0.0250	0.0296	-0.0810	0.0238	0.0007
Diabetes (Yes)	2.6433	1.3918	0.0577	-	-	-
Diabetes (Yes)×Entry-Age	0.5372	0.2281	0.0186	-	-	-
Hypertension (Yes)	3.7852	0.7046	0.0000	7.7663	0.6228	2.11E-34
Hypertension (Yes)×Time	0.2518	0.0919	0.0062	0.2363	0.0818	0.0039
Hypertension (Yes)×Entry-Age	-	-	-	0.3333	0.0757	1.12E-05
Lipid-lowering drugs (Yes)	10.0653	4.9305	0.0414	-2.4072	0.7726	0.0019
Lipid-lowering drugs (Yes)×Time	0.9069	0.4854	0.0619	-	-	-
Education (not beyond secondary school)	0.4946	0.5001	0.3228	-	-	-
R (Obs. vs. Pred.)		0.770			0.811	
R^2		0.312			0.451	

Table C.7: LME models examining the association between $|P_b|$ and traditional CV risk factors for men and women.

	Men			Women		
Variables	Estimate	SE	P-value	Estimate	SE	P-value
Intercept	27.1468	0.7945	1.16E-197	25.7834	0.8803	9.57E-157
Time	-0.2374	0.0222	7.81E-26	-0.2467	0.0535	4.23E-06
Entry-Age	0.0303	0.0206	0.1413	0.0851	0.0231	0.0002
HR	-0.1167	0.0119	2.84E-22	-0.1035	0.0125	2.14E-16
Diabetes (Yes)	0.8516	0.6313	0.1775	-	-	-
Diabetes (Yes)×Entry-Age	0.2321	0.1028	0.0241	-	-	-
Smoker (Ex-smoker)	-0.5598	0.3304	0.0903	-0.4195	0.4404	0.3410
Smoker (Never smoked)	-0.9376	0.3234	0.0038	-0.7357	0.3716	0.0479
Smoker (Ex-smoker)×Time	-	-	-	0.0154	0.0655	0.8141
Smoker (Never smoked)×Time	-	-	-	0.1040	0.0581	0.0738
Hypertension (Yes)	3.5643	0.2415	1.27E-46	5.2166	0.2368	2.79E-96
Hypertension (Yes)×Entry-Age	-	-	-	0.1649	0.0379	1.39E-05
Lipid-lowering drugs (Yes)	-6.6480	2.2426	0.0031	-1.0349	0.3898	0.0080
Lipid-lowering drugs (Yes)×Time	0.6239	0.2216	0.0049	-	-	-
R (Obs. vs. Pred.)		0.837			0.700	
R^2		0.432			0.387	

BIBLIOGRAPHY

[1] World Health Organization website, *https://www.who.int/health-topics/cardiovascular-diseases*, Cardiovascular diseases, (online; accessed 01 Feb. 2021).

[2] S. Laurent, P. Boutouyrie, R. Asmar, I. Gautier, B. Laloux, L. Guize, P. Ducimetiere and A. Benetos, 'Aortic stiffness is an independent predictor of all-cause and cardiovascular mortality in hypertensive patients', *Hypertension*, vol. 37, no. 5, pp. 1236–1241, 2001.

[3] C. Vlachopoulos, K. Aznaouridis, M. F. O'Rourke, M. E. Safar, K. Baou and C. Stefanadis, 'Prediction of cardiovascular events and all-cause mortality with central haemodynamics: A systematic review and meta-analysis', *European Heart Journal*, vol. 31, no. 15, pp. 1865–1871, 2010.

[4] Y. Ben-Shlomo, M. Spears, C. Boustred, M. May, S. G. Anderson, E. J. Benjamin, P. Boutouyrie, J. Cameron, C.-H. Chen, J. K. Cruickshank, S.-J. Hwang, E. G. Lakatta, S. Laurent, J. Maldonado, G. F. Mitchell, S. S. Najjar, A. B. Newman, M. Ohishi, B. Pannier, T. Pereira, R. S. Vasan, T. Shokawa, K. Sutton-Tyrell, F. Verbeke, K.-L. Wang, D. J. Webb, T. W. Hansen, S. Zoungas, C. M. McEniery, J. R. Cockcroft and I. B. Wilkinson, 'Aortic pulse wave velocity improves cardiovascular event prediction. An individual participant meta-analysis of prospective observational data from 17635 subjects', *Journal of the American College of Cardiology*, vol. 63, no. 7, pp. 636–646, 2014.

[5] E. J. Benjamin, P. Muntner, A. Alonso, M. S. Bittencourt, C. W. Callaway, A. P. Carson, A. M. Chamberlain, A. R. Chang, S. Cheng, S. R. Das *et al.*, 'Heart disease and stroke statistics—2019 update: A report from the American Heart Association', *Circulation*, vol. 139, no. 10, e56–e528, 2019.

[6] N. Westerhof, P. Sipkema, G. V. D. Bos and G. Elzinga, 'Forward and backward waves in the arterial system', *Cardiovascular research*, vol. 6, no. 6, pp. 648–656, 1972.

[7] S. S. Franklin, W. Gustin IV, N. D. Wong, M. G. Larson, M. A. Weber, W. B. Kannel and D. Levy, 'Hemodynamic patterns of age-related changes in blood pressure: The Framingham Heart Study', *Circulation*, vol. 96, no. 1, pp. 308–315, 1997.

[8] W. W. Nichols, M. O'Rourke and C. Vlachopoulos, 'McDonald's blood flow in arteries: theoretical, experimental and clinical principles', 6th ed. CRC press, 2011.

[9] M. F. O'Rourke and W. W. Nichols, 'Aortic diameter, aortic stiffness, and wave reflection increase with age and isolated systolic hypertension', *Hypertension*, vol. 45, no. 4, pp. 652–658, 2005.

[10] G. F. Mitchell, H. Parise, E. J. Benjamin, M. G. Larson, M. J. Keyes, J. A. Vita, R. S. Vasan and D. Levy, 'Changes in arterial stiffness and wave reflection with advancing age in healthy men and women. the Framingham Heart Study', *Hypertension*, vol. 43, no. 6, pp. 1239–1245, 2004.

[11] G. F. Mitchell, P. R. Conlin, M. E. Dunlap, Y. Lacourciere, J. M. O. Arnold, R. I. Ogilvie, J. Neutel, J. L. Izzo Jr and M. A. Pfeffer, 'Aortic diameter, wall stiffness, and wave reflection in systolic hypertension', *Hypertension*, vol. 51, no. 1, pp. 105–111, 2008.

[12] P. Reymond, F. Merenda, F. Perren, D. Rüfenacht and N. Stergiopulos, 'Validation of a one-dimensional model of the systemic arterial tree', *American Journal of Physiology-Heart and Circulatory Physiology*, vol. 297, no. 1, H208–H222, 2009.

[13] S. M. Grundy, G. J. Balady, M. H. Criqui, G. Fletcher, P. Greenland, L. F. Hiratzka, N. Houston-Miller, P. Kris-Etherton, H. M. Krumholz, J. LaRosa *et al.*, 'Primary prevention of coronary heart disease: guidance from Framingham. A statement for healthcare professionals from the AHA Task Force on Risk Reduction', *Circulation*, vol. 97, no. 18, pp. 1876–1887, 1998.

[14] The Reference Values for Arterial Stiffness' Collaboration, 'Determinants of pulse wave velocity in healthy people and in the presence of cardiovascular risk factors: 'establishing normal and reference values'', *European Heart Journal*, vol. 31, no. 19, pp. 2338–2350, 2010.

[15] E. R. Rietzschel, M. L. De Buyzere, S. Bekaert, P. Segers, D. De Bacquer, L. Cooman, P. Van Damme, P. Cassiman, M. Langlois, P. van Oostveldt, P. Verdonck, G. De Backer, T. C. Gillebert and on behalf of the Asklepios investigators, 'Rationale, design, methods and baseline characteristics of the Asklepios study', *European Journal of Cardiovascular Prevention & Rehabilitation*, vol. 14, no. 2, pp. 179–191, 2007.

[16] B. Trachet, P. Reymond, J. Kips, A. Swillens, M. De Buyzere, B. Suys, N. Stergiopulos and P. Segers, 'Numerical validation of a new method to assess aortic pulse wave velocity from a single recording of a brachial artery waveform with an occluding cuff', *Annals of Biomedical Engineering*, vol. 38, no. 3, pp. 876–888, 2010.

[17] P. Reymond, N. Westerhof and N. Stergiopulos, 'Systolic hypertension mechanisms: Effect of global and local proximal aorta stiffening on pulse pressure', *Annals of Biomedical Engineering*, vol. 40, no. 3, pp. 742–749, 2012.

[18] O. Vardoulis, T. G. Papaioannou and N. Stergiopulos, 'On the estimation of total arterial compliance from aortic pulse wave velocity', *Annals of Biomedical Engineering*, vol. 40, no. 12, pp. 2619–2626, 2012.

[19] H. Obeid, G. Soulat, E. Mousseaux, S. Laurent, N. Stergiopulos, P. Boutouyrie and P. Segers, 'Numerical assessment and comparison of pulse wave velocity methods aiming at measuring aortic stiffness', *Physiological Measurement*, vol. 38, no. 11, pp. 1953–1967, 2017.

[20] S. Pagoulatou and N. Stergiopulos, 'Evolution of aortic pressure during normal ageing: A model-based study', *PLoS One*, vol. 12, no. 7, e0182173, 2017.

[21] S. Z. Pagoulatou and N. Stergiopulos, 'Estimating left ventricular elastance from aortic flow waveform, ventricular ejection fraction, and brachial pressure: An in silico study', *Annals of Biomedical Engineering*, pp. 1–14, 2018.

[22] V. Bikia, S. Pagoulatou, B. Trachet, D. Soulis, A. Protogerou, T. Papaioannou and N. Stergiopulos, 'Noninvasive cardiac output and central systolic pressure from cuff-pressure and pulse wave velocity: A model-based study', *IEEE Journal of Biomedical and Health Informatics*, 2019.

[23] R. E. Klabunde, 'Cardiovascular physiology concepts', 2nd ed. Lippincott Williams & Wilkins, 2011.

[24] F. N. van de Vosse and N. Stergiopulos, 'Pulse wave propagation in the arterial tree', *Annual Review of Fluid Mechanics*, vol. 43, pp. 467–499, 2011.

[25] J. A. Chirinos and P. Segers, 'Noninvasive evaluation of left ventricular afterload: Part 1: Pressure and flow measurements and basic principles of wave conduction and reflection', *Hypertension*, vol. 56, no. 4, pp. 555–562, 2010.

[26] J. E. Wagenseil and R. P. Mecham, 'Vascular extracellular matrix and arterial mechanics', *Physiological Reviews*, vol. 89, no. 3, pp. 957–989, 2009.

[27] G. J. Tortora and B. Derrickson, 'Principles of Anatomy & Physiology', 15th ed. John Wiley & Sons, Inc., 2017.

[28] C. Caro, T. Pedley, R. Schroter, W. Seed and K. Parker, 'The Mechanics of the Circulation', 2nd ed. Cambridge University Press, 2012.

[29] P. Lacolley, V. Regnault, P. Segers and S. Laurent, 'Vascular smooth muscle cells and arterial stiffening: Relevance in development, aging, and disease', *Physiological Reviews*, vol. 97, no. 4, pp. 1555–1617, 2017.

[30] W. W. Nichols, S. J. Denardo, I. B. Wilkinson, C. M. McEniery, J. Cockcroft and M. F. O'Rourke, 'Effects of arterial stiffness, pulse wave velocity, and wave reflections on the central aortic pressure waveform', *The Journal of Clinical Hypertension*, vol. 10, no. 4, pp. 295–303, 2008.

[31] N. Westerhof, N. Stergiopulos, M. I. Noble and B. E. Westerhof, 'Snapshots of hemodynamics: An aid for clinical research and graduate education', 3rd ed. Switzerland: Springer, 2019.

[32] P. Ponikowski, A. A. Voors, S. D. Anker, H. Bueno, J. G. Cleland, A. J. Coats, V. Falk, J. R. Gonzalez-Juanatey, V.-P. Harjola, E. A. Jankowska *et al.*, '2016 ESC guidelines for the diagnosis and treatment of acute and chronic heart failure: The task force for the diagnosis and treatment of acute and chronic heart failure of the European Society of Cardiology (ESC) developed with the special contribution of the Heart Failure Association (HFA) of the ESC', *European Heart Journal*, vol. 37, no. 27, pp. 2129–2200, 2016.

[33] M. R. Zile and D. L. Brutsaert, 'New concepts in diastolic dysfunction and diastolic heart failure: Part I: Diagnosis, prognosis, and measurements of diastolic function', *Circulation*, vol. 105, no. 11, pp. 1387–1393, 2002.

[34] S. Gafoor, J. Franke, S. Lam, M. Reinartz, S. Bertog, L. Vaskelyte, I. Hofmann and H. Sievert, 'Devices in heart failure: The new revolution', *Circulation Journal*, vol. 79, no. 2, pp. 237–244, 2015.

[35] M. F. O'Rourke, 'Arterial aging: Pathophysiological principles', *Vascular Medicine*, vol. 12, no. 4, pp. 329–341, 2007.

[36] S. Greenwald, 'Ageing of the conduit arteries', *Journal of Pathology*, vol. 211, no. 2, pp. 157–172, 2007.

[37] R. Virmani, A. Avolio, W. Mergner, M. Robinowitz, E. Herderick, J. Cornhill, S. Guo, T. Liu, D. Ou and M. O'Rourke, 'Effect of aging on aortic morphology in populations with high and low prevalence of hypertension and atherosclerosis. Comparison between occidental and chinese communities.' *The American Journal of Pathology*, vol. 139, no. 5, p. 1119, 1991.

[38] J. Sugawara, K. Hayashi, T. Yokoi and H. Tanaka, 'Age-associated elongation of the ascending aorta in adults', *JACC: Cardiovascular Imaging*, vol. 1, no. 6, pp. 739–748, 2008.

[39] C. S. Lam, V. Xanthakis, L. M. Sullivan, W. Lieb, J. Aragam, M. M. Redfield, G. F. Mitchell, E. J. Benjamin and R. S. Vasan, 'Aortic root remodeling over the adult life course: Longitudinal data from the Framingham Heart Study', *Circulation*, vol. 122, no. 9, pp. 884–890, 2010.

[40] L. Horny, T. Adamek and R. Zitny, 'Age-related changes in longitudinal prestress in human abdominal aorta', *Archive of Applied Mechanics*, vol. 83, no. 6, pp. 875–888, 2013.

[41] A. Benetos, S. Laurent, A. Hoeks, P. Boutouyrie and M. Safar, 'Arterial alterations with aging and high blood pressure. A noninvasive study of carotid and femoral arteries.' *Arteriosclerosis and Thrombosis: a Journal of Vascular Biology*, vol. 13, no. 1, pp. 90–97, 1993.

[42] C. M. McEniery, I. B. Wilkinson and A. P. Avolio, 'Age, hypertension and arterial function', *Clinical and Experimental Pharmacology and Physiology*, vol. 34, no. 7, pp. 665–671, 2007.

[43] J. Blacher, A. P. Guerin, B. Pannier, S. J. Marchais, M. E. Safar and G. M. London, 'Impact of aortic stiffness on survival in end-stage renal disease', *Circulation*, vol. 99, no. 18, pp. 2434–2439, 1999.

[44] J. Blacher, B. Pannier, A. P. Guerin, S. J. Marchais, M. E. Safar and G. M. London, 'Carotid arterial stiffness as a predictor of cardiovascular and all-cause mortality in end-stage renal disease', *Hypertension*, vol. 32, no. 3, pp. 570–574, 1998.

[45] S. Laurent, J. Cockcroft, L. Van Bortel, P. Boutouyrie, C. Giannattasio, D. Hayoz, B. Pannier, C. Vlachopoulos, I. Wilkinson, H. Struijker-Boudier and on behalf of the European Network for Non-invasive Investigation of Large Arteries, 'Expert consensus document on arterial stiffness: Methodological issues and clinical applications', *European Heart Journal*, vol. 27, no. 21, pp. 2588–2605, 2006.

[46] J. A. Chirinos, P. Segers, T. Hughes and R. Townsend, 'Large-artery stiffness in health and disease: JACC state-of-the-art review', *Journal of the American College of Cardiology*, vol. 74, no. 9, pp. 1237–1263, 2019.

[47] J. C. Bramwell and A. V. Hill, 'The velocity of the pulse wave in man', *Proceedings of the Royal Society of London. Series B, Containing Papers of a Biological Character*, vol. 93, no. 652, pp. 298–306, 1922.

[48] D. McDonald, 'Regional pulse-wave velocity in the arterial tree.' *Journal of Applied Physiology*, vol. 24, no. 1, pp. 73–78, 1968.

[49] K. Cruickshank, L. Riste, S. G. Anderson, J. S. Wright, G. Dunn and R. G. Gosling, 'Aortic pulse-wave velocity and its relationship to mortality in diabetes and glucose intolerance: An integrated index of vascular function?', *Circulation*, vol. 106, no. 16, pp. 2085–2090, 2002.

[50] P. Boutouyrie, A. I. Tropeano, R. Asmar, I. Gautier, A. Benetos, P. Lacolley and S. Laurent, 'Aortic stiffness is an independent predictor of primary coronary events in hypertensive patients: A longitudinal study', *Hypertension*, vol. 39, no. 1, pp. 10–15, 2002.

[51] A. P. Guerin, J. Blacher, B. Pannier, S. J. Marchais, M. E. Safar and G. M. London, 'Impact of aortic stiffness attenuation on survival of patients in end-stage renal failure', *Circulation*, vol. 103, no. 7, pp. 987–992, 2001.

[52] A. G. Sorace, M. L. Robbin, H. Umphrey, C. A. Abts, J. L. Berry, M. E. Lockhart, M. Allon and K. Hoyt, 'Ultrasound measurement of brachial artery elasticity prior to hemodialysis access placement', *Journal of Ultrasound in Medicine*, vol. 31, no. 10, pp. 1581–1588, 2012.

[53] K. Sutton-Tyrrell, S. S. Najjar, R. M. Boudreau, L. Venkitachalam, V. Kupelian, E. M. Simonsick, R. Havlik, E. G. Lakatta, H. Spurgeon, S. Kritchevsky, M. Pahor, D. Bauer, A. Newman and for the Health ABC Study, 'Elevated aortic pulse wave velocity, a marker of arterial stiffness, predicts cardiovascular events in well-functioning older adults', *Circulation*, vol. 111, no. 25, pp. 3384–3390, 2005.

[54] G. F. Mitchell, S.-J. Hwang, R. S. Vasan, M. G. Larson, M. J. Pencina, N. M. Hamburg, J. A. Vita, D. Levy and E. J. Benjamin, 'Arterial stiffness and cardiovascular events: The Framingham Heart Study', *Circulation*, vol. 121, no. 4, pp. 505–511, 2010.

[55] Y. Ohyama, B. Ambale-Venkatesh, C. Noda, J.-Y. Kim, Y. Tanami, G. Teixido-Tura, A. R. Chugh, A. Redheuil, C.-Y. Liu and C. O. Wu, 'Aortic arch pulse wave velocity assessed by magnetic resonance imaging as a predictor of incident cardiovascular events: The MESA (Multi-Ethnic Study of Atherosclerosis)', *Hypertension*, vol. 70, no. 3, pp. 524–530, 2017.

[56] A. P. Avolio, S. G. Chen, R. P. Wang, C. L. Zhang, M. F. Li and M. F. O'Rourke, 'Effects of aging on changing arterial compliance and left ventricular load in a northern Chinese urban community', *Circulation*, vol. 68, no. 1, pp. 50–58, 1983.

[57] A. P. Avolio, F. Q. Deng, W. Q. Li, Y. F. Luo, Z. D. Huang, L. F. Xing and M. F. O'Rourke, 'Effects of aging on arterial distensibility in populations with high and low prevalence of hypertension: Comparison between urban and rural communities in China', *Circulation*, vol. 71, no. 2, pp. 202–210, 1985.

[58] C. M. McEniery, Yasmin, I. R. Hall, A. Qasem, I. B. Wilkinson, J. R. Cockcroft and on behalf of the ACCT Investigators, 'Normal vascular aging: Differential effects on wave reflection and aortic pulse wave velocity: The Anglo-Cardiff Collaborative Trial (ACCT)', *Journal of the American College of Cardiology*, vol. 46, no. 9, pp. 1753–1760, 2005.

[59] C. M. McEniery, Yasmin, K. M. Maki-Petaja, B. J. McDonnell, M. Munnery, S. S. Hickson, S. S. Franklin, J. R. Cockcroft and I. B. Wilkinson, 'The impact of cardiovascular risk factors on aortic stiffness and wave reflections depends on age: The Anglo-Cardiff Collaborative Trial (ACCT III)', *Hypertension*, vol. 56, no. 4, pp. 591–597, 2010.

[60] B. M. Kaess, J. Rong, M. G. Larson, N. M. Hamburg, J. A. Vita, D. Levy, E. J. Benjamin, R. S. Vasan and G. F. Mitchell, 'Aortic stiffness, blood pressure progression, and incident hypertension', *JAMA*, vol. 308, no. 9, pp. 875–881, 2012.

[61] S. S. Najjar, A. Scuteri, V. Shetty, J. G. Wright, D. C. Muller, J. L. Fleg, H. P. Spurgeon, L. Ferrucci and E. G. Lakatta, 'Pulse wave velocity is an independent predictor of the longitudinal increase in systolic blood pressure and of incident hypertension in the Baltimore Longitudinal Study of Aging', *Journal of the American College of Cardiology*, vol. 51, no. 14, pp. 1377–1383, 2008.

[62] M. AlGhatrif, J. B. Strait, C. H. Morrell, M. Canepa, J. Wright, P. Elango, A. Scuteri, S. S. Najjar, L. Ferrucci and E. G. Lakatta, 'Longitudinal trajectories of arterial stiffness and the role of blood pressure: The Baltimore Longitudinal Study of Aging', *Hypertension*, vol. 62, no. 5, pp. 934–941, 2013.

[63] A. Scuteri, C. H. Morrell, M. Orrù, J. B. Strait, K. V. Tarasov, L. A. P. Ferreli, F. Loi, M. G. Pilia, A. Delitala, H. Spurgeon, S. S. Najjar, M. AlGhatrif and E. G. Lakatta, 'Longitudinal perspective on the conundrum of central arterial stiffness, blood pressure, and aging', *Hypertension*, vol. 64, no. 6, pp. 1219–1227, 2014.

[64] A. Scuteri, C. H. Morrell, D. A. Fegatelli, E. Fiorillo, A. Delitala, M. Marongiu, D. Schlessinger and F. Cucca, 'Arterial stiffness and multiple organ damage: A longitudinal study in population', *Aging Clinical and Experimental Research*, pp. 1–8, 2019.

[65] P. Segers, E. R. Rietzschel, M. L. De Buyzere, S. J. Vermeersch, D. De Bacquer, L. M. Van Bortel, G. De Backer, T. C. Gillebert, P. R. Verdonck and on behalf of the Asklepios investigators, 'Noninvasive (input) impedance, pulse wave velocity, and wave reflection in healthy middle-aged men and women', *Hypertension*, vol. 49, no. 6, pp. 1248–1255, 2007.

[66] O. H. Franco, A. Peeters, L. Bonneux and C. De Laet, 'Blood pressure in adulthood and life expectancy with cardiovascular disease in men and women: Life course analysis', *Hypertension*, vol. 46, no. 2, pp. 280–286, 2005.

[67] P. M. Nilsson, 'Early vascular aging (EVA): Consequences and prevention', *Vascular Health and Risk Management*, vol. 4, no. 3, pp. 547–552, 2008.

[68] P. M. Nilsson, P. Boutouyrie and S. Laurent, 'Vascular aging: A tale of EVA and ADAM in cardiovascular risk assessment and prevention', *Hypertension*, vol. 54, no. 1, pp. 3–10, 2009.

[69] S. Laurent, P. Boutouyrie, P. G. Cunha, P. Lacolley and P. M. Nilsson, 'Concept of extremes in vascular aging: From early vascular aging to supernormal vascular aging', *Hypertension*, vol. 74, no. 2, pp. 218–228, 2019.

[70] P. M. Nilsson, 'Early vascular aging in hypertension', *Frontiers in Cardiovascular Medicine*, vol. 7, no. 6, pp. 1–5, 2020.

[71] P. Segers, E. R. Rietzschel and J. A. Chirinos, 'How to measure arterial stiffness in humans', *Arteriosclerosis, Thrombosis, and Vascular Biology*, vol. 40, no. 5, pp. 1034–1043, 2020.

[72] I. B. Wilkinson, C. M. McEniery, G. Schillaci, P. Boutouyrie, P. Segers, A. Donald, P. J. Chowienczyk *et al.*, 'Artery Society guidelines for validation of non-invasive haemodynamic measurement devices: Part 1, arterial pulse wave velocity', *Artery Research*, vol. 4, no. 2, pp. 34–40, 2010.

[73] T. Weber, S. Wassertheurer, B. Hametner, S. Parragh and B. Eber, 'Noninvasive methods to assess pulse wave velocity: Comparison with the invasive gold standard and relationship with organ damage', *Journal of Hypertension*, vol. 33, no. 5, pp. 1023–1031, 2015.

[74] A. Yamashina, H. Tomiyama, K. Takeda, H. Tsuda, T. Arai, K. Hirose, Y. Koji, S. Hori and Y. Yamamoto, 'Validity, reproducibility, and clinical significance of noninvasive brachial-ankle pulse wave velocity measurement', *Hypertension Research*, vol. 25, no. 3, pp. 359–364, 2002.

[75] K. Shirai, J. Utino, K. Otsuka and M. Takata, 'A novel blood pressure-independent arterial wall stiffness parameter; Cardio-Ankle Vascular Index (CAVI)', *Journal of Atherosclerosis and Thrombosis*, vol. 13, no. 2, pp. 101–107, 2006.

[76] M. Alivon, T. Vo-Duc Phuong, V. Vignon, E. Bozec, H. Khettab, O. Hanon, M. Briet, J.-M. Halimi, M. Hallab, M. Plichart, K. Mohammedi, M. Marre, P. Boutouyrie and S. Laurent, 'A novel device for measuring arterial stiffness using finger-toe pulse wave velocity: Validation study of the pOpmètre®', *Archives of Cardiovascular Disease*, vol. 108, no. 4, pp. 227–234, 2015.

[77] L. M. Van Bortel, S. Laurent, P. Boutouyrie, P. Chowienczyk, J. Cruickshank, T. De Backer, J. Filipovsky, S. Huybrechts, F. U. Mattace-Raso, A. D. Protogerou, G. Schillaci, P. Segers, S. Vermeersch and T. Weber, 'Expert consensus document on the measurement of aortic stiffness in daily practice using carotid-femoral pulse wave velocity', *Journal of Hypertension*, vol. 30, no. 3, pp. 445–448, 2012.

[78] R. R. Townsend, I. B. Wilkinson, E. L. Schiffrin, A. P. Avolio, J. A. Chirinos, J. R. Cockcroft, K. S. Heffernan, E. G. Lakatta, C. M. McEniery and G. F. Mitchell, 'Recommendations for improving and standardizing vascular research on arterial stiffness: A scientific statement from the American Heart Association', *Hypertension*, vol. 66, no. 3, pp. 698–722, 2015.

[79] R. R. Townsend, 'Arterial stiffness: Recommendations and standardization', *Pulse*, vol. 4, no. Suppl. 1, pp. 3–7, 2016.

[80] T. Weber, M. Ammer, M. Rammer, A. Adji, M. F. O'Rourke, S. Wassertheurer, S. Rosenkranz and B. Eber, 'Noninvasive determination of carotid–femoral pulse wave velocity depends critically on assessment of travel distance: A comparison with invasive measurement', *Journal of Hypertension*, vol. 27, no. 8, pp. 1624–1630, 2009.

[81] S. A. Huybrechts, D. G. Devos, S. J. Vermeersch, D. Mahieu, E. Achten, T. L. de Backer, P. Segers and L. M. van Bortel, 'Carotid to femoral pulse wave velocity: A comparison of real travelled aortic path lengths determined by MRI and superficial measurements', *Journal of Hypertension*, vol. 29, no. 8, pp. 1577–1582, 2011.

[82] P. Segers, J. Kips, B. Trachet, A. Swillens, S. Vermeersch, D. Mahieu, E. Rietzschel, M. De Buyzere and L. Van Bortel, 'Limitations and pitfalls of non-invasive measurement of arterial pressure wave reflections and pulse wave velocity', *Artery Research*, vol. 3, no. 2, pp. 79–88, 2009.

[83] J. Blacher, R. Asmar, S. Djane, G. M. London and M. E. Safar, 'Aortic pulse wave velocity as a marker of cardiovascular risk in hypertensive patients', *Hypertension*, vol. 33, no. 5, pp. 1111–1117, 1999.

[84] T. Shokawa, M. Imazu, H. Yamamoto, M. Toyofuku, N. Tasaki, T. Okimoto, K. Yamane and N. Kohno, 'Pulse wave velocity predicts cardiovascular mortality: Findings from the Hawaii-Los Angeles-Hiroshima study', *Circulation Journal*, vol. 69, no. 3, pp. 259–264, 2005.

[85] F. U. Mattace-Raso, T. J. van der Cammen, A. Hofman, N. M. van Popele, M. L. Bos, M. Schalekamp, R. Asmar, R. S. Reneman, A. P. Hoeks and M. M. Breteler, 'Arterial stiffness and risk of coronary heart disease and stroke: The Rotterdam Study', *Circulation*, vol. 113, no. 5, pp. 657–663, 2006.

[86] P. Boutouyrie, M. Briet, C. Collin, S. Vermeersch and B. Pannier, 'Assessment of pulse wave velocity', *Artery Research*, vol. 3, no. 1, pp. 3–8, 2009.

[87] A. Khir, A. O'Brien, J. Gibbs and K. Parker, 'Determination of wave speed and wave separation in the arteries', *Journal of Biomechanics*, vol. 34, no. 9, pp. 1145–1155, 2001.

[88] A. W. Khir, M. J. P. Swalen, J. Feng and K. H. Parker, 'Simultaneous determination of wave speed and arrival time of reflected waves using the pressure–velocity loop', *Medical & Biological Engineering & Computing*, vol. 45, no. 12, pp. 1201–1210, 2007.

[89] J. Feng and A. W. Khir, 'Determination of wave speed and wave separation in the arteries using diameter and velocity', *Journal of Biomechanics*, vol. 43, no. 3, pp. 455–462, 2010.

[90] S. I. Rabben, N. Stergiopulos, L. R. Hellevik, O. A. Smiseth, S. Slordahl, S. Urheim and B. Angelsen, 'An ultrasound-based method for determining pulse wave velocity in superficial arteries', *Journal of Biomechanics*, vol. 37, no. 10, pp. 1615–1622, 2004.

[91] R. Kowalski, R. Beare, M. Willemet, J. Alastruey, J. J. Smolich, M. M. Cheung and J. P. Mynard, 'Robust and practical non-invasive estimation of local arterial wave speed and mean blood velocity waveforms', *Physiological Measurement*, vol. 38, no. 11, pp. 2081–2099, 2017.

[92] A. Swillens and P. Segers, 'Assessment of arterial pressure wave reflection: Methodological considerations', *Artery Research*, vol. 2, no. 4, pp. 122–131, 2008.

[93] N. Stergiopulos, J. J. Meister and N. Westerhof, 'Evaluation of methods for estimation of total arterial compliance', *American Journal of Physiology-Heart and Circulatory Physiology*, vol. 268, no. 4, H1540–H1548, 1995.

[94] Z. Liu, K. P. Brin and F. C. P. Yin, 'Estimation of total arterial compliance: An improved method and evaluation of current methods', *American Journal of Physiology-Heart and Circulatory Physiology*, vol. 251, no. 3, H588–H600, 1986.

[95] N. Stergiopulos, J.-J. Meister and N. Westerhof, 'Simple and accurate way for estimating total and segmental arterial compliance: The pulse pressure method', *Annals of Biomedical Engineering*, vol. 22, no. 4, pp. 392–397, 1994.

[96] J. P. Murgo, N. Westerhof, J. P. Giolma and S. A. Altobelli, 'Aortic input impedance in normal man: Relationship to pressure wave forms.' *Circulation*, vol. 62, no. 1, pp. 105–116, 1980.

[97] P. Segers, J. Mynard, L. Taelman, S. Vermeersch and A. Swillens, 'Wave reflection: Myth or reality?', *Artery Research*, vol. 6, no. 1, pp. 7–11, 2012.

[98] T. Weber and J. A. Chirinos, 'Pulsatile arterial haemodynamics in heart failure', *European Heart Journal*, vol. 39, no. 43, pp. 3847–3854, 2018.

[99] P. Segers, M. F. O'Rourke, K. Parker, N. Westerhof, A. Hughes and on behalf of the Participants of the 2016 Workshop on Arterial Hemodynamics: Past, present and future, 'Towards a consensus on the understanding and analysis of the pulse waveform: Results from the 2016 Workshop on Arterial Hemodynamics: Past, present and future', *Artery Research*, vol. 18, pp. 75–80, 2017.

[100] P. Segers, E. R. Rietzschel, M. L. De Buyzere, D. De Bacquer, L. M. Van Bortel, G. De Backer, T. C. Gillebert and P. R. Verdonck, 'Assessment of pressure wave reflection: Getting the timing right!', *Physiological Measurement*, vol. 28, no. 9, pp. 1045–1056, 2007.

[101] N. Westerhof and B. E. Westerhof, 'A review of methods to determine the functional arterial parameters stiffness and resistance', *Journal of Hypertension*, vol. 31, no. 9, pp. 1769–1775, 2013.

[102] T. S. Phan, J. K. Li, P. Segers, M. Reddy-Koppula, S. R. Akers, S. T. Kuna, T. Gislason, A. I. Pack and J. A. Chirinos, 'Aging is associated with an earlier arrival of reflected waves without a distal shift in reflection sites', *Journal of the American Heart Association*, vol. 5, no. 9, e003733, 2016.

[103] K. H. Parker and C. J. Jones, 'Forward and backward running waves in the arteries: Analysis using the method of characteristics', *Journal of Biomechanical Engineering*, vol. 112, no. 3, pp. 322–326, 1990.

[104] A. D. Hughes and K. H. Parker, 'Forward and backward waves in the arterial system: Impedance or wave intensity analysis?', *Medical & Biological Engineering & Computing*, vol. 47, no. 2, pp. 207–210, 2009.

[105] K. H. Parker, 'An introduction to wave intensity analysis', *Medical & Biological Engineering & Computing*, vol. 47, no. 2, pp. 175–188, 2009.

[106] J. P. Mynard and J. J. Smolich, 'Novel wave power analysis linking pressure-flow waves, wave potential, and the forward and backward components of hydraulic power', *American Journal of Physiology-Heart and Circulatory Physiology*, vol. 310, no. 8, H1026–H1038, 2016.

[107] P. Reymond, Y. Bohraus, F. Perren, F. Lazeyras and N. Stergiopulos, 'Validation of a patient-specific one-dimensional model of the systemic arterial tree', *American Journal of Physiology-Heart and Circulatory Physiology*, vol. 301, no. 3, H1173–H1182, 2011.

[108] N. Stergiopulos, D. F. Young and T. R. Rogge, 'Computer simulation of arterial flow with applications to arterial and aortic stenoses', *Journal of Biomechanics*, vol. 25, no. 12, pp. 1477–1488, 1992.

[109] C. A. Taylor, T. J. Hughes and C. K. Zarins, 'Finite element modeling of blood flow in arteries', *Computer Methods in Applied Mechanics and Engineering*, vol. 158, no. 1-2, pp. 155–196, 1998.

[110] J. T. Ottesen, M. S. Olufsen and J. K. Larsen, 'Applied mathematical models in human physiology'. SIAM, 2004.

[111] S. Sherwin, V. Franke, J. Peiró and K. Parker, 'One-dimensional modelling of a vascular network in space-time variables', *Journal of Engineering Mathematics*, vol. 47, no. 3-4, pp. 217–250, 2003.

[112] J. Alastruey, K. H. Parker and S. J. Sherwin, 'Arterial pulse wave haemodynamics', in *11th International Conference on Pressure Surges*, Virtual PiE Led t/a BHR Group Lisbon, Portugal, vol. 30, 2012, pp. 401–443.

[113] N. Westerhof, J.-W. Lankhaar and B. E. Westerhof, 'The arterial windkessel', *Medical & Biological Engineering & Computing*, vol. 47, no. 2, pp. 131–141, 2009.

[114] N. Westerhof, F. Bosman, C. J. De Vries and A. Noordergraaf, 'Analog studies of the human systemic arterial tree', *Journal of Biomechanics*, vol. 2, no. 2, pp. 121–143, 1969.

[115] N. Stergiopulos, B. E. Westerhof and N. Westerhof, 'Total arterial inertance as the fourth element of the windkessel model', *American Journal of Physiology-Heart and Circulatory Physiology*, vol. 276, no. 1, H81–H88, 1999.

[116] N. Stergiopulos, P. Segers and N. Westerhof, 'Use of pulse pressure method for estimating total arterial compliance in vivo', *American Journal of Physiology-Heart and Circulatory Physiology*, vol. 276, no. 2, H424–H428, 1999.

[117] D. H. Fitchett, 'LV-arterial coupling: Interactive model to predict effect of wave reflections on LV energetics', *American Journal of Physiology-Heart and Circulatory Physiology*, vol. 261, no. 4, H1026–H1033, 1991.

[118] P. Segers, N. Stergiopulos, J. J. Schreuder, B. E. Westerhof and N. Westerhof, 'Left ventricular wall stress normalization in chronic pressure-overloaded heart: A mathematical model study', *American Journal of Physiology-Heart and Circulatory Physiology*, vol. 279, no. 3, H1120–H1127, 2000.

[119] P. Reymond, O. Vardoulis and N. Stergiopulos, 'Generic and patient-specific models of the arterial tree', *Journal of Clinical Monitoring and Computing*, vol. 26, no. 5, pp. 375–382, 2012.

[120] M. S. Olufsen, C. S. Peskin, W. Y. Kim, E. M. Pedersen, A. Nadim and J. Larsen, 'Numerical simulation and experimental validation of blood flow in arteries with structured-tree outflow conditions', *Annals of Biomedical Engineering*, vol. 28, no. 11, pp. 1281–1299, 2000.

[121] B. N. Steele, J. Wan, J. P. Ku, T. J. Hughes and C. A. Taylor, 'In vivo validation of a one-dimensional finite-element method for predicting blood flow in cardiovascular bypass grafts', *IEEE Transactions on Biomedical Engineering*, vol. 50, no. 6, pp. 649–656, 2003.

[122] M. Willemet, V. Lacroix and E. Marchandise, 'Validation of a 1D patient-specific model of the arterial hemodynamics in bypassed lower-limbs: Simulations against in vivo measurements', *Medical Engineering & Physics*, vol. 35, no. 11, pp. 1573–1583, 2013.

[123] K. S. Matthys, J. Alastruey, J. Peiró, A. W. Khir, P. Segers, P. R. Verdonck, K. H. Parker and S. J. Sherwin, 'Pulse wave propagation in a model human arterial network: Assessment of 1-D numerical simulations against in vitro measurements', *Journal of Biomechanics*, vol. 40, no. 15, pp. 3476–3486, 2007.

[124] J. Alastruey, A. W. Khir, K. S. Matthys, P. Segers, S. J. Sherwin, P. R. Verdonck, K. H. Parker and J. Peiró, 'Pulse wave propagation in a model human arterial network: Assessment of 1-D visco-elastic simulations against in vitro measurements', *Journal of Biomechanics*, vol. 44, no. 12, pp. 2250–2258, 2011.

[125] D. Bessems, C. G. Giannopapa, M. C. Rutten and F. N. van de Vosse, 'Experimental validation of a time-domain-based wave propagation model of blood flow in viscoelastic vessels', *Journal of Biomechanics*, vol. 41, no. 2, pp. 284–291, 2008.

[126] M. Saito, Y. Ikenaga, M. Matsukawa, Y. Watanabe, T. Asada and P.-Y. Lagrée, 'One-dimensional model for propagation of a pressure wave in a model of the human arterial network: Comparison of theoretical and experimental results', *Journal of Biomechanical Engineering*, vol. 133, no. 12, 2011.

[127] W. Huberts, K. Van Canneyt, P. Segers, S. Eloot, J. Tordoir, P. Verdonck, F. van De Vosse and E. Bosboom, 'Experimental validation of a pulse wave propagation model for predicting hemodynamics after vascular access surgery', *Journal of Biomechanics*, vol. 45, no. 9, pp. 1684–1691, 2012.

[128] P. Reymond, F. Perren, F. Lazeyras and N. Stergiopulos, 'Patient-specific mean pressure drop in the systemic arterial tree, a comparison between 1-D and 3-D models', *Journal of Biomechanics*, vol. 45, no. 15, pp. 2499–2505, 2012.

[129] N. Xiao, J. Alastruey and C. Alberto Figueroa, 'A systematic comparison between 1-D and 3-D hemodynamics in compliant arterial models', *International Journal for Numerical Methods in Biomedical Engineering*, vol. 30, no. 2, pp. 204–231, 2014.

[130] S. Vennin, A. Mayer, Y. Li, H. Fok, B. Clapp, J. Alastruey and P. Chowienczyk, 'Noninvasive calculation of the aortic blood pressure waveform from the flow velocity waveform: A proof of concept', *American Journal of Physiology-Heart and Circulatory Physiology*, vol. 309, no. 5, H969–H976, 2015.

[131] A. Avolio, 'Multi-branched model of the human arterial system', *Medical and Biological Engineering and Computing*, vol. 18, no. 6, pp. 709–718, 1980.

[132] J. Alastruey, K. Parker, J. Peiró, S. Byrd and S. Sherwin, 'Modelling the circle of Willis to assess the effects of anatomical variations and occlusions on cerebral flows', *Journal of Biomechanics*, vol. 40, no. 8, pp. 1794–1805, 2007.

[133] A. Swillens, L. Lanoye, J. De Backer, N. Stergiopulos, P. R. Verdonck, F. Vermassen and P. Segers, 'Effect of an abdominal aortic aneurysm on wave reflection in the aorta', *IEEE Transactions on Biomedical Engineering*, vol. 55, no. 5, pp. 1602–1611, 2008.

[134] M. H. Heusinkveld, W. Huberts, J. Lumens, T. Arts, T. Delhaas and K. D. Reesink, 'Large vessels as a tree of transmission lines incorporated in the CircAdapt whole-heart model: A computational tool to examine heart-vessel interaction', *PLoS Computational Biology*, vol. 15, no. 7, e1007173, 2019.

[135] K. Kadry, S. Pagoulatou, Q. Mercier, G. Rovas, V. Bikia, H. Müller, D. Adamopoulos and N. Stergiopulos, 'Biomechanics of diastolic dysfunction: A one-dimensional computational modeling approach', *American Journal of Physiology-Heart and Circulatory Physiology*, vol. 319, no. 4, H882–H892, 2020.

[136] P. Reymond, P. Crosetto, S. Deparis, A. Quarteroni and N. Stergiopulos, 'Physiological simulation of blood flow in the aorta: Comparison of hemodynamic indices as predicted by 3-D FSI, 3-D rigid wall and 1-D models', *Medical Engineering & Physics*, vol. 35, no. 6, pp. 784–791, 2013.

[137] L. Formaggia, J.-F. Gerbeau, F. Nobile and A. Quarteroni, 'On the coupling of 3D and 1D Navier–Stokes equations for flow problems in compliant vessels', *Computer Methods in Applied Mechanics and Engineering*, vol. 191, no. 6-7, pp. 561–582, 2001.

[138] P. J. Blanco, S. M. Watanabe, M. A. R. F. Passos, P. A. Lemos and R. A. Feijóo, 'An anatomically detailed arterial network model for one-dimensional computational hemodynamics', *IEEE Trans Biomed Eng*, vol. 62, no. 2, pp. 736–753, 2015.

[139] G. A. Holzapfel, 'Nonlinear Solid Mechanics. A Continuum Approach for Engineering'. Wiley, 2000.

[140] G. J. Langewouters, 'Visco-elasticity of the human aorta in vitro in relation to pressure and age', PhD thesis, 1982.

[141] G. J. Langewouters, K. H. Wesseling and W. J. A. Goedhard, 'The static elastic properties of 45 human thoracic and 20 abdominal aortas in vitro and the parameters of a new model', *Journal of Biomechanics*, vol. 17, no. 6, pp. 425–435, 1984.

[142] J. R. Womersley, 'Method for the calculation of velocity, rate of flow and viscous drag in arteries when the pressure gradient is known', *The Journal of Physiology*, vol. 127, no. 3, p. 553, 1955.

[143] J. R. Womersley, ‘An elastic tube theory of pulse transmission and oscillatory flow in mammalian arteries’, Aerospace Research Labs Wright-Patterson AFB OH, Tech. Rep., 1957.

[144] K. Sagawa, ‘The end-systolic pressure-volume relation of the ventricle: Definition, modifications and clinical use.’ *Circulation*, vol. 63, no. 6, pp. 1223–1227, 1981.

[145] K. Sagawa, ‘Cardiac contraction and the pressure-volume relationship’. Oxford, UK: Oxford University Press, 1988, p. 15.

[146] H. Senzaki, C.-H. Chen and D. A. Kass, ‘Single-beat estimation of end-systolic pressure-volume relation in humans. A new method with the potential for noninvasive application’, *Circulation*, vol. 94, no. 10, pp. 2497–2506, 1996.

[147] D. Campos Arias, F. Londono, T. Rodríguez Moliner, D. Georgakopoulos, N. Stergiopulos and P. Segers, ‘Hemodynamic impact of the C-Pulse cardiac support device: A one-dimensional arterial model study’, *Artificial Organs*, vol. 41, no. 10, E141–E154, 2017.

[148] A. Kantrowitz, R. R. Cardona and P. S. Freed, ‘Weaning from the intraaortic balloon pump’, in *Comprehensive Intraaortic Balloon Counterpulsation.* S. J. Quaal, Ed., 2nd ed. Sydney: Mosby, 1993, pp. 398–410.

[149] S. Scheidt, G. Wilner, H. Mueller, D. Summers, M. Lesch, G. Wolff, J. Krakauer, M. Rubenfire, P. Fleming, G. Noon, N. Oldham, T. Killip and A. Kantrowitz, ‘Intra-aortic balloon counterpulsation in cardiogenic shock. Report of a cooperative clinical trial’, *New England Journal of Medicine*, vol. 288, no. 19, pp. 979–984, 1973.

[150] R. Umakanthan, S. J. Hoff, N. Solenkova, M. A. Wigger, M. E. Keebler, A. Lenneman, M. Leacche, T. G. DiSalvo, H. Ooi, A. J. Naftilan, J. G. Byrne and R. M. Ahmad, ‘Benefits of ambulatory axillary intra-aortic balloon pump for circulatory support as bridge to heart transplant’, *The Journal of Thoracic and Cardiovascular Surgery*, vol. 143, no. 5, pp. 1193–1197, 2012.

[151] M. Capoccia, C. T. Bowles, J. R. Pepper, N. R. Banner and A. R. Simon, ‘Evidence of clinical efficacy of counterpulsation therapy methods’, *Heart Failure Reviews*, vol. 20, no. 3, pp. 323–335, 2015.

[152] K. D. Sjauw, A. E. Engström, M. M. Vis, R. J. van der Schaaf, J. Baan, K. T. Koch, R. J. de Winter, J. J. Piek, J. G. Tijssen and J. P. Henriques, ‘A systematic review and meta-analysis of intra aortic balloon pump therapy in ST-elevation myocardial infarction: Should we change the guidelines?’, *European Heart Journal*, vol. 30, no. 4, pp. 459–468, 2009.

[153] J. M. White and P. N. Ruygrok, 'Intra-aortic balloon counterpulsation in contemporary practice. Where are we?', *Heart, Lung and Circulation*, vol. 24, no. 4, pp. 335–341, 2015.

[154] A. N. Davies, W. S. Peters, T. Su, C. E. Sullivan, T. Perkidides, F. P. Milsom and G. White, 'Extra-ascending aortic versus intra-descending aortic balloon counterpulsation. Effect on coronary artery blood flow', *Heart Lung and Circulation*, vol. 14, no. 3, pp. 178–186, 2005.

[155] M. E. Legget, W. S. Peters, F. P. Milsom, J. S. Clark, T. M. West, R. L. French and A. F. Merry, 'Extra-aortic balloon counterpulsation: An intraoperative feasibility study', *Circulation*, vol. 112, no. 9_supplement, pp. I-26–I-31, 2005.

[156] C. S. Hayward, W. S. Peters, A. F. Merry, P. N. Ruygrok, P. Jansz, G. O'Driscoll, R. I. Larbalestier, J. A. Smith, B. Ho, M. E. Legget and F. P. Milsom, 'Chronic extra-aortic balloon counterpulsation: First-in-human pilot study in end-stage heart failure', *The Journal of Heart and Lung Transplantation*, vol. 29, no. 12, pp. 1427–1432, 2010.

[157] A. Cheng, G. Monreal, M. L. William, M. Sobieski and M. S. Slaughter, 'Extended extra-aortic counterpulsation with the C-Pulse device does not alter aortic wall structure', *ASAIO Journal*, vol. 60, no. 6, e5–e7, 2014.

[158] W. T. Abraham, S. Aggarwal, S. D. Prabhu, R. Cecere, S. V. Pamboukian, A. J. Bank, B. Sun, W. E. Pae Jr, C. S. Hayward, P. M. McCarthy, W. S. Peters, P. Verta, M. S. Slaughter and for the C-Pulse Trial Study Group, 'Ambulatory extra-aortic counterpulsation in patients with moderate to severe chronic heart failure', *JACC: Heart Failure*, vol. 2, no. 5, pp. 526–533, 2014.

[159] V. L. Sales and P. M. McCarthy, 'Understanding the C-Pulse device and its potential to treat heart failure', *Current Heart Failure Reports*, vol. 7, no. 1, pp. 27–34, 2010.

[160] A. Zambanini, S. L. Cunningham, K. H. Parker, A. W. Khir, S. A. McG. Thom and A. D. Hughes, 'Wave-energy patterns in carotid, brachial, and radial arteries: A noninvasive approach using wave-intensity analysis', *American Journal of Physiology-Heart and Circulatory Physiology*, vol. 289, no. 1, H270–H276, 2005.

[161] A. M. Dell'Aquila, S. R. Schneider, P. Risso, H. Welp, D. G. Glockner, S. Alles, J. R. Sindermann and M. Scherer, 'Is implantation of a left ventricular assist device in patients with critical or impending cardiogenic shock an absolute contraindication? Looking back at our past experience trying to identify contraindicative risk factors', *Artificial Organs*, vol. 39, no. 12, pp. 998–1004, 2015.

[162] J. E. Davies, Z. I. Whinnett, D. F. Francis, C. H. Manisty, J. Aguado-Sierra, K. Willson, R. A. Foale, I. S. Malik, A. D. Hughes, K. H. Parker and J. Mayet, 'Evidence of a dominant backward-propagating "suction" wave responsible for diastolic coronary filling in humans, attenuated in left ventricular hypertrophy.' *Circulation*, vol. 113, no. 14, pp. 1768–1778, 2006.

[163] C. Kolyva, G. M. Pantalos, G. A. Giridharan, J. R. Pepper and A. W. Khir, 'Discerning aortic waves during intra-aortic balloon pumping and their relation to benefits of counterpulsation in humans', *Journal of Applied Physiology*, vol. 107, no. 5, pp. 1497–1503, 2009.

[164] A. Schulz, T. Krabatsch, J. D. Schmitto, R. Hetzer, M. Seidel, P. M. Dohmen and H. Hotz, 'Preliminary results from the C-Pulse® OPTIONS HF European Multicenter Post-Market Study', *Medical Science Monitor Basic Research*, vol. 22, pp. 14–19, 2016.

[165] D. Campos Arias, N. Stergiopulos, T. Rodríguez Moliner and P. Segers, 'Mapping the site-specific accuracy of loop-based local pulse wave velocity estimation and reflection magnitude: A 1d arterial network model analysis', *Physiological Measurement*, vol. 40, no. 7, 14pp, 2019.

[166] K. Shirai, N. Hiruta, M. Song, T. Kurosu, J. Suzuki, T. Tomaru, Y. Miyashita, A. Saiki, M. Takahashi, K. Suzuki and M. Takata, 'Cardio-Ankle Vascular Index (CAVI) as a novel indicator of arterial stiffness: Theory, evidence and perspectives', *Journal of Atherosclerosis and Thrombosis*, vol. 18, no. 11, pp. 924–938, 2011.

[167] A. Swillens, L. Taelman, J. Degroote, J. Vierendeels and P. Segers, 'Comparison of non-invasive methods for measurement of local pulse wave velocity using FSI-simulations and in vivo data', *Annals of Biomedical Engineering*, vol. 41, no. 7, pp. 1567–1578, 2013.

[168] P. Segers, A. Swillens, L. Taelman and J. Vierendeels, 'Wave reflection leads to over- and underestimation of local wave speed by the PU- and QA-loop methods: Theoretical basis and solution to the problem', *Physiological Measurement*, vol. 35, no. 5, pp. 847–861, 2014.

[169] A. Borlotti, Y. Li, K. H. Parker and A. W. Khir, 'Experimental evaluation of local wave speed in the presence of reflected waves', *Journal of Biomechanics*, vol. 47, no. 1, pp. 87–95, 2014.

[170] A. Borlotti, A. W. Khir, E. R. Rietzschel, M. L. De Buyzere, S. Vermeersch and P. Segers, 'Noninvasive determination of local pulse wave velocity and wave intensity: Changes with age and gender in the carotid and femoral arteries of healthy human', *Journal of Applied Physiology*, vol. 113, no. 5, pp. 727–735, 2012.

[171] J. Alastruey, 'Numerical assessment of time-domain methods for the estimation of local arterial pulse wave speed', *Journal of Biomechanics*, vol. 44, no. 5, pp. 885–891, 2011.

[172] M. Negoita, A. D. Hughes, K. H. Parker and A. W. Khir, 'Non-invasive technique for determining local pulse wave velocity in humans ascending aorta', in *2017 Computing in Cardiology (CinC)*, IEEE, vol. 44, 2017, pp. 1–4.

[173] A. W. Khir, M. Y. Henein, T. Koh, S. K. Das, K. H. Parker and D. G. Gibson, 'Arterial waves in humans during peripheral vascular surgery', *Clinical Science*, vol. 101, no. 6, pp. 749–757, 2001.

[174] L. Vera, D. Campos Arias, S. Muylle, N. Stergiopulos, P. Segers and G. van Loon, 'A 1D computer model of the arterial circulation in horses: An important resource for studying global interactions between heart and vessels under normal and pathological conditions', *PLoS One*, vol. 14, no. 8, e0221425, 2019.

[175] J. P. Mynard and J. J. Smolich, 'One-dimensional haemodynamic modeling and wave dynamics in the entire adult circulation', *Annals of Biomedical Engineering*, vol. 43, no. 6, pp. 1443–1460, 2015.

[176] D. Bessems, M. Rutten and F. Van De Vosse, 'A wave propagation model of blood flow in large vessels using an approximate velocity profile function', *Journal of Fluid Mechanics*, vol. 580, pp. 145–168, 2007.

[177] R. R. Wemple and L. F. Mockros, 'Pressure and flow in the systemic arterial system', *Journal of Biomechanics*, vol. 5, no. 6, pp. 629–641, 1972.

[178] O. Vardoulis, E. Coppens, B. Martin, P. Reymond, P. Tozzi and N. Stergiopulos, 'Impact of aortic grafts on arterial pressure: A computational fluid dynamics study', *European Journal of Vascular and Endovascular Surgery*, vol. 42, no. 5, pp. 704–710, 2011.

[179] S. Epstein, M. Willemet, P. J. Chowienczyk and J. Alastruey, 'Reducing the number of parameters in 1D arterial blood flow modeling: Less is more for patient-specific simulations', *American Journal of Physiology-Heart and Circulatory Physiology*, vol. 309, no. 1, H222–H234, 2015.

[180] T. Dobroserdova, S. Simakov, T. Gamilov, R. Pryamonosov and E. Sakharova, 'Patient-specific blood flow modelling for medical applications', in *MATEC Web of Conferences*, EDP Sciences, vol. 76, 2016, p. 05 001.

[181] T. Gamilov, Y. Ivanov, P. Kopylov, S. Simakov and Y. Vassilevski, 'Patient specific haemodynamic modeling after occlusion treatment in leg', *Mathematical Modelling of Natural Phenomena*, vol. 9, no. 6, pp. 85–97, 2014.

[182] M. Ploeg, V. Saey, G. van Loon and C. Delesalle, 'Thoracic aortic rupture in horses', *Equine Veterinary Journal*, vol. 49, no. 3, pp. 269–274, 2017.

[183] M. Ploeg, V. Saey, C. De Bruijn, A. Gröne, K. Chiers, G. van Loon, R. Ducatelle, P. Van Weeren, W. Back and C. Delesalle, 'Aortic rupture and aorto-pulmonary fistulation in the Friesian horse: Characterisation of the clinical and gross post mortem findings in 24 cases', *Equine Veterinary Journal*, vol. 45, no. 1, pp. 101–106, 2013.

[184] C. H. Lyle, K. Blissitt, R. Kennedy, B. Mc Gorum, J. Newton, T. Parkin, A. Stirk and L. Boden, 'Risk factors for race-associated sudden death in Thoroughbred racehorses in the UK (2000–2007)', *Equine Veterinary Journal*, vol. 44, no. 4, pp. 459–465, 2012.

[185] C. Lyle, F. A. Uzal, B. McGorum, H. Aida, K. Blissitt, J. Case, J. Charles, I. Gardner, N. Horadagoda, K. Kusano, K. Lam, J. D. Pack, T. Parkin, R. Slocombe, B. Stewart and L. Boden, 'Sudden death in racing Thoroughbred horses: An international multicentre study of post mortem findings', *Equine Veterinary Journal*, vol. 43, no. 3, pp. 324–331, 2011.

[186] H. Gelberg, J. Zachary, J. Everitt, R. Jensen and D. Smetzer, 'Sudden death in training and racing Thoroughbred horses', *Journal of the American Veterinary Medical Association*, vol. 187, no. 12, pp. 1354–1356, 1985.

[187] H. Platt, 'Sudden and unexpected deaths in horses: A review of 69 cases', *British Veterinary Journal*, vol. 138, no. 5, pp. 417–429, 1982.

[188] T. Ueno, Y. Nambo, Y. Tajima and T. Umemura, 'Pathology of lethal peripartum broad ligament haematoma in 31 thoroughbred mares', *Equine Veterinary Journal*, vol. 42, no. 6, pp. 529–533, 2010.

[189] N. M. Williams and U. K. Bryant, 'Periparturient arterial rupture in mares: A postmortem study', *Journal of Equine Veterinary Science*, vol. 32, no. 5, pp. 281–284, 2012.

[190] J. Frederick, S. Giguère, K. Butterworth, A. Pellegrini-Masini, R. Casas-Dolz and M. M. Turpin, 'Severe phenylephrine-associated hemorrhage in five aged horses', *Journal of the American Veterinary Medical Association*, vol. 237, no. 7, pp. 830–834, 2010.

[191] R. Barone, 'Anatomie comparée des mammifères domestiques: Angiologie', 2nd ed. Vigot, 2011, vol. 5.

[192] J. Boegli, C. C. Schwarzwald and K. J. Mitchell, 'Diagnostic value of noninvasive pulse pressure measurements in warmblood horses with aortic regurgitation', *Journal of Veterinary Internal Medicine*, vol. 33, no. 3, pp. 1446–1455, 2019.

[193] D. C. Poole and H. H. Erickson, 'Highly athletic terrestrial mammals: Horses and dogs', *Comprehensive Physiology*, vol. 1, no. 1, pp. 1–37, 2011.

[194] A. L. Raisis, L. Young, H. Meire, P. M. Taylor, K. Walsh and P. Lekeux, 'Variability of doppler ultrasound measurements of hindlimb blood flow in conscious horses', *Equine Veterinary Journal*, vol. 32, no. 2, pp. 125–132, 2000.

[195] C. M. Brown and J. R. Holmes, 'Haemodynamics in the horse: 2. Intracardiac, pulmonary arterial and aortic pressures', *Equine Veterinary Journal*, vol. 10, no. 4, pp. 207–215, 1978.

[196] S. M. Reed, W. M. Bayly and D. C. Sellon, 'Equine Internal Medicine-E-Book', 4th ed. Elsevier Health Sciences, 2017, p. 418.

[197] C. M. Brown and J. R. Holmes, 'Haemodynamics in the horse: 3. Duration of the phases of the cardiac cycle', *Equine Veterinary Journal*, vol. 10, no. 4, pp. 216–223, 1978.

[198] L. Aslanidou, B. Trachet, P. Reymond, R. A. Fraga-Silva, P. Segers and N. Stergiopulos, 'A 1D model of the arterial circulation in mice', *ALTEX*, vol. 33, no. 1, pp. 13–28, 2016.

[199] M. F. O'Rourke, 'Pressure and flow waves in systemic arteries and the anatomical design of the arterial system.' *Journal of Applied Physiology*, vol. 23, no. 2, pp. 139–149, 1967.

[200] G. G. Belz, 'Elastic properties and windkessel function of the human aorta', *Cardiovascular Drugs and Therapy*, vol. 9, no. 1, pp. 73–83, 1995.

[201] D. Campos Arias, M. L. De Buyzere, J. A. Chirinos, E. R. Rietzschel and P. Segers, 'Longitudinal changes of input impedance, pulse wave velocity, and wave reflection in a middle-aged population: The Asklepios study', *Hypertension*, vol. 77, no. 4, pp. 1154–1165, 2021.

[202] P. Hallock, 'Arterial elasticity in man in relation to age as evaluated by the pulse wave velocity method', *Archives of Internal Medicine*, vol. 54, no. 5, pp. 770–798, 1934.

[203] M. Eliakim, D. Sapoznikov and J. Weinman, 'Pulse wave velocity in healthy subjects and in patients with various disease states', *American Heart Journal*, vol. 82, no. 4, pp. 448–457, 1971.

[204] A. U. Ferrari, A. Radaelli and M. Centola, 'Invited review: Aging and the cardiovascular system', *Journal of Applied Physiology*, vol. 95, no. 6, pp. 2591–2597, 2003.

[205] H.-Y. Lee and B.-H. Oh, 'Aging and arterial stiffness', *Circulation Journal*, vol. 74, no. 11, pp. 2257–2262, 2010.

[206] G. de Simone, M. J. Roman, M. J. Koren, G. A. Mensah, A. Ganau and R. B. Devereux, 'Stroke volume/pulse pressure ratio and cardiovascular risk in arterial hypertension', *Hypertension*, vol. 33, no. 3, pp. 800–805, 1999.

[207] T. Weber, J. Auer, M. F. O'Rourke, E. Kvas, E. Lassnig, G. Lamm, N. Stark, M. Rammer and B. Eber, 'Increased arterial wave reflections predict severe cardiovascular events in patients undergoing percutaneous coronary interventions', *European Heart Journal*, vol. 26, no. 24, pp. 2657–2663, 2005.

[208] C. U. Choi, E. B. Park, S. Y. Suh, J. W. Kim, E. J. Kim, S.-W. Rha, H. S. Seo, D. J. Oh and C. G. Park, 'Impact of aortic stiffness on cardiovascular disease in patients with chest pain: Assessment with direct intra-arterial measurement', *American Journal of Hypertension*, vol. 20, no. 11, pp. 1163–1169, 2007.

[209] P. Boutouyrie, S. Laurent, A. Benetos, X. J. Girerd, A. Hoeks and M. E. Safar, 'Opposing effects of ageing on distal and proximal large arteries in hypertensives', *Journal of Hypertension. Supplement: official journal of the International Society of Hypertension*, vol. 10, no. 6, S87–S91, 1992.

[210] G. F. Mitchell, Y. Lacourcière, J.-P. Ouellet, J. L. Izzo, J. Neutel, L. J. Kerwin, A. J. Block and M. A. Pfeffer, 'Determinants of elevated pulse pressure in middle-aged and older subjects with uncomplicated systolic hypertension. The role of proximal aortic diameter and the aortic pressure-flow relationship', *Circulation*, vol. 108, no. 13, pp. 1592–1598, 2003.

[211] G. F. Mitchell, C. Y. Guo, E. J. Benjamin, M. G. Larson, M. J. Keyes, J. A. Vita, R. S. Vasan and D. Levy, 'Cross-sectional correlates of increased aortic stiffness in the community: The Framingham Heart Study', *Circulation*, vol. 115, no. 20, pp. 2628–2636, 2007.

[212] W. W. Nichols, M. F. O'Rourke, A. P. Avolio, T. Yaginuma, J. P. Murgo, C. J. Pepine and C. R. Conti, 'Effects of age on ventricular-vascular coupling', *The American Journal of Cardiology*, vol. 55, no. 9, pp. 1179–1184, 1985.

[213] T. Weber, M. F. O'Rourke, M. Ammer, E. Kvas, C. Punzengruber and B. Eber, 'Arterial stiffness and arterial wave reflections are associated with systolic and diastolic function in patients with normal ejection fraction', *American Journal of Hypertension*, vol. 21, no. 11, pp. 1194–1202, 2008.

[214] A. Scuteri, S. S. Najjar, D. C. Muller, R. Andres, H. Hougaku, E. J. Metter and E. G. Lakatta, 'Metabolic syndrome amplifies the age-associated increases in vascular thickness and stiffness', *Journal of the American College of Cardiology*, vol. 43, no. 8, pp. 1388–1395, 2004.

[215] J. A. Chirinos, 'Discerning the age-related heterogeneity in heart failure with preserved ejection fraction', *Journal of the American College of Cardiology*, vol. 74, no. 5, pp. 613–616, 2019.

[216] G. Verbeke and G. Molenberghs, 'Linear Mixed Models for Longitudinal Data'. New-York: Springer, 2000.

[217] G. Molenberghs, H. Thijs, I. Jansen, C. Beunckens, M. G. Kenward, C. Mallinckrodt and R. J. Carroll, 'Analyzing incomplete longitudinal clinical trial data', *Biostatistics*, vol. 5, no. 3, pp. 445–464, 2004.

[218] C. H. Morrell, L. J. Brant and L. Ferrucci, 'Model choice can obscure results in longitudinal studies', *Journals of Gerontology Series A: Biomedical Sciences and Medical Sciences*, vol. 64, no. 2, pp. 215–222, 2009.

[219] P. C. Johnson, 'Extension of Nakagawa & Schielzeth's R^2_{GLMM} to random slopes models', *Methods in Ecology and Evolution*, vol. 5, no. 9, pp. 944–946, 2014.

[220] S. Nakagawa, P. C. Johnson and H. Schielzeth, 'The coefficient of determination R^2 and intra-class correlation coefficient from generalized linear mixed-effects models revisited and expanded', *Journal of the Royal Society Interface*, vol. 14, no. 134, p. 20 170 213, 2017.

[221] C. W. Tsao, F. Washington, S. K. Musani, L. L. Cooper, A. Tripathi, N. M. Hamburg, E. J. Benjamin, R. S. Vasan, G. F. Mitchell and E. R. Fox, 'Clinical correlates of aortic stiffness and wave amplitude in black men and women in the community', *Journal of the American Heart Association*, vol. 7, no. 21, e008431, 2018.

[222] M. F. O'Rourke and C. S. Hayward, 'Arterial stiffness, gender and heart rate', *Journal of Hypertension*, vol. 21, no. 3, pp. 487–490, 2003.

[223] V. Subramanya, B. Ambale-Venkatesh, Y. Ohyama, D. Zhao, C. C. Nwabuo, W. S. Post, E. Guallar, P. Ouyang, S. J. Shah, M. A. Allison, C. E. Ndumele, D. Vaidya, D. A. Bluemke, J. A. Lima and E. D. Michos, 'Relation of sex hormone levels with prevalent and 10-year change in aortic distensibility assessed by MRI: The Multi-Ethnic Study of Atherosclerosis', *American Journal of Hypertension*, vol. 31, no. 7, pp. 774–783, 2018.

[224] J. J. DuPont, R. M. Kenney, A. R. Patel and I. Z. Jaffe, 'Sex differences in mechanisms of arterial stiffness', *British Journal of Pharmacology*, vol. 176, no. 21, pp. 4208–4225, 2019.

[225] A. A. Malayeri, S. Natori, H. Bahrami, A. G. Bertoni, R. Kronmal, J. A. Lima and D. A. Bluemke, 'Relation of aortic wall thickness and distensibility to cardiovascular risk factors (from the Multi-Ethnic Study of Atherosclerosis [MESA])', *The American Journal of Cardiology*, vol. 102, no. 4, pp. 491–496, 2008.

[226] K.-L. Wang, H.-M. Cheng, S.-H. Sung, S.-Y. Chuang, C.-H. Li, H. A. Spurgeon, C.-T. Ting, S. S. Najjar, E. G. Lakatta, F. C. Yin *et al.*, 'Wave reflection and arterial stiffness in the prediction of 15-year all-cause and cardiovascular mortalities: A community-based study', *Hypertension*, vol. 55, no. 3, pp. 799–805, 2010.

[227] G. F. Mitchell, 'Effects of central arterial aging on the structure and function of the peripheral vasculature: Implications for end-organ damage', *Journal of Applied Physiology*, vol. 105, no. 5, pp. 1652–1660, 2008.

[228] P. H. Charlton, J. Mariscal Harana, S. Vennin, Y. Li, P. Chowienczyk and J. Alastruey, 'Modeling arterial pulse waves in healthy aging: A database for in silico evaluation of hemodynamics and pulse wave indexes', *American Journal of Physiology-Heart and Circulatory Physiology*, vol. 317, no. 5, H1062–H1085, 2019.

[229] A. L. Beale, S. Nanayakkara, L. Segan, J. A. Mariani, M. T. Maeder, V. van Empel, D. Vizi, S. Evans, C. S. Lam and D. M. Kaye, 'Sex differences in heart failure with preserved ejection fraction pathophysiology: A detailed invasive hemodynamic and echocardiographic analysis', *JACC: Heart Failure*, vol. 7, no. 3, pp. 239–249, 2019.

[230] Y. Sotomi, S. Hikoso, D. Nakatani, H. Mizuno, K. Okada, T. Dohi, T. Kitamura, A. Sunaga, H. Kida, B. Oeun *et al.*, 'Sex differences in heart failure with preserved ejection fraction', *Journal of the American Heart Association*, vol. 10, no. 5, e018574, 2021.

[231] K. Moorhead, C. Doran, J. Chase and T. David, 'Lumped parameter and feedback control models of the auto-regulatory response in the circle of Willis', *Computer Methods in Biomechanics and Biomedical Engineering*, vol. 7, no. 3, pp. 121–130, 2004.

[232] J. Alastruey, S. Moore, K. Parker, T. David, J. Peiró and S. Sherwin, 'Reduced modelling of blood flow in the cerebral circulation: Coupling 1-D, 0-D and cerebral auto-regulation models', *International Journal for Numerical Methods in Fluids*, vol. 56, no. 8, pp. 1061–1067, 2008.

[233] A. Kantrowitz and A. Kantrowitz, 'Experimental augmentation of coronary flow by retardation of the arterial pressure pulse', *Surgery*, vol. 34, no. 4, pp. 678–687, 1953.

[234] H. v. Hörnicke, W. v. Engelhardt and H.-J. Ehrlein, 'Effect of exercise on systemic blood pressure and heart rate in horses', *Pflügers Archiv*, vol. 372, no. 1, pp. 95–99, 1977.

[235] W. O. Reece, H. H. Erickson, J. P. Goff and E. E. Uemura, 'Dukes' physiology of domestic animals', 13th ed. John Wiley & Sons, 2015.

[236] L. Vera, G. Van Steenkiste, A. Decloedt, K. Chiers and G. van Loon, 'Age-related differences in blood pressure, ultrasound-derived arterial diameters and arterial wall stiffness parameters in horses', *Equine Veterinary Journal*, vol. 52, no. 6, pp. 868–875, 2020.

[237] J. L. Rodgers, J. Jones, S. I. Bolleddu, S. Vanthenapalli, L. E. Rodgers, K. Shah, K. Karia and S. K. Panguluri, 'Cardiovascular risks associated with gender and aging', *Journal of Cardiovascular Development and Disease*, vol. 6, no. 2, p. 19, 2019.

[238] H. B. Dwight, 'Tables of integrals and other mathematical data', 3rd ed. New York: The Macmillan Company, 1957.